

Electronic Thesis and Dissertation Repository

8-19-2011 12:00 AM

On Developing Novel Energy-Relates Nanostructured Materials by Atomic Layer Deposition

Xiangbo Meng, *The University of Western Ontario*

Supervisor: Dr. Sun, Xueliang, *The University of Western Ontario*

A thesis submitted in partial fulfillment of the requirements for the Doctor of Philosophy degree in Mechanical and Materials Engineering

© Xiangbo Meng 2011

Follow this and additional works at: <https://ir.lib.uwo.ca/etd>

 Part of the [Nanoscience and Nanotechnology Commons](#), and the [Other Materials Science and Engineering Commons](#)

Recommended Citation

Meng, Xiangbo, "On Developing Novel Energy-Relates Nanostructured Materials by Atomic Layer Deposition" (2011). *Electronic Thesis and Dissertation Repository*. 247.
<https://ir.lib.uwo.ca/etd/247>

This Dissertation/Thesis is brought to you for free and open access by Scholarship@Western. It has been accepted for inclusion in Electronic Thesis and Dissertation Repository by an authorized administrator of Scholarship@Western. For more information, please contact wlsadmin@uwo.ca.

**ON DEVELOPING NOVEL ENERGY-RELATED
NANOSTRUCTURED MATERIALS BY ATOMIC LAYER
DEPOSITION**

(Spine Title: Nanostructured Materials by Atomic Layer Deposition)

(Thesis Format: Integrated-Article)

By

Xiangbo Meng

Graduate Program in Engineering Science
Department of Mechanical and Materials Engineering

A thesis submitted in partial fulfillment
of the requirements for the degree of
Doctor of Philosophy

The School of Graduate and Postdoctoral Studies
The University of Western Ontario
London, Ontario, Canada

© Xiangbo Meng 2011

THE UNIVERSITY OF WESTERN ONTARIO
THE SCHOOL OF GRADUATE AND POSTDOCTORAL STUDIES

CERTIFICATION OF EXAMINATION

Supervisor

Dr. Xueliang (Andy) Sun

Examiners

Dr. Sean Barry

Co-Supervisor

Dr. Paul Charpentier

Dr. Jun Yang

Supervisory Committee

Dr. Jun Yang

Dr. Jeffrey T. Wood

The thesis by

Xiangbo Meng

entitled:

**On Developing Novel Energy-related Nanostructured Materials by
Atomic Layer Deposition**

is accepted in partial fulfillment of the
requirements for the degree of
Doctor of Philosophy

Date: August 19, 2011

Dr. Barry Hoffmaster
Chair of the Thesis Examination Board

ABSTRACT

This thesis presents the fabrication of a series of novel nanostructured materials using atomic layer deposition (ALD). In contrast to traditional methods including chemical vapor deposition (CVD), physical vapor deposition (PVD), and solution-based processes, ALD benefits the synthesis processes of nanostructures with many unrivalled advantages such as atomic-scale control, low temperature, excellent uniformity and conformality. Depending on the employed precursors, substrates, and temperatures, the ALD processes exhibited different characteristics. In particular, ALD has capabilities in fine-tuning compositions and structural phases. In return, the synthesis and the resultant nanostructured materials show many novelties.

This thesis covers ALD processes of four different metal oxides including iron oxide, tin oxide, titanium oxide, and lithium titanium oxide. Four different substrates were used in the aforementioned ALD processes, i.e., undoped carbon nanotubes (CNTs), nitrogen-doped CNTs (N-CNTs), porous templates of anodic aluminum oxide (AAO), and graphene nanosheets (GNS). In practice, owing to their distinguished properties and structural characters, the substrates contributed to various novel nanostructures including nanotubes, coaxial core-shell nanotubes, and three-dimensional (3D) architectures. In addition, the surface chemistry of the substrates and their interactions with ALD precursors also were considered.

The ALD process of iron oxide (ALD-Fe₂O₃) was the first one studied and it was fulfilled on both undoped CNTs and N-CNTs by using ferrocene and oxygen as precursors. It was found that N-CNTs are better than undoped CNTs for the ALD-Fe₂O₃, for they provide reactive sites directly due to their inherent properties. In contrast, undoped CNTs need pretreatment via covalent acid oxidation or non-covalent modification to create reactive sites before the ALD-Fe₂O₃ could proceed on their surface. This work resulted in different CNT-Fe₂O₃ core-shell structures with controlled growth of crystalline α -Fe₂O₃.

Another metal oxide, tin dioxide (SnO₂) was performed using tin chloride (SnCl₄) and water as ALD precursors. It was synthesized into different nanostructures based on N-

CNTs, AAO, and GNS. The work on N-CNTs disclosed that the ALD-SnO₂ is favored by doped nitrogen atoms but the effects of different nitrogen-doping configurations vary with growth temperatures. In comparison, the ALD-SnO₂ on AAO and GNS mainly relies on hydroxyl groups. A common finding from the studies is that growth temperatures influence the resultant SnO₂, leading to amorphous, crystalline phase, or the mixtures of the aforementioned two. In addition, the cyclic nature of ALD contributes to controlled growth of SnO₂. Based on the results from the ALD-SnO₂ on AAO, it was concluded that the ALD-SnO₂ experience three different growth modes with temperature, i.e., layer-by-layer, layer-by-particle, and evolutionary particles. The layers are in amorphous phase while the particles are in crystalline rutile phase. The aforementioned understandings on ALD-SnO₂ led to pure SnO₂ nanotubes based on AAO, CNT-SnO₂ core-shell coaxial nanotubes, and GNS-based SnO₂ 3D architectures with controlled growth and structural phases.

The third metal oxide, titanium dioxide (TiO₂) was deposited using titanium isopropoxide (TTIP) and water as ALD precursors. It was found that the ALD-TiO₂ is tunable from amorphous to crystalline anatase phase with temperature while the resultant deposition is controllable from nanoparticles to nanofilms as well. Based on different substrate, i.e., AAO, acid-pretreated CNTs, and GNS, TiO₂ was fabricated with different nanostructures including nanotubes, core-shell coaxial nanotubes, and 3D architectures. In particular, the resultant nanostructures are distinguished with controlled phases and morphologies of TiO₂.

Different from the above binary metal oxides, the last metal oxide, lithium titanium oxide (Li₄Ti₅O₁₂, LTO) is a ternary compound. The route for ALD-LTO is based on combining and tuning two sub-ALD systems. One sub-ALD system is for TiO₂ using TTIP and water, and another sub-ALD system is for lithium-containing films using lithium tert-butoxide (LTB) and water as precursors. It was revealed that, through suitably matching the ratios of the two sub-ALD systems and annealing the resultant films, LTO is successfully synthesized on N-CNTs. However, this pioneering work shows a bit rutile TiO₂ with LTO, and thus further effort is needed in future work.

In summary, the discoveries in this thesis contribute to a better understanding on various ALD systems and provide a series of novel nanostructured materials for various potential applications. In particular, these materials are promising candidate materials for energy-related devices, such lithium-ion batteries, fuel cells, and solar cells.

Keywords: Atomic layer deposition, Nanostructured materials, Metal oxides, Iron oxide, Tin dioxide, Titanium dioxide, Lithium titanium oxide, Anodic aluminum oxide, Carbon nanotubes, Graphene nanosheets, Nanotube arrays, Core-shell coaxial nanotubes, Three-dimensional networks, Renewable clean energy devices, Lithium-ion batteries, Fuel Cells, Solar cells.

CO-AUTHORSHIP

1.

Title: Emerging Applications of Atomic Layer Deposition for Lithium-ion Batteries

Authors: Xiangbo Meng and Xueliang Sun

This review paper was designed and wrote by Xiangbo Meng under the guidance of Dr. Xueliang Sun. The initial draft and the followed modifications of this manuscript were conducted by Xiangbo Meng under the supervision of Dr. Xueliang Sun. The final version of this manuscript is to be submitted for publishing.

2.

Title: Heterostructural Coaxial Nanotubes of CNT@Fe₂O₃ via Atomic Layer Deposition: Effects of Surface Functionalization and Nitrogen-doping

Authors: Xiangbo Meng, Mihnea Ionescu, Mohammad Norouzi Banis, Yu Zhong, Hao Liu, Yong Zhang, Shuhui Sun, Ruying Li, and Xueliang Sun

All the experimental and theoretical work was carried out by Xiangbo Meng under the guidance of Dr. Xueliang Sun. The initial draft and the followed modifications of this manuscript were conducted by Xiangbo Meng under the supervision of Dr. Xueliang Sun. The other coauthors contributed to the formation of the final version with discussion and related characterization. The final version of this manuscript has been published in *Journal of Nanoparticle Research*, 2011, 13, 1207-1218.

3.

Title: Three Growth Modes and Mechanisms for Highly Structure-tunable SnO₂ Nanotube Arrays of Template-directed Atomic Layer Deposition

Authors: Xiangbo Meng, Yong Zhang, Shuhui Sun, Ruying Li, and Xueliang Sun

All the experimental and theoretical work was carried out by Xiangbo Meng under the guidance of Dr. Xueliang Sun. The initial draft and the followed modifications of this manuscript were conducted by Xiangbo Meng under the supervision of Dr. Xueliang Sun. The other coauthors contributed to the formation of the final version with discussion and related characterization. The final version of this manuscript has been published in

Journal of Materials Chemistry, 2011, **21**, 12321-12330.

4.

Title: Nitrogen-doped carbon nanotubes coated by atomic layer deposited SnO₂ with controlled morphology and phase

Authors: Xiangbo Meng, Yu Zhong, Yifan Sun, Mohammad Norouzi Banis, Ruying Li, and Xueliang Sun

All the experimental and theoretical work was carried out by Xiangbo Meng under the guidance of Dr. Xueliang Sun. The initial draft and the followed modifications of this manuscript were conducted by Xiangbo Meng under the supervision of Dr. Xueliang Sun. The other coauthors contributed to the formation of the final version with discussion and related characterization. The final version of this manuscript has been published in *Carbon*, 2011, 49, 1133-1144.

5.

Title: Non-Aqueous Approach to Synthesize Amorphous/Crystalline Metal Oxide-Graphene Nanosheet Hybrid Composites

Authors: Xiangbo Meng, Dongsheng Geng, Jian Liu, Mohammad Norouzi Banis , Yong Zhang, Ruying Li, and Xueliang Sun

All the experimental and theoretical work was carried out by Xiangbo Meng under the guidance of Dr. Xueliang Sun. The initial draft and the followed modifications of this manuscript were conducted by Xiangbo Meng under the supervision of Dr. Xueliang Sun. The other coauthors contributed to the formation of the final version with discussion and related characterization. The final version of this manuscript has been published in *Journal of Physical Chemistry C*, 2010, 114, 18330-18337.

6.

Title: Controllable Atomic Layer Deposition of One-dimensional nanostructured TiO₂

Authors: Xiangbo Meng, Mohammad Norouzi Banis, Dongsheng Geng, Yong Zhang, Ruying Li, and Xueliang Sun

All the experimental and theoretical work was carried out by Xiangbo Meng under the

guidance of Dr. Xueliang Sun. The initial draft and the followed modifications of this manuscript were conducted by Xiangbo Meng under the supervision of Dr. Xueliang Sun. The other coauthors contributed to the formation of the final version with discussion and related characterization. The final version of this manuscript is to be submitted for publishing.

7.

Title: Controllable Synthesis of Graphene-based Titanium Dioxide Nanocomposites by Atomic Layer Deposition

Authors: Xiangbo Meng, Dongsheng Geng, Jian Liu, Ruying Li, and Xueliang Sun

All the experimental and theoretical work was carried out by Xiangbo Meng under the guidance of Dr. Xueliang Sun. The initial draft and the followed modifications of this manuscript were conducted by Xiangbo Meng under the supervision of Dr. Xueliang Sun. The other coauthors contributed to the formation of the final version with discussion and related characterization. The final version of this manuscript has been published in *Nanotechnology*, 2011, 22, 165602.

8.

Title: Tunable Atomic Layer Deposition of CNT-based Lithium Titanium Oxide Nanocomposites

Authors: Xiangbo Meng, Jian Liu, Mohammad Norouzi Banis, Jinli Yang, Ruying Li, and Xueliang Sun

All the experimental and theoretical work was carried out by Xiangbo Meng under the guidance of Dr. Xueliang Sun. The initial draft and the followed modifications of this manuscript were conducted by Xiangbo Meng under the supervision of Dr. Xueliang Sun. The other coauthors contributed to the formation of the final version with discussion and related characterization. The final version of this manuscript is to be submitted for publishing.

*I dedicate this book to my beloved wife who
shares my dreams and sacrifices for them!*

ACKNOWLEDGEMENTS

This thesis is the account of my 32-month devoted work in the fields of materials engineering at The University of Western Ontario (UWO), Canada.

Upon this point, I would like to express my deep gratitude first to my supervisor, Dr. Xueliang (Andy) Sun, the Canada Research Chair in Development of Nanomaterials for Clean Energy and the Director of Nanomaterials and Energy Group (NEG), a professor in the Department of Mechanical & Materials Engineering (MME) at UWO. We got to know each other in 2005. At that moment I was studying for my first PhD degree in Chemical & Biochemical Engineering at UWO. Dr. Sun is a basketball fan and the case also goes to me. So, he kindly brought me into a team for fun and offered my family with a driving every time, for we had no vehicles. I did enjoy a lot of time from basketball with Dr. Sun and other fans. Later on, not just basketball, I found we were also having others in common, such as fishing. Thanks to these games, we got lots of joys in remembrance. When the time approached my graduation in 2008, I started to think about my future career and some tiny things commonly called nano interested me. Fortunately, I received a chance to work in Dr. Sun's group and got to know more about nano and its uses. My fresh touch on nano started with a system named atomic layer deposition. Again, I would like to appreciate Dr. Sun's trust which granted me this project. Especially, Dr. Sun's timely guidance helped me deliver the first article and the following ones. In particular, his strong support made my NSERC PDF application a success and a Student Award at the 11th International Conference on Atomic Layer Deposition (2011, Cambridge, MA, USA). Now, when it is approaching the finishing of my PhD in materials engineering, the time in Dr. Sun's group and his persistent help are for sure the most precious treasures for my future career.

I am also very grateful to Mrs. Ruying Li, Dr. Sun's wife and a research engineer in the group. Besides teaching me a lot of skills on characterizing nanomaterials, Mrs. Li gave her support in my experiments as well. Furthermore, Mrs. Li provide her warm assistance

on our routine life. My family members, not just me, will cherish her kindness and her contagious personalities.

I want to extend my appreciation to my advisory committee member, Dr. Jun Yang, a professor in MME at UWO for his advice to my studies in every stage. Also, particularly I would like to thank Dr. Yang for his strong support to my application of NSERC PDF. All his help contributed to my fruitful studies in MME. Also, I appreciate his insightful comments on my defense.

I further deeply appreciate Dr. Sean Barry, a professor in the Department of Chemistry at Carleton University and a world-class expert on ALD, for his careful examination on my thesis and for his beneficial discussion and comments as well. I also would like to thank Dr. Paul Charpentier, a professor in the Department of Biochemical and Chemical Engineering at UWO and Dr. Jeffrey Wood, a professor in MME at UWO. As examiners of my defense, they both provided many helpful suggestions to improve my thesis.

My thanks also go to all my group members, the talented researchers with many excellent professional skills. Without their collaboration, my project could not have been done so smoothly. Specially, I would extend my thanks to Mr. Yu Zhong for CNTs, Dr. Dongsheng Geng for GNS, Dr. Yong Zhang for AAO and Raman, Mr. Mohammad Norouzi Banis and Ms. Jinli Yang for XRD, and Mr. Jian Liu for FTIR and CNTs. Also, thanks for helpful discussions from the couple, Dr. Shuihui Sun and Dr. Gaixia Zhang.

I would also like to thank the help from Cambridge Nanotech for their instruction and help on our ALD system. Particularly, my thanks go to Dr. Eric Deguns who provided lots of helpful discussion on ALD. In addition, I appreciate Mr. Fred Pearson at McMaster University, who assisted me with HRTEM observation.

Specially, I owe my parents, Fanxi Meng and Haisu Feng for their understanding and support on my pursuits. Their persistence, kindness, and honesty are always of the greatest worth and have already rooted in my life. I would also like to thank my sisters,

Fengguo Meng and Xiangping Meng for their sharing of my responsibility in taking care of our parents.

Finally, I am indebted to my dear wife, Aiying Shao for her years' support and love. Without her tireless dedication to our family, this thesis would not have been delivered. It is my luck to experience the life with her. I would also like to say "thanks" to my lovely daughter, Kexin and my cute son, Keming for their contributions to our family with so much happiness and proud.

Xiangbo Meng

TABLE OF CONTENTS

CERTIFICATE OF EXAMINATION.....	ii
ABSTRACT.....	iii
CO-AUTHORSHIP	vi
DEDICATION.....	ix
ACKNOWLEDGEMENTS	x
TABLE OF CONTENTS.....	xiii
LIST OF TABLES.....	xix
LIST OF FIGURES	xx
LIST OF APPENDICES.....	xxix
LIST OF ABBREVIATIONS.....	xxx

CHAPTER 1.	GENERAL INTRODUCTION.....	1
1.1	Introduction.....	2
	1.1.1 Atomic layer deposition and its applications.....	2
	1.1.2 Energy challenges and solutions.....	3
	1.1.3 The opportunities with nanostructured materials.....	6
1.2	Objectives.....	8
1.3	Thesis Structure.....	10
1.4	Major Contributions.....	12
	References.....	15

CHAPTER 2.	LITERATURE REVIEW.....	19
2.1	Atomic Layer Deposition	20
	2.1.1 A briefing on traditional film deposition techniques.....	20
	2.1.2 Mechanisms.....	21

	2.1.3	Characteristics.....	24
2.2		Emerging Applications of Atomic Layer Deposition for Lithium-ion Batteries.....	29
	2.2.1	Background.....	29
	2.2.2	ALD on designing novel battery components.....	32
	2.2.3	ALD on surface-modifying battery electrodes.....	44
	2.2.4	Conclusions and outlooks.....	59
2.3		Challenges of Atomic Layer Deposition	62
	2.3.1	Rapid deposition	62
	2.3.2	Deposition of single and multi-elemental materials..	62
	2.3.3	Mass production	62
2.4		Summary.....	63
		References.....	64
CHAPTER 3.		EXPERIMENTAL APPARATUS AND MATERIALS.....	79
3.1		Experimental Setup and Procedures.....	80
	3.1.1	Experimental setup.....	80
	3.1.2	Experimental procedures.....	81
3.2		Materials and Synthesis Strategies.....	82
	3.2.1	Substrates and precursors.....	82
	3.2.2	Strategies for nanostructures.....	84
3.3		Characterization Techniques.....	85
		References.....	86
CHAPTER 4.		HETEROSTRUCTURAL COAXIAL NANOTUBES OF CNT@Fe₂O₃ VIA ATOMIC LAYER DEPOSITION: EFFECTS OF SURFACE FUNCTIONALIZATION AND NITROGEN-DOPING	88
4.1		Introduction.....	90
4.2		Experimental.....	91

4.2.1	Synthesis and functionalization of CNTs.....	91
4.2.2	ALD-Fe ₂ O ₃ processes.....	93
4.2.3	Characterization techniques.....	94
4.3	Results and Discussion.....	94
4.3.1	Effects of surface functionalization.....	94
4.3.2	Effects of N-doping Results.....	99
4.4	Conclusions.....	104
	Acknowledgements	105
	References.....	106

CHAPTER 5.	THREE GROWTH MODES AND MECHANISMS FOR HIGHLY STRUCTURE-TUNABLE SnO₂ NANOTUBE ARRAYS OF TEMPLATE-DIRECTED ATOMIC LAYER DEPOSITION.....	112
5.1	Introduction.....	114
5.2	Experimental.....	116
5.2.1	Template-directed ALD-SnO ₂ for tubular arrays...116	
5.2.2.	Characterization	117
5.3	Results and Discussion	117
5.3.1	Results.....	117
5.3.2	Discussion.....	127
5.4	Conclusions.....	136
	Acknowledgements.....	136
	References.....	138
	Supporting Information.....	142

CHAPTER 6.	NITROGEN-DOPED CARBON NANOTUBES COATED BY ATOMIC LAYER DEPOSITED SnO₂ WITH CONTROLLED MORPHOLOGY AND PHASE.....	146
6.1	Introduction.....	148
6.2	Experimental.....	150

6.2.1	Synthesis of N-CNTs.....	150
6.2.2	ALD-SnO ₂	150
6.2.3	Characterization.....	150
6.3	Results and Discussion.....	151
6.3.1	Results.....	151
6.3.2	Discussion.....	158
6.4	Conclusions.....	169
	Acknowledgements.....	170
	References.....	171

CHAPTER 7. NON-AQUEOUS APPROACH TO SYNTHESIZE AMORPHOUS/CRYSTALLINE METAL OXIDE-GRAPHENE NANOSHEET HYBRID COMPOSITES.....176

7.1	Introduction.....	178
7.2	Experimental.....	181
7.2.1	Preparation of GNS.....	181
7.2.2	ALD-SnO ₂	183
7.2.3	Characterization.....	183
7.3	Results and Discussion.....	184
7.4	Conclusions.....	194
	Acknowledgements.....	194
	References.....	195
	Supporting Information.....	200

CHAPTER 8. CONTROLLABLE ATOMIC LAYER DEPOSITION OF ONE-DIMENSIONAL NANOSTRUCTURED TiO₂.....202

8.1	Introduction.....	204
8.2	Experimental.....	205
8.2.1	ALD-TiO ₂	205
8.2.2	Functionalization of substrates.....	206
8.2.3	Characterization.....	207

8.3.1	Results and Discussion.....	207
8.3.1	Results.....	207
8.3.2	Discussion.....	216
8.4	Conclusions.....	217
	Acknowledgements.....	217
	References.....	218
	Supporting Information.....	222
CHAPTER 9.	CONTROLLABLE SYNTHESIS OF GRAPHENE-BASED TITANIUM DIOXIDE NANOCOMPOSITES BY ATOMIC LAYER DEPOSITION.....	223
9.1	Introduction.....	225
9.2	Experimental.....	227
9.2.1	Preparation of GNS	227
9.2.2	ALD-TiO ₂	227
9.2.3	Characterization.....	228
9.3	Results and Discussion.....	228
9.3.1	Results.....	228
9.3.2	Discussion.....	238
9.4	Conclusions.....	243
	Acknowledgements.....	244
	References.....	245
	Supporting Information.....	251
CHAPTER 10.	ALTOMIC LAYER DEPOSITION OF LITHIUM TITANIUM OXIDE.....	257
10.1	Introduction.....	259
10.2	Experimental.....	260
10.2.1	Synthesis of N-CNTs.....	260
10.2.2	ALD-LTO.....	260
10.2.3	Characterization.....	261

10.3	Results and Discussion.....	262
10.3.1	ALD of lithium-containing compound.....	262
10.3.2	ALD-LTO.....	265
10.4	Conclusions.....	268
	Acknowledgements.....	268
	References.....	269
CHAPTER 11.	GENERAL DISCUSSION.....	272
CHAPTER 12.	CONCLUSIONS AND SUGGESTIONS.....	275
12.1	Conclusions.....	276
12.2	Suggestions.....	278
APPENDICES	280
CURRICULUM VITAE	286

LIST OF TABLES

.....**Chapter 2**.....

Table I	Comparison of deposition properties for PVD, CVD, and ALD	28
Table II	Overview of the materials grown by ALD	28
Table III	Nanostructured anode materials by ALD	36

LIST OF FIGURES

CHAPTER 2

Figure 2.1	A model ALD process by depositing Al ₂ O ₃ using TMA and water as precursors. (a) the initial substrate covered by hydroxyl groups; (b) TMA molecules reacting with hydroxyl groups, leading to a new intermediate layer; (c) the substrate covered with a new-created intermediate layer; (d) H ₂ O molecules reacting with the intermediate layer, leading to new hydroxyl groups; (e) the substrate covered again by hydroxyl groups.	22
Figure 2.2	The examples for ALD-fabricated nanostructures. (a) the layered Al ₂ O ₃ -ZnO nanolaminates on Si substrates; (b) SiO ₂ -coated TiO ₂ composite nanoparticles; (c) hollow TiO ₂ nanoribbons; (d) coaxial HfO ₂ nanotubes; (e) three-layered discontinued TiO ₂ 3D nanofilms; and (f) complex 3D Al ₂ O ₃ nanostructures.	27
Figure 2.3	Main ALD strategies for fabricating nanostructured materials. (a) the strategy for nanotube arrays using AAO, exemplified by the fabrication of SnO ₂ nanotubes; (b) the strategy for nanotubes using CNTs; (c) the strategy for 3D networks of nanotubes based on nanocellulose aerogel; and (d) the strategy for 3D nanostructures based on GNS, exemplified by ALD-TiO ₂ on GNS.	35
Figure 2.4	SEM image of (a) the peptide template and (b) the TiO ₂ network (inset: magnified image of cross sectional TiO ₂ hollow nanoribbon). (c) Rate capability of the TiO ₂ network, and the 25 nm and 100 nm nanoparticles from C/5 to 5C for 10 cycles.	37
Figure 2.5	The electrochemical performance of TiO ₂ -(Ni-TMV) nanocomposites as anode of LIBs. (a) low-magnification SEM image for the TiO ₂ -coated TMV; (b) high-magnification TEM image for a single composite nanorod where TMV (18 nm), Ni (~20 nm), and TiO ₂ (~ 20 nm). (c) Capacity vs. cycle number for electrodes with and without TMV.	38
Figure 2.6	ALD-TiO ₂ coated Al nanorods used as anodes of 3D microbatteries. (a) Al nanorod arrays; (b) an ALD-TiO ₂ coated Al nanorod; and (c) normalized capacity (mAh/cm ² of geometrical surface area) for the 3D microbattery with TiO ₂ deposited on an Al nanorod current collector and the 2D electrode with TiO ₂ deposited on a flat plate. The galvanostatic cycling current is 0.001 mA.	40
Figure 2.7	A 3D all-solid-state lithium-ion battery.	43

Figure 2.8	SEM/EDS analyses of ALD-Al ₂ O ₃ electrodes. (a) FE-SEM cross-sectional image of NG composite electrode coated with 5 cycles of ALD-Al ₂ O ₃ . Numbers indicate regions in which Al was analyzed with EDS. (b) Weight fraction of Al as a function of depth. (c) Electrochemical performance of different anodes at 50 °C.	47
Figure 2.9	Schematic representation of the effects of volume expansion upon (a) bare particles, (b) an ALD coated nano-MoO ₃ particle, and (c) a particle from an ALD coated porous anode.	50
Figure 2.10	Charge-discharge cycle performance of electrodes fabricated by the bare LiCoO ₂ powders and the ALD-Al ₂ O ₃ coated LiCoO ₂ powders using 2, 6, and 10 ALD cycles.	52
Figure 2.11	ALD-Al ₂ O ₃ modified nano-LiCoO ₂ particles. (a) 2-cycle ALD-Al ₂ O ₃ coated nanoparticles (left), showing the presence of Al by XDS spectrum (right); (b) HR-TME image for a bare nanoparticle; (c) HR-TEM image for a 2-cycle ALD-Al ₂ O ₃ coated nanoparticle; and (d) cycleability of different cathodes fabricated by bare bulk-LiCoO ₂ , bare nano-LiCoO ₂ , and 2-cycle ALD-Al ₂ O ₃ coated nano-LiCoO ₂ .	54
Figure 2.12	Modification of ALD-Al ₂ O ₃ on LiMn ₂ O ₄ cathodes. (a) The bare LiMn ₂ O ₄ micropowders; (b) 20-cycle ALD-Al ₂ O ₃ coated LiMn ₂ O ₄ micropowders; (c) XPS spectrum from LiMn ₂ O ₄ cathode coated by 4-cycle Al ₂ O ₃ ; and (d) Cycling performance of (A) bare LiMn ₂ O ₄ cathode, cathodes coated with (B) 20-cycle and (C) 10-cycle of ALD-Al ₂ O ₃ . These samples were cycled at a current density of 240 mA/g over the voltage range of -0.3 – 0.8 V.	57

..... **CHAPTER 3**

Figure 3.1	Experimental setup for atomic layer deposition: A – chamber, B – substrate, C1-3 – precursor cylinders, D1-3 – solenoid valves, E – ALD ebox, F – computer, G – vacuum pump.	80
Figure 3.2	A screen snapshot on the LabVIEW program of the ALD system.	81

..... **CHAPTER 4**

Figure 4.1	The pristine undoped CNTs: (a) low magnification and (b) high magnification SEM image; (c) conventional and (insert) high resolution TEM image.	95
Figure 4.2	200-cycle ALD of iron oxide deposition on the undoped CNTs: without surface pretreatment (a) SEM image and (b) TEM image; treated by 2h nitric acid (c) low magnification and (d) high magnification SEM image; treated by 2 h SDS (e) low magnification and (f) high magnification SEM image; treated by 1 h nitric acid and 1 h SDS in sequence (g) low magnification and (h) high magnification SEM image.	96
Figure 4.3	XRD patterns of the ALD iron oxide on the undoped CNTs treated by nitric acid and SDS, respectively.	97
Figure 4.4	The N-doped CNTs: (a) low magnification and (b) high magnification SEM image; (c) HRTEM image.	100
Figure 4.5	The ALD iron oxide on N-doped CNTs illustrated by: SEM images (a) 50 cycles, (c) 70 cycles, and (e) 100 cycles; TEM images (b) 50 cycles; (d) 70 cycles, and (f) 100 cycles.	101
Figure 4.6	Phase and composition characteristics of the ALD iron oxide (70 ALD cycles) on the N-doped CNTs: (a) XRD patterns, (b) TEM image, and (c) HRTEM image.	102

..... **CHAPTER 5**

Figure 5.1	Schematic fabrication of SnO ₂ nanotubes via template-directed ALD. (a) the ALD-SnO ₂ coating on an AAO template, (b) the ALD-coated AAO template, (c) the mechanically polished AAO template, and (d) the received SnO ₂ nanotube array.	117
Figure 5.2	XRD spectra of 1000-cycle ALD-SnO ₂ at different growth temperatures: (a) 150, (b) 200, (c) 300, and (d) 400 °C.	118
Figure 5.3	The growth characteristics of ALD-SnO ₂ at 150 °C. (a) EDS spectrum of the ALD-SnO ₂ on AAO; top views of AAO after (b) 1000 and (c) 1500 cycles of ALD-SnO ₂ ; the template-removed SnO ₂ in the forms of (d) clusters and (e) nanotubes corresponding to 1000 and 1500 cycles, respectively.	119
Figure 5.4	The growth characteristics of ALD-SnO ₂ at 200 °C. (a) SEM side views of AAO pores after 500, 1000, and 1500 cycles of ALD-SnO ₂ ; (b) the received nanotube	121

arrays of ALD-SnO₂ of 1000 and 1500 cycles after AAO templates were etched away; (c) TEM image for a piece of debris of the deposited SnO₂ after 1500-cycle ALD-SnO₂ (inset: SAED patterns); (d) high-magnification TEM image for a local area as indicated in (c); (e) HRTEM image for a local area as indicated in (c); and (f) HRTEM image for a local area of the beneath layer as indicated in (e).

Figure 5.5

The growth characteristics of ALD-SnO₂ at 300 °C. (a) SEM side views of AAO pores coated with the ALD-SnO₂ of 200, 400, 600, 800, and 1000 cycles (as marked on the left-bottom corner of each case); (b) SEM images for the received SnO₂ nanotubes after 400, 800, and 1000 ALD-cycles (insets: top-views on ALD-SnO₂ of 400 and 800 cycles); (c) the TEM image for the SnO₂ nanotubes of 800 ALD-cycles; (d) the high magnification TEM image for a part of a SnO₂ nanotube in (c) (inset: SAED patterns); (e) the HRTEM image for a local area in (d).

123

Figure 5.6

The growth characteristics of ALD-SnO₂ at 400 °C. (a) SEM side views of AAO pores coated with the ALD-SnO₂ of 400, 600, 800, and 1000 cycles (as marked on the left-bottom corner of each case); (b) SEM images for the received SnO₂ nanotubes after 400, 600, 800, and 1000 ALD-cycles; (c) the TEM image for the SnO₂ nanotubes of 600 ALD-cycles; (d) the high magnification TEM image for one end of a SnO₂ nanotube in (c) (inset: SAED patterns); (e) and (f) the HRTEM images for two local areas in (d).

126

Figure 5.7

Three growth models for ALD-SnO₂ nanotube arrays. At a temperature lower than 200 °C, the ALD-SnO₂ was built up in AAO pores in a mode of (a) layer-by-layer growth, as schematically shown in (a1-4) with uniform films of increasing thickness; in the range 200-400 °C, the ALD-SnO₂ experienced a mode of (b) layer-by-particle growth: (b1) amorphous layers prevailed at the initial stage but random nucleation happened with increased films, (b2) crystals grew laterally and radially while new nuclei appeared with increased films, (b3) crystals saturated on the surface and amorphous layers stopped growing, (b4) crystals stopped their lateral growth and competed with each other for their radial growth; at a temperature no less than 400 °C, the ALD-SnO₂ transferred to a mode of (c) evolutionary particle: (c1) nuclei formed immediately on the substrate surface at the starting of the ALD process, (c2) crystals grew quickly with increased ALD-cycles, (c3) crystals saturated on the substrate surface, (c4) crystals grew predominantly in their radial direction. In (a5), (b5), and (c5), the

133

	produced nanotubes were schematically illustrated.	
Figure SI-5.1.	ALD-SnO ₂ at 300 °C. SEM images of side-views of AAO pores after (a) 200, and (c) 600 ALD-SnO ₂ cycles; and SEM images of top-views of AAO pores after (b) 400, and (d) 600 ALD-SnO ₂ cycles.	142
Figure SI-5.2	The growth characteristics of ALD-SnO ₂ at 250 °C. (a) SEM side views of AAO pores coated with the ALD-SnO ₂ of 200, 400, 600, 800, and 1000 cycles (as marked on the left-bottom corner of each case); (b) SEM images for the received SnO ₂ nanotubes after 600, 800, and 1000 ALD-cycles; (c) the TEM image for the SnO ₂ nanotubes of 800 ALD-cycles (inset: SAED patterns); (d) the HRTEM image for a local area in (c).	143
Figure SI-5.3	Figure SI-5.3 The growth characteristics of ALD-SnO ₂ at 350 °C. (a) SEM side views of AAO pores coated with the ALD-SnO ₂ of 200, 400, 600, 800, and 1000 cycles (as marked on the left-bottom corner of each case); (b) SEM images for the received SnO ₂ nanotubes after 400, 600, 800, and 1000 ALD-cycles; (c) the arrays of SnO ₂ nanotubes of 1000 ALD-cycles.	144
Figure SI-5.4	XRD spectra of 200-cycle ALD-SnO ₂ at different growth temperatures: (a) 200, (b) 250, (c) 300, (d) 350, and (e) 400 °C.	145

..... **CHAPTER 6**

Figure 6.1	SEM images of N-CNTs with (a) low magnification, and (b) high magnification; (c) XRD spectra of N-CNTs coated with 200-cycle ALD-SnO ₂ at (▲) 200 °C and (■) 400 °C; (d) EDS spectra of N-CNTs coated with 200-cycle ALD-SnO ₂ at 200 °C.	152
Figure 6.2	ALD-SnO ₂ on N-CNTs at 200 °C. SEM images after (a) 50, (c) 100, and (e) 200 ALD cycles; TEM images after (b) 50, (d) 100, and (f) 200 ALD cycles (insert: SAED patterns); (g and h) HRTEM images of 200-cycle ALD-SnO ₂ .	153
Figure 6.3	ALD-SnO ₂ on N-CNTs at 400 °C. SEM images after (a) 50, (b) 100, (c) 200, (d) 400 ALD cycles; (e) TEM image of 100-cycle ALD-SnO ₂ (insert: SAED patterns); (f and g) HRTEM images of 100-cycle ALD-SnO ₂ .	155
Figure 6.4	ALD-SnO ₂ on N-CNTs at 300 °C. SEM images after (a) 50, (b) 100, and (c) 200 ALD cycles; (d) TEM image of 200-cycle ALD-SnO ₂ (insert: SAED patterns); (e and f) HRTEM images of 200-cycle ALD-SnO ₂ .	157
Figure 6.5	Survey scans of XPS spectra for (a) pristine N-CNTs, as well as N-CNTs coated with 100-cycle ALD-SnO ₂ at (b) 200 °C and (c) 400 °C.	160

Figure 6.6	High-resolution XPS spectra of C 1s peak for (a) pristine N-CNTs as well as for N-CNTs coated with 100-cycle ALD-SnO ₂ at (b) 200 °C and (c) 400 °C (insert: comparison of C 1s peaks).	161
Figure 6.7	High-resolution XPS spectra of N 1s peak for (a) pristine N-CNTs as well as for N-CNTs coated with 100-cycle ALD-SnO ₂ at (b) 200 °C and (c) 400 °C.	163
Figure 6.8	Schematic diagram of ALD-SnO ₂ on N-CNTs. (a) The first ALD-SnO ₂ cycle functionalized the surface of N-CNTs: (1) pristine N-CNTs decorated by N-doping defects, (2) SnCl ₄ chemically adsorbed on N-CNTs in the first ALD half reaction induced by N-doping defects, and (3) OH functional groups generated in the second ALD half reaction induced by H ₂ O. (b) The temperature-dependent ALD-SnO ₂ on N-CNTs: (1) N-CNTs (blue rings indicating interlinked nodes) uniformly covered by OH groups at low (L: 200 °C) and intermediate (I: 300 °C) temperature, but with more OH groups around interlinked nodes at high (H: 400 °C) temperature; (2) the half-reaction of SnCl ₄ dominated by ligand exchange (L), chlorination (H), as well as a competition (I) between the two, respectively; (3) the half-reaction of H ₂ O dominated by ligand exchange in all the cases (L, I, and H); (4) N-CNTs deposited with tiny amorphous (L), crystalline (H), as well as coexisting amorphous-crystalline nanoparticles (I) after m-cycles ($m \leq 100$) of ALD-SnO ₂ ; (5) N-CNTs deposited with coaxial amorphous film (L), coalesced crystalline nanoparticles (H), as well as coaxial amorphous film decorated with crystalline nanoparticles (I) after k-cycles ($k > 100$) of ALD-SnO ₂ .	168

..... CHAPTER 7

Figure 7.1	Schematic illustration of the precise approach to tune the morphology and amorphous-crystalline phases via atomic layer deposition technique (ALD). (a) ALD-SnO ₂ process employed on graphene nanosheets (GNS) using SnCl ₄ and H ₂ O as the two precursors to form amorphous/crystalline SnO ₂ -GNS nanocomposites; (b) uniformly distributed amorphous SnO ₂ nanoparticles on GNS surface and (c) amorphous SnO ₂ thin film formed on GNS surface by growing nanoparticles; (d) small crystalline SnO ₂ nanoparticles uniformly distributed on GNS surface and (e) large SnO ₂ nanoparticles uniformly distributed on GNS surface with higher density.	180
Figure 7.2	Characteristics of GNS: SEM images of (a) low magnification, and (b) high	182

	magnification; (c) XRD, (d) FTIR, and (e) Raman spectra.	
Figure 7.3	(a) XRD spectra of (♦) GNS, (♣) SnO ₂ -GNS nanocomposites synthesized at 200 °C, and (♠) SnO ₂ -GNS nanocomposites synthesized at 400 °C; (b) EDS spectra for SnO ₂ -GNS nanocomposites synthesized at 200 °C.	186
Figure 7.4	Amorphous SnO ₂ -GNS nanocomposites: (a) 100 ALD cycles of SnO ₂ ; (b) 200 ALD cycles of SnO ₂ ; (c) 300 ALD cycles of SnO ₂ ; (d) low magnification TEM image of 300-cycle SnO ₂ ; (e) and (f) HRTEM images of 300-cycle SnO ₂ .	188
Figure 7.5	Crystalline SnO ₂ -GNS nanocomposites: (a) 100 ALD cycles of SnO ₂ ; (b) 200 ALD cycles of SnO ₂ ; (c) 300 ALD cycles of SnO ₂ ; (d) low magnification TEM image of 300-cycle SnO ₂ ; (e) and (f) HRTEM images of 300-cycle SnO ₂ .	190
Figure 7.6	Schematic illustration of surface reactions occurred in ALD-SnO ₂ due to different growth temperatures: (on left side) amorphization for 200 °C, and (on the right side) crystallization for 400 °C.	193
Figure SI-7.1	SEM images for natural graphite of (a) lower magnification and (b) higher magnification, as well as graphite oxide of (c) lower magnification and (d) higher magnification.	200
Figure SI-7.2	SEM images for amorphous SnO ₂ -GNS nanocomposites: 100 ALD cycles of SnO ₂ with (a) lower magnification and (b) higher magnification of SEM image; 200 ALD cycles of SnO ₂ with (c) lower magnification and (d) higher magnification of SEM image.	201

CHAPTER 8

Figure 8.1	(a) XRD patterns induced by ALD-TiO ₂ at 150 (A) and 250 °C (B). (b) EDS spectrum of ALD-TiO ₂ at 150 °C.	208
Figure 8.2	Template-directed ALD-TiO ₂ at 150 °C. SEM images showing AAO templates deposited with (a) 500- and (b) 600-cycle ALD-TiO ₂ , and SEM images showing the received nanotubes arrays after (c) 500- and (d) 600-cycle ALD-TiO ₂ . (e) TEM image of the received nanotubes (inset: SAED pattern). (f) HR-TEM image of a local area as marked with “P” in (e).	209
Figure 8.3	Template-directed ALD-TiO ₂ at 250 °C. SEM images showing AAO templates deposited with (a) 200- (b) 300-, and (c) 500-cycle ALD-TiO ₂ . The received nanotubes shown by (d) SEM, (e) TEM (inset: SAED pattern), and (f) HR-TEM image (inset: the position for the piece examined by HR-TEM).	211
Figure 8.4	XRD patterns of (A) pristine CNTs, and 300-cycle ALD-TiO ₂ on CNTs at (B)	212

	150 and (C) 250 °C.	
Figure 8.5	ALD-TiO ₂ on CNTs at 150 °C. SEM images of (a) 100, (c) 200, and (e) 300 cycles of ALD-TiO ₂ . TEM images of (b) 100, (d) 200, and (f) 300 cycles of ALD-TiO ₂ . (g) HR-TEM image of 100-cycle ALD-TiO ₂ .	214
Figure 8.6	ALD-TiO ₂ on CNTs at 250 °C. SEM images of (a) 100, (c) 200, and (e) 300 cycles of ALD-TiO ₂ . TEM images of (b) 100 (inset: HR-TEM image of nanoparticles), (d) 200, and (f) 300 cycles of ALD-TiO ₂ .	215
Figure SI-8.1	SEM images of (a,b) as-received, (c,d) 1h oxidized, and (e,f) 2h oxidized CNTs	222

CHAPTER 9

Figure 9.1	(a) SEM images of GNS; (b) TEM image, and (c) HRTEM image of GNS; (d) XRD and (e) FTIR spectra of NG, GO, and GNS.	229
Figure 9.2	High-magnification SEM images of (a) pristine GNS, and 300-cycle ALD-TiO ₂ on GNS at (b) 150 °C, (c) 200 °C as well as (d) 250 °C. Insets are low-magnification SEM images. (e) XRD spectra of 300-cycle ALD-TiO ₂ on GNS at 150 °C, 200 °C, and 300 °C. (f) EDS spectra of 300-cycle ALD-TiO ₂ on GNS at 150 °C.	231
Figure 9.3	High-magnification SEM images of ALD-TiO ₂ on GNS at 150 °C after (a) 50 cycles, (b) 75 cycles (inset for a higher magnification SEM image), (c) 100 cycles, and (d) 200 cycles. (e) TEM and (f) HRTEM image of 75-cycle ALD-TiO ₂ on GNS at 150 °C.	233
Figure 9.4	High-magnification SEM images of ALD-TiO ₂ on GNS at 200 °C after (a) 50 cycles, (b) 75 cycles, (c) 100 cycles, and (d) 200 cycles. (e) TEM and (f) HRTEM image of 75-cycle ALD-TiO ₂ on GNS at 200 °C.	235
Figure 9.5	High-magnification SEM images of ALD-TiO ₂ on GNS at 250 °C after (a) 50 cycles, (b) 75 cycles, (c) 100 cycles, and (d) 200 cycles. (e) TEM and (f) HRTEM image of 75-cycle ALD-TiO ₂ on GNS at 250 °C.	237
Figure 9.6	The growth rates (GPC) of ALD-TiO ₂ with temperatures.	241
Figure SI-9.1	SEM images of (a) NG, (b) GO, and (c) GNS powders.	251
Figure SI-9.2	SEM images for ((a) and (b)) 100-cycle, ((c) and (d)) 200-cycle, and ((e) and (f)) 300-cycle ALD-TiO ₂ on GNS at 150 °C under a supply of 1.0-s TTIP and 2.0-s water.	252
Figure SI-9.3	SEM images for ((a) and (b)) 100-cycle, ((c) and (d)) 200-cycle, and ((e) and (f)) 300-cycle ALD-TiO ₂ on GNS at 200 °C under a supply of 1.0-s TTIP and 2.0-s	253

	water.	
Figure SI-9.4	SEM images for ((a) and (b)) 100-cycle, ((c) and (d)) 200-cycle, and ((e) and (f)) 300-cycle ALD-TiO ₂ on GNS at 250 °C under a supply of 1.0-s TTIP and 2.0-s water.	254
Figure SI-9.5	SEM images for ((a) and (b)) 100-cycle, ((c) and (d)) 200-cycle, and ((e) and (f)) 300-cycle ALD-TiO ₂ on GNS at 150 °C under a supply of 0.5-s TTIP and 1.0-s water.	255
Figure SI-9.6	SEM images for 200-cycle ALD-TiO ₂ on GNS at 150 °C under ((a) and (b)) a supply of 0.8-s TTIP and 1.0-s water as well as ((c) and (d)) a supply of 1.2-s TTIP and 2.5-s water.	256

..... **CHAPTER 10**

Figure 10.1	XRD patterns induced by the ALD of using Li(O ^t Bu) and water: (a) a sample coated by a layer of 100-cycle lithium-containing film, (b) a sample coated by a layer of 100-cycle of lithium-containing film and an extra ALD-TiO ₂ of 100 cycles, (c) a sample coated by a layer of 100-cycle lithium-containing film with 3 h extended heat treatment at 250 °C, (d) the former sample coated with an extra ALD-TiO ₂ of 100 cycles, and (e) a sample coated by a layer of 100-cycle lithium-containing film but annealed at 800 °C for 3 h. (○) is used to identify the peaks of Li ₂ CO ₃ and (●) is used to identify the peaks of CHLi ₂ O.H ₂ O.	263
Figure 10.2	ALD-lithium-containing films using Li(O ^t Bu) and water. SEM images for (a) 50 (inset: SEM image after 1 min electron bombardment) and (b) 100 ALD-cycles, and a comparison (c) before and (d) after 1 min electron bombardment on a 100-cycle deposited sample.	265
Figure 10.3	XRD patterns for ALD-LTO of 40 cycles: (a) directly deposited samples as well as annealed samples at (b) 950 and (c) 850 °C for 3 h. (□) is used to identify the peaks of TiO ₂ and (■) is used to identify the peaks of Li ₄ Ti ₅ O ₁₂ .	266
Figure 10.4	SEM images of ALD-LTO after (a) 20, (b) 30, and (c) 40 cycles at 250 °C, and SEM images of the 40-cycle samples annealed at (d, f) 850, and (e, g) 950 °C. The insets show the samples with lower magnification.	267

LIST OF APPENDICES

APPENDIX I	PERMISSION FROM AMERICAN CHEMICAL SOCIETY (ACS) FOR PUBLISHED ARTICLE	281
APPENDIX II	PERMISSION FROM ELSEVIER FOR PUBLISHED ARTICLE.....	282
APPENDIX III	PERMISSION FROM INSTITUTE OF PHYSICS (IOP) FOR PUBLISHED ARTICLE.....	283
APPENDIX IV	PERMISSION FROM ROYAL SOCIETY OF CHEMISTRY (RSC) FOR PUBLISHED ARTICLE.....	284
APPENDIX V	PERMISSION FROM SPRINGER FOR PUBLISHED ARTICLE	285

LIST OF ABBREVIATIONS

A

- AAO:** anodic aluminum oxide
AFM: atomic force microscopy
ALD: atomic layer deposition
ASS-LIBs : all-solid-state lithium-ion batteries

C

- CMOS :** complementary metal-oxide-semiconductor
CNTs: carbon nanotubes
CVD: chemical vapor deposition

D

- DOE:** Department of Energy

E

- ECs:** electrical cars
EDS : energy dispersive X-ray spectroscopy
EVs: electrical vehicles

F

- FCs:** fuel cells
FTIR: Fourier transform infrared spectroscopy

G

- GM:** General Motor
GNS: graphene nanosheets
GPC: growth per cycle

H

HEVs: hybrid electrical vehicles

HR-TEM: high resolution transmission electron microscopy

I

ICE: internal combustion engine

L

LIBs: lithium-ion batteries

LLT: lithium lanthanum titanate

LTB: lithium tert-butoxide

LTO: lithium titanium oxide, $\text{Li}_4\text{Ti}_5\text{O}_{12}$

M

MO-GNCs: metal oxide-graphene nanocomposites

MWCNTs: multiwalled carbon nanotubes

N

NG: natural graphite

N-CNTs: nitrogen-doped carbon nanotubes

P

PEMFCs: proton exchange membrane fuel cells

PHEVs: plug-in hybrid electrical vehicles

PVD: physical vapor deposition

S

SAED : selected area electron diffraction

SCs: solar cells

SEI: solid electrolyte interface

SEM: scanning electron microscopy
SDS: sodium dodecyl sulfate
SWCNTs: single-walled carbon nanotubes
SR: synchrotron-radiation

T

TEM: transmission electron microscope
TFEL: thin film electroluminescent
TMA: trimethylaluminum
TMV: tobacco mosaic virus
TTIP: titanium tetra-isopropoxide

X

XAS: X-ray adsorption spectroscopy
XPS: X-ray photoelectron spectrometer
XRD: X-ray diffraction

CHAPTER 1

GENERAL INTRODUCTION

1.1 Introduction

1.1.1 Atomic layer deposition and its applications

Atomic layer deposition (ALD) is a thin film deposition process first emerged in 1970s, credited to Suntola and co-workers [1]. Distinguished from other deposition techniques such as chemical vapor deposition (CVD), physical vapor deposition (PVD), and other solution-based methods, ALD as a chemical vapor method operates with a unique mechanism relying on two gas-solid half-reactions to produce an ultimate material [2]. The reactions of ALD feature the characteristics of surface-controlled and self-terminating nature. In return, ALD performs the deposition of films in a layer-by-layer mode and it is especially superior in controlling films at the atomic level. As a result, ALD provides the deposited films with excellent uniformity and unrivalled conformality. In essence, ALD works with a temperature lower than the decomposition of the used precursors, typically lower than 400 °C even down to room temperature. In addition, ALD requires no catalysts and has no needs on solvents. All the aforementioned characteristics contribute ALD to be a unique but precise deposition technique.

Ascribed to the above-mentioned advantages, ALD is particularly suitable for production of high-quality thin films. Its initial applications were limited to the growth of II-VI materials and dielectric thin films for electroluminescent display devices [2], but it was later widened for the growth of III-V compounds [3]. Besides its successes in the areas of semiconductors, ALD has been gaining more applications since the beginning of the 21st century, owing to an increasing recognition on its versatile capabilities. The new widened applications of ALD are closely related with nanotechnology which offers new opportunities for many areas with novel components [4,5]. Recent reviews conducted Knez et al [6], Kim et al [7], and George [8] jointly provide a comprehensive view on the latest progress of ALD, especially on the fabrication of nanostructured materials. The new tendencies of ALD in nanotechnology are offering ALD many more opportunities in new areas such as sensors, solar cells, fuel cells, lithium-ion batteries.

1.1.2 Energy challenges and solutions

A. Energy challenges facing modern society

With ever-growing population and limited resources, the modern and civilized society of the mankind is facing more pressures than ever before. It is reported that the world population is growing with an annually increasing rate of more than 0.081 billions a year, but food and energy as two essential resources are posing challenges for the modern society [9]. First, the limited food production capability in the earth will not be capable to produce sufficient food supply for the mankind in the foreseeable future. On the other hand, the energy supply from all the conceivable energy resources (fossil fuel, solar, geothermal, and nuclear energy resources) will be seriously short in the future even with a fixed human population of about 10 billion [9]. In particular, each energy source has some undesirable characteristics [10]: processes of using fossil fuels produce carbon dioxide and perhaps also other contaminants, such as nitrogen oxides, sulphur oxides and ash; nuclear plants produce radioactive fission products; hydroelectric plants require dams and large lakes; solar energy and wind energy require large areas and are limited geographically; geothermal sources are limited to very few locations. At present, most of the world's energy supply comes from fossil and nuclear sources [9,10]. In particular, about two-thirds of the world's total electric power is generated from fossil fuels [10], and electricity generation provides around 40% of humanity's total energy use [11]. However, world oil production has peaked and the world supply of oil is projected to last approximately 40-60 years if use continues at current production rates [12]. Natural gas is considered adequate for about 30 years and coal for less than 100 years [12]. Consequently, mankind has to face the issues of resource limitation. In addition, the combustion of fossil fuels releases harmful emissions into the air, influencing the greenhouse effect and the direct health of people, especially in urban areas. Thus, to meet increasing global demands for energy and to allow for the depletion of fossil fuel supplies in coming years, alternative "clean" energy sources, which do not depend on fossil fuels and which have a tolerable environmental impact, must be developed.

B. Solutions

To meet the challenges posed by the fading fossil fuels and the demands on mitigating environmental pollution incurred by the combustion of fossil energy, renewable means of producing and storing electricity are expected to be increasingly important in the future and could compete with existing technologies based on the strides in condensed-matter physics and materials technology. In this way, solar cells, fuel cells (FCs), lithium-ion batteries (LIBs), and supercapacitors are being developing as potential candidates. Of them, FCs and LIBs stand out for energy conversion and storage, respectively [10].

FCs are electrochemical cells of converting chemical energy to electrical energy, consisting of two electrodes and a layer of electrolyte. The voltage of the cell depends on the difference between the two half-cell reactions happened in an anode and a cathode, respectively. There are many different types of FCs, but they commonly use hydrogen or methanol as the fuel and produce little pollutants [13]. For example, the most promising one for electrical cars (ECs) are proton exchange membrane fuel cells (PEMFCs), using hydrogen as the anode fuel and producing water on the side of cathode as the product. Direct methanol fuel cells (DMFCs) uses methanol as the anode fuel and produce CO_2 and water, particularly suitable for portable electronics such as cell phones, MP3s. Commonly, they are fed with oxygen in the cathode. Thus, FCs are apparently clean and environmentally friendly. To boost the half-cell reactions, catalysts are required and platinum (Pt) is the most efficient and widely used one. However, FCs as an alternative promising energy conversion technology are by no means new devices and emerged in the middle of the 19th century [13]. Their development has lagged behind the more well-known steam engine and internal combustion engine (ICE), mainly due to economic factors, materials problems, and certain inadequacies in the operation of electrochemical devices. One of the major factors [13] that influenced the development of FCs over the last few years is the worldwide concern about the environmental consequences of fossil fuel use in the day-to-day production of electricity and for the propulsion of vehicles. The dependence of the industrialized nations on oil became apparent during the oil crises and, recently, pressure on fossil fuel reserves is a cause for anxiety. More importantly,

however, is the increasing societal awareness, over the last few decades, concerning issues of environmental pollution. In 2003, the former US president George W. Bush announced a US\$1.2-billion hydrogen-fuel initiative to develop commercial fuel-cell vehicles by 2020 [14]. In 2009, US President Barack Obama released a budget for fiscal year 2010, including more than US\$2.3-billion for energy efficiency and renewable energy [15]. Later in September 2009, nine major car manufacturers (Daimler, Ford, General Motor (GM), Honda, Hyundai, Kia, Renault, Nissan, and Toyota) signed a joint statement suggesting that fuel-cell vehicles could hit dealerships by 2015 [14]. The main advantages of FCs are their higher efficiencies, compared to an ICE, and their lower emissions. However, fuel cells are still suffering from some critical issues in both cost and durability. As is well known, the catalyst platinum (Pt) is unacceptable expensive, accounting for US\$60 per gram at the current price [14]. Thus, the reduction of Pt use is obviously important. GM is expecting to reduce the use of Pt from 80 grams currently to 30 grams in the near future [14]. Another challenge is posed by the degradation of platinum-based catalyst layer, happened in both the Pt catalyst and carbon support [16]. To reduce cost and improve durability of FCs, some solutions root in: (1) modifying Pt catalyst; (2) developing non-Pt catalyst; (3) using novel carbon supports; (4) employing non-carbon supports.

Besides FCs, LIBs represent another technical route of great potential for clean energy. LIBs are one of the great successes of modern materials electrochemistry, also consisting of an anode (negative), a cathode (positive), and an electrolyte [17]. This technology has become a commercial reality through the efforts of the Sony Corporation [18] and others, and is used widely today in portable computer and telecommunications devices, especially as these devices get smaller and more efficient [10]. Compared with mature batteries technologies, such as lead-acid or Ni-Cd, LIBs are still in their infancy, leaving much hope for improvement [19]. Compared to FCs, according to the US Secretary of Department of Energy (DOE) Steven Chu, LIBs show more possibility for electrical cars [18]. To better serve the modern society, LIBs are facing some challenges in further improvements in both specific energy and power. Typically, carbon materials are used as negative electrodes while air-stable Li-based metal (usually cobalt but sometimes nickel

or manganese) oxides are employed as positive electrodes. However, carbon materials are approaching their capacity limit. Demand and competition is driving the quest for higher storage capacity, longer operating times, faster recharging times, and other optimization of performance [10]. As a consequence, LIBs are experiencing intensive studies mainly focused on improving specific energy and power [20]. In addition, safety and reliability are also important for further improvements.

1.1.3. The opportunities with nanostructured materials

It has been more and more acknowledged that, to tackle the issues with FCs and LIBs (even solar cells and supercapacitors), nanomaterials are taking very critical roles, because of the unusual mechanical, electrical and optical properties endowed by confining the dimensions of such materials and because of the combination of bulk and surface properties to the overall behavior [21].

In FCs, one of the most important challenges for the ultimate fuel cell commercialization is the preparation of active, robust and low-cost electrocatalysts [22]. Pt is one main factor for the cost. One of the present approaches in order to increase the catalyst dispersion involves the deposition of Pt nanoparticles on carbon black support (Acetylene Black, Vulcan XC-72, and Ketjen Black [23]) [21], and supported catalysts show higher activity and stability in comparison to bulk metal catalysts [23]. However, carbon blacks experienced degradation in a chemical or electrochemical process in FCs [16]. In recent decades, nanostructured carbon materials were explored as catalyst supports, and carbon nanotubes (CNTs) are the most well-known nanostructured carbon. The reported studies have shown that CNTs were superior to carbon blacks as catalyst supports in FCs [16,23]. More recently, since the discovery of graphene in 2004 [24], the interest on this two-dimensional carbon crystal being supports in FCs is growing. On the other hand, many studies disclosed that nanostructured transition metal oxides (e.g. SnO₂ [25], TiO₂ [25,26], CeO₂ [25], V₂O₅ [27], NbO₂/Nb₂O₅ [28], etc.) are crucial in help Pt or Pd gain higher catalytic activity in comparison to pure Pt or Pd. Thus, the addition of transition metal

oxides is cost-effective for FCs. In addition, nanostructured transition metal oxides were also investigated as alternative catalysts, such as ZrO_2 , TiO_2 , SnO_2 , Nb_2O_5 , and Co_3O_4 [29,30]. In particular, metal oxides can be potentially used as supports in place of carbon materials in FCs with improved durability [31]. Thus, transition metal oxides have multiple applications in FCs in helping reduce cost and increase durability.

On the side of LIBs, nanomaterials can be used as electrodes, and there are several potential advantages as well as disadvantages [21]. Favorably, nanomaterials can provide (i) better accommodation of the strain of lithium insertion/removal, improving cycle life; (ii) new reactions not possible with bulk materials; (iii) higher electrode/electrolyte contact area leading to higher charge/discharge rates; (iv) short path lengths for electronic transport (permitting operation with low electronic conductivity or at higher power); and (v) short path lengths for lithium ion transport (permitting operation with low lithium ion conductivity or high power). Unfavorably, they may lead to (i) an increase in undesirable electrode/electrolyte reactions due to high surface area, leading to self-discharge, poor cycling and calendar life; (ii) inferior packing of particles leading to lower volumetric energy densities unless special compaction methods are developed; and (iii) potentially more complex synthesis. Currently many carbon materials (e.g., natural and synthetic graphite, petroleum coke, carbon fibers) were generally developed as anodes but approaching their limits in capacity [13-15]. Thus, in order to increase anode capacities, carbon alternatives are searched and it was discovered that nanosized materials presented very promising performances in high capacity, capacity retention, and high recharging rate [32]. Of them, transition metal oxides cover a wide range of various nanostructured candidates as promising LIB anodes: SnO_2 [33], TiO_2 [34], Co_3O_4 [35], Fe_2O_3 [36], MnO_2 [37], etc. In parallel, carbon-based nanocomposites were found to be able to provide more advantages [21]. For example, SnO_2 is one of the most promising materials for next generation of LIBs, presenting very high capacity. However, SnO_2 suffers from a large volume expansion up to 300% in charging-discharging processes [38,39], which incurs aggregation and thereby badly influences the reversibility. As one solution, carbon-based SnO_2 nanocomposites, for example, SnO_2/CNT nanocomposites, were demonstrated with enhanced performance due to the combined advantages of SnO_2 and

CNTs [40]. More recent studies, similar to the cases of FCs, are paying a special interest on graphene and graphene-based metal oxides as anode candidates of LIBs.

Based on the above review, it is apparent that nanostructured metal oxides as well as carbon-based metal oxide nanocomposites are commonly crucial for the successes of both FCs and LIBs. Thus, the development on them has practical significance for future energy conversion and storage technologies.

1.2 Objectives

Renewable clean energy devices are promising to supply alternative energies for our society. However, FCs and LIBs have urgent needs on advanced nanostructured materials in order to improve their performance. On the other hand, ALD has the capabilities to synthesize novel nanomaterials with many advantages over its counterparts such as CVD, PVD, and solution-based methods. Due to its late emergence for nanotechnology, there is still a large area for ALD to explore.

In this context, the author devoted to study ALD processes with different precursors on various substrates in order to prepare novel nanostructured materials with controlled manners. The efforts were mainly focused on synthesizing nanostructures of several popular metal oxides including Fe_2O_3 , SnO_2 , TiO_2 , and $\text{Li}_4\text{Ti}_5\text{O}_{12}$. Determined by the employed substrates, the aforementioned metal oxides were synthesized into nanotubes, core-shell structured nanocomposites, or graphene-based 3D nanocomposites. In particular, the author elucidated the influences of ALD parameters on the fabrication of the listed metal oxides. In general, ALD is subject to the influences from three key parameters, i.e., precursors, substrates, and temperatures. As a consequence, the thesis not only succeeded in the synthesis of the above-mentioned metal oxides with novel nanostructures but also contribute to the understanding of the growth characteristics of various ALD processes. In addition, the synthesized nanostructured metal oxides are promising candidates in energy devices. The main research objectives are listed below.

(1). To synthesize different nanostructures with different substrates. ALD surface-controlled nature determines that the resultant nanostructures rely on the characteristics of substrates. In this study, four kinds of substrates were employed, including porous anodic aluminum oxide (AAO) templates, undoped carbon nanotubes (CNTs), nitrogen-doped CNTs (N-CNTs), and graphene nanosheets (GNS). In return, nanotubes, CNT-based core-shell nanostructures, and GNS-based 3D architectures were developed with different ALD processes of metal oxides.

(2) To study the growth characteristics of various ALD processes based on different substrates. Besides their dominance on the ultimate nanostructures, substrates are among the critical parameters influencing ALD growth characteristics. The influences may be incurred by the difference on the density of reactive sites between different substrates, or by their inherent properties such as structures.

(3). To investigate the growth characteristics of various ALD processes with temperatures. Temperatures are another key factor. Previous studies disclosed that ALD-deposited thin films might experience a phase-transformation with increased temperatures. Furthermore, increasing temperatures may also change the surface conditions of substrates, leading to some change on the growth characteristics.

(4). To investigate the morphological evolution of the deposited materials with increased ALD-cycles. A distinguishing characteristic of ALD is its deposition precision at the atomic level. Through controlling ALD cycles, precise control on the morphologies and thereby on the deposited materials can be designed in purpose.

(5). To gain understandings on underlying mechanisms of various ALD processes. The general mechanism for various ALD processes is quite straightforward. However, different precursors are likely to induce different growth characteristics, for they may induce different surface reactions. Thus, it is essential to explore the underlying mechanisms for each precursor system.

(6). To explore ALD as a technique to tune the composition of complicated compounds. ALD has widely successes for binary metal oxides or other binary compounds, but ternary or more complicated compounds often take important roles in many areas. For example, $\text{Li}_4\text{Ti}_5\text{O}_{12}$ is a particularly important material as LIB anode and offers many advantages. Thus, it is of great importance to develop ternary or more complicated compound via ALD.

1.3 Thesis structure

This thesis consists of twelve chapters and fulfills the requirements on “Integrated-Article” form as outlined in the *Thesis Regulation Guide* by the School of Graduate and Postdoctoral Studies (SGPS) of The University of Western Ontario. It is built up with the following arrangement.

Chapter 1: generally introduces the background of ALD and its potential applications. In this section, the capabilities of ALD for nanostructured materials are highlighted in energy-related devices, for energy needs represent our most urgent challenges in our society. Besides some general strategies of ALD for nanostructures, the research objectives, the thesis structures, and the major contributions from this study are clearly stated.

Chapter 2: presents a clearer picture of ALD and its characteristics with more detained information. To highlight the superiority of ALD in energy-related devices, a thorough review on emerging applications of ALD in LIBs is conducted. In the meantime, the challenges facing ALD are also summarized.

Chapter 3: outlines the experimental setup, apparatus, materials, and conditions in the study. It also provides the information about experimental methods and procedures.

Chapter 4: describes the ALD of iron oxide on two kinds of carbon nanotubes (CNTs), i.e., undoped and nitrogen-doped CNTs, using ferrocene and oxygen as precursors. This study provided a case study on the effect of reactive sites on ALD processes and on the synthesis of 1D core-shell nanostructures. In this study, the influences of the two kinds of CNTs are compared and clarified. In return, 1D core-shell CNT-based crystalline α -Fe₂O₃ nanocomposites are fabricated.

Chapter 5: studies the ALD-SnO₂ of using SnCl₄ and water as precursors on porous AAO templates with the preparation of highly structure-tunable SnO₂ nanotube arrays. This study disclosed that the ALD-SnO₂ exhibits three growth modes with temperature, i.e., layer-by-layer, layer-by-particle, and evolutionary particles. In particular, the layers are amorphous while the particles are crystalline. To better understand the underlying mechanisms, the effects of temperatures on surface chemistry are discussed with three proposed growth models.

Chapter 6: investigates the effects of doped-nitrogen of N-CNTs on the ALD-SnO₂ of using SnCl₄ and water as precursors. This study revealed that, besides the influences of temperatures on structural phases, the doped-nitrogen atoms are responsible for the success of the ALD-SnO₂ on N-CNTs. It further disclosed that, however, the effects of the doped-nitrogen are closely related with their doping configurations and also show temperature-dependent characteristics. This study provides a route to produce 1D CNT-SnO₂ nanocomposites with tunable deposition.

Chapter 7: makes an attempt to fulfill the ALD-SnO₂ of using SnCl₄ and water as precursors on graphene nanosheets (GNS). GNS as substrate offers high specific areas and excellent electrical conductivity. The synthesized SnO₂-GNS 3D nanocomposites feature the deposited SnO₂ component with controlled morphologies and structural phases.

Chapter 8: fulfill the fabrication of 1D nanostructures of TiO₂ via ALD with two substrates, i.e., AAO and CNTs. The precursors are titanium isopropoxide (TTIP) and water. With the deposition of TiO₂, the former produces TiO₂ nanotubes while the latter

offers TiO₂-CNT composites. It also disclosed that temperatures are critical for tuning the deposited TiO₂ from amorphous to crystalline anatase phase.

Chapter 9: examine the ALD-TiO₂ on GNS, using titanium isopropoxide (TTIP) and water as precursors. It demonstrated that ALD is a fine-tuning route to prepare TiO₂-GNS nanocomposites. Besides controlled morphologies of TiO₂, ALD is able to tune the phases of the deposited TiO₂ from amorphous to crystalline anatase phase by selecting suitable temperatures. It is another case to produce GNS-based metal oxide 3D nanocomposites.

Chapter 10: exploits ALD as a viable route to deposit ternary lithium titanium oxide (LTO, Li₄Ti₅O₁₂) on N-CNTs by combining two sub-ALD systems. One sub-ALD system is TiO₂ using TTIP and water as precursors, and another sub-ALD system is for the deposition of lithium-containing films using lithium tert-butoxide (LTB) and water as precursors. This work demonstrated that, through suitably adjusting the ratio between the two sub-ALD systems and annealing at high temperatures, LTO can be fabricated into 1D CNT-based nanocomposites.

Chapter 11: attempts to provide a general discussion on the synthesized nanostructured materials. It highlights the routes employed in the thesis and their benefits.

Chapter 12: summarize the successes from the thesis and informs of the contributions. In addition, some personal opinions and suggestions from the author are also offered.

1.4 Major contributions

The major contributions of the study can be summarized as follows:

(1). A thorough review was conducted on emerging applications of ALD for LIBs. It timely informs readers of the most recent progress and future research tendencies.

(2). α -Fe₂O₃ as an important energy-related material was successfully synthesized into 1D CNT-based nanocomposites, and the effects of undoped and N-doped CNTs were clarified and discussed.

(3). A systematic study was conducted on ALD-SnO₂ in which SnCl₄ and water were used as precursors. It is disclosed that growth temperatures are critical in determining the growth modes of ALD-SnO₂ and there are three growth modes with ALD-SnO₂, i.e., layer-by-layer, layer-by-particle, and evolutionary particles. This study contributes to the understanding of potential mechanisms with three proposed growth models.

(4). Using N-CNTs as substrates, SnO₂-CNTs nanocomposites were synthesized. Besides controlling the morphologies and structural phases of the deposited SnO₂, the effects of the doped-N atoms were investigated and elucidated.

(5). Based on GNS, ALD-SnO₂ was performed with different temperatures and ALD-cycles. In return, 3D architected SnO₂-GNS was fabricated with tunable SnO₂ components. First, the deposited SnO₂ can be controlled from amorphous to crystalline rutile phase by adjusting growth temperatures. In addition, the deposited SnO₂ can be tuned from small nanoparticles to nanofilms (or big nanoparticles) by increasing ALD-cycles.

(6). Controllable 1D TiO₂ nanostructures were synthesized based on two different substrates, i.e., AAO and CNTs. The first route provides aligned TiO₂ arrays while the second route produces CNT-TiO₂ core-shell nanocomposites. In both cases, the deposited TiO₂ is tunable in structures from amorphous to crystalline anatase phase and in morphologies from nanoparticles to nanofilms.

(7). ALD-TiO₂ was synthesized into 3D architected TiO₂-GNS nanocomposites, based on GNS substrates. Due to tunable phases and evolutionary morphologies of the deposited TiO₂, the synthesized TiO₂-GNS nanocomposites present multi-choices. In addition, a

transition was observed at an intermediate temperature, leading to the deposited TiO_2 being present amorphous and crystalline phase at the same time.

(8). A pioneered work was conducted to synthesize $\text{Li}_4\text{Ti}_5\text{O}_{12}$ on N-CNTs. This work was based on two sub-ALD systems, TiO_2 and a lithium-containing compound. Suitably tuning the ratio between the two sub-ALD systems, it was disclosed that the designed $\text{Li}_4\text{Ti}_5\text{O}_{12}$ was realized by high-temperature annealing. This work for the first time provides a controllable route to synthesize CNT-based $\text{Li}_4\text{Ti}_5\text{O}_{12}$ nanocomposites.

References

- [1] T. Suntola and J. Antson, Method for producing compound thin films, 1977, US patent 4058430.
- [2] T. Suntola, Atomic layer epitaxy, *Mat. Sci. Report*, 1989, **4**, 261-312.
- [3] A. Usui, Atomic layer epitaxy of III-V compounds: chemistry and applications, *Proc. IEEE*, 1992, **80**, 1641-1653.
- [4] M. Ritala and M. Leskelä, Atomic layer epitaxy—a valuable tool for nanotechnology, *Nanotechnology*, 1999, **10**, 19-24.
- [5] R. L. Puurunen, Surface chemistry of atomic layer deposition: a case study for the trimethylaluminum/water process, *J. Appl. Phys.*, 2005, **97**, 121301.
- [6] M. Knez, K. Nielsch, and L. Niinistö, Synthesis and surface engineering of complex nanostructures by atomic layer deposition, *Adv. Mater.*, 2007, **19**, 3425-3438.
- [7] H. Kim, H.-B.-R. Lee, and W.-J. Maeng, Applications of atomic layer deposition to nanofabrication and emerging nanodevices, *Thin Solid Films*, 2009, **517**, 2563-2580.
- [8] S. M. George, Atomic layer deposition; an overview, *Chem. Rev.*, 2010, **110**, 111-131.
- [9] K. Tomabechi, Energy resources in the future, *Energies*, 2010, **3**, 686-695.
- [10] M. S. Dresselhaus, I. L. Thomas, Alternative energy technologies, *Nature*, 2001, **414**, 332-337.
- [11] Q. Schiermeier, J. Tollefson, T. Scully, A. Witze, and O. Morton, Electricity without carbon, *Nature*, 2008, **454**, 816-823
- [12] D. Pimentel, A. Marklein, M. A. Toth, M. Karpoff, G. S. Paul, R. McCormack, J. Kyriazis, and T. Krueger, Biofuel impacts on world food supply: use of fossile fuel, land and water resources, *Energies*, 2008, **1**, 41-78.
- [13] L. Carrette, K. A. Friedrich, and U. Stimming, Fuel cells: principles, types, fuels, and applications, *ChemPhysChem*, 2000, **1**, 162-193.
- [14] J. Tollefson, Fuel of the future?, *Nature*, 2010, **464**, 1262-1264.

- [15] A. Witze, Obama requests US science funding, *Nature*, **2009**. doi:10.1038/news.2009.457.
- [16] S. Zhang, X. Yuan, J. N. C. Hin, H. Wang, K. A. Friedrich, and M. Schulze, A review of platinum-based catalyst layer degradation in proton exchange membrane fuel cells, *J. Power Sources*, 2009, **194**, 588-600.
- [17] D. S. Su and R. Schlögl, Nanostructured carbon and carbon nanocomposites for electrochemical energy storage applications, *ChemSusChem*, 2010, **3**, 136-168.
- [18] M. Armand and J. M. Tarascon, Building better batteries, *Nature*, 2008, **451**, 652-657.
- [19] J. M. Tarascon and M. Armand, Issues and challenges facing rechargeable lithium batteries, *Nature*, 2001, **414**, 359-367.
- [20] B. Scrosati and J. Garche, Lithium batteries: status, prospects and future, *J. Power Sources*, 2010, **195**, 2419-2430.
- [21] A. S. Aricò, P. Bruce, B. Scrosati, J. M. Tarascon, and W. V. Schalkwijk, Nanostructured materials for advanced energy conversion and storage devices, *Nature Mater.*, 2005, **4**, 366-377.
- [22] C. J. Zhong, J. Luo, B. Fang, B. N. Wanjala, P. N. Njoki, R. Loukrakpam, and J. Yin, Nanostructured catalysts in fuel cells, *Nanotechnology*, 2010, **21**, 062001.
- [23] H. Liu, C. Song, L. Zhang, J. Zhang, H. Wang, and D. P. Wilkinso, A review of anode catalysis in the direct methanol fuel cell, *J. Power Sources*, 2006, **155**, 95-110.
- [24] K. S. Novoselov, S. V. Morozov, D. Jiang, Y. Zhang, S. V. Dubonos, I. V. Grigorieval, and A. A. Firsov, Electric field effect in atomically thin carbon films, *Science*, 2004, **306**, 666-669.
- [25] H. Yuan, D. Guo, X. Qiu, W. Zhu, and L. Chen, Influence of metal oxides on Pt catalysts for methanol electrooxidation using electrochemical impedance spectroscopy, *J. Power Sources*, 2009, **188**, 8-13.
- [26] E. N. Muhamad, T. Takeguchi, G. Wang, Y. Anzai, and W. Ueda, Electrochemical characteristics of Pd anode catalyst modified with TiO₂ nanoparticles in polymer electrolyte fuel cell, *J. Electrochem. Soc.*, 2009, **156**, B32-B37.
- [27] P. Justin and G. R. Rao, Enhanced activity of methanol electro-oxidation on Pt-V₂O₅/C catalysts, *Catal. Today*, 2009, **141**, 138-143.

- [28] K. Sasaki, L. Zhang, and R. R. Adzic, Niobium oxide-supported platinum ultra-low amount electrocatalysts for oxygen reduction, *Phys. Chem. Chem. Phys.*, 2008, **10**, 159-167.
- [29] Y. Liu, A. Ishihara, S. Mitsushima, N. Kamiya, and K. Ota, Transition metal oxides as DMFC cathodes without platinum, *J. Electrochem. Soc.*, 2007, **154**, B664-B669.
- [30] A. Serov and C. Kwak, Review of non-platinum anode catalysts for DMFC and PEMFC application, *Appl. Catal. B: Environmental*, 2009, **90**, 313-320.
- [31] Q. Wang, A. Wei, X. Zhao, and S. Zhang, Novel metal oxide support with water activation ability for use in direct methanol fuel cells, *Chinese J. Chem.*, 2009, **27**, 1649-1656.
- [32] P. Poizot, S. Laruelle, S. Grugeon, L. Dupont, and J.-M. Tarascon, Nano-sized transition-metal oxides as negative-electrode materials for lithium-ion batteries *Nature*, 2000, **407**, 496-499.
- [33] S. Chou, J. Wang, H. Liu, and S. Dou, SnO₂ meso-scale tubes: one-step, room temperature electrodeposition synthesis and kinetic investigation for lithium storage, *Electrochem. Comm.*, 2009, **11**, 242-246.
- [34] M. J. Lindsay, M. G. Blackford, D. J. Attard, V. Luca, M. Skyllas-Kazacos, and C. S. Griffith, Anodic titania films as anode materials for lithium ion batteries, *Electrochim. Acta*, 2007, **52**, 6401-6411.
- [35] F. Zhan, B. Geng, and Y. Guo, Porous Co₃O₄ nanosheets with extraordinarily high discharge capacity for lithium batteries, *Chem. Eur. J.*, 2009, **15**, 6169-6174.
- [36] H. Liu, G. Wang, J. Park, J. Wang, H. Liu, and C. Zhang, Electrochemical performance of α -Fe₂O₃ nanorods as anode material for lithium-ion cells, *Electrochim. Acta*, 2009, **54**, 1733-1736.
- [37] A. L. M. Reddy, M. M. Shaijumon, S. R. Gowda, and P. M. Ajayan, Coaxial MnO₂/carbon nanotube array electrodes for high-performance lithium batteries, *Nano Lett.*, 2009, **9**, 1002-1006.
- [38] I. A. Courtney and J. R. Dahn, Electrochemical and in situ x-ray diffraction studies of the reaction of lithium with tin oxide composites, *J. Electrochem. Soc.*, 1997, **144**, 2045-2052.

- [39] I. A. Courtney and J. R. Dahn, Key factors controlling the reversibility of the reaction of lithium with SnO_2 and Sn_2BPO_6 glass, *J. Electrochem. Soc.*, 1997, **144**, 2943-2948.
- [40] G. An, N. Na, X. Zhang, Z. Miao, S. Miao, K. Ding, and Z. Liu, SnO_2 /carbon nanotube nanocomposites synthesized in supercritical fluids: highly efficient materials for use as a chemical sensor and as the anode of a lithium-ion battery, *Nanotechnology*, 2007, **18**, 435707.

CHAPTER 2

LITERATURE REVIEW

2.1 Atomic layer deposition

2.1.1 A briefing on traditional film deposition techniques

Before we discuss atomic layer deposition (ALD), it is necessary to know the other two film deposition techniques, chemical vapor deposition (CVD) and physical vapor deposition (PVD).

In a CVD process, a solid material is deposited onto a heated substrate surface as a result of chemical reactions in gas phase in a proper reactor. The deposition reaction can be of several types including pyrolysis, reduction, oxidation, compound formation, and disproportionation, etc [1]. The precursors utilized in CVD should satisfy several requirements [2]: (1) having sufficient vapor pressure to allow transport to the substrate surface, (2) being easy to decompose to the desired product at an acceptable temperature, and (3) having no association or reaction in the gas phase.

Different from CVD, PVD includes all methods in which the vapor particles are ejected from a source into the vacuum by a physical process [1]. PVD is divided into two main classes, i.e., evaporation and sputtering. In PVD processes, atoms or small clusters of atoms are removed from a source (solid or liquid). These atoms are traveling in a vacuum chamber reaching a substrate to form a thin film. The rate of deposition depends mainly on system pressure, source-substrate distance and substrate temperature. The nucleation and the growth of thin films generally occur via condensation of individual atoms or polyatomic species striking the substrate surface.

Both CVD and PVD have a long history with human society and they have widely applied for depositing a broad variety of films. However, the two commonly suffer from some drawbacks. They both are source-controlled processes in which films are deposited continuously. A problem commonly encountered by them is the precise control on deposited films. In addition, they both are not good at conformal deposition, especially for trenched structures. Thus, there are needs for a technique enabling uniform and

conformal deposition. In this way, ALD fits the needs, associated with many other advantages, as will be discussed in the following sections.

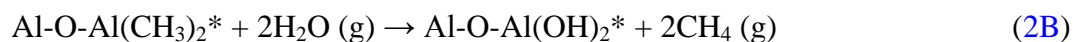
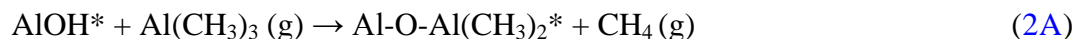
2.1.2 Mechanisms

ALD by nature is a vapor-phase thin film deposition process, first emerged in 1970s and credited to Suntola and his co-workers [3]. Its initial application was about the synthesis of II-VI and III-V compounds for thin film electroluminescent (TFEL) display devices [4,5]. Since then, ALD experienced a slow progress. Concurred with the demanding needs in scaling complementary metal-oxide-semiconductor (CMOS), ALD is now undergoing its renaissance starting from the right beginning of the 21st century. Different from its traditional counterparts such as chemical vapor deposition (CVD) and physical vapor deposition (PVD) whose deposition are dominated by the supply of precursor sources, ALD is a surface-controlled process in which the growth of films is dictated by two self-terminating gas-solid surface reactions.

To demonstrate the underlying mechanisms of ALD processes, a classical ALD process for the binary compound Al₂O₃ is schematically illustrated in [figure 2.1](#). Two precursors are exclusively required for a binary ALD. The most successful ALD process of Al₂O₃ (ALD-Al₂O₃) uses trimethylaluminum (TMA) and water as precursors, as shown in [figure 2.1](#). In a CVD process, the TMA and water reaction is described by an overall reaction [6]:



In comparison, the ALD-Al₂O₃ proceeds with two half-reactions as suggested as follows: [6]:



where the asterisks (*) designate the species carried by or attached on substrates by chemisorption, and (g) the gas phase of byproducts. In practice, an ALD-Al₂O₃ process includes four repetitive steps: (1) a supply of the aluminum source precursor TMA to induce a surface reaction (i.e., [2A](#)) with the reactive sites (e.g., -OH, [figure 2.1\(a\)](#)) on a substrate or on a former-deposited film, and thereby to form an intermediate layer (i.e., -

$\text{Al}(\text{CH}_3)_2$, figure 2.1(b) and (c) with the release of CH_4 as the byproduct; (2) a purging phase following the self-terminated reaction 2A to evacuate the oversupplied non-reacted TMA and the gaseous byproduct CH_4 ; (3) A supply of an oxygen precursor H_2O to start a

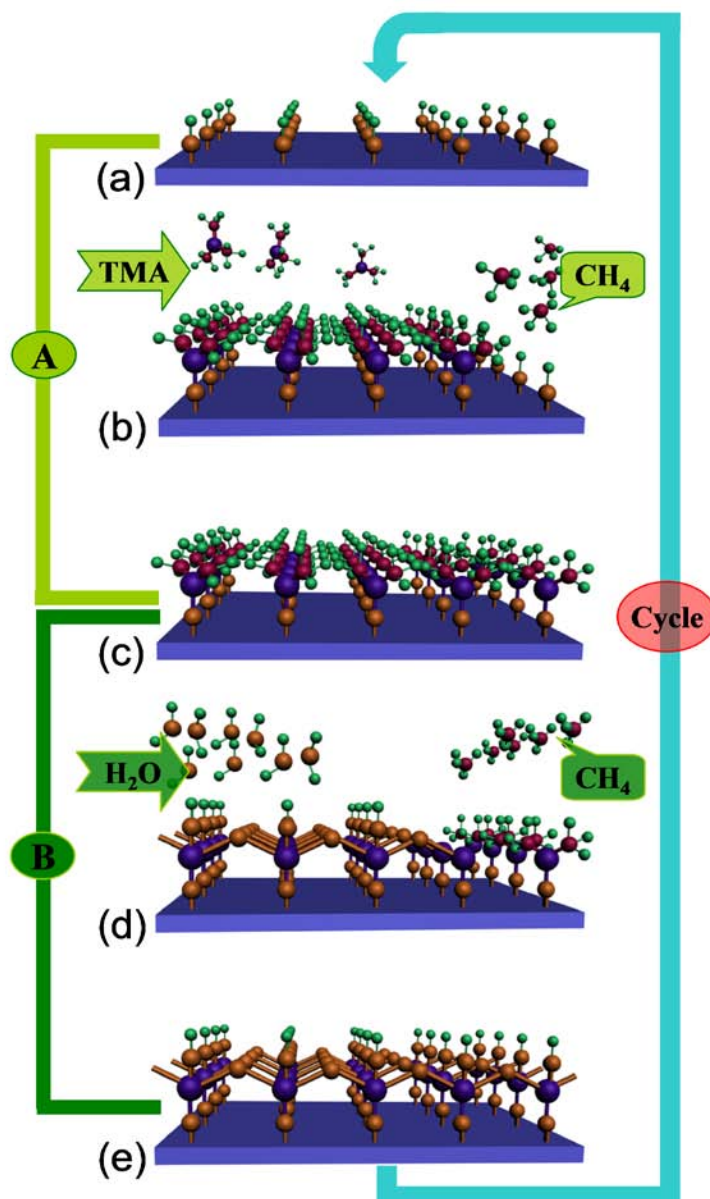


Figure 2.1 A model ALD process by depositing Al_2O_3 using TMA and water as precursors. (a) the initial substrate covered by hydroxyl groups; (b) TMA molecules reacting with hydroxyl groups, leading to a new intermediate layer; (c) the substrate covered with a new-created intermediate layer; (d) H_2O molecules reacting with the intermediate layer, leading to new hydroxyl groups; (e) the substrate covered again by hydroxyl groups.

second surface reaction (i.e., 2B, figure 2.1(d)) with the reactive groups (i.e., $-\text{CH}_3$) of the intermediate product and to produce the target product Al_2O_3 as well as new reactive sites (i.e., $-\text{OH}$, figure 2.1(e)); (4) another purging phase to evacuate the oversupplied non-reacted precursor H_2O and the gaseous byproduct CH_4 . Obviously, ALD is cyclic in operation and proceeds in a layer-by-layer manner.

It needs to be emphasized that, for an ALD process as illustrated above, there are three key parameters determining the deposition features. They are substrates, temperatures, and precursors. First, as shown by figure 2.1, a substrate is required to be initially functionalized with reactive sites [7]. The first half-reaction relies on the interaction between the surface reactive sites and the first precursor. The reaction terminates with a new created layer when the surface reactive sites are saturated. Thus the gas-solid reaction is by nature self-limiting. The new layer provides reactive sites for a following half-reaction while the oversupplied precursor and by-products are purged by vacuum. Similarly, the second half-reaction creates a new layer with functional groups for the following reactions and is also self-terminating. As a consequence, the two half-reactions combine to produce the target material in a well-controlled growth manner. Obviously, the initial coverage of reactive sites affects the growth of deposited materials. As an important factor, the growth temperature is also crucial for sustaining ALD characteristics. As stated above, ALD performs in a self-limiting manner and therefore it requires the adsorption of precursors to be chemisorption rather than physisorption [8]. Thus, the lowest temperature should be able to minimize physisorbed ligands. On the other hand, a suitable ALD temperature should not decompose any precursor. Otherwise, the deposition proceeds in a CVD manner other than ALD. In comparison to CVD, ALD typically employs much lower temperatures even down to a room temperature [9]. There may exist a range of temperature in which the growth of ALD is comparatively constant, called ALD window. As for ALD precursors, they should be able to provide sufficient vapors and their concentrations in the gas phase must exceed a threshold value to saturate all of the adsorption sites on substrates [10] in order to achieve continuous monolayer coverage. The fractional coverage increases linearly with precursor partial pressure initially, but then levels off to 100% once a threshold pressure has been exceeded. This threshold must

be determined experimentally from deposition rates and film properties and usually chemisorption occurs on time scales of tens of milliseconds [11]. It is worth noting that precursors take effect on the ALD growth, closely related to their properties. Furthermore, the purging of oversupplied precursors and by-products is also critical for avoiding continuous processes (e.g., CVD and PVD) and for accurately controlling the ALD growth of materials. Hence, the purge flow rates must be sufficiently high to reduce the concentrations of oversupplied precursors and byproducts to trace levels after their respective steps [10], or the purges have to be elongated.

2.1.3 Characteristics

In return for its unique reaction mechanisms and operation, ALD offers a series of distinguished advantages for resultant films over its vapor-phase counterparts (e.g., CVD and PVD) and other solution-based methods.

A. Low growth temperature

One of main features of ALD, especially compared to CVD, is its much lower growth temperature (typically less than 400 °C). In particular, ALD succeeded in depositing many materials with low temperatures lower than 100 °C, even down to room temperature (RT). Gasser et al conducted the first ALD experiments at RT for depositing SiO₂ from Si(NCO)₄ and water in 1994 [9]. Later in 1997, Luo et al [12] deposited CdS on ZnSe(100) at RT in a ultra-high-vacuum ALD system using Cd(CH₃)₂ and H₂S as precursors. Almost at the same time, George's group [13] at University of Colorado discovered that ALD-SiO₂ can be performed at RT by catalyzing the surface reactions of SiCl₄ and water with pyridine (C₅H₅N), though traditional ALD processes are catalyst-free. Other metal oxides deposited by ALD at or around RT include B₂O₃ [14], Al₂O₃ [15,16], TiO₂ [16], ZnO [17], ZrO₂ [18] and SnO₂ [19], etc. In addition, some metals such as Cu [20] and Pd [21] were also deposited by ALD at temperatures lower than 100 °C. This benefit is particularly attractive for coating heat-sensitive materials such as polymers or biomaterials.

B. Atomic-scale and stoichiometric deposition

Due to its layer-by-layer self-limiting nature, ALD affords another advantage in enabling the deposited films precisely controlled at the atomic level. This character makes ALD superior to CVD, PVD, and solution-based methods. In general, the growth rates of ALD are at the order of magnitude of angstroms (typically less than 2 Å per cycle), jointly determined by the employed precursors, temperatures, and substrates. For example, the growth rate for ALD- Al_2O_3 of using TMA and water reaches a maximum of 1.33 Å/cycle in the range 100 - 125 °C while lower values at higher or lower temperatures [15]. In contrast, the ALD- Al_2O_3 of using $\text{Al}(\text{CH}_3)_2\text{Cl}$ and water achieved the maximum growth rate of approximately 0.8 Å/cycle in a narrow temperature range from 180 to 250 °C [22], and the ALD- Al_2O_3 of using $(\text{CH}_3)_2(\text{C}_2\text{H}_5)\text{N}:\text{AlH}_3$ and water resulted in a much higher growth rate of 2.5 nm/cycle under growth temperatures lower than 200 °C [23]. It worth pointing out that, attempting to overcome the traditional ALD slowness in deposition, Gordon's group at Harvard University developed a pair of precursors, TMA and tris(tert-butoxy)silanol $[(\text{Bu}^t\text{O})_3\text{SiOH}]$ which realized a rapid growth of SiO_2 with a rate of 12 nm/cycle in the temperature range from 200 to 300 °C [24]. However, this kind of cases is really rare in ALD processes.

In addition to the control on growth rates, ALD is capable of stoichiometrically tuning the compositions of deposited materials. As a whole, the ALD-deposited materials stoichiometry is close to their theoretic values, but growth temperatures and precursors may play some influence. Using Rutherford backscattering spectrometry (RBS), for example, Groner et al [15] demonstrated that the O/Al ratios due to the ALD- Al_2O_3 of TMA and water close to 1.50 in the range 33 – 177 °C, varying from 1.34 to 1.70. They also pointed out that there is no systematic trend with growth temperatures. Using time-of-flight elastic recoil detection analysis (TOF-ERDA), Niinistö et al [25] studied the ALD of gadolinium oxide films. They disclosed that, using $\text{Gd}(\text{thd})_3$ and O_3 as ALD precursors, the resultant Gd/O ratios are lower than the theoretic value of 0.67 but increase from 0.41 to 0.55 with growth temperatures increasing from 225 to 350 °C. In contrast, the ALD precursors of $(\text{CpCH}_3)_3\text{Gd}$ and water contributed to higher Gd/O ratios

increasing from 0.57 to 0.64 with increasing temperatures from 150 to 250 °C. Furthermore, Kukli et al [26] demonstrated that ALD-HfO₂ is stoichiometric dioxides when the deposition was preformed at 300 °C with HfCl₄ or HfI₄ and water as precursors. Thus, suitable choices on ALD parameters are crucial for controlling both growth rates and compositions of deposited films.

C. Excellent uniformity and conformality

Another benefit from ALD unique mechanisms is excellent uniformity and unrivalled conformality of deposited films over CVD, PVD, and solution-based methods. Atomic force microscopy (AFM) disclosed that, for instance, ALD-Al₂O₃ on flat substrates presents a surface roughness of 1 - 3 Å for a deposition in the range 200 - 560 Å [27-29]. A much smaller surface roughness of 0.7 Å was even reported by Lee et al [30]. Apart from the uniformity, ALD offers non-planar substrates with highly conformal films as well. There has been a dramatically increasing amount of work reported on various conformal nanostructures by ALD in the past decade. Some representative ALD-induced nanostructures are shown in figure 2.2, such as the layered Al₂O₃-ZnO nanolaminates on Si substrates (figure 2.2(a)) [31], SiO₂-coated TiO₂ composite nanoparticles (figure 2.2(b)) [32], hollow TiO₂ nanoribbons (figure 2.2(c)) [33], coaxial HfO₂ nanotubes (figure 2.2(d)) [34], three-layered discontinued TiO₂ 3D nanofilms (figure 2.2(e)) [35], and complex 3D Al₂O₃ nanostructures (figure 2.2(f)) [36]. Moreover, ALD to date synthesized a large variety of materials, ranging from inorganic to organic classes. In Puurunen's review [8], the author made a comprehensive and thorough summary on ALD successes previous to 2005, though update progresses are revealing more classes of materials synthesized by ALD. Historically, a large amount of reviews was conducted on ALD by researchers, herein we would like to recommend the ones made recently by Knez et al [37], Kim et al [38], and George [39] to readers for the progresses in developing various novel nanostructures and emerging applications in the past decade. Now ALD has widely broadened its applications compared to the initial uses for semiconductors. Among the new trends for ALD, there is an increasing interest in employing ALD for energy conversion and storage such as fuel cells (FCs), solar cells (SCs), and lithium-ion

batteries (LIBs), due to its impressive superiorities to other techniques.

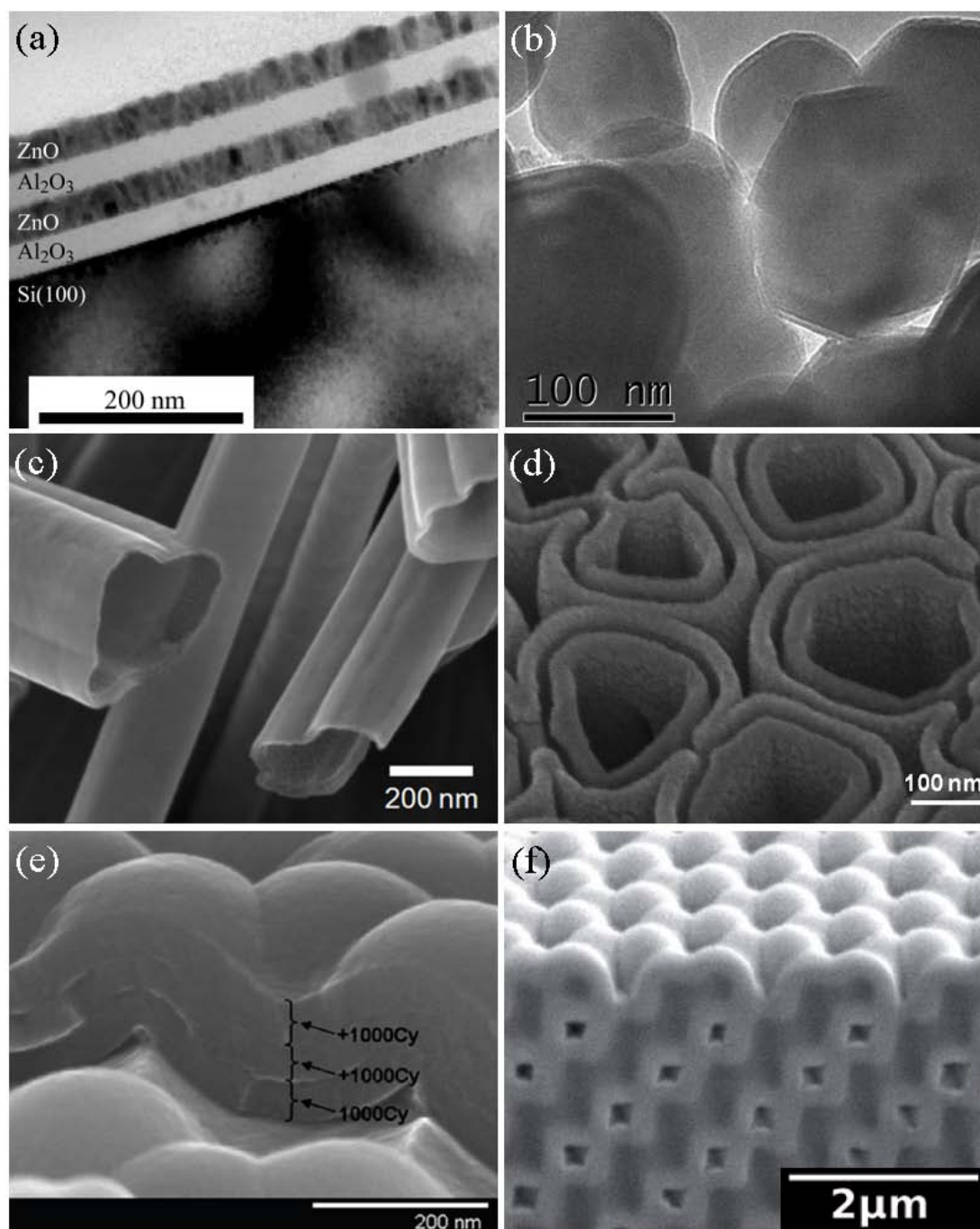


Figure 2.2 The examples for ALD-fabricated nanostructures. (a) the layered Al_2O_3 - ZnO nanolaminates on Si substrates; (b) SiO_2 -coated TiO_2 composite nanoparticles; (c) hollow TiO_2 nanoribbons; (d) coaxial HfO_2 nanotubes; (e) three-layered discontinued TiO_2 3D nanofilms; and (f) complex 3D Al_2O_3 nanostructures.

Table I. Comparison of deposition properties for PVD, CVD, and ALD [2].

Deposition conditions	PVD	CVD	ALD
Vacuum requirement	$<10^{-2}$ Torr	$10^{-3}-10^2$ Torr	$10^{-4}-1$ Torr
Deposition thickness range	5 nm \rightarrow 10 μ m	10 nm \rightarrow 3 μ m	0.1–40 nm
Uniformity control	nm	nm	0.1 nm
Deposition rate	10–1000 nm/min	10–1000 nm/min	<0.2 nm/cycle; <1.0 nm/min typical
Conformality	15% at 4:1 aspect ratio	0%–100% at 4:1 aspect ratio	100% at 15:1 aspect ratio
Contamination/ Particles	Indirect only (flaking)	Particles can exist due to gas phase reactions	Low: no gas phase chemistry

Table II. Overview of the materials grown by ALD [8].

Legend:

- the pure element has been grown
- compounds with O
- compounds with N
- compounds with S
- other compounds
- compounds with Te
- compounds with Se

1	2																	18
1																		2
3	4																	10
11	12																	18
19	20	21	22	23	24	25	26	27	28	29	30	31	32	33	34	35	36	
37	38	39	40	41	42	43	44	45	46	47	48	49	50	51	52	53	54	
55	56	57	72	73	74	75	76	77	78	79	80	81	82	83	84	85	86	
87	88	89	104	105	106	107	108	109	110	111	February 2005							
Lanthanoids*		58	59	60	61	62	63	64	65	66	67	68	69	70	71			
Actinoids**		90	91	92	93	94	95	96	97	98	99	100	101	102	103			

In summary, ALD provides a series of advantages for film deposition, as discussed above. In Table I, the differences between ALD, and CVD and PVD are compared. It is apparent that ALD is especially good at depositing high quality, pinhole-free, highly conformal

thin films. Furthermore, ALD covers a large range of materials for deposition, which were summarized by Puurunen [8], as shown in Table II. Due to the advantages offered by ALD, its applications are broadening quickly from the initial semiconductors to more promising areas. In this review, we are going to exemplify the emerging applications of ALD for energy-related devices with the case for lithium-ion batteries (LIBs). This review mainly covers two ways. First, ALD is used to design high-performance and new battery components including anodes, cathodes, and inorganic solid electrolytes. Second, ALD is employed as an effective tool to surface-modifying battery anodes and cathodes with thin films for enhanced performance. As will be demonstrated, ALD performs in a precise and flexible manner for all these applications, and the resultant performance is closely related with ALD's characteristics. We hope that this work will be insightful for follow-up studies and help boost the applications of ALD in other areas.

2.2 Emerging applications of atomic layer deposition for lithium-ion batteries

2.2.1 Background

Nowadays people in our civilized society are enjoying more entertainments and conveniences than ever before, such as vehicles for transportation, cell phones for communication, video camcords for memory, MP3 players for music, laptops for internet, and so on. It is apparent that all the comforts need stable and reliable energy supplies. In contrast to the constant increasing needs on energy, however, fossil fuels (coal, petroleum, and natural gas) as our main energy sources are depleting while their combustion is causing greenhouse effect and pollutions on our environments as well [40]. In other words, we are being threatened with the loss of the comforts by the shortage of available energies. Thus, seeking renewable clean energy sources as alternatives becomes urgent. Of potential energy sources, nuclear, solar, and wind energy are principal candidates [40-42]. However, all of them are commonly exposed to some drawbacks. Nuclear plants, for example, produce radioactive fission products and also pose potential risks on security [40]. The recent nuclear leakage caused by earthquakes in Japan forces us to rethink the

use of nuclear energy. On the other side, solar and wind energy require large areas. They are also limited geographically and operate intermittently. Thus, energy storage is required for all the aforementioned alternative energies [41] and the energy security lies in the heart of our mobility, our prosperity and our daily comfort [43].

To meet the energy needs, batteries as chemical devices are ideal for storing electrical energy as chemical energy [44]. Over a long history for batteries, LIBs are now taking dominance for various applications, due to their high energy and power density over former generation batteries [42,44]. A LIB cell conventionally consists of a carbon anode (negative electrode), a lithium metal oxide cathode (positive electrode, e.g., LiCoO_2), and an ionically conductive “electrolyte” between the two electrodes. Electrolytes can be a liquid, a solid polymer, or an inorganic solid [44]. In most cases, LIBs use liquid electrolytes containing a lithium salt such as LiPF_6 , LiBF_4 , LiClO_4 , LiBC_4O_8 (LiBOB), and $\text{Li}[\text{PF}_3(\text{C}_2\text{F}_5)_3]$ (LIFAP), which dissolves in a mixture of organic alkyl carbonate solvents like ethylene, dimethyl, diethyl, and ethyl methyl carbonate (i.e., EC, DMC, DEC, EMC, respectively) [45]. An external connection between the two electrodes induces a spontaneous flow of electrons from an anode to a cathode, due to their different chemical potentials dictated by the materials chemistry which occurs at each [46]. As called the rocking chair batteries, LIBs rely on the shuttle of lithium-ions back and forth between the two electrodes during charge-discharge cycles. Both cell voltage and capacity are governed by the materials chemistry [46,47]. LIBs were first commercialized in 1991 by Sony Corporation [46,48]. Currently, they can provide a voltage of the order of 4 V and a specific energy ranging from 100 to 150 Wh/kg [10]. There are three main domains of application for LIBs [42,44,45]: portable electronics, transport, and stationary storage. The first is so far the most developed and largest in terms of the number of produced units while the other two are expected to be boosted in the coming years [44]. At present, the construction of large stationary batteries as centralized facilities is prohibitively expensive [42]. A most notable scaled-up application is for hybrid electrical vehicles (HEVs), plug-in hybrid electrical vehicles (PHEVs), and pure electrical vehicles (EVs) [45]. Unfortunately, conventional LIBs (e.g., C/ LiCoO_2 batteries) suffer from a series of problems in cost, safety, cell energy density (voltage \times capacity), rate of charge-

discharge, and service life [49,50] for transport use, whose roots lie in anodes, cathodes, electrolytes, or the interrelations between them [51,52]. More specifically, LIBs must be able to operate at realistic temperatures (a range from -46 to +66 °C) with 5000 charge-discharge cycles and a 15-year calendar life [53]. However, these are still challenging for current LIBs technologies. Therefore, intensive research is being conducted worldwide on new materials for next generation LIBs. Since nanostructured materials were disclosed by Poizot et al [54] to be more advantageous than bulk materials as electrodes, a large variety of nanomaterials and their composites were investigated, as reviewed by many researchers [42,45,47,55-65]. The benefits offered by nanomaterials include [54,56,60,64]: (1) improved cycle life due to better accommodation of the strain of lithium insertion/disinsertion; (2) new reactions not possible with bulk materials; (3) higher discharge-charge rates due to higher electrode/electrolyte contact area; (4) short path lengths for both electron and lithium ion transport. Associated with these benefits, however, nanoelectrodes are supposed to be with some disadvantages such as undesirable reactions due to high surface area, inferior packing leading to lower volumetric energy densities, and more complex synthesis. Thus, researchers have also been seeking solutions from electrolytes/separators [66-71] and other strategies to modify electrodes and electrolytes [72-77]. Of them, surface coating of electrodes [59,60,73-77] was proved to be an effective venue for improving the performance of LIBs and it covers different types of materials depending on the nature of electrodes. For example, carbon coating was widely adopted for both anode and cathode materials in order to enhance electrical conductivity, buffer volume change, or stabilize solid electrolyte interface (SEI) films [59,60,73,75]. In addition, the coatings of metals (e.g., Ag), metal oxides (e.g., Al₂O₃, SnO₂, ZrO₂, MgO, and ZnO), and other classes were also demonstrated to be beneficial for a better performance of LIBs [59,60,73-77].

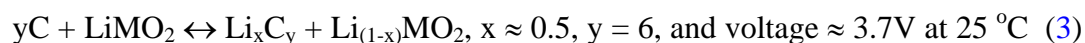
In addressing the various challenges facing LIBs, ALD appears to be a promising tool for LIBs in the past few years and is attracting an increasing interest, for it is capable of enhancing the performance of LIBs via multiple routes in a more precise and flexible manner. As will be demonstrated this work, ALD is used not only for accurately exploiting various high-performance LIB components including anodes, cathodes and

electrolytes, but for effective modification of electrode materials with ultrathin coatings down to subnanometers as well. For the former, ALD was revealed to a viable route to synthesize novel nanostructures with dramatically increased capacity of electrodes and to fine-tune the composition of electrolytes. For the latter, ALD displayed to be the only precise venue to directly coat prefabricated electrodes with high-quality thin films, besides coating electrode materials as usually did previously by other techniques. This article represents the first effort to thoroughly review the recent work on employing ALD as a tunable and precise tool for high-performance LIBs, aimed at timely informing colleague researchers of this state of art technique and its versatile capabilities for enhancing the performance of LIBs. This review covers four parts in total. Following this Introduction, we concentrate on the precise synthesis of novel LIB components, i.e., anodes, cathodes, and electrolytes by ALD in the second section. Furthermore, a recent boost on using ALD as a route to modify both anodes and cathodes is covered in the third part and the resultant effects on high-performance of LIBs are presented with potential mechanisms. As a concluding remark, the last part summarizes the successes of ALD in LIBs and, in particular, gives outlooks and expectations on future studies as well. We believe that this work will bring a blow of fresh air for the development of LIBs and thereby help researchers make efforts for further breakthroughs of next generation LIBs.

2.2.2 ALD on designing novel battery components

A. Anodes

In conventional LIBs, carbon materials are exclusively used as anodes while lithium metal oxides LiMO_2 ($M = \text{Co}, \text{Ni}$, e.g., LiCoO_2) are used for cathodes. In most cases, the employed liquid electrolyte is LiPF_6 in EC-DMC [49]. This configuration of $\text{C}/(\text{LiPF}_6$ in EC-DMC)/ LiMO_2 operates on a process [45,49]:



in which the lithium ions reversibly insert and extract between the two electrodes with a concomitant removal and addition of electrons. The carbon anodes have a limited theoretical capacity of 372 mAh/g [45,56,62,64]. Additionally, carbon materials suffer

from capacity degradation incurred by irreversible side reactions occurred between lithium ions and/or the solvent and the anode surface, leading to the formation of SEI during charge-discharge cycles [51,78]. As such, better alternative anode materials have been sought in the past decade. Lithium alloys such as lithium-silicon (Li-Si) and lithium-tin (Li-Sn) are promising to provide higher specific capacity in replace of carbon materials, accounting for 4000 and 990 mAh/g, respectively [45,49]. Unfortunately, the lithium alloys encounter the large volume expansion-contraction (300 - 400%) during charge-discharge cycles, leading to mechanical stresses and thereby the resultant disintegration of the anodes with subsequent failure [45,49]. Due to the aforementioned issues faced by the carbon and metallic anodes, metal oxides (e.g., TiO_2 , MnO_2 , Fe_2O_3 , Co_3O_4 , and SnO_2 etc) and other compounds were exploited as alternatives [45,49,54,56,60-62,64]. Of them, titanium oxide (TiO_2) and lithium titanium oxide ($\text{Li}_4\text{Ti}_5\text{O}_{12}$, LTO) are attractive, despite their relatively low specific capacity (335 mAh/g for TiO_2 and 175 mAh/g for LTO) and higher voltage level (1.2 – 2.0 V vs. Li^+/Li) [45,49]. Their common benefits include negligible volume change for improved cycleability, no electrolyte decomposition, and therefore no SEI formation and improved safety [45,49,62].

A1. ALD-induced nanostructured anode materials

In her excellent review, Puurunen [8] made an extensive and thorough categorization on ALD precursors exposed in literature prior to 2005. As disclosed by Puurunen's review [8], ALD had ubiquitous successes on potential anode materials, such as Si, MnO_x , Fe_2O_3 , CoO_x , NiO, ZnO, SnO_2 , etc. It worth pointing out that at that time the ALD processes were mainly based on flat substrates such as silicon wafers, and only a few nanostructures were reported. In recent years, more and more nanostructured materials were developed with ALD and many of them are promising as candidate anodes of LIBs. In Table III, we summarized the progress on nanostructured anode materials synthesized by ALD. The ultimate nanostructures are mainly determined by the employed substrates. In general, the substrates mainly consist of three types: porous templates, carbon-based materials, and biological materials. The first class includes anodic aluminum oxide (AAO)

and polycarbonate (PC) templates, the second one has polyacrylonitrile nanofibers (PAN-NF), carbon nanotubes (CNTs) and graphene nanosheets (GNS), and the last covers nanocellulose (NC), tobacco mosaic virus (TMV), and peptide. There are others. For example, Al nanorods (Al-NRd) were used as substrates as well [87].

Ascribed to the different substrates used, as a result, ALD induced several principles and therefore contributed to different ultimate nanostructures such as nanotube arrays (NT-A), nanotube networks (NT-N), nanoribbon networks (NRb-N), nanorod arrays (NRd-A), and 3D networks (3D-N). In Figure 2.3, we summarize the main strategies and the resultant nanostructures. Figure 2.3(a) displays a traditional but typical thought to produce nanotube arrays using AAO templates. Actually, this route is also applicable to PC filters. One difference between AAO and PC lies in their etching processes. Typically, sodium hydroxide (NaOH) or potassium hydroxide (KOH) is used to remove AAO while chloroform (CHCl_3) is employed to dissolve PC [90]. In addition, AAO is thermally stable while PC is only suitable for low temperature ($< 140\text{ }^\circ\text{C}$) ALD processes [90]. Another idea for ALD-induced nanostructures is based on 1D substrates such as nanotubes, nanofibers, nanoribbons, and nanorods etc. In figure 2.3(b), we illustrate this route using ALD-coating on CNTs. Depending on the pristine arrangement of substrates, the resultant nanostructures can be aligned arrays or networks of the aforementioned 1D structures. In many cases, calcination is used for removing the core substrates, improving the crystallinity of synthesized nanostructures, or for the two. Besides the aforementioned two, a recently boosted strategy with ALD is based on biological substrates including NC, peptide, and TMV. This kind of practice was benefited by low temperatures ($< 150\text{ }^\circ\text{C}$) of ALD. As shown in figure 2.3(c), researchers [86] demonstrated ALD- TiO_2 and ZnO on NC aerogel, resulting in their nanotube networks after calcination. Similarly, other researchers developed hollow nanoribbon networks, as summarized in Table III. The most recent nanostructure from ALD is based on GNS. As is well-known, graphene is attracting an increasing attention since it was discovered in 2004 [109]. The reason lies in a series of exceptional properties of graphene, such as high electric conductivity [110] and specific surface area [111]. Thus, graphene-based nanocomposites are expected to provide better performance than any individual component in many applications. In this

way, researchers used solution-based methods and developed several graphene-based metal oxides showing higher capacities, rate capabilities, and stability in LIBs [112,113]. In figure 2.3(d), we schematically demonstrate our recent work, ALD-TiO₂ on GNS [93]. That work disclosed that ALD can provide more benefits, for the deposited materials can be tuned in their morphologies growing from nanoparticles to nanofilms with ALD-cycles and in their textures evolving from amorphous to crystalline phase with temperature. Thus, ALD is a more flexible and controllable strategy for preparation of graphene-based nanocomposites.

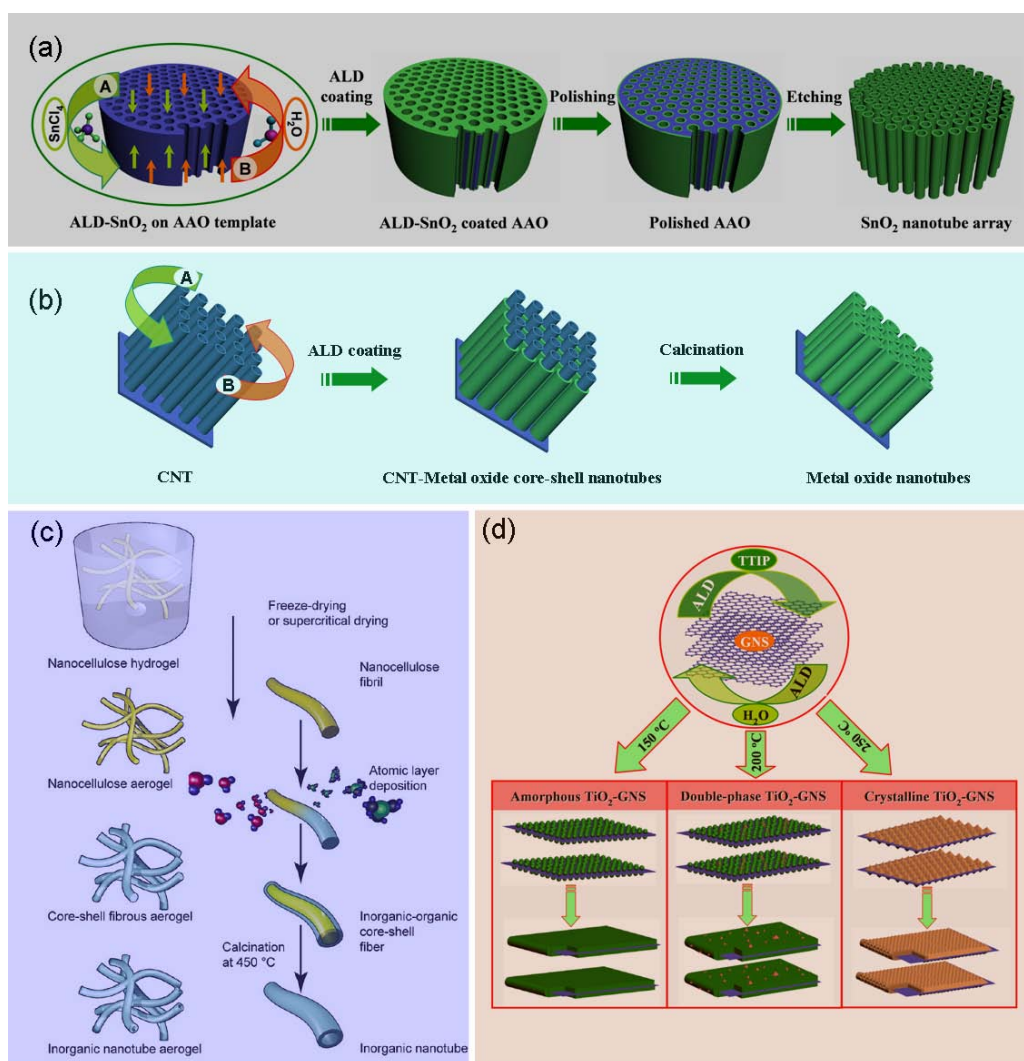


Figure 2.3 Main ALD strategies for fabricating nanostructured materials. (a) the strategy for nanotube arrays using AAO, exemplified by the fabrication of SnO₂ nanotubes; (b) the strategy for nanotubes using CNTs; (c) the strategy for 3D networks of nanotubes based on nanocellulose aerogel; and (d) the strategy for 3D nanostructures based on GNS, exemplified by ALD-TiO₂ on GNS.

Table III Nanostructured anode materials by ALD

Material	Precursor A	Precursor B	Temp. (°C)	Substrate	Nanostructure	Ref.
TiO₂	TiCl ₄	H ₂ O	100-400	AAO	NT-A	79-85
			150	NC	NT-N	86
	TiI ₄	H ₂ O	200	Al-NRd	NRd-A	87
			300	GNS	3D-N	88
	Ti(NMe ₂) ₄	H ₂ O	150	TMV	NT-A	89
	Ti(O ⁱ Pr) ₄	H ₂ O	70-160	AAO	NT-A	90,91
			80-140	PC	NT-A	90,92
			150-250	GNS	3D-N	93
			35	TMV	NT-N	16
			140	Peptide	NRb-N	33,94
	NH ₃	140	Peptide	NRb-N	95	
	NH ₃ +O ₂	140	Peptide	NRb-N	95	
Fe₂O₃	Fe(Cp) ₂	O ₂	400	AAO	NT-A	96
			350	CNT	NT-N	97
	Fe ₂ (O ⁱ Bu) ₆	H ₂ O	130-170	AAO	NT-A	98
ZnO	Zn(C ₂ H ₅) ₂	H ₂ O	40-200	CNT	NT-N	99-101
			200	AAO	NT-A	102
			250	AAO	NT-A, NRd-A	103
			150	NC	NT-N	86
SnO₂	SnCl ₄	H ₂ O	200-400	AAO	NT-A	104
			200-400	CNT	NT-N	105
			200-400	GNS	3D-N	106
	C ₁₂ H ₂₄ O ₄ Sn	O ₂	100	PAN-NF	NT-N	107
	Sn(OCMe ₃) ₄	AcOH	75-250	CNT	NT-N	108
	C ₁₂ H ₂₆ N ₂ Sn	H ₂ O ₂	50-250	--	NT-A	19

It is apparent that, based on the above discussion, ALD provides versatile routes and a series of advantages for synthesizing anode materials of LIBs. The novelties in structures are being demonstrated to be effective in electrochemical performance in the following section as well.

A2. High electrochemical performance

As reviewed in literature [54,61,62,64], previous studies used various vapor-phase and solution-based methods for synthesizing novel anode materials of high performance. Only recently ALD as a tool was reported for developing anode materials, featuring its high preciseness and tunability in structures, compositions, and growth of deposited materials. Due to its late emergence, the electrochemical testing on ALD-induced anode materials is still limited but shows very promising performance, as will be demonstrated below.

The first effort was reported by Kim et al [95] with a 3D network of hollow TiO_2 nanoribbons. The researchers first deposited an amorphous TiO_2 layer on biotemplates of peptide assembly (see figure 2.4(a)) at 140 °C using titanium tetra-isopropoxide (TTIP, $\text{Ti}(\text{O}^i\text{Pr})_4$) and a mixture of NH_3 and O_2 as precursors. The as-synthesized materials were treated at 400 °C for 1 h and the applied biotemplates were removed. As a result, a network of crystalline anatase TiO_2 hollow ribbons with 15 nm thick walls (see figure 2.4(b)) was received for electrochemical testing. It was demonstrated that, applied with an

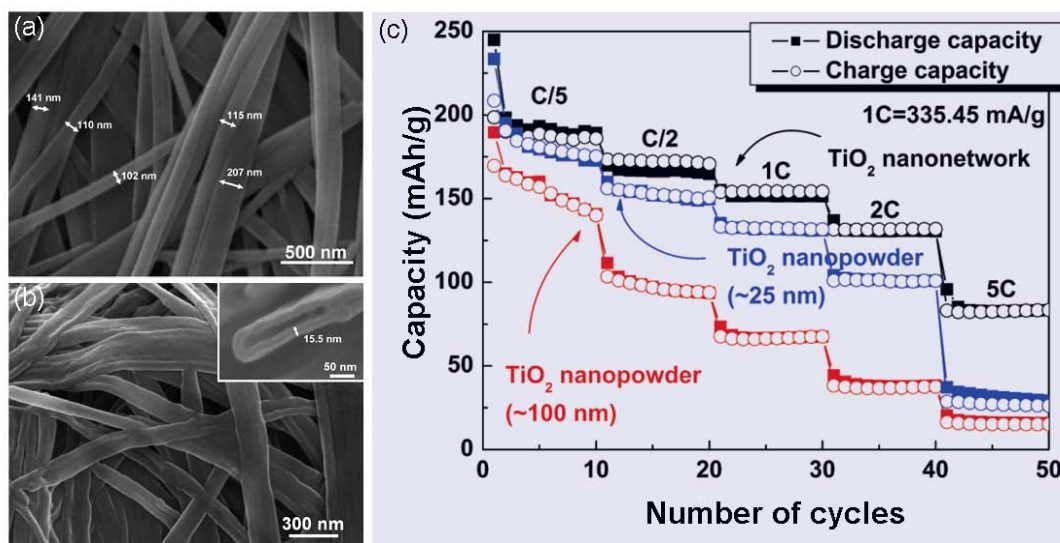
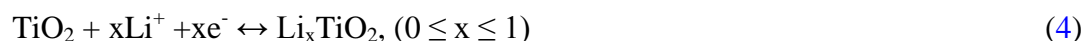


Figure 2.4 SEM image of (a) the peptide template and (b) the TiO_2 network (inset: magnified image of cross sectional TiO_2 hollow nanoribbon). (c) Rate capacity of the TiO_2 network, and the 25 nm and 100 nm nanoparticles from C/5 to 5C for 10 cycles.

electrolyte of 1 M LiPF₆ in a 1:1 mixture of EC-DMC, the ultimate 3D network of anatase TiO₂ ribbons exhibited higher specific capacity, rate capability, and cycleability than two TiO₂ nanoparticles (25 and 100 nm in size, respectively) (see figure 2.4(c)). In general, a reversible Li insertion/extraction in anatase TiO₂ is expressed by the following reaction and the resultant volume change is less than 4% [62]:



Kim et al [95] attributed the improved performance of the resultant electrode to its unique 3D network and the hollow structure of TiO₂ nanoribbons, for electronic conduction is facile through the network and Li ions can diffuse from both the outside and the hollow space of the tubes. A more recent work conducted by Gerasopoulos et al [89] revealed another 3D nanostructure of Ni/TiO₂ core-shell nanocomposite anodes synthesized using TMV substrates for ALD-TiO₂. The researchers deposited TiO₂ using tetrakis-dimethyl amido titanium (TDMAT, Ti(NMe₂)₄) and water as ALD precursors at 150 °C, and received amorphous TiO₂ on TMV (see figure 2.5(a) and (b)). They annealed the core-shell structures at 450 °C in air for 3 h and therefore transferred TiO₂ from amorphous to

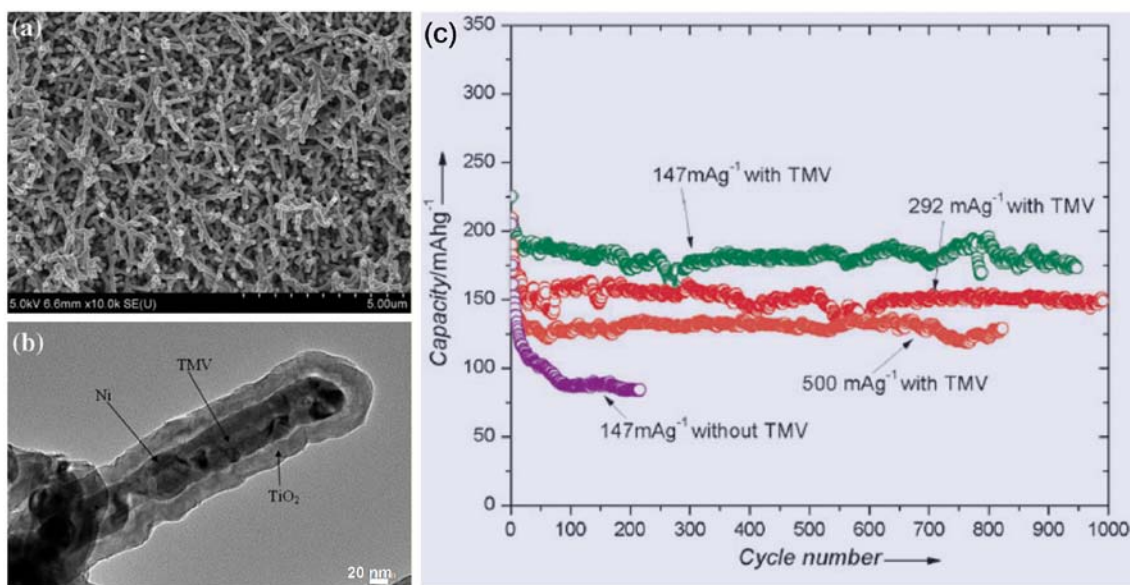


Figure 2.5 The electrochemical performance of TiO₂-(Ni-TMV) nanocomposites as anode of LIBs. (a) low-magnification SEM image for the TiO₂-coated TMV; (b) high-magnification TEM image for a single composite nanorod where TMV (18 nm), Ni (~20 nm), and TiO₂ (~20 nm). (c) Capacity vs. cycle number for electrodes with and without TMV.

anatase phase. Using the fabricated 3D nanostructured anatase TiO₂ (20 nm in wall thickness, see [figure 2.5\(b\)](#)) as anodes and the same electrolyte as used by Kim et al [95], Gerasopoulos et al [89] disclosed that the capacity of the nanostructured anodes stabilizes at 180 – 185 mAh/g at a current rate of 147mA/g in 850 cycles while a control sample of TiO₂ nanofilms (with similar thickness but without TMV on steel substrates) stabilizes at around 90 mAh/g (see [figure 2.5\(c\)](#)). The morphology of the 3D TiO₂ anodes was examined after cycles and clearly displayed a sustained 3D structure of the TMV. Under higher current densities, the differences between the 3D anodes and the control film anode became larger. Gerasopoulos et al believed that the low impedance of the nanostructured anodes benefits their high rate performance.

Another interesting work with ALD-TiO₂ anodes was performed by Cheah et al [87]. The researchers deposited a uniform layer of 17 nm thick TiO₂ ([figure 2.6\(b\)](#)) on aluminum nanorods ([figure 2.6\(a\)](#)) using TiI₄ and water as precursors at 200 °C. The growth of aluminum nanorods have been previously reported by the researchers using a direct electrodeposition procedure [114]. It was also observed that, besides a conformal layer of ALD-grown anatase TiO₂ on aluminum nanorods, there exists a 4 nm thin layer of Al₂O₃ ([figure 2.6\(b\)](#)) between the TiO₂ layer and the Al nanorodes, due to exposure of Al nanorods to air before ALD-TiO₂. The synthesized nanostructure was employed as an anode in a microbattery for electrochemical testing. Aluminum nanorodes act as current collector, TiO₂ layers are anodes and lithium metal is used as a counter electrode with a glass fiber separator soaked in the electrolyte of 1 M LiClO₄-PC. In comparison to a 2D 17 nm thick TiO₂ film assembled into a cell as the control sample, the 3D electrode showed an increase in total capacity by a factor of 10 (see [figure 2.6\(c\)](#)), owing to the higher amount of TiO₂ deposited onto the 3D nanostructured Al current collector. For both the 3D and 2D electrodes, their measured capacity values are close to their theoretical values and maintained upon cycling. Further examination on the rate capability of the nanostructured 3D TiO₂ electrode disclosed its excellent stability in capacity retention after 50 cycles.

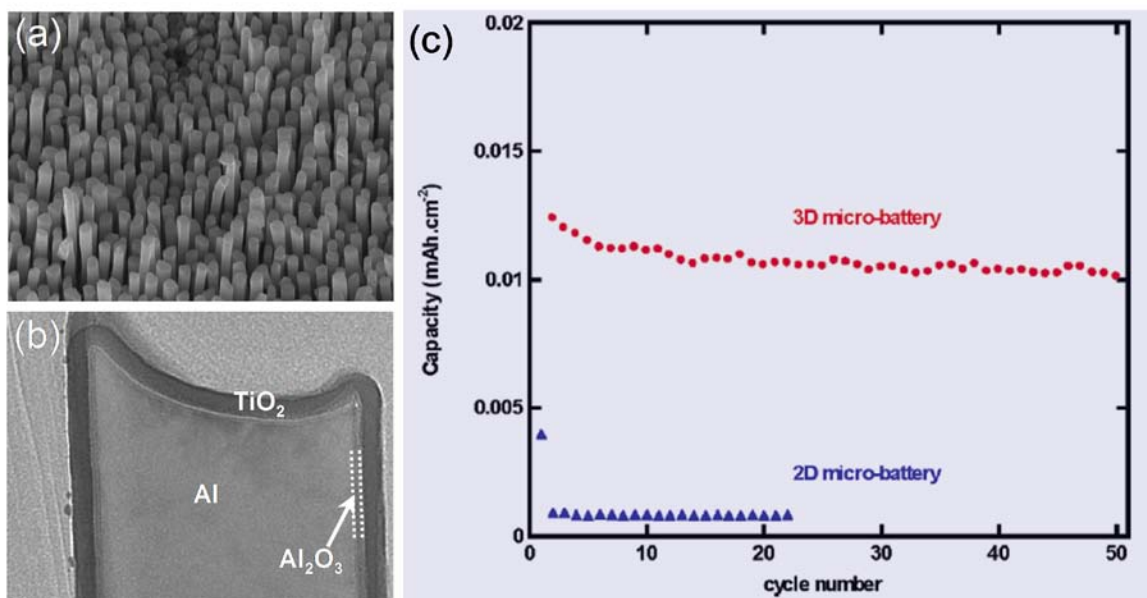
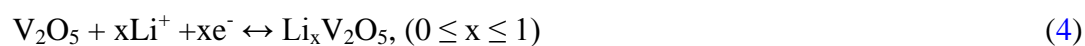


Figure 2.6 ALD-TiO₂ coated Al nanorods used as anodes of 3D microbatteries. (a) Al nanorod arrays; (b) an ALD-TiO₂ coated Al nanorod; and (c) normalized capacity (mAh/cm² of geometrical surface area) for the 3D microbattery with TiO₂ deposited on an Al nanorod current collector and the 2D electrode with TiO₂ deposited on a flat plate. The galvanostatic cycling current is 0.001 mA.

The afore-discussed cases clearly indicate that ALD is a facile and precise route for designing novel nanostructured anode materials and the resultant TiO₂ anodes exhibit high performance in cycleability, rate capability, and capacity. It worth pointing out that, partially due to the recent emergence of ALD in LIBs, the above ALD-TiO₂ anode materials represent to date the only electrochemically tested ALD successes for anodes. We believe, however, that there will be more ALD-induced nanostructures (as summarized in [Table III](#)) to be reported with high performance in the coming days. In addition, we are also expecting more anode materials synthesized by ALD, such as silicon, cobalt oxides, and others.

B. Cathodes

Starting from Goodenough's pioneering work [115,116], now a series of cathode materials of LIBs was developed, including LiCoO₂, LiMnO₂, LiMn₂O₄, LiNiO₂, LiNi_{0.5}Mn_{0.5}O₂, LiNi_{1/3}Mn_{1/3}Co_{1/3}O₂, LiFePO₄, and V₂O₅ [42,59,61,63,117]. Most of them are ternary or quaternary elemental compounds. The only one synthesized by ALD to date is V₂O₅ as cathodes of microbatteries. As a widely useful metal oxide, in earlier studies V₂O₅ has been prepared by a variety of methods including vapor-phase and solution-based strategies, as reviewed by Wang et al [58,59], and Beke [118]. V₂O₅ has a layered structure with a theoretical capacity of 442 mAh/g for LIBs [117], and it was Whittingham [119] who first reported the reversible electrochemical lithium intercalation into V₂O₅. Previously, Baba et al [120] developed a prototype of all-solid-state lithium-ion batteries (ASS-LIBs) using sputtered V₂O₅ as cathode materials and the cells demonstrated excellent electrochemical stability. Using ALD as a designing route, Badot et al first successfully deposited amorphous V₂O₅ with vanadyl triisopropoxide (VTOP, VO(OⁱPr)₃) and water as precursors in the range 45 to 150 °C [121,122]. The researchers further demonstrated that the annealed (at 400 °C) 700 nm thick V₂O₅ films offer excellent electrochemical stability and cycleability for lithium ion insertion/extraction between 3 and 3.8 V in 1 M LiClO₄-PC (propylene carbonate) [121]. A reversible Li insertion/extraction in anatase V₂O₅ is expressed by the following reaction [63,121]:



Later on, Baddour-Hadjean et al [123] systematically studied the phase changes of an 800 nm thick ALD-V₂O₅ film (annealed at 450 °C) as a cathode of LIBs during insertion/extraction of lithium ions using a Raman spectroscopy. More recently, Le Van et al [124] used XPS and Raman to further confirm that the ALD-deposited amorphous vanadium oxide is mainly composed of V₂O₅. More importantly, they first disclosed that the amorphous V₂O₅ is superior to crystalline films as cathodes. The amorphous film with an optimal 200 nm thickness exhibited higher capacity and better cycleability in 1 M LiClO₄-PC than its crystalline counterparts, accounting for a constant 455 mAh/g at C/10 (one charge-discharge cycle for 10 h).

C. Solid electrolytes

There are mainly three classes of electrolytes for use of LIBs, i.e., liquid, polymer solid, and inorganic solid electrolytes [44]. In comparison, liquid electrolytes are most widely used while inorganic solid electrolytes are still in their infancy [44]. Conventional batteries contain liquid electrolytes, using highly volatile and flammable organic solvents. As a consequence, there have always been safety issues arising from the combustible organic electrolytes and the issues become more serious with the increasing size of LIBs for use in EVs [125]. The ultimate solution to the safety issues lies in the development of solvent-free and nonflammable inorganic solid electrolytes [49,125]. Inorganic solid electrolytes are especially crucial for the development of all-solid-state rechargeable microbatteries which will play a key role in many autonomous devices [126], such as small medical implants, hearing aids, intergrated lighting solutions, and many others. In order to improve the safety and to prevent the risk of electrolyte leakage, replacement of the liquid with a safer and stable solid-state electrolyte is a stringent requirement. Traditionally, physical vapor deposition (PVD) techniques (e.g., sputtering and evaporation) take the dominance on manufacturing the components of microbatteries with planar configurations [69,117]. However, the 2D planar thin film batteries suffer from many challenges, as reviewed by Patil et al [117]. To address the challenges for higher volumetric energy density, 3D architected battery configurations were proposed, as exposed in the reviews by Long et al [127] and Roberts et al [128]. Another alternative approach has recently proposed by Notten et al [129], and the principle is illustrated in figure 2.7. By depositing different functional layers into the trenches, the surface area can be enhanced and thereby the energy density can be improved by several orders of magnitude higher than planar thin film batteries, as demonstrated in the aforementioned case of ALD-TiO₂ conducted by Cheah et al [87]. The development of 3D batteries has the need to distinguish conformal deposition techniques [128], and it is obvious that ALD is particularly advantageous for this goal. Thus, Baggetto et al [126] suggested ALD as a promising deposition technique for the development of all-solid-state LIBs (ASS-LIBs). In the above sections, we showed that ALD is viable for both anodes (e.g., ALD-TiO₂ [87]) and cathodes (e.g., ALD-V₂O₅ [121-124]) of microbatteries. The recent progress on

solid electrolytes further supports ALD as a key tool for ASS-LIBs, as will be introduced below.

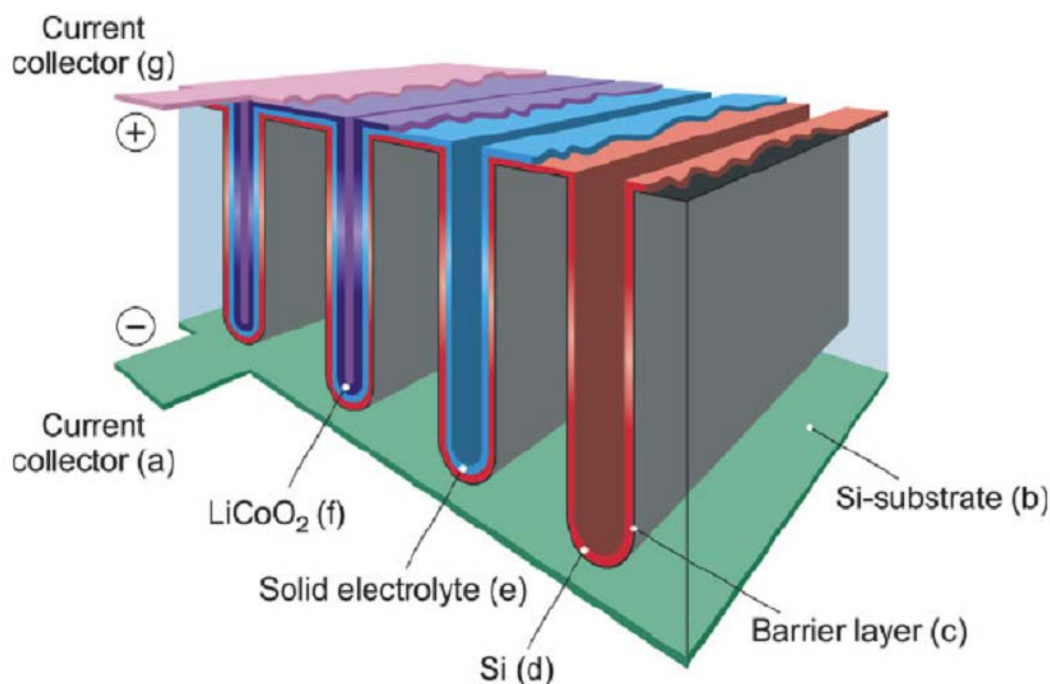


Figure 2.7 A 3D all-solid-state lithium-ion battery.

Lithium is an important constituent not only in cathode but also in inorganic solid electrolytes of LIBs [68,69]. Recent research [130,131] jointly conducted by researchers in Norway and Finland disclosed that ALD has the capability to deposit lithium-containing materials consisting of ternary or quaternary elements, serving as inorganic solid electrolytes in ASS-LIBs. Putkonen et al [130] studied the effects of five different lithium-containing compounds as ALD precursors on depositing lithium-containing thin films, including a lithium β -diketonate Li(thd), a lithium alkoxide Li(O^tBu), a lithium cyclopentadienyl LiCp, a lithium alkyl n-butyllithium n-BuLi, and lithium dicyclohexylamide. Their systematic work revealed that, combined with suitable oxygen

sources such as ozone or water, Li(thd) and Li(O^tBu) are two useful precursors for preparation of different lithium-containing films. In the same work, the researchers also demonstrated that the Li(thd)-ozone sub-ALD system can incorporate with the La(thd)₃-ozone sub-ALD system to produce lithium lanthanate films comprising of tunable constituents of lithium, carbon, lanthanum, and oxygen. They also pointed out that, in comparison to the Li(thd)-ozone system, the Li(O^tBu)-water system is more beneficial for lithium-containing film deposition, for there is less carbon content produced. In a later work, Aaltonen et al [131] investigated the deposition of lanthanum titanate and lithium lanthanum titanate (LLT). The latter is considered as a very promising solid-state electrolyte, showing very high lithium ionic conductivity at room temperature [68,69]. Through varying the pulsing ratio of different precursors, the researchers demonstrated that ALD is advantageous over previous methods such as sputtering and sol-gel for depositing ternary and quaternary systems. For ALD-LLT, they combined three subsystems, i.e., Li(O^tBu)-water, La(thd)₃-ozone, and TiCl₄-water to deposit LLT at 225 °C and controlled the composition ratio of the three subsystems (i.e., Li₂O, La₂O₃, and TiO₂) by adjusting their sequence and subcycles. According to their successful case, TiO₂-La₂O₃-Li₂O was chosen for the ALD-LLT deposition sequence and the LLT deposition was tuned with controlled sub-cycles using various characterization tools for examination. The as-deposited LLT films are amorphous and deviate from the composition of crystalline LLT. Annealed at 800 °C in oxygen for 3 h, a 100 nm thick Li_{0.32}La_{0.30}TiO_z film matches well with the X-ray diffraction (XRD) patterns of Li_{0.33}La_{0.557}TiO₃. However, as pointed out by Aaltonen et al [131], there is some variance existing with the annealed film with respect to the reported Li_{0.33}La_{0.557}TiO₃. In addition, there is an excess of titanium in the deposited film and some XRD peaks are not identified as well. In any case, the researchers [130,131] first demonstrated that ALD is a tunable and viable route for depositing solid electrolytes of LIBs and their work will inspire more effort on development of inorganic solid electrolytes.

2.2.3. ALD on surface-modifying battery electrodes

As is well known, LIBs are currently plagued by their capacity degradation, reduced life,

and potential risks in safety. The reasons lie in unwanted side reactions occurring during charge-discharge cycles, causing electrolyte decomposition, SEI formation, and active material dissolution [51,52,78]. To address these issues and thereby to enhance the performance of LIBs, earlier studies found that surface modification of electrodes as a strategy is a viable venue and has been extensively investigated. For carbon anodes, the previously used modification methods are included in the reviews by Fu et al [72] and Verma et al [78]. Aimed at modified cathode materials, several reviews were also conducted by Aurbach et al [52], Wang et al [59], Fu et al [73], Li et al [74], Yi et al [75], Myung et al [76], and Chen et al [77]. Recently, there is an increasing interest in using ALD to coat both anode and cathode materials with ultrathin films even down to subnanometers for enhancing the performance of LIBs, which has not been realized before. In contrast to previous solution-based methods, recent progress in ALD paves a way for precise surface coating of electrode materials with more flexibility and significantly enhanced performance. As will be discussed below, ALD also demonstrates to be a material- and cost-saving strategy for modifying electrode materials. A unique characteristic with this vapor-phase route, more importantly, is ALD being able to coat prefabricated electrodes directly, and this has never been possible for solution-based routes as widely used.

A. ALD-coated anodes

In conventional LIBs, carbon materials are exclusively used as anodes. During the first charge, the electrolyte undergoes reduction at the negatively polarized surface of carbon materials. This forms a passive layer comprising of inorganic and organic electrolyte decomposition products, called solid electrolyte interface, i.e., SEI [51,73,78]. As pointed out by Verma et al [78], SEI is essentially formed on the surface of the carbonaceous negative active materials, thus their inherent properties (such as specific surface area, crystallographic structure, structural perfectness, as well as morphology) of carbon materials take effect on the SEI. Previous studies applied various methods to modify active carbon materials for enhanced their reversibility and capacity [64,73,78]. Of them, surface coating plays an important role. Only recently, Jung et al developed ALD- Al_2O_3

to directly coat the anodes of natural graphite (NG) powders ($\sim 5 \mu\text{m}$, HPM850, Asbury Graphite Mills Inc.) [132]. It was found that ALD precursors (i.e., TMA and water) can diffuse through the pores of the composite anode to deposit a conformal Al_2O_3 film in the torturous path of the entire electrode structure. As shown in figure 2.8, the effect of 5-cycle ALD- Al_2O_3 on the composite anode was examined using EDS (electron dispersive spectrometry). Figure 2.8(a) shows the cross-sectional image of the composite anode, and the SEM (scanning electron microscopy) sample was prepared by FIB (focused ion beam). The composite anode shows a porous structure. EDS analyses on seven regional areas (see figure 2.8(b)) revealed that the ALD- Al_2O_3 is uniformly performed on the porous composite anode. Their following electrochemical tests with 1 M LiPF_6 in a 1:1 mixture of EC-DMC showed that, as disclosed in figure 2.8(c), this ALD- Al_2O_3 coated anode can sustain a very stable electrochemical performance while a bare anode dramatically decreases at a highly elevated temperature of $50 \text{ }^\circ\text{C}$, accounting for a 98% and 26% capacity retention after 200 charge-discharge cycles, respectively. It was also revealed that, however, a composite anode made by ALD- Al_2O_3 pre-coated NG powders behaves worse than the bare anode. Jung et al [132] believed that the coated composite anode is benefited by a stable “artificial” SEI thin film of Al_2O_3 that protects the NG surfaces from undesirable decomposition reactions with the electrolyte. In contrast, the anode fabricated by ALD- Al_2O_3 pre-coated NG powders is hindered by the insulating Al_2O_3 films, for the films inhibits electron conduction paths between NG particles and the current collector.

Besides the aforementioned case for the carbon anode, recent research also exposed ALD being applied to other alternative anodes for surface modification. In an earlier study, Snyder et al [133] employed ALD-TiN thin film on LTO powders in order to improve their interparticle electronic conductance. LTO is a promising anode in replacement of carbon materials, ascribed to its advantages such as zero strain, no SEI and lithium metal plating formed, and stability with high temperature ($75 - 80 \text{ }^\circ\text{C}$) during charge-discharge cycles [133,134]. However, it suffers from its insulating nature, leading to capacity fading with charge-discharge cycles. To improve LTO's electronic conductivity, as a consequence, many strategies have been previously used and surface modification appears to be an effective one with multi-choices on coating materials (e.g., Ag, carbon,

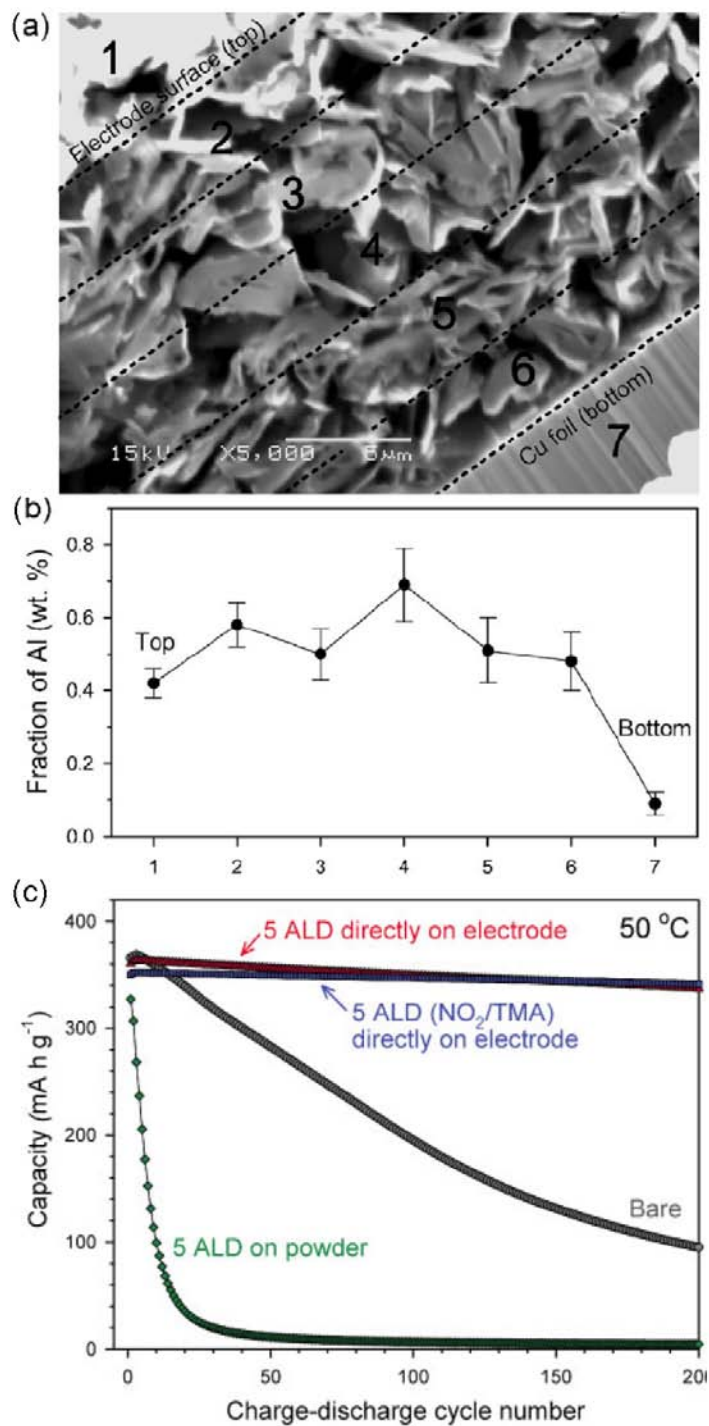


Figure 2.8 SEM/EDS analyses of ALD-Al₂O₃ electrodes. (a) FE-SEM cross-sectional image of NG composite electrode coated with 5 cycles of ALD-Al₂O₃. Numbers indicate regions in which Al was analyzed with EDS. (b) Weight fraction of Al as a function of depth. (c) Electrochemical performance of different anodes at 50 °C.

SnO₂, TiN, as well as organic compounds) [134]. TiN provides a series of beneficial factors as a surface coating material such as its hard, refractory, and metallic properties. For example, a recent study coated LTO with TiN by a method of heat treatment using urea as nitrogen source and the modified the LTO displayed improved rate capability and cycleability [135]. In comparison, ALD provides a more facile and controllable route for surface modification, due to its cyclic and self-limiting nature. Using TiCl₄ and NH₃ as precursors, Snyder et al [133] coated LTO nanoparticles of 25 nm with ALD-TiN at 500 °C and the modified LTO powders were characterized by in situ and ex situ methods. A 200-cycle coating led to an average thickness of approximately 5.8 nm, accounting for an approximate growth rate of 0.3 Å/cycle. Their following electrochemical tests in 1 M LiPF₆-(1:1 EC-DMC) revealed that the modified LTO electrode shows remarkably improved performance and its specific capacity nearly maintains the theoretical value of 167.5 mAh/g over numerous charge-discharge cycles at different charge rates. In contrast, the unmodified LTO electrode displays a drastic decrease in specific capacity with increased charge rates and reaches its lowest specific capacity of 60 mAh/g after the third charge at C/5. Decreasing the charge rate to C/10 in the following charge cycles, the specific capacity of the unmodified LTO electrode increases to those obtained during previous charges at C/10. Snyder et al [133] attributed this to the deformation of the LTO lattice. Also, Snyder et al [133] pointed out that the improved capacity of the modified electrode are due to several factors: (1) the change in particle morphology occurred at high temperature of ALD; (2) removal of electrically non-conducting carbonate species during ALD; (3) the improved electrical contact of LTO particles due to the presence of the TiN thin film.

Another functional role played by ALD coatings is to sustain morphologies of anode materials. In this case, Riley et al investigated the effects of ALD-Al₂O₃ on MoO₃ nanoparticles [136]. In contrast to little volume expansion with NG, MoO₃ suffers from 100% volume expansion in charge-discharge cycles. Through coating the pre-fabricated MnO₃ nanoparticles anode with 4-cycle ALD-Al₂O₃, Riley et al [136] found that the coated anode in 1 M LiPF₆-(1:1 EC-DMC) is free from fracturing and this help improve its cycleability with stable and high specific capacity. Conversely, an anode fabricated by

ALD- Al_2O_3 pre-coated MnO_3 nanoparticles displays a worsened electrochemical performance even compared to the bare MnO_3 nanoparticles anode. The researchers explained the underlying mechanisms with an illustration, as shown in [figure 2.9](#). The white circles represent MnO_3 nanoparticles, the black smaller circles indicate the conductive additive, and the grey surfaces signify ALD coatings. The bare MnO_3 suffered from fracturing during charge-discharge cycles, due to evident volume expansion. As a consequence, the fracturing led to failure of electrical contact of partial active materials and thus a fading capacity with electrochemical testing cycles (as illustrated in [figure 2.9\(a\)](#)). The ALD- Al_2O_3 pre-coated MoO_3 nanoparticles, on the other hand, worsened the electronic conductivity between nanoparticles and thereby led to the decrease in capacity of the fabricated anode (see [figure 2.9\(b\)](#)). In sharp contrast, a direct ALD- Al_2O_3 coating on the pre-fabricated MnO_3 nanoparticles anode is able to “knit” the anode materials together and retains electric conductivity/mechanical integrity (see [figure 2.9\(c\)](#)), though cracking must occur with the coated MoO_3 anode. In addition, the enhanced stability of the coated anode may also be partially attributed to the physical insulation of the MnO_3 from direct contact with the liquid electrolyte due to the partial surface coating even after cracking. In particular, in a later work [137] they clearly demonstrated that the coated anode is improved in mechanical stability with 4-cycle ALD- Al_2O_3 . The adhesion of the composite anode on the current collector is more than doubled while the electrode hardness increases by close to 50%. In this way, a more recent work reported by Dafinone et al [138] also demonstrated that 1 nm (10 ALD-cycles) thick ALD- Al_2O_3 can dramatically improve the mechanical durability of $\text{TiO}_2/\text{SiO}_2$ nanoparticle layer-by-layer films on inorganic and organic substrates. As demonstrated by the researchers, the benefits still include little change to the structure and functional properties of the nanoparticle films, uniform coatings to the nanoparticle films from the substrate to the top surface, and low temperature accessible to polymers and plastics. In another work conducted by Lee et al [139], ALD- TiO_2 is also reported for effectively improving the electrochemical performance of anode materials of high volume expansion in 1 M LiPF_6 - (1:1 EC-DMC). Lee et al [139] fulfilled ALD- TiO_2 on anode materials of ZnO nanorods using TiCl_4 and water as precursors at 500 °C. ZnO as an alternative anode material of LIBs has a high theoretical capacity. However, severe morphology and volume changes

were previously observed in charge-discharge cycles and deteriorated the performance of ZnO as electrodes [140,141]. Lee et al [139] demonstrated that the 200-cycle ALD-TiO₂ (~11 nm) coated ZnO nanorods anode exhibited an improved reversible capacity, accounting for 447 mAh/g compared to 358 mAh/g for the bare ZnO nanorods. The researchers noticed that, due to the ALD-TiO₂ coating, the coated ZnO nanorods maintain their nanostructures perpendicular to the substrate while the bare ZnO nanorods can only survive for 30 cycles. Thus, it is believed that ALD-TiO₂ reduces the degree of reactions between ZnO and the electrolyte and thereby improves the stability of charge-discharge cycles.

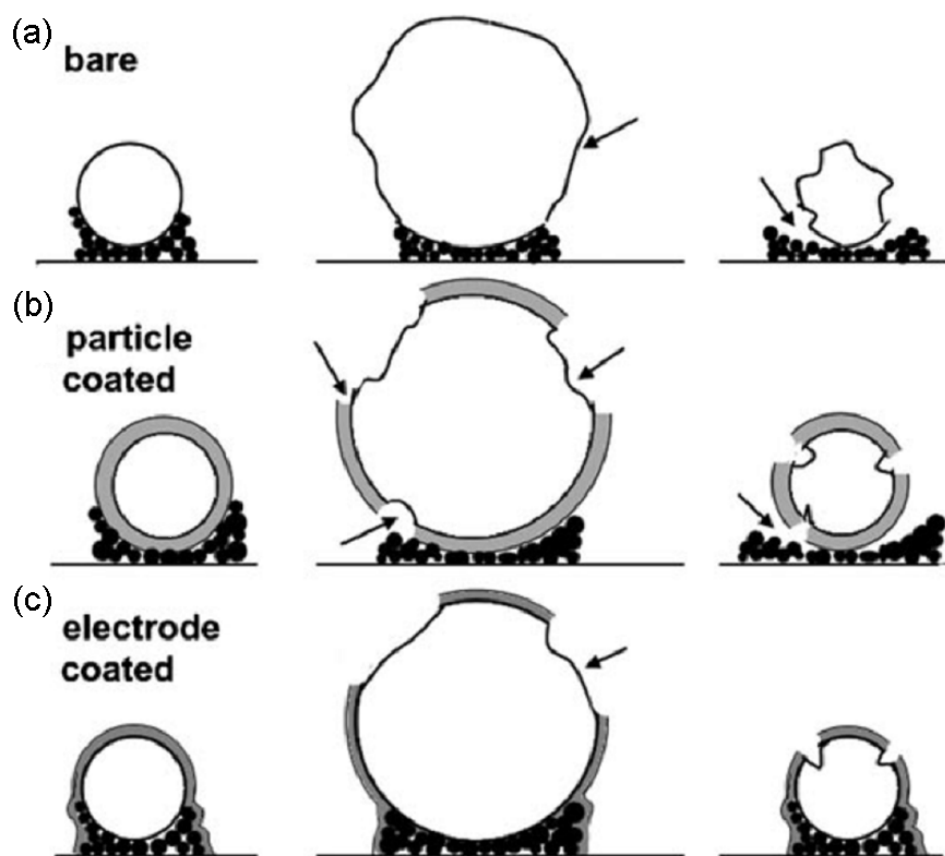


Figure 2.9 Schematic representation of the effects of volume expansion upon (a) bare particles, (b) an ALD coated nano-MoO₃ particle, and (c) a particle from an ALD coated porous anode.

B. Cathodes

The cathode active materials in LIBs are largely responsible for many factors such as toxicity, thermal stability, safety, and energy and power density. The direct contact of cathode materials with liquid electrolytes leads to many detrimental side reactions occurring at ambient temperature slowly, resulting in slow degradation of electrode materials and ultimately reduced battery performance. Researchers tried to substitute partial active elements with alkaline metals and Al in order to stabilize electrode structures and thereby to enhance cycleability and thermal stability event at highly oxidized states [51]. However, such substitution often lowered capacity and Li^+ diffusion, for the substituents are commonly electrochemically inactive ingredients. In comparison, surface coating is much simpler and more beneficial. In particular, this route has no influence on the amount of electrochemically active elements of cathodes and therefore it does not incur any loss in capacity of cathodes.

Since surface modification of cathodes was initially patented by Amatucci and Tarascon [142], many research groups have demonstrated its viability for significantly improving the reversibility and reliability in the high voltage region (above 4.3 V vs. Li) by using nanoscale oxide coatings, as reviewed in literature [73-77]. The effects of various surface coatings were recently categorized to four classes by Chen et al [77]: (1) higher charge conductivity; (2) modification of cathode surface chemistry for improved performance; (3) HF scavengers which suppress metal dissolution from cathode materials; (4) physically protective barriers which impede side reactions between cathode materials and electrolytes.

As a widely used cathode material for commercial LIBs, LiCoO_2 (first reported by Goodenough [115]) suffers structural degradation during charge-discharge cycles. Earlier studies demonstrated that the electrochemical performance of LiCoO_2 can be enhanced by various surface coatings such as carbon, Li_2CO_3 , LiMn_2O_4 , $\text{Li}_4\text{Ti}_5\text{O}_{12}$, MgO , Al_2O_3 , AlPO_4 , SiO_2 , TiO_2 , ZrO_2 , SnO_2 , La_2O_3 , etc [74,143-148]. The main strategies employed are solution-based. Recently, ALD was developed as a surface-coating route for cathode

materials, featuring its low temperature and precise vapor-phase deposition. The first work on using ALD-coating for modifying cathode materials was reported by Jung et al [149]. They used ALD- Al_2O_3 to coat LiCoO_2 micropowders (7-10 μm , L106, LICO Technology) and found that the fabricated cathodes by the coated powders show dramatically improved capacity retention vs. the charge-discharge cycles regardless of the ALD coating thickness. In comparison to a 45% capacity retention for the bare LiCoO_2 powders, the coated LiCoO_2 powders exhibited a capacity retention of 89% after 120 charge-discharge cycles in the 3.3-4.5 V (vs. Li/Li^+) range (see figure 2.10) in 1 M LiPF_6 - (1:1 EC-DMC). In addition, they also disclosed that LiCoO_2 powders coated by 2-cycle ALD- Al_2O_3 show an initial capacity comparable to that of the bare LiCoO_2 powders. XPS (X-ray photoelectron spectrometry) revealed the coated Al_2O_3 layers are in the range ~ 3

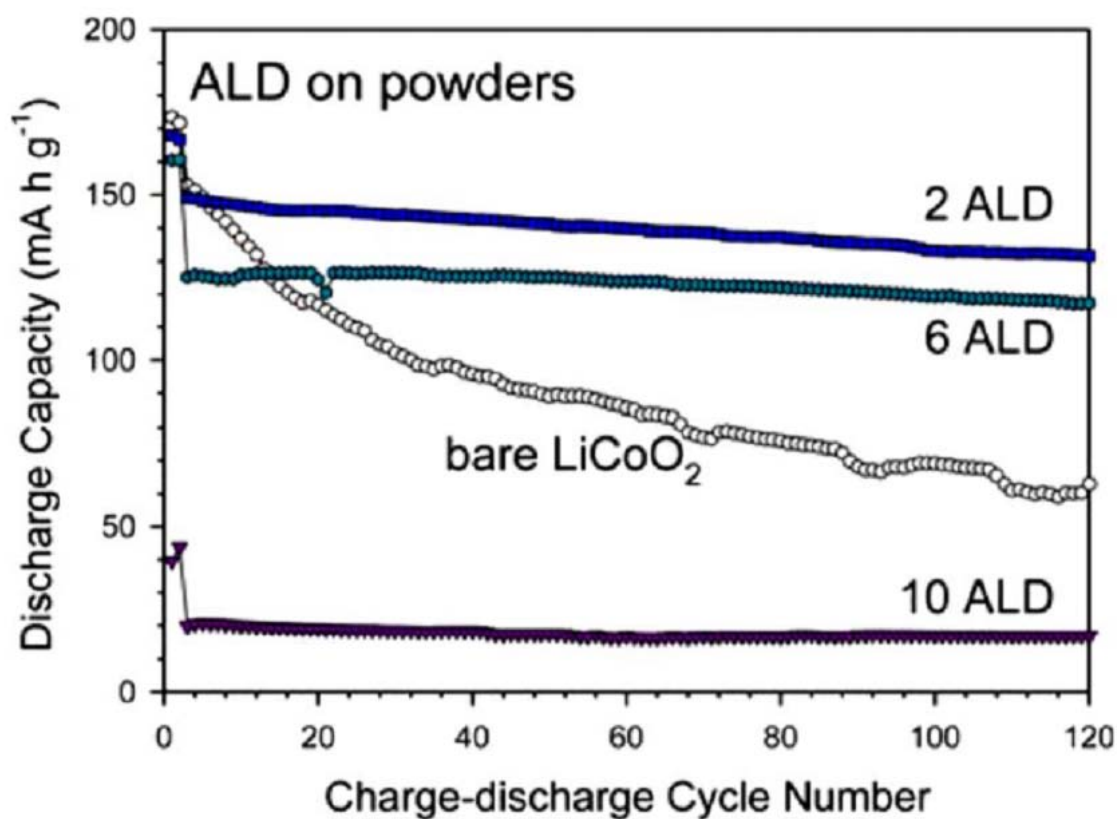


Figure 2.10 Charge-discharge cycle performance of electrodes fabricated by the bare LiCoO_2 powders and the ALD- Al_2O_3 coated LiCoO_2 powders using 2, 6, and 10 ALD cycles.

to 4 Å in thickness. In contrast, it was found that the initial capacity decreases with 6- and 10-cycle ALD- Al_2O_3 coated powders as the current density increases from 0.1 to 1 C rate, attributed to the restricted electron transport and possibly to the slower Li^+ diffusion kinetics in the ALD- Al_2O_3 layers. Furthermore, Jung et al [149] also revealed that the interface between the electrolyte and the ALD- Al_2O_3 coated LiCoO_2 cathodes is very stable. Therefore, they postulated several mechanisms to explain the enhanced performance induced by ALD- Al_2O_3 coatings: (1) ALD- Al_2O_3 coatings help suppress the structural instabilities related to lithium insertion and extraction but would not have the mechanical strength to withstand lattice expansions; (2) ALD- Al_2O_3 coatings may act as a solid electrolyte and may prevent the direct contact between the cathode surface and the electrolyte; (3) ALD- Al_2O_3 coatings serve as a scavenger for HF resulting from the reaction of the trace amounts of water with LiPF_6 in the electrolyte. For the last one, their XPS results suggested the possible formation of some AlF_3 for the coated powders. Besides ALD- Al_2O_3 coatings, Jung et al [149] also investigated the surface modification effects of ALD-ZnO (using $\text{Zn}(\text{CH}_2\text{CH}_3)_2$ and water as precursors) on the powders in the same study. Unfortunately, there was no improvement observed in the cycle performance from the electrodes fabricated by ALD-ZnO coated LiCoO_2 powders, compared to the electrodes prepared by the bare LiCoO_2 powders. Jung et al [149] believe that it is due to the instability of the ALD-ZnO layers on the LiCoO_2 powders and this is supported by their XPS results. In addition, Jung et al [149] further examined the performance of 2-cycle ALD- Al_2O_3 directly coated pre-fabricated LiCoO_2 composite cathodes. It was found that this route also improves capacity retention and the directly coated composite cathodes are only slightly inferior to the cathodes fabricated by the ALD- Al_2O_3 coated powders in capacity retention. The latter ALD method, in comparison to previous wet chemical methods as disclosed in the review by Myung et al [76], offers several additional advantages: (1) less coating materials, accounting for 3-4 Å with respect to 100-1000 Å in film thickness fulfilled by wet chemical methods; (2) without the use of solvents; (3) direct coating of composite electrodes, which is not applicable for wet chemical methods. Shortly after, a research team from Taiwan [150] also employed the latter route to coat prefabricated LiCoO_2 (micropowders, LICO Technology) cathodes directly with ALD- Al_2O_3 . Similarly, their electrochemical characterization further

confirmed that low ALD cycles (less than 50 cycles) help improve capacity, compared to the bare LiCoO_2 powders using the electrolyte of 1 M LiPF_6 in a 3:2:5 mixture of EC-PC-DEC. However, further increasing ALD cycles reduced storage capacity. It is evident that, therefore, ALD provides a facile but efficient route for surface modification of electrodes. More recently, Scott et al [151] reported a more interesting work on nanosized LiCoO_2 (400 nm) composite cathode coated by 2-cycle ALD- Al_2O_3 , using the electrolyte of 1 M LiPF_6 -(1:1 EC-DMC). As shown in figure 2.11(a), Scott et al confirmed the existence of Al_2O_3 after 2 ALD-cycles using EDS. High resolution TEM (HR-TEM) images exhibited the change before (figure 2.11(b)) and after (figure 2.11(c)) 2-cycle ALD- Al_2O_3 . In particular, electrochemical testing disclosed that, as shown by figure 2.11(d), the directly coated cathodes exhibit a remarkably improved capacity retention after 200 charge-discharge cycles in the 3.3-4.5 V (vs. Li/Li^+) range, accounting for a discharge capacity of

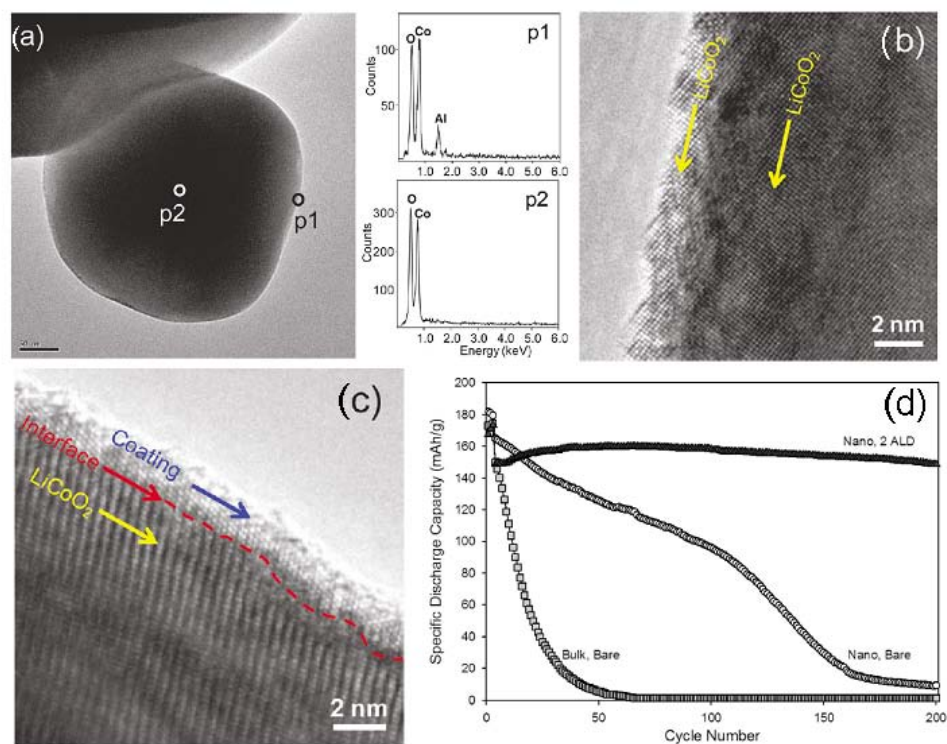


Figure 2.11 ALD- Al_2O_3 modified nano- LiCoO_2 particles. (a) 2-cycle ALD- Al_2O_3 coated nanoparticles (left), showing the presence of Al by EDS spectrum (right); (b) HR-TME image for a bare nanoparticle; (c) HR-TEM image for a 2-cycle ALD- Al_2O_3 coated nanoparticle; and (d) cycleability of different cathodes fabricated by bare bulk- LiCoO_2 , bare nano- LiCoO_2 , and 2-cycle ALD- Al_2O_3 coated nano- LiCoO_2 .

133 mAh/g at 1400 mA/g (7.8 C) and a 250% improvement in reversible capacity compared to the cathode prepared by bare nanoparticles. The researchers also demonstrated that the bare LiCoO₂ micropowders (5 μm) as the control sample show poor performance and lose their capacity after 50 charge-discharge cycles. In addition, a 6-cycle thicker ALD-Al₂O₃ coating produced detrimental effects due to an incurred larger overpotential. As for the underlying mechanisms, Scott et al [151] believe that, besides the reduced size of LiCoO₂ nanoparticles, the enhanced capacity of nano-LiCoO₂ composite cathodes is due to the suppression of cobalt dissolution from the LiCoO₂. They contended that ALD-Al₂O₃ produces an ultrathin Al₂O₃ film barrier residing between the LiCoO₂ cathode and the liquid electrolyte. In addition, the nanoparticles could reduce the diffusion paths of Li⁺.

Apart from the aforementioned work on LiCoO₂, recently researchers also reported surface modification of other cathode materials by ALD. LiNi_{1/3}Mn_{1/3}Co_{1/3}O₂ being a replacement material for LiCoO₂ can reduce the cost and toxicity of Co, and it was first proposed by Ohzuku and Makimura [152]. Unfortunately, LiNi_{1/3}Mn_{1/3}Co_{1/3}O₂ shows poorer rate capability and considerable capacity loss at high current density, in spite of its higher discharge capacity, lower cost, and higher safety with respect to LiCoO₂ [153,154]. To improve the electrochemical characteristics of LiNi_{1/3}Mn_{1/3}Co_{1/3}O₂, different surface coatings (e.g., Y₂O₃ [153], AlF₃ [154], and Al₂O₃ [155,156]) via solution-based methods were previously investigated and displayed enhanced performance to some extent. Different from the aforementioned work, Riley et al [157] employed ALD-Al₂O₃ to modify LiNi_{1/3}Mn_{1/3}Co_{1/3}O₂ cathode materials. Riley et al [157] synthesized LiNi_{1/3}Mn_{1/3}Co_{1/3}O₂ nanoparticles (200 - 400 nm) by combustion. Through coating the LiNi_{1/3}Mn_{1/3}Co_{1/3}O₂ particles with varying thicknesses of ALD-Al₂O₃, Riley et al found that the ALD-Al₂O₃ coatings of 2 – 6 cycles improve the reversible stability of charge-discharge cycles in 1 M LiPF₆-(1:1 EC-DMC). In comparison to the bare particles, a 2-cycle ALD-Al₂O₃ coating exhibited little change in initial capacity. Associated with increased ALD-Al₂O₃ coatings, it was observed that the specific capacity in first cycle decreased due to slower ionic mobility. In spite of a lower resultant initial capacity, the capacity for the particles coated with 4- and 6-cycle ALD-Al₂O₃ is still greater than the

bare particles after 40 and 70 charge-discharge cycles, attributed to the improved electrochemical stability. It was also noticed that, however, a 10-cycle ALD- Al_2O_3 coating is detrimental to the overall performance of $\text{LiNi}_{1/3}\text{Mn}_{1/3}\text{Co}_{1/3}\text{O}_2$. The reason lies in the insulating nature of Al_2O_3 for electron and ion transportation. Additionally, a thick coating tends to physically isolate individual particles from direct contact with conductive acetylene black. In a further examination on the effect of ALD-coating thicknesses on $\text{LiNi}_{1/3}\text{Mn}_{1/3}\text{Co}_{1/3}\text{O}_2$ capacity retention when cycled with an upper cutoff of 4.5 V, Riley et al [157] disclosed that 80% initial capacity could be hold after 110 cycles when an ALD coating is less than 6 cycles. Once the coating thickness exceeds $\sim 12 \text{ \AA}$ (corresponding to 6 ALD cycles), the electrochemical stability is significantly affected by reduced kinetics associated with ion and electron transport. In comparison to the coatings of several or even several tens of nanometers induced by wet chemical methods, the ALD coatings are obviously much thinner and favorable. The researchers postulated that the ALD-induced electrochemical improvement of LIBs is due to a more pure Al_2O_3 coating than other methods and thereby ALD coatings require less oxide materials for modifying electrode materials.

The third cathode material reported recently by ALD modification is LiMn_2O_4 . The spinel LiMn_2O_4 has been extensively studied for the replacement of LiCoO_2 in LIBs due to its low cost and high safety. Unfortunately, LiMn_2O_4 suffers capacity degradation especially at elevated temperature ($> 55 \text{ }^\circ\text{C}$) and the reasons lie in several ways including its unstable structure, the decomposition of electrolyte, the dissolution of manganese ions, and Jahn-Teller distortion, etc [75]. Surface coatings (e.g., metals such as Co [158] and Au [159], metal oxides such as Al_2O_3 [160], TiO_2 [161,162], ZnO [163], and Cr_2O_3 [164], and others as reviewed in literature [75]) as the solutions were mainly investigated via solution-based methods and displayed some electrochemical enhancement. Recently, Guan et al [165] investigated the effects of ALD- Al_2O_3 coatings on the electrochemical performance of a kind of commercial LiMn_2O_4 micropowders (1 - 8 μm) in a potential range of -0.3 – 0.8 V vs. Ag/Ag^+ . Figure 2.12(a) and (b) show the morphological change before (figure 2.12(a)) and after (figure 2.12(b)) 20-cycle ALD- Al_2O_3 . Figure 2.12(c) shows XPS spectrum from LiMn_2O_4 cathode coated by 4-cycle Al_2O_3 , confirming the

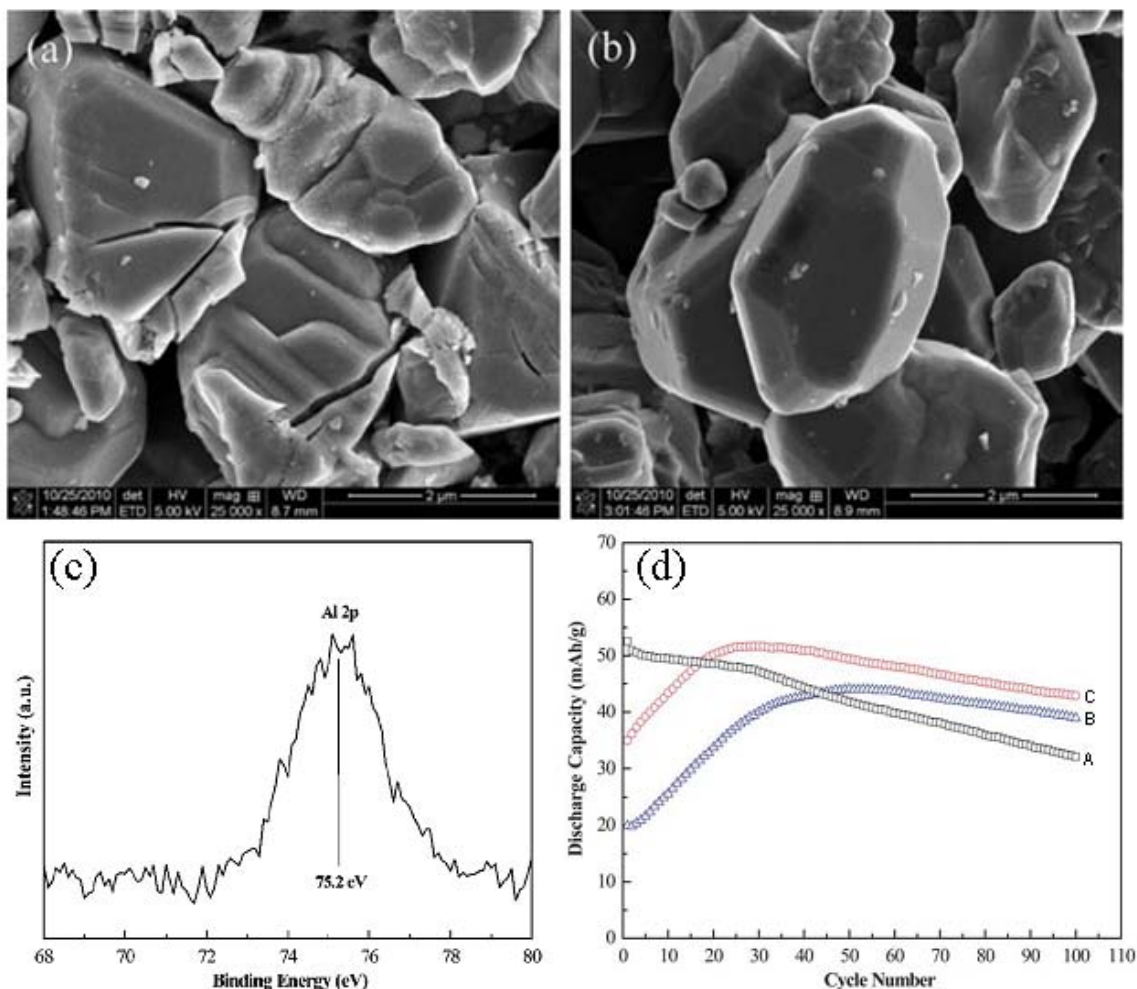


Figure 2.12 Modification of ALD- Al_2O_3 on LiMn_2O_4 cathodes. (a) The bare LiMn_2O_4 micropowders; (b) 20-cycle ALD- Al_2O_3 coated LiMn_2O_4 micropowders; (c) XPS spectrum from LiMn_2O_4 cathode coated by 4-cycle Al_2O_3 ; and (d) Cycling performance of (A) bare LiMn_2O_4 cathode, cathodes coated with (B) 20-cycle and (C) 10-cycle of ALD- Al_2O_3 . These samples were cycled at a current density of 240 mA/g over the voltage range of -0.3 – 0.8 V.

presence of Al element. Using a bare cathode as the control sample, they examined the performance of one 10- and 20-cycle ALD- Al_2O_3 coated cathode in 1 M LiClO_4 -PC. Guan et al [165] found that the discharge capacity of the bare cathode continued to decrease from 52.6 to 32.1 mAh/g over 100 cycles (see figure 2.12(d)), owing to dissolution of Mn^{2+} ions, Jahn-Teller distortion effect of Mn^{3+} ions, and decomposition of

electrolyte components on the electrode. In contrast, ALD- Al_2O_3 coatings led to lower initial capacities for the two coated cathodes, possibly due to the presence of insulating Al_2O_3 coatings. More importantly, the two ALD- Al_2O_3 coated LiMn_2O_4 cathodes exhibited improved capacity retention and their capacities are higher than that of the bare cathode after a long-time cycling. In addition, the capacity of the 10-cycle ALD-coated cathode increases and gradually becomes larger than that of the bare cathode from the 18th cycle, leading to a capacity of 42.9 mAh/g at the 100th cycle. The capacity of the 20-cycle ALD-coated cathode also experiences an increase from 20 mAh/g and exceeds the capacity of the bare one from 44th cycle, accounting for a capacity of 38.9 mAh/g at the 100th cycle. Obviously, the effect of ALD- Al_2O_3 coatings on the cycleability of LiMn_2O_4 cathodes is thickness-dependent. The thinner 10-cycle coating shows higher capacities and better cycleability than the thicker 20-cycle coated cathode, due to less surface resistance. Thus there exists an optimal cycling number of ALD- Al_2O_3 for the best electrochemical performance. Furthermore, Guan et al [165] confirmed that ALD- Al_2O_3 coatings were partially dissolved in electrolyte, for there is no Al element revealed by XPS on a 4-cycle ALD- Al_2O_3 coated cathode after 100 charge-discharge cycles. They believed that, for the two coated cathodes, the dissolution of manganese led to formation of new phases with the expense of LiMn_2O_4 and this prevented the capacity from further increasing and resulted in the decreasing capacity. Due to the protection of the ALD- Al_2O_3 coatings, however, the coated cathodes delivered higher capacities than the bare cathode after 100 cycles. Based on a growth of 2.0 Å/cycle for ALD- Al_2O_3 , Guan et al [165] concluded that the ALD- Al_2O_3 coatings (< 4 nm) are much thinner than the ones (50 – 100 nm in thickness) previously prepared by wet chemical methods but produced a comparable performance. They also believed that the reason may lie in the variances of coating quality resulted from different methods.

Based on the above updated progress of surface modification with ALD, it is obvious that previous solution-based methods are exposed to several drawbacks: (1) inability to form uniform thin film; (2) operation under high temperatures; (3) a long time for growth, and (4) use of solvents. In contrast, ALD shows some corresponding advantages for surface modification: (1) uniform and conformal deposition of ultrathin film even down to

subnanometers; (2) low growth temperature (typically less than 200 °C for modification coatings) even down to room temperature; (3) flexible growth of coatings enabling an effective modification in a few minutes; (4) direct vapor growth mode free of solvent use; and (5) high film quality of deposited oxides.

2.2.4. Conclusions and outlooks

In this review, we present that ALD as a vapor-phase thin film technique is attracting great interest in LIBs, owing to its capabilities in proving a series of advantages. For examples, the surface-controlled nature of ALD makes it a versatile tool for synthesizing various nanostructures and the low growth temperature of ALD render it to be a viable technique for depositing materials onto organic or biological substrates. Furthermore, the cyclic operation leads ALD to control deposited films at the atomic scale and its vapor-phase diffusion contributes to in-depth coating on complex structures and porous systems with unraveled conformality and uniformity.

The recent progress in LIBs, as reviewed in this work, demonstrated that ALD can serve for high-performance LIBs in all-round ways. In essence, ALD can be used to seek solutions for cost, safety, energy density, rate capability, and service life of next generation LIBs. First, ALD can be employed for developing all three key LIB components, i.e., anodes, cathodes, and electrolytes, distinguishing itself from other traditional techniques by its preciseness, low temperature, conformality, and uniformity. Furthermore, ALD has a wide range of choices on precursors and ultimate materials. Thus, ALD provides a highly flexible and facile concept for nanosynthesis. On the other hand, ALD can be used for modifying LIB electrodes with ultrathin but high-quality films, resulting in dramatically improved electrochemical performance in specific capacity, rate capability, and cycleability. In this way, ALD exhibits to be a material-saving but effective technique compared to its counterparts. Therefore, ALD puts itself a leading position for future development of LIBs. Due to its comprehensive abilities for developing next generation LIBs, ALD will boost a more extensive and intensive investigation on high-performance LIBs. However, mainly due to its latest recognition for

LIBs, there is a big space left for future investigation. Here we think there are several areas for ALD deserving persistent studies in the coming years.

A. Future investigation on new LIB components

As discussed in this review, ALD is a versatile tool for designing anodes, cathodes, and inorganic electrolytes as well. In the case of anode materials, first, the nanostructures induced by ALD-TiO₂ were the only cases investigated but exhibited very promising performance in LIBs. Thus, various nanostructures of other candidate anode materials are expected to be studied with electrochemical testing. Furthermore, ALD is also anticipated to develop other high capacity materials, such as Si and Sn. In particular, previous practice indicated that ALD had successes in Si thin films, as indicated by Puurunen's review [8]. Another important anode material that should be mentioned here is LTO.

In the case of cathodes, ALD to date has only succeeded in V₂O₅ and there are more deserving our expectation, such as LiCoO₂, LiMnO₂, LiMn₂O₄, LiNiO₂, LiNi_{0.5}Mn_{0.5}O₂, LiNi_{1/3}Mn_{1/3}Co_{1/3}O₂, and LiFePO₄. As for this scope, the recent ALD success [131] on LLT electrolyte is inspiring. It is possible to combine two ALD subsystems to fabricate the ultimate cathodes with controlled compositions. Similar situations are also on the side of inorganic solid electrolytes. Besides LLT, there are more for future studies.

B. Future understanding on ALD-induced surface coatings

As clearly revealed in this review, ALD impressed us with its capabilities in modifying anodes and cathodes with ultrathin films even down to subnanometers. Furthermore, ALD presents two routes for modification, either on electrode materials or on directly on prefabricated electrodes. More importantly, the ALD-induced coatings contributed to dramatically enhanced electrochemical performance of all the electrodes. These distinguished characters of ALD remind us that ALD merit a more extensive investigation. First, there are only limited ALD-coatings exposed with their effects so far in previous studies, and therefore other materials should be studied. Second, it is also necessary to

gain a better understanding on the underlying mechanisms of ALD-induced coatings so that we can better design next generation LIBs.

In regard to the latter issues, we think that in situ techniques merit our expectation. To meet this challenge, synchrotron-radiation (SR) techniques are undoubtedly ideal, for they offer the means and the capability to probe in situ the complex interface of electrochemical systems. Of them, in situ X-ray absorption spectroscopy (XAS) and high-resolution X-ray diffraction (XRD) are two particularly significant tools for electrochemical processes. The former one is important, for it can be applied to determine both atomic and electronic structure which are necessary to understand the relationships among the atomic structure, the electronic structure and the electrochemical performance (including stability) [166]. In this way, Deb and Cairns [166] made an excellent comprehensive review on the applications of XAS to LIBs. More recently, McBreen [167], and Marco and Veder [168] further summarized the applications of SR techniques in LIBs. In particular, XAS is element-specific and allows investigation of the chemical environment of a constituent element in a composite material [166-168]. In addition, XAS requires only short-range order, so it can provide structural information on amorphous solids, liquids, gases, and other complexes [166-168]. SR-XRD, on the other hand, allows in situ studies of structural parameters during electrochemical cycling of LIBs [168], which are essential to understanding battery performance during charge-discharge cycling. Besides the aforementioned two, there are also other SR techniques usable for the studies of LIBs [167]. All these are expected to disclose more information on the roles of ALD-deposited materials.

In summary, recent studies demonstrated that ALD is a facile but attractive technique for developing high-performance LIBs, showing all-around capabilities as discussed in this review. We believe that ALD will receive a more extensive employment in LIBs in the coming years and its roles will be elucidated as well. In particular, this review implies another potential technical route for the applications of ALD, i.e., the combination of the ALD design and modification together for optimal performance of LIBs, which has not been exposed in literature.

2.3 Challenges facing atomic layer deposition

As discussed above, ALD exhibits many advantages over its counterparts. However, there are several challenges facing ALD and they are expected to be addressed in future studies.

2.3.1 Rapid deposition

As an atomic-scale precise deposition technique, ALD is suffering from its slowness and this may limit ALD in some applications. As an unusual case, Gordon's group realized a rapid growth of SiO₂ with a growth rate 12 nm/cycle in the range of 200 – 300 °C [24]. It is over 100 times higher than most of ALD processes. The reason lies in the precursors developed by them. As also indicated in [Table I](#), the slowness of ALD is its only weakness in comparison to CVD and PVD. Thus, it is very intriguing to develop rapid ALD systems in future studies and it is believed that rapid ALD requires special precursors.

2.3.2 Deposition of single and multi-elemental materials

Another challenge is to broaden their deposition for a larger range of materials, especially for single and multi-elemental materials. As clearly shown by [Table II](#), ALD are most successful for binary compounds. In contrast, there is a large space left for single and multi-elemental materials, for they are important candidates in many applications. For example, Sn and Li₄Ti₅O₁₂ are important anode materials for LIBs but not reported yet by ALD.

2.3.3 Mass production

To date, the preparation of nanostructured materials via ALD is still lab-scale. In some cases, mass production will be crucial for application. In the case of LIBs, for instance, electrode requires ALD to enable to provide materials in a large amount. The fluidized

bed ALD reactor [169] and rotary ALD reactor [170] are two reported technologies so far, but their throughput and reliability have not commercially confirmed yet.

2.4 Summary

The unique mechanisms and characteristics of ALD render it powerful and versatile capabilities for fabrication of nanostructured materials as well as thin films in controlled manners. In the meantime, the applications of ALD are being broadened. In this review, the emerging applications of ALD are specially elucidated for LIBs, for currently there is increasing research strength for renewable clean energy sources. Despite these successes, ALD are still facing some challenges. It is expected that future studies will strengthen both fundamentals and applications of ALD.

References

- [1] A. Z. Moshfegh, PVD growth method: physics and technology, *Physics and Technology of Thin Films*, 2004, 28-53
- [2] J. E. Crowell, Chemical methods of thin film deposition: chemical vapor deposition, atomic layer deposition, and related technologies, *J. Vac. Sci. Technol. A*, 2003, **21**, S88-S95.
- [3] T. Suntola, and J. Antson, Method for producing compound thin films, 1977, US patent 4058430.
- [4] T. Suntola, Atomic layer epitaxy, *Mater. Sci. Rep.*, 1989, **4**, 261-312.
- [5] H. Kim, Atomic layer deposition of metal and nitride thin films: current research efforts and applications for semiconductor device processing, *J. Vac. Sci. Technol. B*, 2003, **21**, 2231-2261.
- [6] A. C. Dillon, A. W. Ott, J. D. Way, and S. M. George, Surface chemistry of Al₂O₃ deposition using Al(CH₃)₃ and H₂O in a binary reaction sequence, *Surf. Sci.*, 1995, **322**, 230-242.
- [7] J. E. Crowell, Chemical methods of thin film deposition: chemical vapor deposition, atomic layer deposition, and related technologies, *J. Vac. Sci. Technol. A*, 2003, **21**, S88-S95.
- [8] R. L. Puurunen, Surface chemistry of atomic layer deposition: a case study for the trimethylaluminum/water process, *J. Appl. Phys.*, 2005, **97**, 121301.
- [9] W. Gasser, Y. Uchida, and M. Matsumura, Quasi-monolayer deposition of silicon dioxide, *Thin Solid Films*, 1994, **250**, 213-218.
- [10] A. Paranjpe, S. Gopinath, T. Omstead, and R. Bubber, Atomic layer deposition of AlO_x for thin film head gap applications, *J. Electrochem. Soc.* 2001, **1486**, G465-G471.
- [11] M. Leskelä, and M. Ritala, Atomic layer deposition chemistry: recent development and future challenges, *Angew. Chem. Int. Ed.*, 2003, **42**, 5548-5554.
- [12] Y. Luo, D. Slater, M. Han, J. Moryl, and R. M. Osgood, Low-temperature, chemically driven atomic-layer epitaxy: in situ monitored growth of CdS/ZnSe(100), *Appl. Phys. Lett.*, 1997, **71**, 3799-3801.
- [13] J. W. Klaus, O. Sneh, and S. M. George, Growth of SiO₂ at room temperature with

the use of catalyzed sequential half-reactions, *Science*, 1997, **278**, 1934-1936.

[14] M. Putkonen, and L. Niinistö, Atomic layer deposition of B₂O₃ thin films at room temperature, *Thin Solid Films*, 2006, **514**, 145-149.

[15] M. D. Groner, F. H. Fabreguette, J. W. Elam, and S. M. George, Low-temperature Al₂O₃ atomic layer deposition, *Chem. Mater.*, 2004, **16**, 639-645.

[16] M. Knez, A. Kadri, C. Wege, U. Gösele, H. Jeske, and K. Nielsch, Atomic layer deposition on biological macromolecules: metal oxides coating of tobacco mosaic virus and ferritin, *Nano Lett.*, 2006, **6**, 1172-1177.

[17] Y.-M. Chang, S.-R. Jian, H.-Y. Lee, C.-M. Lin, and J.-Y. Juang, Enhanced visible photoluminescence from ultrathin ZnO films grown on Si-nanowires by atomic layer deposition, *Nanotechnology*, 2010, **21**, 385705.

[18] B. H. Lee, S. Cho, J. K. Hwang, S. H. Kim, and M. M. Sung, UV-enhanced atomic layer deposition of ZrO₂ thin films at room temperature, *Thin Solid Films*, 2010, **518**, 6432-6436.

[19] J. Heo, A. S. Hock, and R. G. Gordon, Low temperature atomic layer deposition of tin oxide, *Chem. Mater.*, 2010, **22**, 4964-4973.

[20] B. H. Lee, J. K. Hwang, J. W. Nam, S. U. Lee, J. T. Kim, S.-M. Koo, A. Baunemann, R. A. Fisher, and M. M. Sung, Low-temperature atomic layer deposition of copper metal thin films: self-limiting surface reaction of copper dimethylamino-2-propoxide with diethylzinc, *Angew. Chem. Int. Ed.*, 2009, **48**, 4536-4539.

[21] G. A. Ten Eyck, S. Pimanpang, H. Bakhru, T.-M. Lu, and G.-C. Wang, Atomic layer deposition of Pd on an oxidized metal substrate, *Chem. Vap. Deposition*, 2006, **12**, 290-294.

[22] K Kukli, M. Ritala, M. Leskelä and J. Jokinen, Atomic layer epitaxy growth of aluminum oxide thin films from a novel Al(CH₃)₂Cl precursor and H₂O *J. Vac. Sci. Technol. A* **15** (1997) 2214-8.

[23] C.-W. Jeong, B.-i. Lee and S.-K. Joo, Growth and characterization of aluminum oxide films by plasma-assisted atomic layer deposition *Mater. Sci. Eng. C* **16** (2001) 59-64.

[24] D. Hausmann, J. Becker, S. Wang, and R. G. Gordon, Rapid vapor deposition of highly conformal silica nanolaminates, *Science*, 2002, **298**, 402-406.

- [25] J. Niinistö, N. Petrova, M. Putkonen, L. Niinistö, K. Arstila, and T. Sajavaara, Gadolinium oxide thin films by atomic layer deposition, *J. Cryst. Growth*, 2005, **285**, 191-200.
- [26] K. Kukli, M. Ritala, M. Leskelä, T. Sajavaara, J. Keinonen, D. C. Gilmer, R. Hegde, R. Rai, and L. Prabhu, Atomic layer deposition of HfO₂ thin films and nanolayered HfO₂-Al₂O₃-Nb₂O₅ dielectrics, *J. Mater. Sci.*, 2003, **14**, 361-367.
- [27] A. W. Ott, K. C. McCarley, J. W. Klaus, J. D. Way, and S. M. George, Atomic layer controlled deposition of Al₂O₃ films using binary reaction sequence chemistry, *Appl. Surf. Sci.*, 1996, **107**, 128-136.
- [28] A. W. Ott, J. W. Klaus, J. M. Johnson, and S. M. George, Al₂O₃ thin film growth on Si(100) using binary reaction sequence chemistry, *Thin Solid Films*, 1997, **292**, 135-144.
- [29] A. Paranjpe, S. Gopinath, T. Omstead, and R. Bubber, Atomic layer deposition of AlO_x for thin film head gap applications, *J. Electrochem. Soc.*, 2001, **1486**, G465-471.
- [30] S. S. Lee, J. Y. Baik, K.-S. An, Y. D. Suh, J.-H. Oh, and Y. Kim, Reduction of incubation period by employing OH-terminated Si(001) substrates in atomic layer deposition of Al₂O₃, *J. Phys. Chem. B*, 2004, **108**, 15128-15132.
- [31] J. W. Elam, Z. A. Sechrist, and S. M. George, ZnO/Al₂O₃ nanolaminates fabricated by atomic layer deposition: growth and surface roughness measurements, *Thin Solid Films*, 2002, **414**, 43-55.
- [32] X. Liang, K. S. Barrett, Y.-B. Jiang, and A. W. Weimer, Rapid silica atomic layer deposition on large quantities of cohesive nanoparticles, *ACS Appl. Mater. Interfaces*, 2010, **2**, 2248-2253.
- [33] T. H. Han, H.-S. Moon, J. O. Hwang, S. I. Seok, S. H. Im, and S. O. Kim, Peptide-templating dye-sensitized solar cells, *Nanotechnology*, 2010, **21**, 185601.
- [34] D. Gu, H. Baumgart, T. M. Abdel-Fattah, and G. Namkoong, Synthesis of nested coaxial multiple-walled nanotubes by atomic layer deposition, *ACS Nano*, 2010, **4**, 753-758.
- [35] E. R. Cleveland, P. Banerjee, I. Perez, S. B. Lee, and G. W. Rubloff, Profile evolution for conformal atomic layer deposition over nanotopography, *ACS Nano*, 2010, **4**, 4637-4644.
- [36] A. Brzezinski, Y.-C. Chen, P. Wiltzius, and P. V. Braun, Complex three-dimensional

conformal surfaces formed by atomic layer deposition: computation and experimental verification, *J. Mater. Chem.*, 2009, **19**, 9126-9130.

[37] M. Knez, K. Nielsch, and L. Niinistö, Synthesis and surface engineering of complex nanostructures by atomic layer deposition, *Adv. Mater.*, 2007, **19**, 3425-3438.

[38] H. Kim, H.-B.-R. Lee, and W.-J. Maeng, Applications of atomic layer deposition to nanofabrication and emerging nanodevices, *Thin Solid Films*, 2009, **517**, 2563-2580.

[39] S. M. George, Atomic layer deposition; an overview, *Chem. Rev.*, 2010, **110**, 111-131.

[40] K. Tomabechi, Energy resources in the future, *Energies*, **2010**, 3, 686-695.

[41] J. B. Goodenough, Cathode materials: a personal perspective, *J. Power Sources*, 2007, **174**, 996-1000.

[42] L.-X. Yuan, Z.-H. Wang, W.-X. Zhang, X.-L. Hu, J.-T. Chen, Y.-H. Huang, and J. B. Goodenough, Development and challenges of LiFePO₄ cathode material for lithium-ion batteries, *Energy Environ. Sci.*, 2011, **4**, 269-284.

[43] M. S. Dresselhaus, I. L. Thomas, Alternative energy technologies, *Nature*, **2001**, 414, 332-337.

[44] M. R. Palacín, Recent advances in rechargeable battery materials: a chemist's perspective, *Chem. Soc. Rev.*, 2009, **38**, 2565-2575.

[45] Z. Yang, J. Zhang, M. C. W. Kintner-Meyer, X. Lu, D. Choi, J. P. Lemmon, and J. Liu, Electrochemical energy storage for green grid, *Chem. Rev.*, 2011. DOI: 10.1021/cr100290v

[46] M. Armand, and J.-M. Tarascon, Building better batteries, *Nature*, 2008, **451**, 652-657.

[47] L. F. Nazar, G. Goward, F. Leroux, M. Duncan, H. Huang, T. Kerr, and J. Gaubicher, Nanostructured materials for energy storage, *Int. J. Inorg. Mater.*, 2001, **3**, 191-200.

[48] J.-M. Tarascon, and M. Armand, Issues and challenges facing rechargeable lithium batteries, *Nature*, 2001, **414**, 359-367.

[49] B. Scrosati, and J. Garche, Lithium batteries: status, prospects and future, *J. Power Sources*, 2010, **195**, 2419-2430.

[50] J. B. Goodenough, and Y. Kim, Challenges for rechargeable Li batteries, *Chem. Mater.*, 2010, **22**, 587-603.

- [51] P. Arora, R. E. White, and M. Doyle, Capacity fade mechanisms and side reactions in lithium-ion batteries, *J. Electrochem. Soc.*, 1998, **145**, 3647-3667.
- [52] D. Aurbach, B. Markovsky, G. Salitra, E. Markevich, Y. Talyossef, M. Koltypin, L. Nazar, B. Ellis, and D. Kovacheva, Review on electrode-electrolyte solution interactions, related to cathode materials for Li-ion batteries, *J. Power Sources*, 2007, **165**, 491-499.
- [53] Idaho National Laboratory, Battery test manual for plug-in hybrid electric vehicle, 2010 (<http://www.inl.gov>).
- [54] P. Poizot, S. Laruelle, S. Grugeon, L. Dupont, and J.-M. Tarascon, Nano-sized transition-metal oxides as negative-electrode materials for lithium-ion batteries, *Nature*, 2000, **407**, 496-499.
- [55] M. S. Whittingham, Lithium batteries and cathode materials, *Chem. Rev.*, 2004, **104**, 4271-4301.
- [56] A. S. Arico, P. Bruce, B. Scrosati, J.-M. Tarascon, and W. V. Schalkwijk, Nanostructured materials for advanced energy conversion and storage devices, *Nature Mater.*, 2005, **4**, 366-377.
- [57] D. Larcher, S. Beattie, M. Morcrette, K. Edström, J.-C. Jumas, and J.-M. Tarascon, Recent findings and prospects in the field of pure metals as negative electrodes for Li-ion batteries, *J. Mater. Chem.*, 2007, **17**, 3759-3772.
- [58] Y. Wang, K. Takahashi, K. Lee, and G. Cao, Nanostructured vanadium oxide electrodes for enhanced lithium-ion intercalation, *Adv. Funct. Mater.*, 2006, **16**, 1133-1144.
- [59] Y. Wang, and G. Cao, Developments in nanostructured cathode materials for high-performance lithium-ion batteries, *Adv. Mater.*, 2008, **20**, 2251-2269.
- [60] Y.-G. Guo, J.-S. Hu, and L.-J. Wan, Nanostructured materials for electrochemical energy conversion and storage devices, *Adv. Mater.*, 2008, **20**, 2878-2887.
- [61] F. Cheng, Z. Tao, J. Liang, and J. Chen, Template-directed materials for rechargeable lithium-ion batteries, *Chem. Mater.*, 2008, **20**, 667-681.
- [62] D. Deng, M. G. Kim, J. Y. Lee, and J. Cho, Green storage materials: nanostructured TiO₂ and Sn-based anodes for lithium-ion batteries, *Energy Environ. Sc.*, 2009, **2**, 818-837.
- [63] B. L. Ellise, K. T. Lee, and L. F. Nazar, Positive electrode materials for Li-ion and

Li-batteries, *Chem. Mater.*, 2010, **22**, 691-714.

[64] D. S. Su, and R. Schlögl, Nanostructured carbon and carbon nanocomposites for electrochemical energy storage applications, *ChemSusChem*, 2010, **3**, 136-168.

[65] H. Manjunatha, G. S. Suresh, and T. V. Venkatesha, Electrode materials for aqueous rechargeable lithium batteries, *J. Solid State Electrochem.*, 2011, **15**, 431-445.

[66] D. Baril, C. Michot, and M. Armand, Electrochemistry of liquids vs. solids: polymer electrolytes, *Solid State Ionics*, 1997, **94**, 35-47.

[67] W. H. Meyer, Polymer electrolytes for lithium-ion batteries, *Adv. Mater.*, 1998, **10**, 439-448.

[68] V. Thangadurai, and W. Weppner, Recent progress in solid oxide and lithium ion conducting electrolytes research, *Ionics*, 2006, **12**, 81-92.

[69] H. Xia, H. L. Wang, W. Xiao, M. O. Lai, and L. Lu, Thin film electrolytes for all-solid-state micro-batteries, *Int. J. Surf. Sci. Eng.*, 2009, **3**, 23-43.

[70] P. Arora, and Z. Zhang, Battery separators, *Chem. Rev.*, 2004, **104**, 4419-4462.

[71] S. S. Zhang, A review on the separators of liquid electrolyte Li-ion batteries, *J. Power Sources*, 2007, **164**, 351-364.

[72] S. S. Zhang, A review on electrolyte additives for lithium-ion batteries, *J. Power Sources*, 2006, **162**, 1379-1394.

[73] L. J. Fu, H. Liu, C. Li, Y. P. Wu, E. Rahm, R. Holze, and H. Q. Wu, Surface modifications of electrode materials for lithium ion batteries, *Solid State Sci.*, 2006, **8**, 113-128.

[74] C. Li, H. P. Zhang, L. J. Fu, H. Liu, Y. P. Wu, E. Rahm, R. Holze, and H. Q. Wu, Cathode materials modified by surface coating for lithium ion batteries, *Electrochim. Acta*, 2006, **51**, 3872-3883.

[75] T.-F. Yi, Y.-R. Zhu, X.-D. Zhu, J. Shu, C.-B. Yue, and A.-N. Zhou, A review of recent development in the surface modification of LiMn_2O_4 as cathode material of power lithium-ion battery, *Ionics*, 2009, **15**, 779-784.

[76] S.-T. Myung, K. Amine, and Y.-K. Sun, Surface modification of cathode materials from nano- to microscale for rechargeable lithium-ion batteries, *J. Mater. Chem.*, 2010, **20**, 7074-7095.

[77] Z. Chen, Y. Qin, K. Amine, and Y.-K. Sun, Role of surface coating on cathode

materials for lithium-ion batteries, *J. Mater. Chem.*, 2010, **20**, 7606-7612.

[78] P. Verma, P. Maire, and P. Novák, A review of the features and analyses of the solid electrolyte interphase in Li-ion batteries, *Electrochim. Acta*, 2010, **55**, 6332-6341.

[79] C. J. W. Ng, H. Gao, and T. T. Y. Tan, Atomic layer deposition of TiO₂ nanostructures for self-cleaning applications, *Nanotechnology*, 2008, **19**, 445604.

[80] L. K. Tan, M. A. S. Chong, and H. Gao, Free-standing porous anodic alumina templates for atomic layer deposition of highly ordered TiO₂ nanotube arrays on various substrates, *J. Phys. Chem. C*, 2008, **112**, 69-73.

[81] L. K. Tan, H. Gao, Y. Zong, and W. Knoll, Atomic layer deposition of TiO₂ to bond free-standing nanoporous alumina templates to gold-coated substrates as planar optical waveguide sensors, *J. Phys. Chem. C*, 2008, **112**, 17576-17580.

[82] Y.-H. Chang, C.-M. Liu, Y.-C. Tseng, C. Chen, C.-C. Chen, and H.-E. Cheng, Direct probe of heterojunction effects upon photoconductive properties of TiO₂ nanotubes fabricated by atomic layer deposition, *Nanotechnology*, 2010, **21**, 225602.

[83] L. K. Tan, M. K. Kumar, W. W. An, and H. Gao, Transparent, well-aligned TiO₂ nanotube arrays with controllable dimensions on glass substrates for photocatalytic applications, *ACS Appl. Mater. Interfaces*, 2010, **2**, 498-503.

[84] C.-M. Liu, C. Chen, and H.-E. Cheng, Growth mechanism of TiO₂ nanotube arrays in nanopores of anodic aluminum oxide on Si substrates by atomic layer deposition, *J. Electrochem. Soc.*, 2011, **158**, K58-K63.

[85] C.-M. Liu, C. Chen, and H.-E. Cheng, Ultraviolet photoresponse of TiO₂ nanotube arrays fabricated by atomic layer deposition, *Electrochem Solid State Lett.*, 2011, **14**, K33-K35.

[86] J. T. Korhonen, P. Hiekkataipale, J. Malm, M. Karppinen, O. Ikkala, and R. H. A. Ras, Inorganic hollow nanotube aerogels by atomic layer deposition onto native nanocellulose templates, *ACS Nano*, 2011, **5**, 1967-1974.

[87] S. K. Cheah, E. Perre, M. Rooth, M. Fondell, A. Hårsta, L. Nyholm, M. Boman, T. Gustafsson, J. Lu, P. Simon, and K. Edström, Self-supported three-dimensional nanoelectrodes for microbattery applications, *Nano Lett.*, 2009, **9**, 3230-3233.

[88] M. Rooth, R. A. Quinlan, E. Widenkvist, J. Lu, H. Grennberg, B. C. Holloway, A. Hårsta, and U. Jansson, Atomic layer deposition of titanium dioxide nanostructures using

carbon nanosheets as a template, *J. Cryst. Growth*, 2009, **311**, 373-377.

[89] K. Gerasopoulos, X. Chen, J. Culver, C. Wang, and R. Ghodssi, Self-assembled Ni/TiO₂ nanocomposite anodes synthesized via electroless plating and atomic layer deposition on biological scaffolds, *Chem. Commun.*, 2010, **46**, 7349-7351.

[90] C. Bae, S. Kim, B. Ahn, J. Kim, M. M. Sung, and H. Shin, Template-directed gas-phase fabrication of oxide nanotubes, *J. Mater. Chem.*, 2008, **18**, 1362-1367.

[91] J. Lee, H. Ju, J. K. Lee, H. S. Kim, and J. Lee, Atomic layer deposition of TiO₂ nanotubes and its improved electrostatic capacitance, *Electrochem. Commun.*, 2010, **12**, 210-212.

[92] H. Shin, D.-K. Jeong, J. Lee, M. M. Sung, and J. Kim, Formation of TiO₂ and ZrO₂ nanotubes using atomic layer deposition with ultraprecise control of the wall thickness, *Adv. Mater.*, 2004, **16**, 1197-1200.

[93] X. Meng, D. Geng, J. Liu, R. Li, and X. Sun, Controllable synthesis of graphene-based titanium dioxide nanocomposites by atomic layer deposition, *Nanotechnology*, 2011, **22**, 165602.

[94] T. H. Han, J. K. Oh, J. S. Park, S.-H. Kwon, S.-W. Kim, and S. O. Kim, Highly entangled hollow TiO₂ nanoribbons templating diphenylalanine assembly, *J. Mater. Chem.*, 2009, **19**, 3512-3516.

[95] S.-W. Kim, T. H. Han, J. Kim, H. Gwon, H.-S. Moon, S.-W. Kang, S. O. Kim, and K. Kang, Fabrication and electrochemical characterization of TiO₂ three-dimensional nanonetwork based on peptide assembly, *ACS Nano*, 2009, **3**, 1085-1090.

[96] M. Rooth, A. Johansson, K. Kukli, J. Aarik, M. Boman, and A. Hårsta, Atomic layer deposition of iron oxide thin films and nanotubes using ferrocene and oxygen as precursors, *Chem. Vap. Deposition*, 2008, **14**, 67-70.

[97] X. Meng, M. Ionescu, M. N. Banis, Y. Zhong, H. Liu, Y. Zhang, S. Sun, R. Li, and X. Sun, Heterostructural coaxial nanotubes of CNT@Fe₂O₃ via atomic layer deposition: effects of surface functionalization and nitrogen-doping, *J. Nanopart. Res.*, 2011, **13**, 1207-1218.

[98] J. Bachmann, J. Jing, M. Knez, S. Barth, H. Shen, S. Mathur, U. Gosele, and K. Nielsch, Ordered iron oxide nanotube arrays of controlled geometry and tunable magnetism by atomic layer deposition, *J. Am. Chem. Soc.*, 2007, **129**, 9554-9555.

- [99] Y.-S. Min, E. J. Bae, J. B. Park, U. J. Kim, W. Park, J. Song, C. S. Hwang, and N. Park, ZnO nanoparticle growth on single-walled carbon nanotubes by atomic layer deposition and a consequent lifetime elongation of nanotube field emission, *Appl. Phys. Lett.*, 2007, **90**, 263104.
- [100] D. S. Kim, S.-M. Lee, R. Scholz, M. Knez, U. Gösele, J. Fallert, H. Kalt, and M. Zacharias, Synthesis and optical properties of ZnO and carbon nanotube based coaxial heterostructures, *Appl. Phys. Lett.*, 2008, **93**, 103108.
- [101] Y.-H. Lin, P.-S. Lee, Y.-C. Hsueh, K.-Y. Pan, C.-C. Kei, M.-H. Chan, J.-M. Wu, T.-P. Perng, and H. C. Shih, Atomic layer deposition of zinc oxide on multiwalled carbon nanotubes for UV photodetector applications, *J. Electrochem. Soc.*, 2011, **158**, K24-K27.
- [102] A. B. F. Martinson, J. W. Elam, J. T. Hupp, and M. J. Pellin, ZnO nanotube based dye-sensitized solar cells, *Nano Lett.*, 2007, **7**, 2183-2187.
- [103] Y.-H. Chang, S.-M. Wang, C.-M. Liu, and C. Chen, Fabrication and characteristics of self-aligned ZnO nanotube and nanorod arrays on Si substrates by atomic layer deposition, *J. Electrochem. Soc.*, 2010, **157**, K236-K241.
- [104] X. Meng, Y. Zhang, S. Sun, R. Li, and X. Sun, Three Growth Modes and Mechanisms for Highly Structure-tunable SnO₂ Nanotube Arrays of Template-directed Atomic Layer Deposition, *J. Mater. Chem.*, 2011, DOI:10.1039/C1JM11511A
- [105] X. Meng, Y. Zhong, Y. Sun, M. N. Banis, R. Li, and X. Sun, Nitrogen-doped carbon nanotubes coated by atomic layer deposited SnO₂ with controlled morphology and phase, *Carbon*, 2011, **49**, 1133-1144.
- [106] X. Meng, D. Geng, J. Liu, M. N. Banis, Y. Zhang, R. Li, and X. Sun, Non-aqueous approach to synthesize amorphous/crystalline metal oxide-graphene nanosheet hybrid composites, *J. Phys. Chem. C*, 2010, **114**, 18330-18337.
- [107] W.-S. Kim, B.-S. Lee, D.-H. Kim, H.-C. Kim, W.-R. Yu, and S.-H. Hong, SnO₂ nanotubes fabricated using electrospinning and atomic layer deposition and their gas sensing performance, *Nanotechnology*, 2010, **21**, 245605.
- [108] C. Marichy, N. Donato, M.-G. Willinger, M. Latino, D. Karpinsky, S.-H. Yu, G. Neri, and N. Pinna, Tin dioxide sensing layer grown on tubular nanostructures by a non-aqueous atomic layer deposition process, *Adv. Funct. Mater.*, 2011, **21**, 658-666.
- [109] K. S. Novoselov, A. K. Geim, S. V. Morozov, D. Jiang, Y. Zhang, S. V. Dubonos, I.

- V. Grigorieva, A. A. Firsov, Electric field effect in atomically thin carbon films, *Science* **2004**, 306, 666-669.
- [110] K. I. Bolotin, K. J. Sikes, Z. Jiang, M. Klima, G. Fudenberg, J. Hone, P. Kim, H. L. Stormer, Ultrahigh electron mobility in suspended graphene, *Solid State Commun.* **2008**, 146, 351-355.
- [111] M. D. Stoller, S. Park, Y. Zhu, J. An, R. S. Ruoff, Graphene-based ultracapacitors, *Nano Lett.* **2008**, 8, 3498-3502.
- [112] D. Wang, D. Choi, J. Li, Z. Yang, Z. Nie, R. Kou, D. Hu, C. Wang, L. V. Saraf, J. Zhang, I. A. Aksay, and J. Liu, Self-assembled TiO₂-graphene hybrid nanostructures for enhanced Li-ion insertion, *ACS Nano*, 2009, **3**, 907-914.
- [113] S. M. Paek, E. Yoo, and I. Honma, Enhanced cyclic performance and lithium storage capacity of SnO₂/graphene nanoporous electrodes with three-dimensionally delaminated flexible structure, *Nano Lett.* **2009**, 9, 72-75.
- [114] E. Perre, L. Nyholm, T. Gustfsson, P.-L. Taberna, P. Simon, and K. Edström, Direct electrodeposition of aluminum nano-rods, *Electrochem. Commun.*, 2008, **10**, 1467-1470.
- [115] K. Mizushima, P. C. Jones, P. J. Wiseman, and J. B. Goodenough, Li_xCoO₂ (0<x≤1): a new cathode material for batteries of high energy density, *Mat. Res. Bull.*, 1980, **15**, 783-789.
- [116] M. M. Thackeray, W. I. F. David, P. G. Bruce, and J. B. Goodenough, Lithium insertion into manganese spinels, *Mat. Res. Bull.*, 1983, **18**, 461-472.
- [117] A. Patil, V. Patil, D. W. Shin, J.-W. Choi, D.-S. Paik, and S.-J. Yoon, Issue and challenges facing rechargeable thin film lithium batteries, *Mater. Res. Bull.*, 2008, **43**, 1913-1942.
- [118] S. Beke, A review of the growth of V₂O₅ films from 1885 to 2010, *Thin Solid Films*, 2011, **519**, 1761-1771.
- [119] M. S. Whittingham, The role of ternary phases in cathode reactions, *J. Electrochem. Soc.*, 1976, **123**, 315-320.
- [120] M. Baba, N. Kumagai, H. Kobayashi, O. Nakano, and K. Nishidate, Fabrication and electrochemical characteristics of all-solid-state lithium-ion batteries using V₂O₅ thin films for both electrodes, *Electrochem. Solid State Lett.*, 1999, **2**, 320-322.

- [121] J. C. Badot, S. Ribes, E. B. Yousfi, V. Vivier, J. P. Pereira-Ramos, N. Baffier, and D. Lincot, Atomic layer epitaxy of vanadium oxide thin films and electrochemical behavior in presence of lithium ions, *Electrochem. Solid State Lett.*, 2000, **3**, 485-488.
- [122] J. C. Badot, A. Mantoux, N. Baffier, O. Dubrunfaut, and D. Lincot, Electrical properties of V₂O₅ thin films obtained by atomic layer deposition (ALD), *J. Mater. Chem.*, 2004, **14**, 3411-3415.
- [123] R. Baddour-Hadjean, V. Golabkan, J. P. Pereira-Ramos, A. Mantoux, and D. Lincot, A Raman study of the lithium insertion process in vanadium pentoxide thin films deposited by atomic layer deposition, *J. Raman Spectrosc.*, 2002, **33**, 631-638.
- [124] K. Le Van, H. Groult, A. Mantoux, L. Perrigaud, F. Lantelme, R. Lindström, R. Baddour-Hadjean, S. Zanna, and D. Lincot, Amorphous vanadium oxide films synthesised by ALCVD for lithium rechargeable batteries, *J. Power Sources*, 2006, **160**, 592-601.
- [125] N. Ohta, K. Takada, L. Zhang, R. Ma, M. Osada, and T. Sasaki, Enhancement of the high-rate capability of solid-state lithium batteries by nanoscale interfacial modification, *Adv. Mater.*, 2006, **18**, 2226-2229.
- [126] L. Baggetto, R. A. H. Niessen, F. Roozeboom, and P. H. L. Notten, High energy density all-solid-state batteries: a challenging concept towards 3D integration, *Adv. Funct. Mater.*, 2008, **18**, 1057-1066.
- [127] J. W. Long, B. Dun, D. R. Rolison, and H. S. White, Three-dimensional battery architectures, *Chem. Rev.*, 2004, **104**, 4463-4492.
- [128] M. Roberts, P. Johns, J. Owen, D. Brandell, K. Edstrom, G. E. Enany, C. Guery, D. Golodnitsky, M. Lacey, C. Lecoeur, H. Mazor, E. Peled, E. Perre, M. M. Shaijumon, P. Simon, and P.-L. Taberna, 3D lithium ion batteries—from fundamentals to fabrication, *J. Mater. Chem.*, 2011, doi:10.1039/c0jm04396f.
- [129] P. H. L. Notten, F. Roozeboom, R. A. H. Niessen, and L. Baggetto, 3-D integrated all-solid-state rechargeable batteries, *Adv. Mater.*, 2007, **19**, 4564-4567.
- [130] M. Putkonen, T. Aaltonen, M. Alnes, T. Sajavaara, O. Nilsen, and H. Fjellvåg, Atomic layer deposition of lithium containing thin films, *J. Mater. Chem.*, 2009, **19**, 8767-8771.
- [131] T. Aaltonen, M. Alnes, O. Nisen, L. Costelle, and H. Fjellvåg, Lanthanum titanate and lithium lanthanum titanate thin films grown by atomic layer deposition, *J. Mater.*

Chem., 2010, **20**, 2877-2881.

[132] Y. S. Jung, A. S. Cavanagh, L. A. Riley, S.-H. Kang, A. C. Dillon, M. D. Groner, S. M. George, and S.-H. Lee, Ultrathin direct atomic layer deposition on composite electrodes for highly durable and safe Li-ion batteries, *Adv. Mater.*, 2010, **22**, 2172-2176.

[133] M. Q. Snyder, S. A. Trebukhova, B Ravdel, M. C. Wheeler, J. DiCarlo, C. P. Tripp, and W. J. DeSisto, Synthesis and characterization of atomic layer deposited titanium nitride thin films on lithium titanate spinel powder as a lithium-ion battery anode, *J. Power Sources*, 2007, **165**, 379-385.

[134] T.-F. Yi, L.-J. Jiang, J. Shu, C.-B. Yue, R.-S. Zhu, and H.-B. Qiao, Recent development and application of $\text{Li}_4\text{Ti}_5\text{O}_{12}$ as anode material of lithium ion battery, *J. Phys. Chem. Solids*, 2010, **71**, 1236-1242.

[135] H.-Q. Gao, X.-Y. Wang, Z.-A. Zhang, Y.-Q. Lai, J. Li, and Y.-X. Liu, Modification of $\text{Li}_4\text{Ti}_5\text{O}_{12}$ anode material with urea as nitrogen source for lithium ion battery, *J. Inorg. Mater.*, 2010, **25**, 983-988.

[136] L. A. Riley, A.S. Cavanagh, S. M. George, Y. S. Jung, Y. Yan, S.-H. Lee, and A. C. Dillon, Conformal surface coatings to enable high volume expansion Li-ion anode materials, *ChemPhysChem*, 2010, **11**, 2124-2130.

[137] L. A. Riley, A. S. Cavanagh, S. M. George, S.-H. Lee, and A. C. Dillon, Improved mechanical integrity of ALD-coated composite electrodes for Li-ion batteries, *Electrochem. Solid State Lett.*, 2011, **14**, A29-A31.

[138] M. I. Dafinone, G. Feng, T. Brugarolas, K. E. Tettey, and D. Lee, Mechanical reinforcement of nanoparticle thin films using atomic layer deposition, *ACS Nano*, DOI:10.1021/nn201167j.

[139] J.-H. Lee, M.-H. Hon, Y.-W. Chung, and I.-C. Leu, The effect of TiO_2 coating on the electrochemical performance of ZnO nanorod as the anode material for lithium-ion battery, *Appl. Phys. A*, 2011, **102**, 545-550.

[140] F. Belliard, and J. T. S. Irvine, Electrochemical performance of ball-milled ZnO-SnO₂ systems as anodes in lithium-ion battery, *J. Power Sources*, 2001, **97-98**, 219-222.

[141] J. Liu, Y. Li, R. Ding, J. Jiang, Y. Hu, X. Ji, Q. Chi, Z. Zhu, and X. Huang, Carbon/ZnO nanorod array electrode with significantly improved lithium storage capability, *J. Phys. Chem. C*, 2009, **113**, 5336-5339.

- [142] G. G. Amatucci, and J.-M. Tarascon, Rechargeable battery cell having surface-treated lithiated intercalation positive electrode, *U.S. Paten 5705291*, 1998.
- [143] L. Liu, Z. Wang, H. Li, L. Chen, and X. Huang, Al₂O₃-coated LiCoO₂ as cathode material for lithium ion batteries, *Solid State Ionics*, 2002, **152-153**, 341-346.
- [144] G. T.-K. Fey, C.-Z. Lu, J.-D. Huang, T. P. Kumar, and Y.-C. Chang, Nanoparticulate coatings for enhanced cyclability of LiCoO₂ cathodes, *J. Power Sources*, 2005, **146**, 65-70.
- [145] G. T.-K. Fey, P. Muralidharan, C.-Z. Lu, and Y.-D. Cho, Enhanced electrochemical performance and thermal stability of La₂O₃-coated LiCoO₂, *Electrochim. Acta*, 2006, **51**, 4850-4858.
- [146] Q. Cao, H. P. Zhang, G. J. Wang, Q. Xia, Y. P. Wu, and H. Q. Wu, A novel carbon-coated LiCoO₂ as cathode material for lithium-ion battery, *Electrochem. Commun.*, 2007, **9**, 1228-1232.
- [147] G. T.-K. Fey, C.-F. Huang, P. Muralidharan, and E. S.-S. Chang, Improved electrochemical performance of LiCoO₂ surface treated with Li₄Ti₅O₁₂, *J. Power Sources*, 2007, **174**, 1147-1151.
- [148] C.-Z. Lu, J.-M. Chen, Y.-D. Cho, W.-H. Hsu, P. Muralidharan, and G. T.-K. Fey, Electrochemical performance of LiCoO₂ cathodes by surface modification using lanthanum aluminum garnet, *J. Power Sources*, 2008, **184**, 392-401.
- [149] Y.-S. Jung, A. S. Cavanagh, A. C. Dillon, M. D. Groner, S. M. George, and S.-H. Lee, Enhanced stability of LiCoO₂ cathodes in lithium-ion batteries using surface modification by atomic layer deposition, *J. Electrochem. Soc.*, 2010, **157**, A75-A81.
- [150] J.-T. Lee, F.-M. Wang, C.-S. Cheng, C.-C. Li, and C.-H. Lin, Low-temperature atomic layer deposited Al₂O₃ thin film on layer structure cathode for enhanced cycleability in lithium-ion batteries, *Electrochim. Acta*, 2010, **55**, 4002-4006.
- [151] I. D. Scott, Y. S. Jung, A. S. Cavanagh, Y. Yan, A. C. Dillon, S. M. George, and S.-H. Lee, Ultrathin coatings on nano-LiCoO₂ for lithium-ion vehicular applications, *Nano Lett.*, 2011, **11**, 414-418.
- [152] T. Ohzuku, and Y. Makimura, Layered lithium insertion material of LiCo_{1/3}Ni_{1/3}Mn_{1/3}O₂ for lithium-ion batteries, *Chem. Lett.*, 2001, **30**, 642-643.
- [153] F. Wu, M. Wang, Y. Su, and S. Chen, Surface modification of LiCo_{1/3}Ni_{1/3}Mn_{1/3}O₂

with Y_2O_3 for lithium-ion battery, *J. Power Sources*, 2009, **189**, 743-747.

[154] H.-Y. Wang, A.-D. Tang, K.-L. Huang, and S.-Q. Liu, Uniform AlF_3 thin layer to improve rate capability of $LiNi_{1/3}Co_{1/3}Mn_{1/3}O_2$ material for Li-ion batteries, *Trans. Nonferrous Met. Soc. China*, 2010, **20**, 803-808.

[155] Z. Yang, X.-H. Li, Z.-X. Wang, and Y.-J. Zhu, Surface modification of spherical $LiNi_{1/3}Co_{1/3}Mn_{1/3}O_2$ with Al_2O_3 using heterogeneous nucleation process, *Trans. Nonferrous Met. Soc. China*, 2007, **17**, 1319-1323.

[156] G. T.-K. Fey, C.-S. Chang, and T. P. Kumar, Synthesis and surface treatment of $LiNi_{1/3}Co_{1/3}Mn_{1/3}O_2$ cathode materials for Li-ion batteries, *J. Solid State Electrochem.*, 2010, **14**, 17-26.

[157] L. A. Riley, S. V. Atta, A. S. Cavanagh, Y. Yan, S. M. George, P. Liu, A. C. Dillon, and S.-H. Lee, Electrochemical effects of ALD surface modification on combustion synthesized $LiNi_{1/3}Mn_{1/3}Co_{1/3}O_2$ as a layered-cathode material, *J. Power Sources*, 2011, **196**, 3317-3324.

[158] X. M. Wu, S. Chen, M. Y. Ma, and J. B. Liu, Synthesis of Co-coated lithium manganese oxide and its characterization as cathode for lithium ion battery, *Ionics*, 2011, **17**, 35-39.

[159] J. Tu, X. B. Zhao, G. S. Cao, J. P. Tu, and T. J. Zhu, Improved performance of $LiMn_2O_4$ cathode materials for lithium ion batteries by gold coating, *Mater. Lett.*, 2006, **60**, 3251-3254.

[160] S.-W. Lee, K.-S. Kim, H.-S. Moon, H.-J. Kim, B.-W. Cho, W.-I. Cho, J.-B. Ju, and J.-W. Park, Electrochemical characteristics of Al_2O_3 -coated lithium manganese spinel as a cathode material for a lithium secondary battery, *J. Power Sources*, 2004, **126**, 150-155.

[161] L. Yu, X. Qiu, J. Xi, W. Zhu, and L. Chen, Enhanced high-potential and elevated-temperature cycling stability of $LiMn_2O_4$ cathode by TiO_2 modification for Li-ion battery, *Electrochim. Acta*, 2006, **51**, 6406-6411.

[162] C. Lai, W. Ye, H. Liu, and W. Wang, Preparation of TiO_2 -coated $LiMn_2O_4$ by carrier transfer method, *Ionics*, 2009, **15**, 389-392.

[163] D. Liu, X. Liu, and Z. He, Surface modification by ZnO coating for improving the elevated temperature performance of $LiMn_2O_4$, *J. Alloy. Comp.*, 2007, **436**, 387-391.

[164] H. Sahan, H. Goktepe, S. Patat, and A. Ulgen, Effect of the Cr_2O_3 coating on

electrochemical properties of spinel LiMn_2O_4 as a cathode material for lithium battery applications, *Solid State Ionics*, 2010, **181**, 1437-1444.

[165] D. Guan, J. A. Jeevarajan, and Y. Wang, Enhanced cycleability of LiMn_2O_4 cathodes by atomic layer deposition of nanosized-thin Al_2O_3 coatings, *Nanoscale*, 2011, **3**, 1465-1469.

[166] A. Deb, and E. J. Cairns, In situ X-ray adsorption spectroscopy—a probe of cathode materials for Li-ion cells, *Fluid Phase Equilib.*, 2006, **241**, 4-19.

[167] J. McBreen, The application of synchrotron techniques to the study of lithium-ion batteries, *J. Solid State Electrochem.*, 2009, **13**, 1051-1061.

[168] R. D. Marco, and J.-P. Veder, In situ structural characterization of electrochemical systems using synchrotron-radiation techniques, *TrAC, Trends Anal. Chem.*, 2010, **29**, 528-537.

[169] L. F. Hakim, S. M. George, and A. W. Weimer, Conformal nanocoating of zirconia nanoparticles by atomic layer deposition in a fluidized bed reactor, *Nanotechnology*, 2005, **16**, S375-S381.

[170] A. S. Cavanagh, C. A. Wilson, A. W. Weimer, and S. M. George, Atomic layer deposition on gram quantities of multi-walled carbon nanotubes, *Nanotechnology*, 2009, **20**, 255602.

CHAPTER 3

EXPERIMENTAL APPARATUS AND PROCEDURES

3.1 Experimental setup and procedures

3.1.1 Experimental setup

The main experimental setup is an ALD (Savannah 100, Cambridge Nanotechnology Inc., USA) system, as schematically illustrated in [figure 3.1](#). This system consists of a ALD reactor (A) to contain substrates (B), several steel cylinders (C) for holding different precursors, solenoid valves (D) to control the supplies of precursors, a ALD ebox (E) connected to a computer (F), and a vacuum pump (G, Pascal 2005 I, Adixon) to sustain low pressures of the reactor chamber.

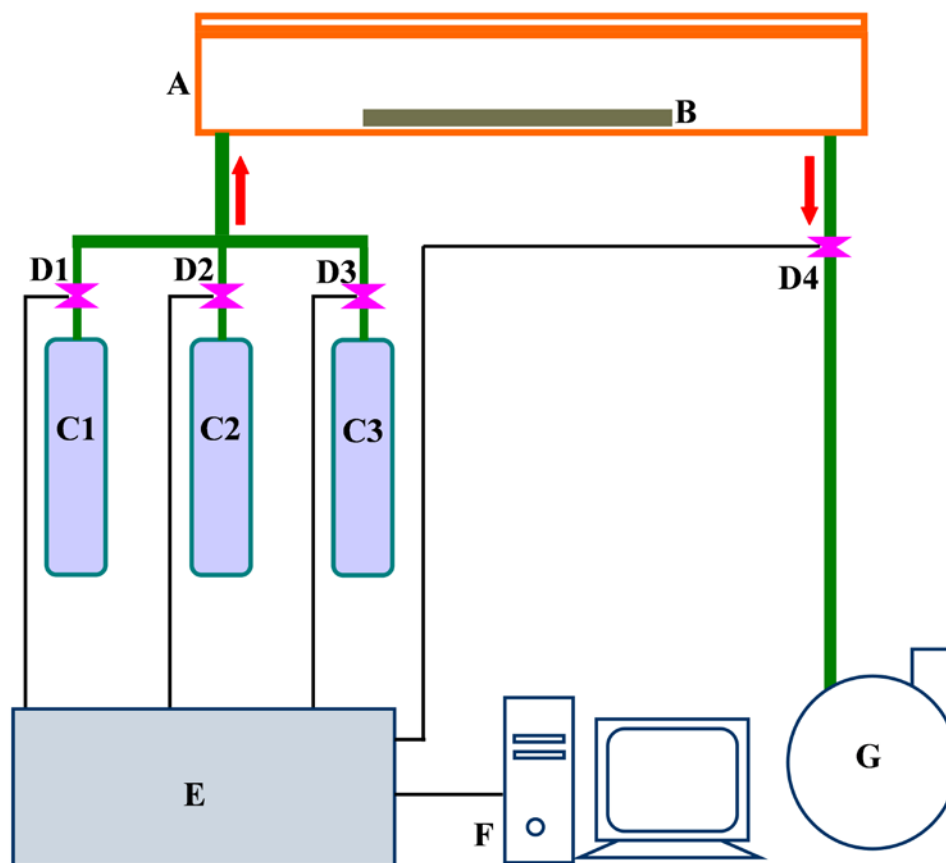


Figure 3.1 Experimental setup for atomic layer deposition (ALD): A – ALD reactor, B – substrate, C1-C3 – precursor cylinders, D1-D3 – solenoid valves, E – ALD ebox, F – computer, G – vacuum pump.

During ALD processes, the deposition behaviors are controlled by a LabVIEW program installed in the computer. ALD parameters such as temperatures and precursor supplies can be set and operated via the program. In addition, the program can also be used to monitor the change of the pressures. Figure 3.2 shows a screen snapshot on the LabVIEW program. The left part of figure 3.2 displays the inputted parameters (the upper part) as well as the changing curve of pressure (the lower part). The right part of figure 3.2 shows the ALD system as illustrated in figure 3.1. In figure 3.2, the pressure curve displays the changing pressures with time, which was operated with an exposure mode. It is easy to observe that the pressures show good repetition with increased cycles.

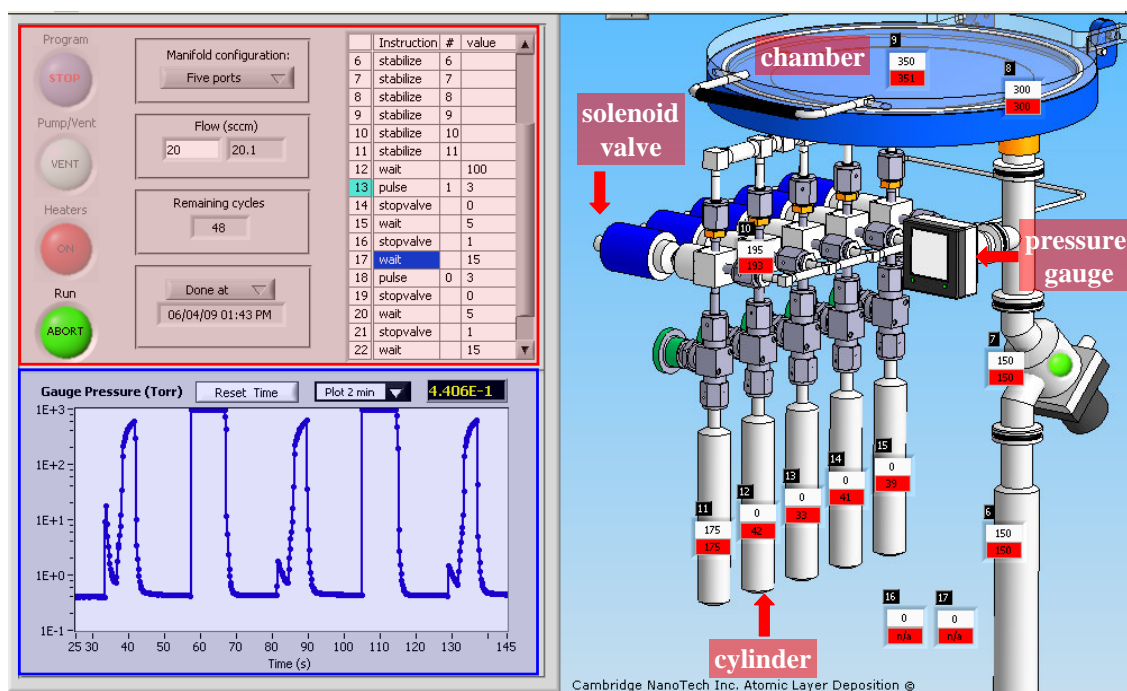


Figure 3.2 A screen snapshot on the LabVIEW program of the ALD system.

3.1.2 Experimental procedures

In an ALD process, one should first load precursors into different cylinders and then a substrate is placed in the ALD reactor chamber. Various ALD parameters are inputted via

the LabVIEW program, such as temperature, supplies of different precursors, and cycling numbers. To initiate an ALD process, one only needs to push down the running icon on the LabVIEW panel. During an ALD process, different precursors are supplied with some certain duration in an alternating manner and between their supplies there are purges to clean the oversupplied precursors and the produced byproducts. To maintain a stable operation of an ALD process, one needs to keep an eye on the pressure curve which shows good repetition with time.

3.2 Materials and synthesis strategies

3.2.1 Substrates and precursors

A. Substrates

A1. Synthesis

As is well-known, ALD is surface-controlled and self-limiting in nature and it contributes to precise nanosynthesis at the atomic level. Thus, various substrates or templates are necessary for the development of nanostructured materials. In this work, we use porous anodic aluminum oxide (AAO) templates, undoped and nitrogen-doped CNTs, and graphene nanosheets (GNS) as substrates to develop various nanomaterials. Besides AAO (Whatman, Anodisc, 60 μm in thickness and 13 mm in diameter) commercially available, CNTs and GNS were fabricated in our group.

Both undoped and nitrogen-doped CNTs were synthesized by thermal CVD methods. A method was to grow the two types of CNTs on a series of carbon papers. The carbon papers were covered with 30 nm thick aluminum at the bottom and 5 nm thick iron at the top. In the presence of Ar, the undoped CNTs were grown through pyrolyzing ethylene (C_2H_4) at 750 $^\circ\text{C}$ [1] while the N-CNTs were produced by pyrolyzing melamine ($\text{C}_3\text{H}_6\text{N}_6$) at 800 $^\circ\text{C}$ [2]. They both are structurally multi-walled, but the N-CNTs received an N

content of around 10.4 at.% determined by x-ray photoelectron spectroscopy (XPS, Kratos Axis Ultra Al(alpha)) [2]. Another method was to grow N-CNTs on carbon papers by a floating catalyst chemical vapor deposition (FCCVD) method. Carbon papers were first coated with a 30 nm thick aluminum buffer layer by sputtering before the growth of N-CNTs. In a process of N-CNT synthesis, 2 g melamine ($C_3N_6H_6$) and 100 mg ferrocene ($Fe(C_5H_5)_2$) were supplied into a oven-heated quartz tube at 950 °C and the growth of N-CNTs occurred on carbon papers at the central area of the tube. For more details, readers can refer to our previous work published elsewhere [3]. The N contents of the synthesized N-CNTs are around 8.4 at.% as determined before.

For preparation of GNS, we first oxidized natural graphite powder (45 μ m, 99.99%, Sigma-Aldrich) using a modified Hummers method [4]. In detail, graphite powder (1 g) was first stirred in concentrated sulphuric acid (23 ml) with a following addition of sodium nitrate (0.5 g) at room temperature. The stirring lasted for 16 h, and then the mixture was cooled down to 0 °C. Thereafter, potassium permanganate (3 g) was added to form a new mixture. Two hours later, the mixture formed a green slurry around 35 °C, and it was stirred for another 3 h. Then, water (46 ml) was slowly added into the paste with an increased temperature around 98 °C. The suspension was remained at this temperature for 30 minutes before it was further diluted with another addition of water and hydrogen peroxide (140 ml). In the following, the suspension was filtered and washed until the pH value of the filtrate was neutral. The as-received slurry is the so-called graphite oxide (GO), which was further dried in a vacuum oven at 60 °C. To prepare GNS, the as-synthesized GO was first flushed by Ar for 20 min in a quartz tube. Then, the quartz tube was promptly moved into a Lindberg tube furnace with a preheated temperature around 1050 °C. After 30 s thermal treatment, GO was reduced into expanded GNS powders.

A2. Functionalization

Owing to their chemical inertness, undoped CNTs were usually functionalized for various deposition processes. There are mainly two methodologies practiced in previous studies:

covalent oxidation and non-covalent surface modification. In the former case, it has been fulfilled with many chemical solutions, including HNO_3 , a mixture of 3:1 $\text{HNO}_3/\text{H}_2\text{SO}_4$, KMnO_4 , and so on [5-13]. In the latter case, it was performed by many surfactants, such as sodium dodecyl sulfate (SDS), and sodium dodecyl benzenesulfonate (SDBS), etc [14-20]. Amongst them, HNO_3 and SDS are the most widely used ones as the covalent and non-covalent approach, respectively [7,15]. In this study, both of HNO_3 and SDS were used to functionalize undoped CNTs for deposition of different metal oxides. The exact conditions of functionalization will be described in following chapters.

B. Precursors

To synthesize different metal oxides, different precursors were employed at suitable growth temperatures. For binary compounds, the used precursors include ferrocene (98%, Sigma Aldrich) and oxygen (99.9%) for iron oxide, tin chloride (99% SnCl_4 , Sigma-Aldrich) and water for tin dioxide, as well as titanium isopropoxide (TTIP, 98%, Sigma-Aldrich) and water for titanium dioxide. For the ternary compound of $\text{Li}_4\text{Ti}_5\text{O}_{12}$ (LTO), the precursors consist of TTIP, lithium tert-butoxide (LTB, $\text{Li}(\text{O}^t\text{Bu})$, 97%, Sigma-Aldrich), and water. TTIP and water reacted to produce TiO_2 while LTB and water reacted to produce lithium-containing compounds. Through adjusting the ratio between TiO_2 and lithium-containing compounds, LTO was prepared with annealing.

3.2.2 Strategies for nanostructures

A. Metal oxide nanotubes

AAO templates are porous with numerous nanosized pores. They are used to synthesize nanotubes of metal oxides, for ALD processes can deposit target materials in the pores with the formation of tubular nanofilms. After the deposition, sodium hydroxide solution can be used to dissolve the AAO template and the nanotubes of metal oxides can be produced.

B. CNT-metal oxide core-shell nanotubes

Another strategy is based on CNTs, in which metal oxides are deposited on the surface of CNTs and form core-shell nanostructures. In particular, undoped CNTs and nitrogen-doped CNTs (N-CNTs) were used in various ALD processes. Undoped CNTs are chemically inert while N-CNTs are chemically active. Thus, undoped CNTs require functionalization pretreatment while N-CNTs can be used directly for ALD processes.

C. 3D Metal oxide-GNS nanocomposites

The last strategy is about fabrication of 3D graphen-based nanocomposites. The employed GNS were home-made in our group. Through applying ALD processes on GNS powder, 3D metal oxide-GNS nanocomposites were synthesized with tunable deposition.

3.3 Characterization techniques

To characterize the as-synthesized nanomaterials, various advanced techniques were used. A field-emission scanning electron microscopy (FE-SEM, Hitachi 4800S) equipped with energy dispersive X-ray spectroscopy (EDS) and transition electron microscopy (TEM, Philips CM10) were employed to observe the morphological changes. A high-resolution TEM (HRTEM, JEOL 2010 FEG), X-ray diffractometer (XRD, Bruker D8 or Inel multi-purpose diffractometer), Raman spectrometry (RXN1-785, Kaiser Optical Systems InCo.), Fourier transform infrared spectroscopy (FTIR, Bruker Tensor 27), and X-ray photoelectron spectroscopy (XPS, Kratos Axis Ultra Al K(alpha)) were applied to gain structural and surface information.

References

- [1] H. Liu, D. Arato, R. Li, Y. Zhang, P. Merel, and X. Sun, Aligned multi-walled carbon nanotubes on different substrates by floating catalyst chemical vapor deposition: Critical effects of buffer layer, *Surf. Coating Tech.*, 2008, **202**, 4114-4120.
- [2] Y. Zhong, M. Jaidann, Y. Zhang, G. Zhang, H. Liu, M. I. Ionescu, R. Li, X. Sun, H. Abou-Rachid, and L. S. Lussierb, Synthesis of high nitrogen doping of carbon nanotubes and modeling the stabilization of filled DAATO@CNTs (10,10) for nanoenergetic materials, *J. Phys. Chem. Solids*, 2010, **71**, 134-139.
- [3] H. Liu, Y. Zhang, R. Li, X. Sun, S. Désilets, H. Abou-Rachid, M. Jaidann, and L.-S. Lussier, Structural and morphological control of aligned nitrogen-doped carbon nanotubes, *Carbon*, 2010, **48**, 1498-1507.
- [4] W. S. Hummers and R. E. Offeman, Preparation of graphitic oxide, *J. Am. Chem. Soc.*, 1958, **80**, 1339.
- [5] V. Datsyuk, M. Kalyva, K. Papagelis, J. Parthenios, D. Tasis, A. Siokou, I. Kallitsis, and C. Galiotis, Chemical oxidation of multiwalled carbon nanotubes, *Carbon*, 2008, **46**, 833-840.
- [6] H. Hu, B. Zhao, M. E. Itkis, and R. C. Haddon, Nitric acid purification of single-walled carbon nanotubes, *J. Phys. Chem. B*, 2003, **107**, 13838-13842.
- [7] T. J. Park, S. Banerjee, T. Hemraj-Benny, and S. S. Wong, Purification strategies and purity visualization techniques for single-walled carbon nanotubes, *J. Mater. Chem.*, 2006, **16**, 141-154.
- [8] M. Pumera, B. Šmid, and K. Veltruská, Influence of nitric acid treatment of carbon nanotubes on their physico-chemical properties, *J. Nanosci. Nanotechnol.*, 2009, **9**, 2671-2676.
- [9] Z. Wang, M. D. Shirley, S. T. Meikle, R. L. D. Whitby, and S. V. Mikhalovsky, The surface acidity of acid oxidized multi-walled carbon nanotubes and the influence of in-situ generated fulvic acids on their stability in aqueous dispersions, *Carbon*, 2009, **47**, 73-79.
- [10] W. Xia, Y. Wang, R. Bergsträber, S. Kundu, and M. Muhler, Surface characterization of oxygen-functionalized multi-walled carbon nanotubes by high-

resolution X-ray photoelectron spectroscopy and temperature-programmed desorption, *Appl. Surf. Sci.*, 2007, **254**, 247-250.

[11] R. Yu, L. Chen, Q. Liu, J. Lin, K. L. Tan, S. C. Ng, H. S. O. Chan, G. Q. Xu, and T. S. Andy Hor, Platinum deposition on carbon nanotubes via chemical modification, *Chem. Mater.*, 1998, **10**, 718-722.

[12] J. Zhang, H. Zou, Q. Qing, Y. Yang, Q. Li, Z. Liu, X. Guo, and Z. Du, Effect of chemical oxidation on the structure of single-walled carbon nanotubes, *J. Phys. Chem. B*, 2003, **107**, 3712-3718.

[13] Z. B. Zhang, J. Li, A. L. Cabezas, and S. L. Zhang, Characterization of acid-treated carbon nanotube thin films by means of raman spectroscopy and field-effect response, *Chem. Phys. Lett.*, 2009, 476, 258-261.

[14] L. Huang, X. Cui, G. Dukovic, and S. P. O'Brien, Self-organizing high-density single-walled carbon nanotube arrays from surfactant suspensions, *Nanotechnology*, 2004, **15**, 1450-1454.

[15] M. F. Islam, E. Rojas, D. M. Bergey, A. T. Johnson, and A. G. Yodh, High weight fraction surfactant solubilization of single-wall carbon nanotubes in water, *Nano Lett.*, 2003, **3**, 269-273.

[16] R. Rastogi, R. Kaushal, S. K. Tripathi, A. L. Sharma, I. Kaur, and L. M. Bharadwaj, Comparative study of carbon nanotube dispersion using surfactants, *J. Colloid Interface Sci.*, 2008, **328**, 421-428.

[17] N. R. Tummala and A. Striolo, SDS surfactants on carbon nanotubes: aggregate morphology, *ACS Nano*, 2009, **3**, 595-602.

[18] M. L. Usrey and M. S. Strano, Controlling single-walled nanotubes surface adsorption with covalent and noncovalent functionalization, *J. Phys. Chem. C*, 2009, **113**, 12443-12453.

[19] E. J. Wanless and W. A. Ducker, Organization of sodium dodecyl sulfate at the graphite-solution interface, *J. Phys. Chem.*, 1996, **100**, 3207-3214.

[20] M. Zhang, L. Su, and L. Mao, Surfactant functionalization of carbon nanotubes (CNTs) for layer-by-layer assembling of CNT multi-layer films and fabrication of gold nanoparticles/CNT nanohybrid, *Carbon*, 2006, **44**, 276-283.

CHAPTER 4

HETEROSTRUCTURAL COAXIAL NANOTUBES OF CNT@Fe₂O₃ VIA ATOMIC LAYER DEPOSITION: EFFECTS OF SURFACE FUNCTIONALIZATION AND NITROGEN-DOPING

A version of this chapter has been published in *Journal of Nanoparticle Research*, 2011, 13, 1207-1218.

This study attempted to synthesize one-dimensional (1D) coaxial nanotubes of Fe₂O₃ based on carbon nanotubes (CNT@Fe₂O₃) via atomic layer deposition (ALD) of using ferrocene and oxygen as precursors. Results disclosed that undoped CNTs were suitable for the ALD of Fe₂O₃ (ALD-Fe₂O₃) only if they were chemically functionalized, due to their inert surface nature. It was further demonstrated that the effects of both covalent and non-covalent methodologies were limited in functionalizing undoped CNTs, leading to random and non-uniform deposition of Fe₂O₃. In sharp contrast, it was found that, as an alternative, nitrogen-doped CNTs (N-CNTs) contributed uniform and tunable ALD-Fe₂O₃, due to their surface active nature induced by incorporated N atoms. Consequently, various 1D heterostructural coaxial nanotubes were obtained with well-controlled growth of Fe₂O₃ on N-CNTs. For a better understanding, the underlying mechanisms were explored based on different N-doping configurations. In addition, high resolution transmission electron microscopy and X-ray diffraction jointly demonstrated that as-deposited Fe₂O₃ is single-phase crystalline α -Fe₂O₃ (hematite). The as-synthesized heterostructural coaxial nanotubes of CNT@Fe₂O₃ may find great potential applications in photocatalysis, gas-sensing, and magnetic fields.

Keywords: Atomic Layer Deposition, Iron Oxide, Carbon Nanotubes, Nitrogen Doping, Coaxial Nanostructures, Nanocomposites

4.1 Introduction

Since its emergence in the 1970s [1], atomic layer deposition (ALD) is currently undergoing a renaissance due to its recognized advantages and the demanding needs in scaling complementary metal-oxide-semiconductor (CMOS) devices [2]. By nature, ALD is a surface-controlled process consisting of two sequential self-limiting half-reactions. As a consequence, ALD has tremendous capabilities to provide more advantages over its counterparts such as chemical vapor deposition (CVD) and physical vapor deposition (PVD): thickness control at the atomic level, excellent conformity for complex structures, very good uniformity with large scale of thin films, and very low growth temperature (even down to room temperature) [3-6]. More recently, especially since the very beginning of the 21st century, the applications of ALD have been widened into nanotechnology for synthesizing various novel nanostructures and nanodevices of different elements and compounds, as reviewed by Knez et al [7] and Kim et al [8].

One of a variety of strategies to apply ALD in nanofabrication is to synthesize one-dimensional (1D) coaxial nanostructures, with exactly controlled size and versatile functions, by selecting 1D templates (e.g., nanotubes, and nanowires, etc.). Potential applications of the 1D coaxial nanostructures have been recently addressed as well, e.g., ZnO-Al₂O₃ core-shell nanowires for field effect transistors [9,10], CuO-Al₂O₃ core-shell nanowires and Cu nanoparticle chains encapsulated by Al₂O₃ nanotubes for plasmon waveguides [11]. Among the 1D templates for the aforementioned nanosynthesis via ALD, carbon nanotubes (CNTs) appear to be a good candidate and contribute to a large number of nanoscale coaxial structures [12-18], which possess enhanced physical and chemical properties due to the coaxial combination of CNTs and the target coatings. However, because of their chemical inertness to ALD precursors and the surface-controlled nature of ALD [19,20], single-walled (SWCNTs) or multi-walled (MWCNTs)) CNTs need surface functionalization through covalent or non-covalent chemical methods [12,13,18].

Iron(III) oxide (Fe₂O₃) as a transition metal oxide has drawn much attention from ALD

due to its potential applications in photocatalysis, gas-sensing, and the magnetic fields. Depending on different templates, earlier studies have fulfilled the ALD of Fe_2O_3 (ALD- Fe_2O_3) with various nanostructures, such as Fe_2O_3 thin films on flat substrates (e.g., Si and glass wafers) [21-24], Fe_2O_3 nanotubes via porous template-directed routes [24-26], and Fe_2O_3 composites based on zirconia nanoparticles [27]. The ALD precursors used in the aforementioned studies include $\text{Fe}(\text{thd})_3$ and ozone [22,23], FeCl_3 and water [21], ferrocene ($\text{Fe}(\text{C}_5\text{H}_5)_2$) and oxygen [24,27], ferrocene and ozone [26], as well as $\text{Fe}_2(\text{O}^t\text{Bu})_6$ and water [25]. However, there have been few efforts to date to synthesize 1D coaxial nanostructures of Fe_2O_3 using ALD. In order to explore the possibility of developing such 1D nanostructure via ALD, recently we attempted to deposit Fe_2O_3 on CNTs. As a consequence, as will be exposed in this article, heterostructural coaxial nanotubes via ALD coating of CNTs with Fe_2O_3 (i.e., $\text{CNT}@\text{Fe}_2\text{O}_3$) were developed with the precursors of ferrocene and oxygen. In this study, two types of CNTs, undoped and nitrogen-doped (N-doped), were employed as templates. It confirmed that functionalized pretreatment of the undoped CNTs is essential for ALD- Fe_2O_3 , due to their inert surface nature. In contrast, it was demonstrated for the first time that N-doped CNTs (N-CNTs), ascribing to their chemically active surface nature, appeared as a more reliable alternative for tunable ALD- Fe_2O_3 . As a consequence, besides the disclosure on the effects of different functionalization methodologies, this work opened a facile avenue to produce various heterostructural coaxial nanotubes of $\text{CNT}@\text{Fe}_2\text{O}_3$ using N-CNTs, which are expected to find great applications in producing functional components for various nanodevices.

4.2 Experimental

4.2.1 Synthesis and functionalization of CNTs

(A) Synthesis

The two types of CNTs were synthesized by thermal CVD methods in a heated horizontal

quartz tube. A series of carbon papers as substrates to grow CNTs were covered with 30 nm thick aluminum at the bottom and 5 nm thick iron at the top. In the presence of Ar, the undoped CNTs were grown through pyrolyzing ethylene (C_2H_4) at 750 °C [28] while the N-CNTs were produced by pyrolyzing melamine ($C_3H_6N_6$) at 800 °C [29]. They both are structurally multi-walled, but the N-CNTs received an N content of around 10.4 at.% determined by x-ray photoelectron spectroscopy (XPS, Kratos Axis Ultra Al(alpha)) [29].

(B) Functionalization

Owing to their chemical inertness, undoped CNTs were usually functionalized for various deposition processes. There are mainly two methodologies practiced in previous studies: covalent oxidation and non-covalent surface modification. In the former case, it has been fulfilled with many chemical solutions, including HNO_3 , a mixture of 3:1 HNO_3/H_2SO_4 , $KMnO_4$, and so on [30-38]. In the latter case, it was preformed by many surfactants, such as sodium dodecyl sulfate (SDS), and sodium dodecyl benzenesulfonate (SDBS), etc [39-45]. Amongst them, HNO_3 and SDS are the most widely used ones as the covalent and non-covalent approach, respectively [32,40].

For an aim of comparison, in this study we employed both covalent and non-covalent methods to modify the surface of undoped CNTs. In the case of covalent oxidation, samples of CNTs were soaked in a concentrated 70% HNO_3 solution at room temperature for 2 h, and then fully rinsed with deionized water (DI H_2O). In the case of non-covalent modification, samples were dipped into the aqueous solution of 1 wt% SDS (concentration greater than the critical micelle concentration [44,45]) at room temperature for 2 h. The 2 h treatment was beneficial in two ways: (1) protecting CNTs from cutting and damage due to extended chemical oxidation of HNO_3 or providing enough wetting to CNTs in the SDS surfactant; (2) facilitating to conduct a comparative study on different functionalization methods. Additionally, the combined effects due to the two aforementioned functionalization methods was examined by treating CNTs with HNO_3 for 1 h, fully rinsing the oxidized samples, and then immersing the samples with SDS for 1 h.

4.2.2 ALD-Fe₂O₃ processes

With the samples of CNTs loaded in a commercial ALD reactor (Savannah 100, Cambridge Nanotechnology Inc., USA), ALD-Fe₂O₃ was performed with ferrocene and oxygen as precursors. Although the two precursors had their ALD successes reported previously on other templates [24,27], there is still a bit of vague in exactly understanding the mechanisms. Generally, it was postulated that this ALD-Fe₂O₃ consists of the two potential half-reactions [27]: (1) ferrocene ligands react with chemisorbed oxygen in the ferrocene pulse, and (2) oxygen reacts with the remaining chemisorbed ferrocene ligands in the oxygen pulse. In this work, ferrocene (98%, Sigma Aldrich) and oxygen (99.9%) were introduced into the ALD reactor in an alternating manner. Prior to the ALD-Fe₂O₃, ferrocene powder as the iron source was heated to 90 °C. As a consequence, the partial pressures for ferrocene and oxygen were 10 and 400 Torr, respectively. Nitrogen was selected as the carrier gas with a flow rate of 20 sccm. The reactor was evacuated in ALD processes by a vacuum pump (Pascal 2005 I, Adixon), and reached a base pressure of around 0.4 Torr. The growth temperature of the substrates was set at 350 °C and the wall temperature of the reactor was 270 °C. In detail, the ALD-Fe₂O₃ processes were composed of several steps: (1) a 3 s supply of ferrocene; (2) a 5 s extended exposure of ferrocene to CNTs; (3) a 25 s nitrogen purge to remove oversupplied ferrocene and possible by-products; (4) a 2 s supply of oxygen; (5) a 5 s extended exposure of oxygen to CNTs; (6) a 25 s nitrogen purge to remove oversupplied oxygen and possible by-products. A whole set of the aforementioned six steps constituted one ALD cycle, and ALD processes could differ in the number of cycles in this study. Compared with the previous studies [24,27], this study applied a higher temperature (90 °C) for preheating ferrocene. The growth temperature (350 °C) was comparable to the lower ones employed in literature [24,27]. Additionally, the dosing of both ferrocene and oxygen in this study was longer than those used by Rooth et al [24] but shorter than the ones by Scheffe et al [27]. In particular, an exposure mode with a longer purging was employed in this study.

4.2.3 Characterization techniques

A field-emission scanning electron microscope (FE-SEM, Hitachi 4800S) was employed to collect the SEM images of the ALD-Fe₂O₃ on CNTs, showing the morphological changes of CNTs. Furthermore, the growth of the ALD-Fe₂O₃ was observed using a transmission electron microscope (TEM, Philips CM10). In addition, the crystalline structure of the ALD-Fe₂O₃ was examined by a high-resolution transmission electron microscope (HRTEM, JEOL 2010 FEG), and its composition was determined by a micro X-ray diffractometer (XRD, Bruker D8).

4.3 Results and Discussion

4.3.1 Effects of surface functionalization

The ALD-Fe₂O₃ was first performed on undoped CNTs. As for the pristine undoped CNTs, their morphological characteristics were shown in [figure 4.1\(a\)](#) and [\(b\)](#) jointly by low- and high-magnification SEM images. They were grown carbon papers with high density and an average diameter in the range of 20 - 60 nm. The conventional and high-resolution TEM images ([figure 4.1\(c\)](#)) further revealed their multiwalled structure.

To investigate the effects of surface modifications, a 200-cycle ALD-Fe₂O₃ was first practiced on the pristine undoped CNTs, as illustrated jointly by SEM image in [figure 4.2\(a\)](#) and TEM image in [figure 4.2\(a\)](#). The two images, compared with [figure 4.1\(b\)](#) and [\(c\)](#), revealed no observable changes on the morphologies of the CNTs, indicating an unsuccessful ALD practice on the pristine undoped CNTs. The only reason lies in the structural perfectness of undoped CNTs [34,46], contributing to a chemically inert characteristic, for there were no active sites for ALD to bond precursor molecules. According to previous studies, in reality only some trace defects (1-3 at.%) were disclosed [37,47]. To promote the ALD-Fe₂O₃ on undoped CNTs, thus, we employed

both covalent and non-covalent chemical methods to modify the surface nature of undoped CNTs and their effects were investigated.

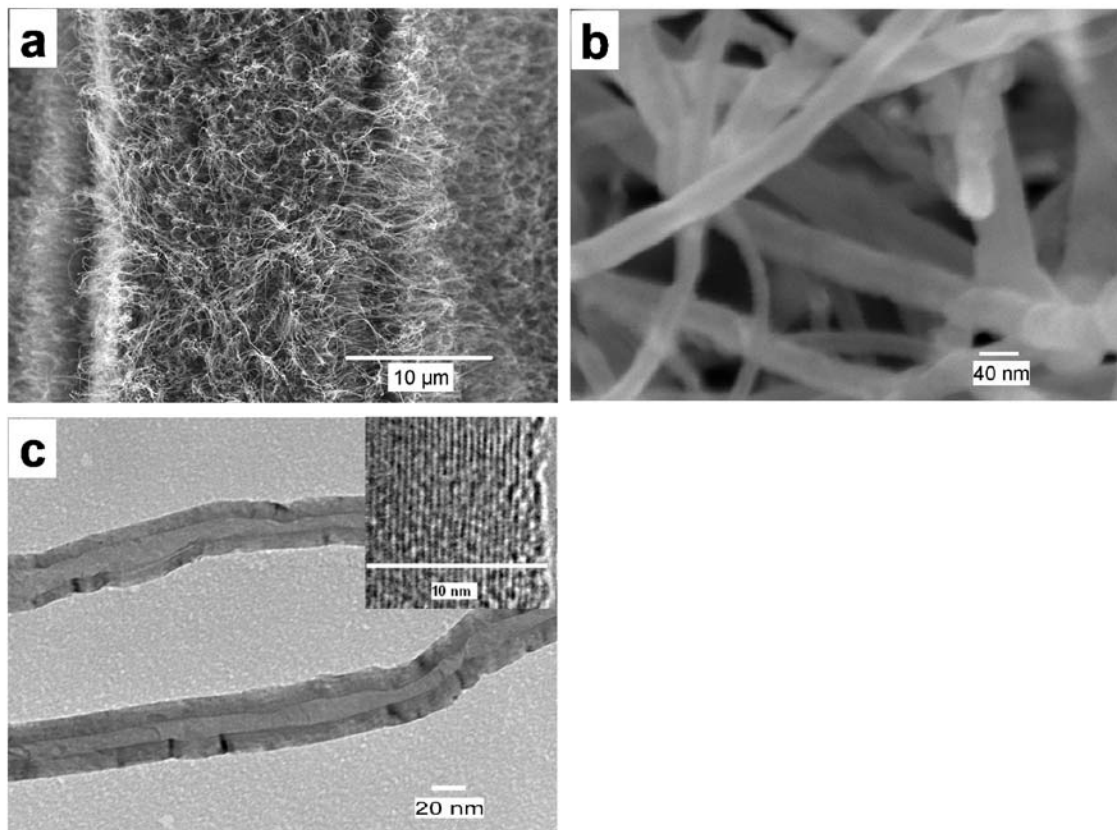


Figure 4.1. The pristine undoped CNTs: (a) low magnification and (b) high magnification SEM image; (c) conventional and (insert) high resolution TEM image.

The first attempt to promote the ALD- Fe_2O_3 was conducted by the pretreatment of undoped CNTs with HNO_3 , and the effect is illustrated in figure 4.2(c) and (d) by SEM images. Obviously, this covalent oxidization method helped the growth of the ALD- Fe_2O_3 in some local regions of CNTs where iron oxide clusters were grown. The clusters ranged in sizes and morphologies from nanoparticles of several tens nanometers to patchy films of hundreds nanometers. In particular, some uncoated areas are easily observed on the CNTs. As an alternative, in comparison, another effort was carried out with a non-

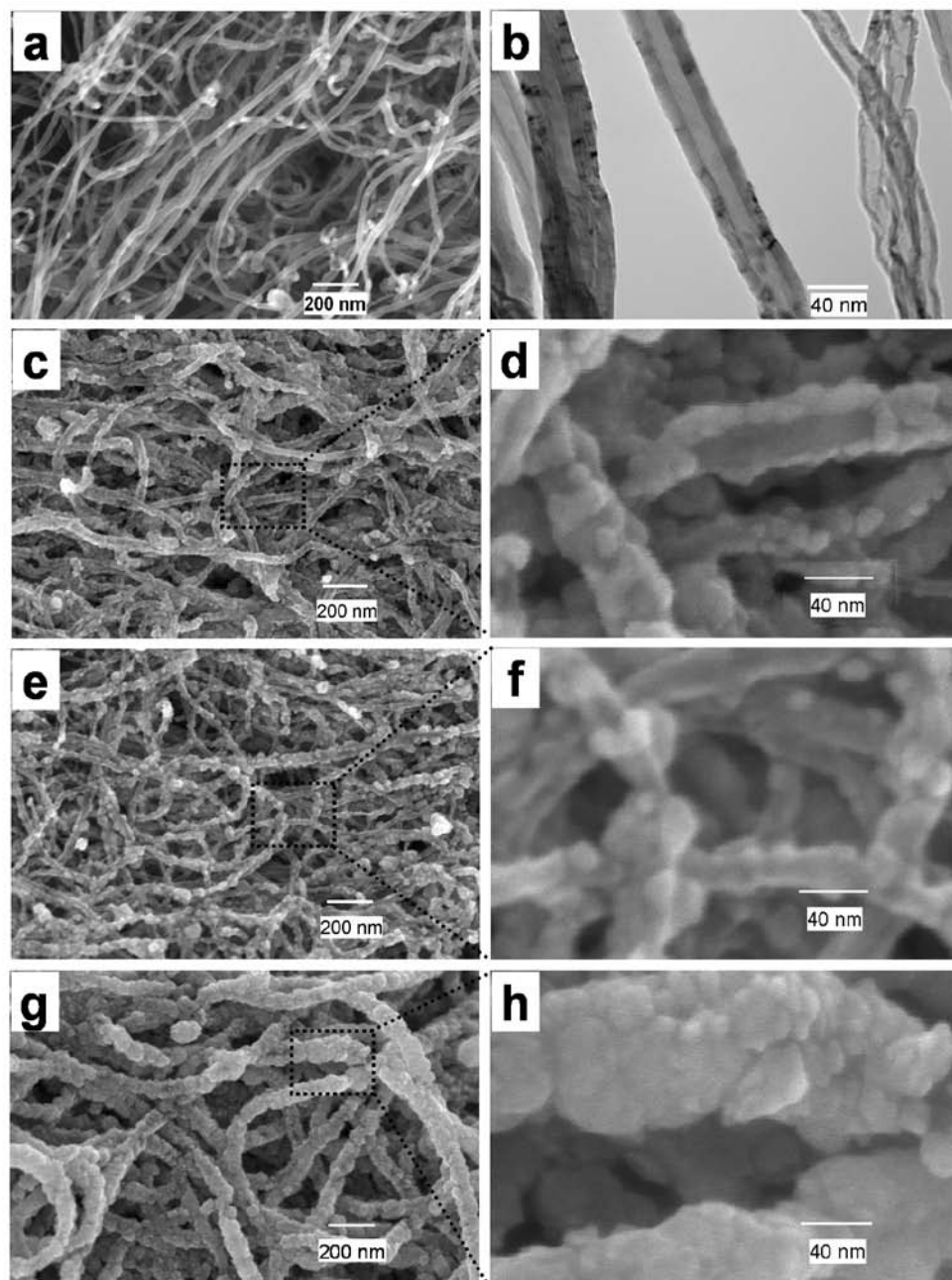
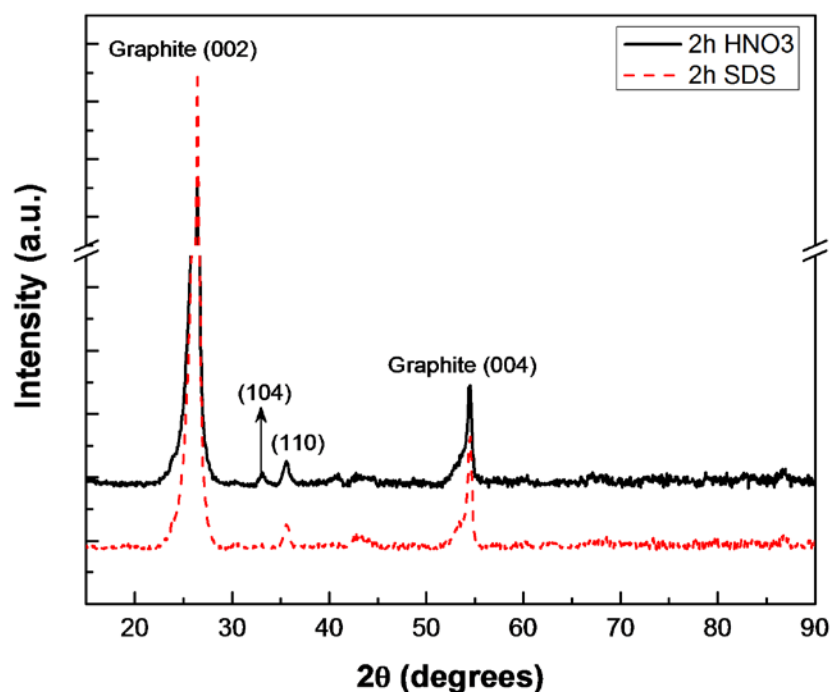


Figure 4.2. 200-cycle ALD of iron oxide deposition on the undoped CNTs: without surface pretreatment (a) SEM image and (b) TEM image; treated by 2h nitric acid (c) low magnification and (d) high magnification SEM image; treated by 2 h SDS (e) low magnification and (f) high magnification SEM image; treated by 1 h nitric acid and 1 h SDS in sequence (g) low magnification and (h) high magnification SEM image.

covalent surfactant, SDS, and its effect is shown in [figure 4.2\(e\)](#) and [\(f\)](#) by SEM images. It was found that the treatment of SDS received a similar effect as the one of HNO_3 : scattered clusters but not continuous film. Furthermore, we also examined the combined effect due to sequential HNO_3 and SDS treatment, as revealed by [figure 4.2\(g\)](#) and [\(h\)](#). In this case, the CNTs were almost fully covered with a fairly thick film, resulting in an increase in diameters from 20 - 60 nm to 60 - 80 nm after 200 ALD cycles. However, it is still remarkable that the coverage is non-uniform. In addition, the coated samples due to HNO_3 treatment and due to SDS treatment were examined by XRD, illustrated in [figure 4.3](#). The XRD patterns show two stronger peaks identified as the reference values of crystalline graphite in the standard card (JCPDS PDF No. 41-1487). They should be caused by the templates and marked as Graphite(002) and Graphite(004), respectively. The other two weaker peaks, as marked as (110) and (104), were confirmed in the standard card (JCPDS PDF No. 33-0664) and contributed crystalline $\alpha\text{-Fe}_2\text{O}_3$ (hematite) to be identified for both cases.



[Figure 4.3](#) XRD patterns of the ALD iron oxide on the undoped CNTs treated by nitric acid and SDS, respectively.

To understand the effects of the covalent and non-covalent functionalization on the ALD-Fe₂O₃, it is essential to know the knowledge of the changed surface nature. In the case of HNO₃ treatment, extensive investigation conducted previously revealed that oxygenated functional groups (e.g., carboxylic (-COOH), hydroxyl (-OH), phenolic (-OH bonded to a phenyl ring (C₆H₅-)), etc.) were introduced to CNTs while metal catalysts and amorphous carbon were removed [30-38]. Due to the various functional groups generated by acid oxidation, consequently, the surface reactivity of CNTs is significantly enhanced [36]. A case study using microwave method [48] disclosed that the oxidized CNTs via HNO₃ promoted the growth of Pt nanoparticles, for the created oxygenated defects provided Pt atoms with large adsorption energy. In the case of the non-covalent SDS functionalization, its widespread use was mainly for dispersing CNTs but not changing their inherent properties [39-41,43,45]. Over a critical solution concentration, SDS molecules would aggregate in interfaces [44]. A recent simulation [42] indicated that the morphologies and coverage of SDS aggregates have strong dependence on the diameter of CNTs, and get better with the increased diameter. In particular, the hydrophobic long-chain hydrocarbon tails of SDS molecules adsorbed onto graphite surface by van der Waals attractions while their hydrophilic sulfate (SO₄²⁻) head groups were exposed and served as ALD nucleation sites [18].

Obviously, both HNO₃ and SDS treatment introduced functional groups to the surface of undoped CNTs and thereby changed their surface reactivity. As a consequence, the created functional groups served as active sites to initiate ALD-Fe₂O₃. In summary, the ALD-Fe₂O₃ on those modified CNTs can be explained with the mechanisms: (1) HNO₃ and/or SDS treatment created functional groups (oxygenated and/or sulfate groups) on the surface of undoped CNTs; (2) ferrocene ligands were partially oxidized by the created groups and thereby Fe chemisorbed on the surface of CNTs with some remaining ligands, indicating the initiation of ALD processes; (3) a following oxygen pulse oxidized the remaining ferrocene ligands with the product of iron(III) oxide as well as new functional groups for the next ferrocene pulse; (4) the following cyclic ferrocene/oxygen pulses sustained the growth of crystalline Fe₂O₃.

As for the partial and non-uniform coverage on the CNTs treated by HNO₃ (figure 4.2(c) and (d)) or SDS (figure 4.2(e) and (f)), the reasons were mainly lied in the variances of CNTs in properties (such as perfectness, curvature, etc.), probably existing between individuals in a population of CNTs and/or regionally on a given CNT. Obviously, the functionalization effect due to HNO₃ or SDS was limited in each case. With reference to the improved coverage (figure 4.2(g) and (h)) due to the combined treatment of HNO₃ and SDS, there are two possibilities: (1) the initial oxidation-created defects improved the following SDS functionalization; (2) the sequential treatment by nitric acid and SDS produced a compensating effect on the creation of functional groups of CNTs. In any case of the two possibilities, there would be more active sites (in the forms of oxygenated or sulfate groups) to initiate the ALD-Fe₂O₃ by oxidizing ferrocene ligands in the first ferrocene pulse, leading to an improved coverage of Fe₂O₃ on the surface of CNTs.

4.3.2 Effects of N-doping

The above results disclosed an unsuccessful ALD-Fe₂O₃ on pristine undoped CNTs due to their structural perfectness, and an arbitrary ALD-Fe₂O₃ on undoped CNTs modified by HNO₃ and/or SDS. In order to synthesize 1D coaxial nanotubes of CNT@Fe₂O₃, we have to better manipulate ALD-Fe₂O₃. Fortunately, N-CNTs were found in our work to serve for this goal, and ALD-Fe₂O₃ was performed on N-CNTs under the same conditions as the ones for undoped CNTs. As shown in figure 4.4(a), the N-CNTs were also grown on carbon papers with high density. They are morphologically bamboo-like and typically in the range of 40 – 80 nm in diameter (figure 4.4(b)). HRTEM image (figure 4.4(c)) also revealed that they are multiwalled in structure.

In sharp contrast to the ALD-Fe₂O₃ on the pristine undoped CNTs (illustrated by figure 4.2(a) and (b)), the practice of ALD-Fe₂O₃ on the pristine N-CNTs exhibited some distinct characteristics. After 50 ALD cycles, as jointly shown by the SEM and TEM images in figure 4.5(a) and (b) respectively, numerous nanoparticles of less than 5 nm were uniformly deposited on the N-CNTs. Furthermore, the TEM image (figure 4.5(b)) also revealed that a continuous but bumpy thin film has been formed by those tiny

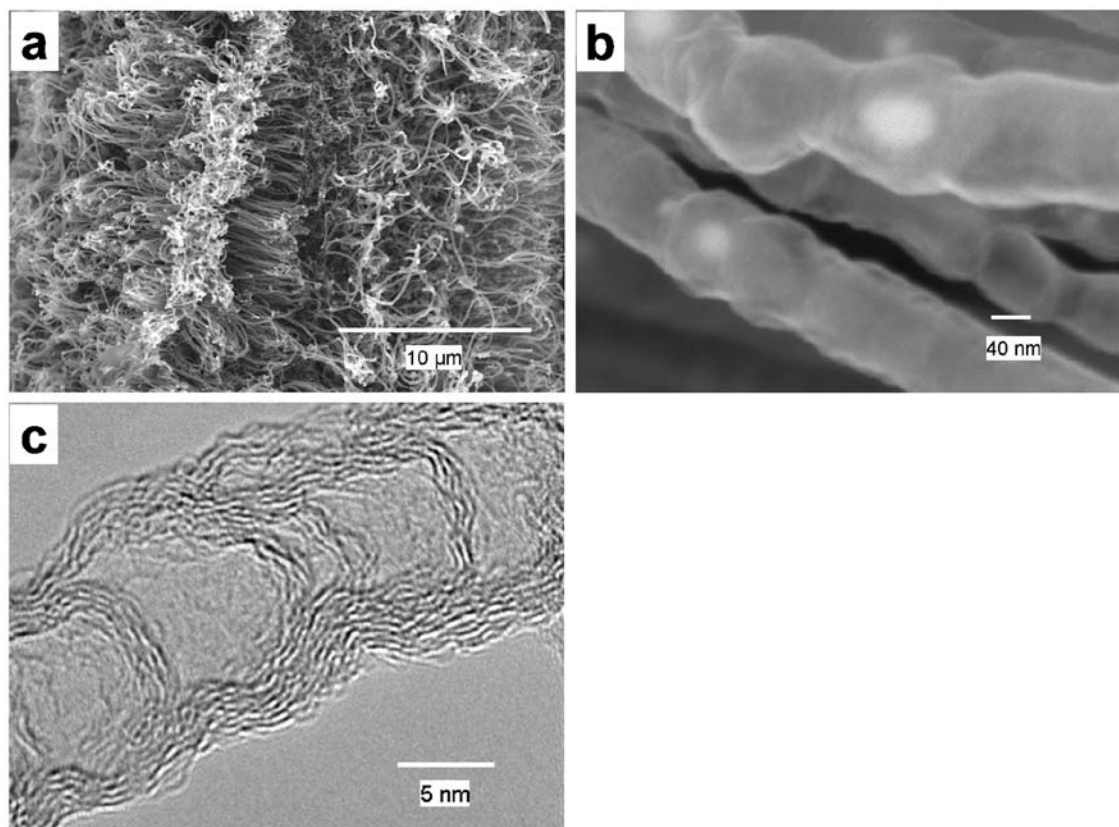


Figure 4.4 The N-doped CNTs: (a) low magnification and (b) high magnification SEM image; (c) HRTEM image.

nanoparticles. In this case, a nanostructure of CNT@Fe₂O₃ nanoparticles was received. With the ALD increased to 70 (figure 4.5(c) and (d)) and 100 cycles (figure 4.5(e) and (f)), it was found that smooth and uniform films were formed on the N-CNTs, resulting in heterostructural coaxial nanotubes of CNT@Fe₂O₃. Remarkably, the growth of ALD-Fe₂O₃ on N-CNTs experienced two distinct stages: island-like (in the first 50 cycles) and 2D growth mode (after 70 cycles). In addition, the film thickness was around 7.7 nm for 70 cycles and 11 nm for 100 cycles, accounting for a nearly linear growth rate of 1.1 Å/cycle on the N-CNTs. In addition, the examinations of XRD and HRTEM were conducted on the samples with a 70-cycle ALD-Fe₂O₃. In figure 4.6(a), the XRD patterns

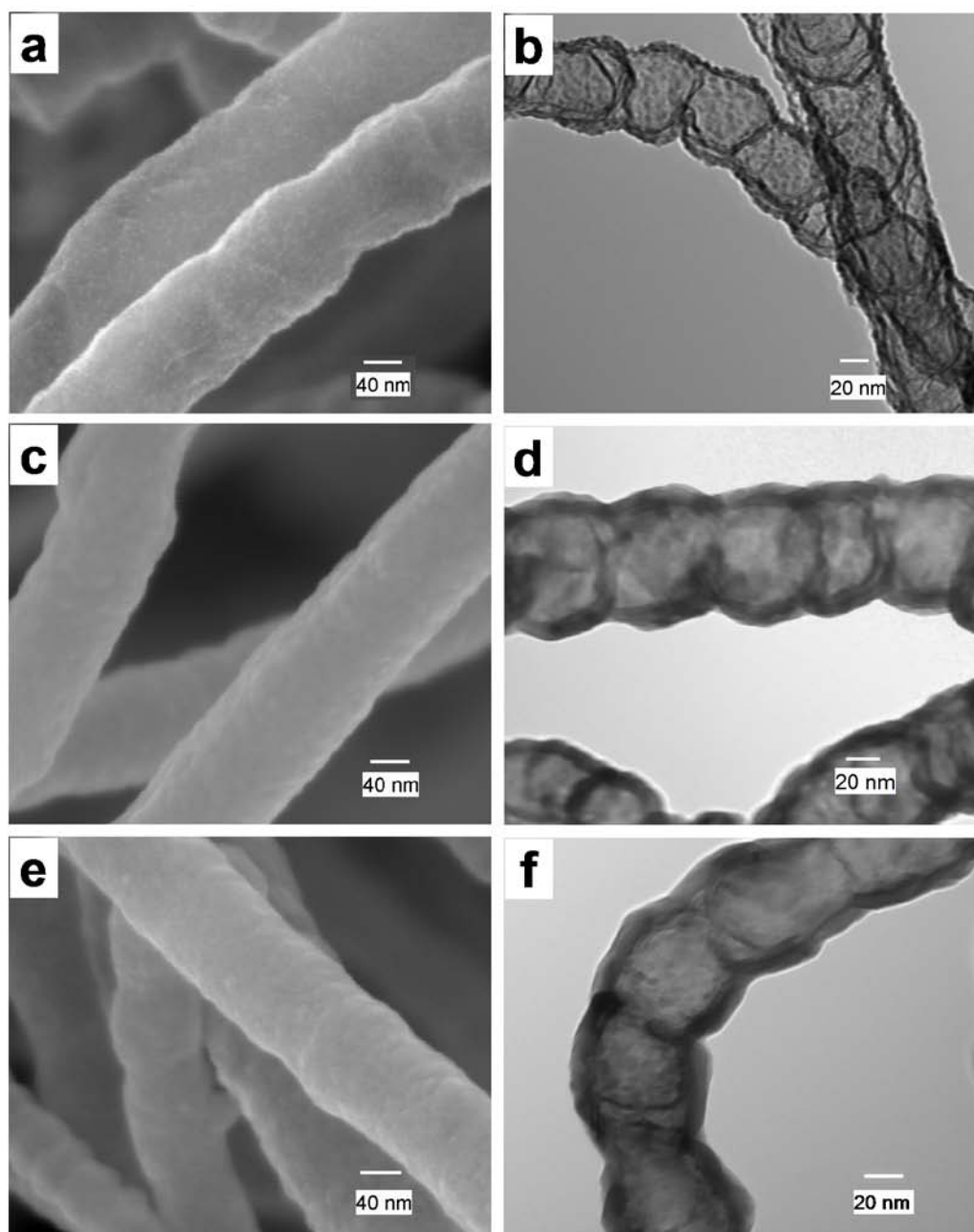


Figure 4.5 The ALD iron oxide on N-doped CNTs illustrated by: SEM images (a) 50 cycles, (c) 70 cycles, and (e) 100 cycles; TEM images (b) 50 cycles; (d) 70 cycles, and (f) 100 cycles.

disclosed that, besides the strong peaks of Graphite(002) and Graphite(004) (PCPDS PDF No. 41-1487) due to the crystalline graphite of the templates, the peaks of (110) and (104) were induced by α -Fe₂O₃ (hematite) (JCPDS PDF No. 33-0664) deposited via ALD. The HRTEM images in figure 4.6(b) and (c) demonstrated a single crystalline structure of as-deposited Fe₂O₃ as well as a 7.7 nm thick film. The measured lattice fringe spacing is 0.27 nm, indicating that the as-deposited Fe₂O₃ grew along a direction parallel to [110]. In comparison with the results exposed in previous studies, the growth rate of 1.1 Å/cycle in this study is a bit lower than the one (1.4 Å/cycle [24]) on Si substrates but higher than the one (0.6 Å/cycle [24]) in AAO pores and the one (0.15 Å/cycle [27]) on zirconia nanoparticles. In particular, different from the crystalline structures received in the work conducted by Rooth et al [24] and by us in this study, amorphous iron oxide was deposited on zirconia nanoparticles by Scheffe et al [27]. All these aforementioned variances on film growth imply that experimental conditions, especially the nature of the employed templates, played important roles in determining the characteristics of film growth, such as growth rates and structural phases.

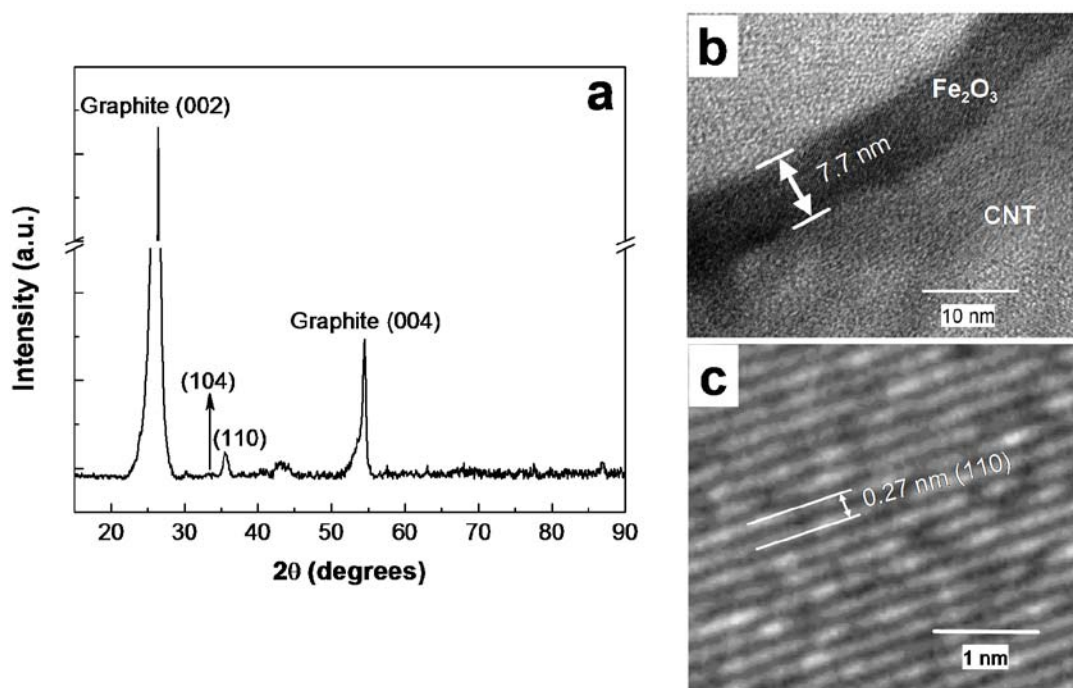


Figure 4.6 Phase and composition characteristics of the ALD iron oxide (70 ALD cycles) on the N-doped CNTs: (a)XRD patterns, (b) TEM image, and (c) HRTEM image.

Obviously, the above-discussed results demonstrated that the N-CNTs behaved favorable for ALD-Fe₂O₃, implying that N-doping played an important role. The underlying mechanisms should be ascribed to the chemically active surface of N-CNTs induced by the intrinsically incorporated N atoms. According to earlier studies [49-52], the doped-N atoms contributed to a variety of N-related defects. Of them, two primary N-bonding configurations were extensively identified, i.e., graphite-like N (GN, in which an N atom replaces a graphitic C atom) and pyridine-like N (PN, in which an N atom is bonded with two C atoms). It was previously revealed that both the GN and PN atoms are responsible for the enhancement of the reactivity of N-CNTs, in spite of different underlying mechanisms associated with them [49,53,54]. The former one results in N-neighboring C atoms activated, while the latter one contributes nonbonding electrons [51,55]. In practice, both experiments and simulations commonly demonstrated that N-CNTs promoted the deposition of transition metals and the PN tends to provide a higher binding energy in comparison to the one by GN [51,55,56].

Based on the above discussion, it is reasonable to believe that in this study the doped-N atoms (no matter which bonding configuration was taken) have facilitated or promoted the adsorption of the molecules of the employed precursors onto the N-CNTs to initiate ALD-Fe₂O₃. As revealed in our previous work [29], the N-CNTs employed in this study were with an N content of 10.4 at. %, and the area composition was 30.2% for GN and 54.6% for PN. On the other hand, the surface-controlled ALD determined that only the chemisorption between precursor molecules and functional groups are valid for the initiation of an ALD process [2]. Thus, one of the precursors (ferrocene and oxygen) must have been chemically adsorbed on N-CNTs at the beginning of ALD. The most recent study [57] revealed that oxygen can chemically adsorb on N-CNTs but can only physically adsorb on undoped CNTs. Thus, the chemisorbed oxygen is one solution for the success of ALD-Fe₂O₃ on N-CNTs. On the other hand, previous successes of transition metals (Ni, Pt) on N-CNTs seem to imply another possibility for the initiation of ALD-Fe₂O₃, i.e., ferrocene might be able to chemically bond with the surface active sites of the N-CNTs. As for this postulation, there was still a lack in understanding. In any case, the doped-N provided the base for the successful ALD-Fe₂O₃ on N-CNTs. After

the initiation, the cyclic ferrocene/oxygen pulses sustained the growth of ALD-Fe₂O₃, having less direct interactions with the surface of N-CNTs.

To understand the growth characteristics of Fe₂O₃ on N-CNTs with ALD cycles, there are two main factors identified previously: the steric hindrance of precursors and the limited number of reactive sites [2,8,58,59]. In the case of this study using ferrocene and oxygen as precursor, it is believed that the N content played an important role influencing the growth of Fe₂O₃. As shown in figure 4.5(b), (d), and (e), there exists a transition from an island-like growth mode to a 2D film growth mode in the range of 50 to 70 cycles, likely incurred by the limited number of reactive sites if not by steric hindrance. Recently, experimental investigation based on a solution method [60] demonstrated that higher N content resulted in smaller platinum particles with higher density deposited on N-CNTs. Therefore, we postulate that higher N content may increase the growth rate of the ALD-Fe₂O₃ and reduce the number of ALD cycles for the formation of coaxial Fe₂O₃ films on N-CNTs. In this way, a systematic investigation is of great interest in the future. In this study, it is worth noting that various coaxial nanotubes of CNT@Fe₂O₃ were synthesized by using N-CNTs, and particularly Fe₂O₃ can be in the form of nanoparticles or films with well-controlled growth through adjusting the ALD cycles. Additionally, N-CNTs were free of any surface modification (which influence the properties of undoped CNTs more or less [37,61]) prior to ALD-Fe₂O₃ and thereby could sustain their inherent properties. More importantly, N-CNTs could be tailored in properties by tuning the doped-N and were demonstrated with improved properties, such as electrical conductivity [62]. Thus, N-doping would contribute two important characteristics of the coaxial CNT@Fe₂O₃ nanotubes: (1) tunable deposition of ALD-Fe₂O₃; (2) tunable properties of N-CNTs. The two advantages would jointly lead to tunable functionality of the CNT@Fe₂O₃ nanodevices for gas-sensing, magnetic, and photocatalytic applications.

4.4 Conclusions

In this study, we attempted to synthesize 1D heterostructural coaxial nanotubes of CNT@Fe₂O₃ via atomic layer deposition of using ferrocene and oxygen as precursors. It

was found that, of the employed undoped and N-doped CNTs, the undoped ones needed chemical functionalization prior to ALD-Fe₂O₃, due to their inert surface nature. Even so, the functionalized undoped CNTs by HNO₃ or/and SDS were only coated with Fe₂O₃ in an arbitrary means, i.e., the as-deposited Fe₂O₃ was random and non-uniform. In sharp comparison, N-CNTs were more favorable for a uniform and tunable ALD-Fe₂O₃, ascribed to their chemically active surface nature induced by intrinsically incorporated N atoms. As a consequence, this study successfully fabricated 1D heterostructural nanotubes of CNT@Fe₂O₃ with tunable Fe₂O₃ from nanoparticles to nanofilms, based on N-CNTs. In addition, it was disclosed that the as-deposited Fe₂O₃ on the N-CNTs shows single-phase crystalline α -Fe₂O₃ (hematite), jointly determined by XRD and HRTEM. Essentially, this study provided an avenue for synthesizing 1D core-shell nanostructures using N-CNT as well as various heterostructural coaxial nanotubes of CNT@Fe₂O₃ being important candidates in many promising applications, such as photocatalysis, gas-sensing, magnetic fields, and other nanodevice fields.

Acknowledgements

This research was supported by the Natural Science and Engineering Research Council of Canada (NSERC), Canada Research Chair (CRC) Program, Canadian Foundation for Innovation (CFI), Ontario Research Fund (ORF), Early Researcher Award (ERA) and the University of Western Ontario. Herein the authors would like to thank Mr. David Tweddell, as well as our colleagues: Dr. Dongsheng Geng, and Dr. Gaixia Zhang for their help and discussion.

References

- [1] T. Suntola and J. Antson J, Method for producing compound thin films. 1977, *U.S. Patent*, 4058430.
- [2] R. L. Puurunen, Surface chemistry of atomic layer deposition: a case study for the trimethylaluminum/water process, *J. Appl. Phys.*, 2005, **97**,121301.
- [3] H. Kim, Atomic layer deposition of metal and nitride thin films: current research efforts and applications for semiconductor device processing, *J Vac Sci Technol B*, 2003, **21**, 2231-2261.
- [4] M. D. Groner, F. H. Fabreguette, J. W. Elam, and S. M. George, Low-temperature Al₂O₃ atomic layer deposition, *Chem. Mater.*, 2004, **16**, 639-645.
- [5] T. Suntola, Atomic layer epitaxy, *Mater. Sci. Rep.*, 1989, **4**, 261-312.
- [6] J. L. van Hemmen, S. B. S. Heil, J. H. Klootwijk, F. Roozeboom, C. J. Hodson, M. C. M. van de Sanden, and W. M. M. Kessel, Plasma and thermal ALD of Al₂O₃ in a commercial 200 mm ALD reactor, *J. Electrochem. Soc.*, 2007, **154**, G165-G169.
- [7] M. Knez, K. Nielsch, and L. Niinistö, Synthesis and surface engineering of complex nanostructures by atomic layer deposition, *Adv. Mater.*, 2007, **19**, 3425-3438.
- [8] H. Kim, H. B. R. Lee, and W. J. Maeng, Application of atomic layer deposition to nanofabrication and emerging nanodevices, *Thin Solid Films*, 2008, **517**, 2563-2580.
- [9] J. Huang, S. Liu, Y. Wang, and Z. Ye, Fabrication of ZnO/Al₂O₃ core-shell nanostructures and crystalline nanotube, *Appl. Surf. Sci.*, 2008, **254**, 5917-5920.
- [10] Y. Yang, D. S. Kim, M. Knez, R. Scholz, A. Berger, E. Pippel, D. Hesse, U. Gösele, and M. Zacharias, Influence of temperature on evolution of coaxial ZnO/Al₂O₃ one-dimensional heterostructures: from core-shell nanowires to spinel nanotubes and porous nanowires, *J. Phys. Chem. C*, 2008, **112**, 4068-4074.
- [11] Y. Qin, S. M. Lee, A. Pan, U. Gösele, and M. Knez, Rayleigh-instability-induced metal nanoparticle chains encapsulated in nanotubes produced by atomic layer deposition, *Nano Lett.*, 2008, **8**, 114-118.
- [12] D. B. Farmer, and R. G. Gordon, ALD of high-k dielectrics on suspended functionalized SWNTs, *Electrochem. Solid-State Lett.*, 2005, **8**, G89-G91.
- [13] D. B. Farmer, and R. G. Gordon, Atomic layer deposition on suspended single-

walled carbon nanotubes via gas-phase noncovalent functionalization, *Nano Lett.*, 2006, **6**, 699-703.

[14] C. F. Herrmann, F. H. Fabreguette, D. S. Finch, R. Geiss, and S. M. George, Multilayer and functional coatings on carbon nanotubes using atomic layer deposition, *Appl. Phys. Lett.*, 2005, **87**, 123110.

[15] D. S. Kim, S. M. Lee, R. Scholz, M. Knez, U. Gösele, J. Fallert, H. Kalt, and M. Zacharias, Synthesis and optical properties of ZnO and carbon nanotube based coaxial heterostructures, *Appl. Phys. Lett.*, 2008, **93**, 103108.

[16] J. S. Lee, B. Min, K. Cho, S. Kim, J. Park, Y. T. Lee, N. S. Kim, M. S. Lee, S. O. Park, and J. T. Moon, Al₂O₃ nanotubes and nanorods fabricated by coating and filling carbon nanotubes with atomic-layer deposition, *J. Cryst. Growth*, 2003, **254**, 443-448.

[17] R. H. A. Ras, M. Kemell, J. de Wit, M. Ritala, G. ten Brinke, M. Leskelä, and O. Ikkala O, Hollow inorganic nanospheres and nanotubes with tunable wall thickness by atomic layer deposition on self-assembled polymeric templates, *Adv. Mater.*, 2007, **19**, 102-106.

[18] G. D. Zhan, X. Du, D. M. King, L. F. Hakim, X. Liang, J. A. McCormick, and A. W. Weimer, Atomic layer deposition on bulk quantities of surfactant-modified single-walled carbon nanotubes, *J. Am. Ceram. Soc.*, 2008, **91**, 831-835.

[19] M. Leskelä and M. Ritala, Atomic layer deposition chemistry: recent development and future challenges, *Angew. Chem. Int. Ed.*, 2003, **42**, 5548-5554.

[20] M. Ritala and M. Leskelä, Atomic layer epitaxy—a valuable tool for nanotechnology? *Nanotechnology*, 1999, **10**, 19-24.

[21] M. Aronniemi, J. Saino, and J. Lahtinen, Characterization and gas-sensing behavior of an iron oxide film prepared by atomic layer deposition, *Thin Solid Films*, 2008, **516**, 6110-6115.

[22] M. Lie, H. Fjellvag, and A. Kjekshus, Growth of Fe₂O₃ thin films by atomic layer deposition, *Thin Solid Films*, 2005, **488**, 74-81.

[23] O. Nilson, M. Lie, S. Foss, H. Fjellvag, and A. Kjekshus, Effect of magnetic field on the growth of α -Fe₂O₃ thin films by atomic layer deposition, *Appl. Surf. Sci.*, 2004, **227**, 40-47.

[24] M. Rooth, A. Johansson, K. Kukli, J. Aarik, M. Boman, and A. Hazrsta, Atomic

layer deposition of iron oxide thin films and nanotubes using ferrocene and oxygen as precursors, *Chem. Vap. Deposition*, 2008, **14**, 67-70.

[25] J. Bachmann, J. Jing, M. Knez, S. Barth, H. Shen, S. Mathur, U. Gösele, and K. Nielsch, Ordered iron oxide nanotube arrays of controlled geometry and tunable magnetism by atomic layer deposition, *J. Am. Chem. Soc.*, 2007, **129**, 9554-9555.

[26] M. Daub, J. Bachmann, J. Jing, M. Knez, U. Gösele, S. Barth, S. Mathur, J. Escrig, D. Altbir, and K. Nielsch, Ferromagnetic nanostructures by atomic layer deposition: from thin films towards core-shell nanotubes, *ECS Transactions*, 2007, **11**, 139-148.

[27] J. R. Scheffe, A. Francés, D. M. King, X. Liang, B. A. Branch, A. S. Cavanagh, S. M. George, and A. W. Weimer, Atomic layer deposition of iron (III) oxide on zirconia nanoparticles in a fluidized bed reactor using ferrocene and oxygen, *Thin Solid Films*, 2009, **517**, 1874-1879.

[28] H. Liu, D. Arato, R. Li, Y. Zhang, P. Merel, and X. Sun, Aligned multi-walled carbon nanotubes on different substrates by floating catalyst chemical vapor deposition: Critical effects of buffer layer, *Surf. Coating Tech.*, 2008, **202**, 4114-4120.

[29] Y. Zhong, M. Jaidann, Y. Zhang, G. Zhang, H. Liu, M. I. Ionescua, R. Li, X. Sun, H. Abou-Rachid, and L. S. Lussierb, Synthesis of high nitrogen doping of carbon nanotubes and modeling the stabilization of filled DAATO@CNTs (10,10) for nanoenergetic materials, *J. Phys. Chem. Solids*, 2010, **71**, 134-139.

[30] V. Datsyuk, M. Kalyva, K. Papagelis, J. Parthenios, D. Tasis, A. Siokou, I. Kallitsis, and C. Galiotis, Chemical oxidation of multiwalled carbon nanotubes, *Carbon*, 2008, **46**, 833-840.

[31] H. Hu, B. Zhao, M. E. Itkis, and R. C. Haddon, Nitric acid purification of single-walled carbon nanotubes, *J. Phys. Chem. B*, 2003, **107**, 13838-13842.

[32] T. J. Park, S. Banerjee, T. Hemraj-Benny, and S. S. Wong, Purification strategies and purity visualization techniques for single-walled carbon nanotubes, *J. Mater. Chem.*, 2006, **16**, 141-154.

[33] M. Pumera, B. Šmid, and K. Veltruská, Influence of nitric acid treatment of carbon nanotubes on their physico-chemical properties, *J. Nanosci. Nanotechnol.*, 2009, **9**, 2671-2676.

[34] Z. Wang, M. D. Shirley, S. T. Meikle, R. L. D. Whitby, and S. V. Mikhalovsky, The

surface acidity of acid oxidized multi-walled carbon nanotubes and the influence of in-situ generated fulvic acids on their stability in aqueous dispersions, *Carbon*, 2009, **47**, 73-79.

[35] W. Xia, Y. Wang, R. Bergsträber, S. Kundu, and M. Muhler, Surface characterization of oxygen-functionalized multi-walled carbon nanotubes by high-resolution X-ray photoelectron spectroscopy and temperature-programmed desorption, *Appl. Surf. Sci.*, 2007, **254**, 247-250.

[36] R. Yu, L. Chen, Q. Liu, J. Lin, K. L. Tan, S. C. Ng, H. S. O. Chan, G. Q. Xu, and T. S. Andy Hor, Platinum deposition on carbon nanotubes via chemical modification, *Chem. Mater.*, 1998, **10**, 718-722.

[37] J. Zhang, H. Zou, Q. Qing, Y. Yang, Q. Li, Z. Liu, X. Guo, and Z. Du, Effect of chemical oxidation on the structure of single-walled carbon nanotubes, *J. Phys. Chem. B*, 2003, **107**, 3712-3718.

[38] Z. B. Zhang, J. Li, A. L. Cabezas, and S. L. Zhang, Characterization of acid-treated carbon nanotube thin films by means of raman spectroscopy and field-effect response, *Chem. Phys. Lett.*, 2009, 476, 258-261.

[39] L. Huang, X. Cui, G. Dukovic, and S. P. O'Brien, Self-organizing high-density single-walled carbon nanotube arrays from surfactant suspensions, *Nanotechnology*, 2004, **15**, 1450-1454.

[40] M. F. Islam, E. Rojas, D. M. Bergey, A. T. Johnson, and A. G. Yodh, High weight fraction surfactant solubilization of single-wall carbon nanotubes in water, *Nano Lett.*, 2003, **3**, 269-273.

[41] R. Rastogi, R. Kaushal, S. K. Tripathi, A. L. Sharma, I. Kaur, and L. M. Bharadwaj, Comparative study of carbon nanotube dispersion using surfactants, *J. Colloid Interface Sci.*, 2008, **328**, 421-428.

[42] N. R. Tummala and A. Striolo, SDS surfactants on carbon nanotubes: aggregate morphology, *ACS Nano*, 2009, **3**, 595-602.

[43] M. L. Usrey and M. S. Strano, Controlling single-walled nanotubes surface adsorption with covalent and noncovalent functionalization, *J. Phys. Chem. C*, 2009, **113**, 12443-12453.

[44] E. J. Wanless and W. A. Ducker, Organization of sodium dodecyl sulfate at the

- graphite-solution interface, *J. Phys. Chem.*, 1996, **100**, 3207-3214.
- [45] M. Zhang, L. Su, and L. Mao, Surfactant functionalization of carbon nanotubes (CNTs) for layer-by-layer assembling of CNT multi-layer films and fabrication of gold nanoparticles/CNT nanohybrid, *Carbon*, 2006, **44**, 276-283.
- [46] K. Balasubramanian and M. Burghard, Chemically functionalized carbon nanotubes, *Small*, 2005, **1**, 180-192.
- [47] H. Hu, P. Bhowmik, B. Zhao, M. A. Hamon, M. E. Itkis, and R. C. Haddon, Determination of the acidic sites of purified single-walled carbon nanotubes by acid-base titration, *Chem. Phys. Lett.*, 2001, **345**, 25-28.
- [48] S.J. Kim, Y. J. Park, E. J. Ra, K. K. Kim, K. H. An, Y. H. Lee, J. Y. Choi, C. H. Park, S. K. Doo, M. H. Park, and C. W. Yang, Defect-induced loading of Pt nanoparticles on carbon nanotubes, *Appl. Phys. Lett.*, 2007, **90**, 023114.
- [49] C. P. Ewels and M. Glerup, Nitrogen doping in carbon nanotubes, *J. Nanosci. Nanotech.*, 2005, **5**, 1345-1363.
- [50] S. van Dommele, A. Romero-Izquierdo, R. Brydson, K. P. de Jong, and J. H. Bitter, Tuning nitrogen functionalities in catalytically grown nitrogen-containing carbon nanotubes, *Carbon*, 2008, **46**, 138-148.
- [51] S. H. Yang, W. H. Shin, J. W. Lee, H. S. Kim, J. K. Kang, and Y. K. Kim YK, Nitrogen-mediated fabrication of transition metal-carbon nanotube hybrid materials, *Appl. Phys. Lett.*, 2007, **90**, 013103.
- [52] S. H. Yang, W. H. Shin, and J. K. Kang, The nature of graphite- and pyridinelike nitrogen configuration in carbon nitride nanotubes: dependence on diameter and helicity, *Small*, 2008, **4**, 437-441.
- [53] S. Peng and K. Cho, Ab Initio study of doped carbon nanotube sensors, *Nano Lett.*, 2003, **3**, 513-517.
- [54] S. Stafström, Reactivity of curved and planar carbon-nitride structures, *Appl. Phys. Lett.*, 2000, **77**, 3941-3943.
- [55] Y. H. Li, T. H. Hung, and C. W. Chen, A first-principles study of nitrogen- and boron-assisted platinum adsorption on carbon nanotubes, *Carbon*, 2009, **47**, 850-855.
- [56] S. Sun, G. Zhang, Y. Zhong, H. Liu, R. Li, X. Zhou, and X. Sun, Ultrathin single crystal Pt nanowires grown on N-doped carbon nanotubes, *Chem. Commun.*, 2009, **45**,

7048-7050.

[57] X. Hu, Y. Wu, H. Li, and Z. Zhang, Adsorption and activation of O₂ on nitrogen-doped carbon nanotubes, *J. Phys. Chem. C*, 2010, **114**, 9603-9607.

[58] M. Leskelä and M. Ritala, Atomic layer epitaxy in deposition of various oxide and nitride, *Journal De Physique IV*, 1995, **C5**, 937-951.

[59] M. Ylilammi, Monolayer thickness in atomic layer deposition, *Thin Solid Films*, 1996, **279**, 124-130.

[60] Y. Chen, J. Wang, H. Liu, R. Li, X. Sun, S. Ye, and S. Knights, Enhanced stability of Pt electrocatalysts by nitrogen doping in CNTs for PEM fuel cells, *Electrochem. Commun.*, 2009, **11**, 2071-2076.

[61] J. Zhao, H. Park, J. Han, and J. P. Lu, Electronic properties of carbon nanotubes with covalent sidewall functionalization, *J. Phys. Chem. B*, 2004, **108**, 4227-4230.

[62] E. N. Nxumalo and N. J. Coville, Nitrogen doped carbon nanotubes from organometallic compounds: a review, *Materials*, 2010, **3**, 2141-2171.

CHAPTER 5

THREE GROWTH MODES AND MECHANISMS FOR HIGHLY STRUCTURE-TUNABLE SnO_2 NANOTUBE ARRAYS OF TEMPLATE-DIRECTED ATOMIC LAYER DEPOSITION

A version of this chapter has been published in *Journal of Materials Chemistry*, 2011, **21**, 12321-12330.

This article presents a vapor-phase strategy to synthesize highly structure-tunable SnO₂ nanotube arrays of high aspect ratio, which features atomic layer deposition of SnO₂ on anodic aluminum oxide templates using SnCl₄ and H₂O as precursors. This systematic study disclosed that there are three distinctive temperature-dependent growth modes, i.e., layer-by-layer, layer-by-particle, and evolutionary particles contributing to the structural uniqueness of the resultant SnO₂ nanotubes. The layers were identified in amorphous phase while the particles in crystalline phase. As a consequence, the synthesized SnO₂ nanotubes are not only phase-controllable but also morphology-transferable with growth temperatures. In a following effort to explore the underlying mechanisms, as another contribution of this study, three growth models were proposed and clarified. Thus, this study offers not just a precise alternative for synthesizing structurally novel nanotubes but scientific insights to fundamentals as well.

Keywords: *Growth Models, Mechanisms, Tunable structures, Nanotubes, Metal oxides, Tin dioxide, Templates, Atomic layer deposition*

5.1 Introduction

Nanostructured materials are nowadays providing modern societies with more and more promising solutions to our facing challenges, e.g., being serving as important components in alternative renewable energy sources in place of the depleting fossil fuels [1]. The main reason lies in their exceptional properties resulted from their size-dependency feature. Therefore, there is an ever-increasing interest in synthesizing various nanostructures. In this context, one dimensional (1D) nanostructures (including nanorods, nanobelts, nanowires, and nanotubes) represent one important class and have been receiving growing attention [2]. In comparison, nanotubes are benefited by their hollow structure as well as higher surface-to-volume ratios, and thereby exhibit many advantages over their solid counterparts in emerging applications. It is demonstrated that, for example, metal oxide nanotubes surpass other forms of nanomaterials including carbon nanotubes (CNTs) in sensing ability, photo catalytic activity, water photolysis efficiency, and photovoltaic behavior [3]. Thus, the development of novel nanotubular metal oxides is apparently critical for future nanodevices.

Among metal oxides, tin (IV) dioxide (SnO_2) is distinguished with a wide-band gap (3.6 eV at 300 K), high optical transparency, low resistance, and high conductivity [4]. As a consequence, SnO_2 nanostructures are found their usefulness in sensors [4,5], batteries [6], solar cells [7], and field emission [8], etc. Under these circumstances, 1D SnO_2 nanotubes have been widely synthesized via various strategies, mainly falling into two categories: solution-based [9-16] and vapor-phase [17-21] methods. Despite these efforts, the previous practices were exposed to some drawbacks as well. In the cases of solution-based processes [9-16], they consist of a series of complex procedures and are usually tedious, ranging from ten to several tens hours. In the cases of vapor-phase methods [17-21], they in general need high temperatures (with the lowest one reported at 800 °C [21]). Furthermore, the two still commonly suffer some apparent deficiency in precisely manipulating the synthesis of nanotubular SnO_2 , and they exclusively produced polycrystalline SnO_2 nanotubes.

To circumvent the disadvantages suffered in the aforementioned studies, we recently explored a new route to synthesize SnO₂ nanotubes, featuring the use of atomic layer deposition (ALD) on anodic aluminum oxide (AAO, i.e., Al₂O₃) templates. As is well known, ALD is surface-controlled process relying on two alternating gas-solid reactions. Thus, it can precisely control the film deposition at the atomic level and provide unrivaled conformality and excellent uniformity [22]. In this study, we performed the synthesis of SnO₂ nanotubes by exercising the ALD of SnO₂ (ALD-SnO₂) on AAO templates. This template-directed ALD process used SnCl₄ and water as precursors. It is apparent that the reaction between the two precursors would produce SnO₂, as described below:



In the ALD-SnO₂ processes, the sequential adsorption of the two kinds of precursor molecules (i.e., SnCl₄ and H₂O) on the inner surfaces of AAO pores resulted in the formation of tubular SnO₂ nanostructures, i.e., SnO₂ nanotubes in aligned arrays. Thus, this template-directed ALD route is advantageous over the ones [17-21] exposed in literature for the fabrication of SnO₂ nanotubes. First of all, the use of AAO templates helped produce nanotubes with aligned arrays of high aspect ratio (up to 300:1). More importantly, this strategy offers high tunability in manipulating the structures of as-synthesized SnO₂ nanotubes. As will be revealed, the ALD-SnO₂ on AAO contributed to the growth of SnO₂ nanotubes with three modes with increased temperatures, i.e., layer-by-layer, layer-by-particle, and evolutionary particles. The layers were identified in amorphous phase while the particles in crystalline phase. Thus, the resultant SnO₂ nanotubes are phase-controllable and morphology-transferable. In particular, the intriguing results ignited our great curiosity to explore the underlying mechanisms and then three growth models were proposed for their occurrences. Therefore, this study not only opened an alternative avenue for synthesizing novel SnO₂ nanotubes in a highly controllable manner, but also provided scientific insights to ALD growth. It is believed that the resultant SnO₂ nanotubes would provide multiple choices as promising components for many important applications.

5.2 Experimental

5.2.1 Template-directed ALD-SnO₂ for tubular nanostructures

ALD-SnO₂ was performed on AAO templates in a commercial ALD reactor (Savannah 100, Cambridge Nanotechnology Inc., USA). AAO templates (Whatman, Anodisc, 60 μm in thickness and 13 mm in diameter) with nominal pore size of 200 nm were first placed in the heated reactor chamber before each ALD process. Then, tin (IV) chloride (99% SnCl₄, Sigma-Aldrich) and deionized water as precursors were supplied into the reactor in an alternating manner when the reactor reached a set temperature. The temperatures (T) were adjusted in the range 150 - 400 °C. Nitrogen served as the carrier gas with a flow rate of 20 sccm and the ALD reactor was sustained at a low level of base pressure (typically 0.4 Torr) by a vacuum pump (Pascal 2005 I, Adixon). The ALD procedures were set as follows: (1) a 0.5-s supply of SnCl₄; (2) a 3.0-s extended exposure of SnCl₄ to AAO; (3) a 10.0-s purge of oversupplied SnCl₄ and any by-products; (4) a 1.0-s supply of H₂O vapor; (5) a 3.0 s extended exposure of H₂O to AAO; (6) a 10.0-s purge of oversupplied H₂O and any by-products. The aforementioned six-step sequence constituted one ALD-SnO₂ cycle and the ALD processes were changeable in their cycling numbers.

In [figure 5.1](#), the fulfillment of the template-directed ALD strategy is schematically illustrated for the fabrication of SnO₂ nanotube arrays. [Figure 5.1\(a\)](#) shows the ALD-SnO₂ coating on an AAO template, in which the SnCl₄ (A) and water (B) pulse proceeded alternatively. When the precursor molecules were penetrating AAO pores, they would chemisorb on the inner surfaces. With increased ALD-cycles, a SnO₂ covering formed on the inner walls of the nanosized pores as well as the outer surface of the AAO template (see [figure 5.1\(b\)](#)). As will be disclosed in this article, the covering characters changed with the ALD cycling numbers as well as growth temperatures. The outer covering of AAO was removed mechanically by fine sandpapers and then an array of SnO₂ nanotubes (see [figure 5.1\(c\)](#)) was exposed. A following 30-min etching of 0.5 M sodium hydroxide (NaOH) dissolved AAO and uncovered an array of separated SnO₂ nanotubes (see [figure](#)

5.1(d)). In the figure 5.1(a)-(c), the cross sections of a few of AAO pores are to better illustrate the change induced by the ALD coating.

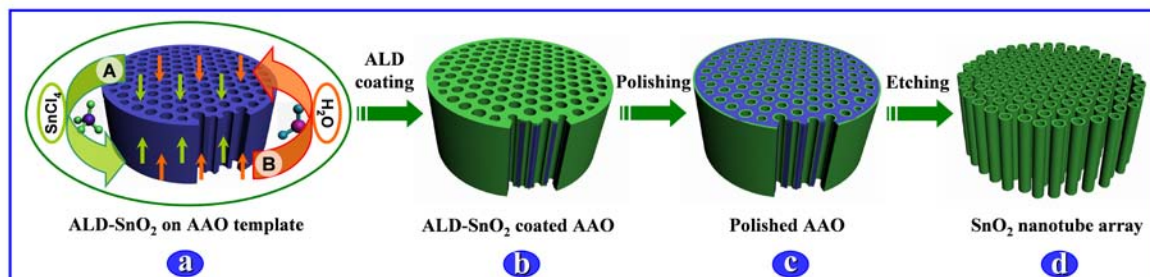


Figure 5.1. Schematic fabrication of SnO₂ nanotubes via template-directed ALD. (a) the ALD-SnO₂ coating on an AAO template, (b) the ALD-coated AAO template, (c) the mechanically polished AAO template, and (d) the received SnO₂ nanotube array.

5.2.2 Characterization

The synthesized SnO₂ nanotubes were characterized using a field-emission scanning electron microscope (FE-SEM, Hitachi 4800S) equipped with energy dispersive X-ray spectroscopy (EDS), transmission electron microscope (TEM, Philips CM10), high-resolution TEM (HRTEM, JEOL 2010 FEG), and micro X-ray diffractometer (XRD, Bruker D8, CuK α radiation, $\lambda = 1.5406 \text{ \AA}$).

5.3 Results and Discussion

5.3.1 Results

Figure 5.2 shows the XRD patterns of 1000-cycle ALD-SnO₂ on AAO at different temperatures, i.e., 150, 200, 300, and 400 °C as indicated by “a”, “b”, “c”, and “d”, respectively. Figure 5.2(a) discloses that there are no characteristic peaks at the growth

temperature of 150 °C, implying the amorphous nature of the deposited SnO₂. In contrast, figure 5.2(b)-(d) show many characteristic peaks when the growth temperatures are higher than 200 °C, consistent to the reference values for the crystalline SnO₂ of tetragonal rutile phase (JCPDS PDF No. 41-1445). In addition, it is also noticeable that the peaks in figure 5.2(b) are much broader and less intensive than the ones in both figure 5.2(c) and (d), indicating that the crystals produced at 200 °C should be much smaller. It is apparent that the temperatures played important roles and induced phase-transition in ALD-SnO₂ processes. To further investigate the temperature-dependent characters of ALD-SnO₂ as well as the resultant SnO₂ nanotubes, we applied various tools such as EDS, SEM, and HRTEM, and the results will be demonstrated in the following parts.

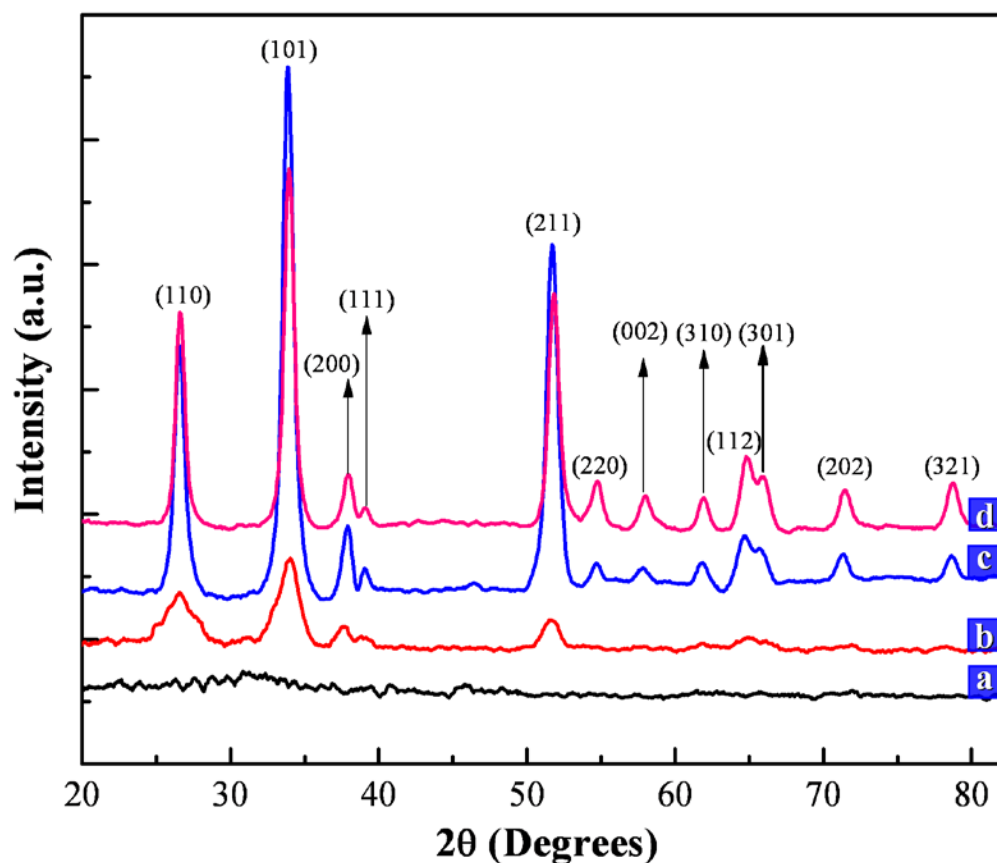


Figure 5.2. XRD spectra of 1000-cycle ALD-SnO₂ at different growth temperatures: (a) 150, (b) 200, (c) 300, and (d) 400 °C.

The growth characteristics of the ALD-SnO₂ were first examined at the temperature of 150 °C, as shown figure 5.3. Figure 5.3(a) shows the EDS spectrum of the ALD-SnO₂ coated AAO, and it demonstrates the presence of Sn. The Al component is attributed to AAO whereas O is partially from AAO and partially from the ALD-SnO₂. Combined with the XRD pattern of figure 5.2(a), it is reasonable to conclude that amorphous SnO₂

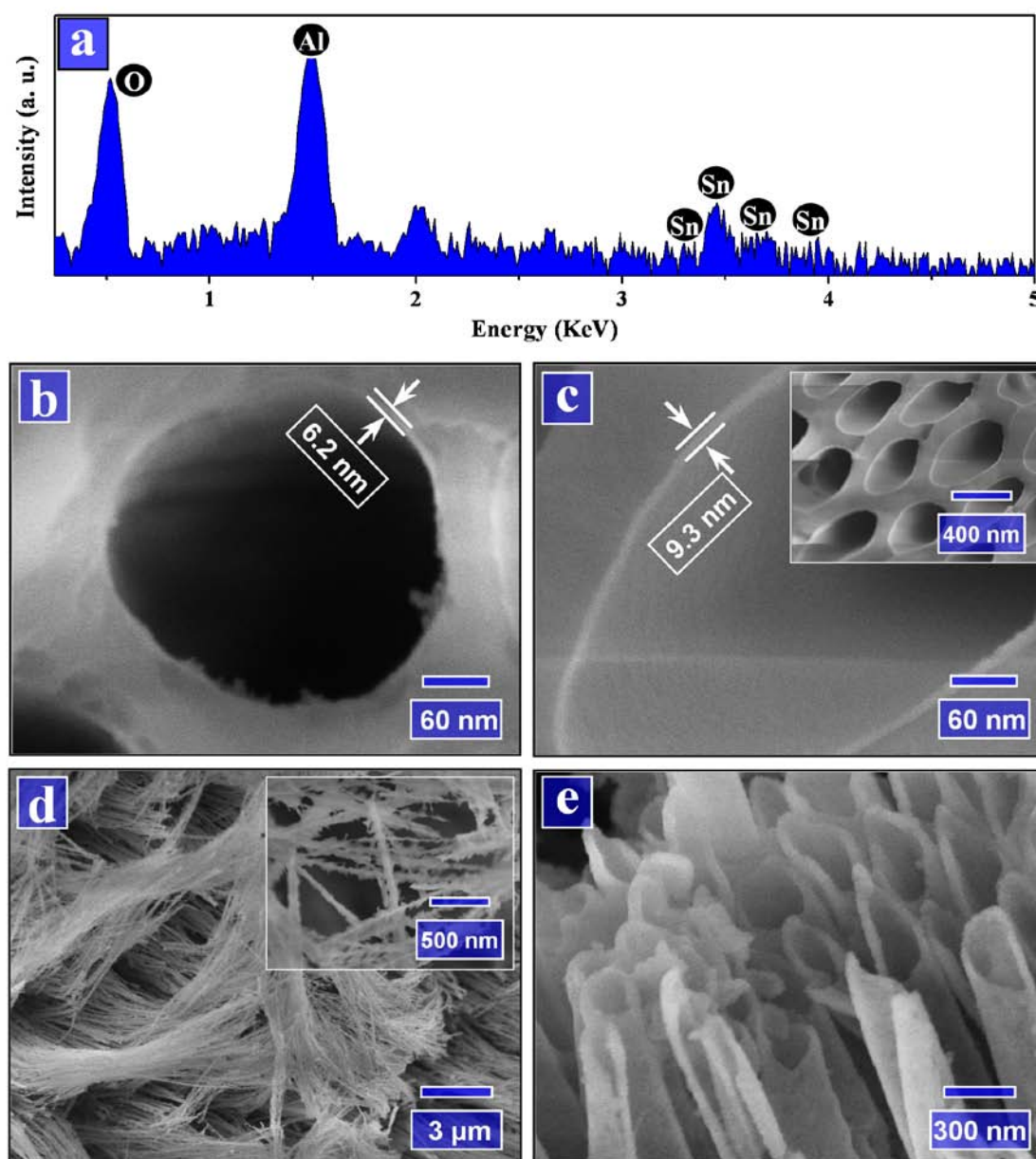


Figure 5.3. The growth characteristics of ALD-SnO₂ at 150 °C. (a) EDS spectrum of the ALD-SnO₂ on AAO; top views of AAO after (b) 1000 and (c) 1500 cycles of ALD-SnO₂; the template-removed SnO₂ in the forms of (d) clusters and (e) nanotubes corresponding to 1000 and 1500 cycles, respectively.

has been deposited on AAO. To obtain the information on the ALD-SnO₂ of the AAO pores, the top views (the SEM images in [figure 5.3\(b\)](#) and [\(c\)](#)) on the polished AAO disclose that a uniform layer has been formed on their inner walls after 1000 and 1500 cycles, accounting for a deposited film of 6.2 and 9.3 nm, respectively. Thus, it is able to know that the ALD-SnO₂ at 150 °C experienced a nearly linear growth rate of 0.062 Å/cycle, accounting for a layer-by-layer growth mode. In addition, [figure 5.3\(c\)](#) clearly shows that the inner surface is very smooth and that the AAO pores were equally coated (the [inset](#) of [figure 5.3\(c\)](#)). To obtain free-standing SnO₂ nanotubes, AAO templates were etched by a 0.5 M NaOH solution. It was found that, in the case of 1000 cycles ([figure 5.3\(d\)](#) and [inset](#)), the nanotubes are easy to split during the etching process. As a result, the resultant pieces leaned against and formed well regulated clusters. A similar phenomenon is previously reported in literature [10]. In the case of 1500 cycles ([figure 5.3\(e\)](#)), SnO₂ nanotubes were achieved, probably due to the improved strength with the increased wall thickness. However, it is noticed that the walls of the SnO₂ nanotubes ([figure 5.3\(e\)](#)) become thickened to around 30 nm. The reason probably lies in their amorphous nature vulnerable to the NaOH solution, leading to a swelling change during the etching process of AAO.

XRD patterns in [figure 5.2\(b\) - \(d\)](#) indicate that phase-transition occurred in ALD-SnO₂ processes when temperatures were increased to 200 °C or higher. To investigate the temperature-dependent effects, the ALD-SnO₂ at 200 °C was examined, as illustrated in [figure 5.4](#). [Figure 5.4\(a\)](#) shows the side-view images to the cross-sections of AAO pores after 500, 1000, and 1500 cycles of ALD-SnO₂. The cycling numbers are indicated on the left-bottom corners of the three images. Obviously, in each case there is a uniform layer deposited in AAO pores and the thickness is identifiable, i.e., 7.0, 8.9, and 9.8 nm as marked in the images. In addition, it is worth noting that there are more and more clusters formed on the top of the layers, consisting of numerous nanoparticles of around 5 nm. In particular, the layers show a decreasing growth per cycle (GPC) while the clusters grow bigger, accounting for 0.14, 0.038, and 0.018 Å/cycle in each sequential 500 cycles. In [figure 5.4\(b\)](#), it is shown that the deposited SnO₂ can produce nanotube arrays when AAO was etched away. Furthermore, [figure 5.4\(c\)](#) shows the TEM image of a piece of

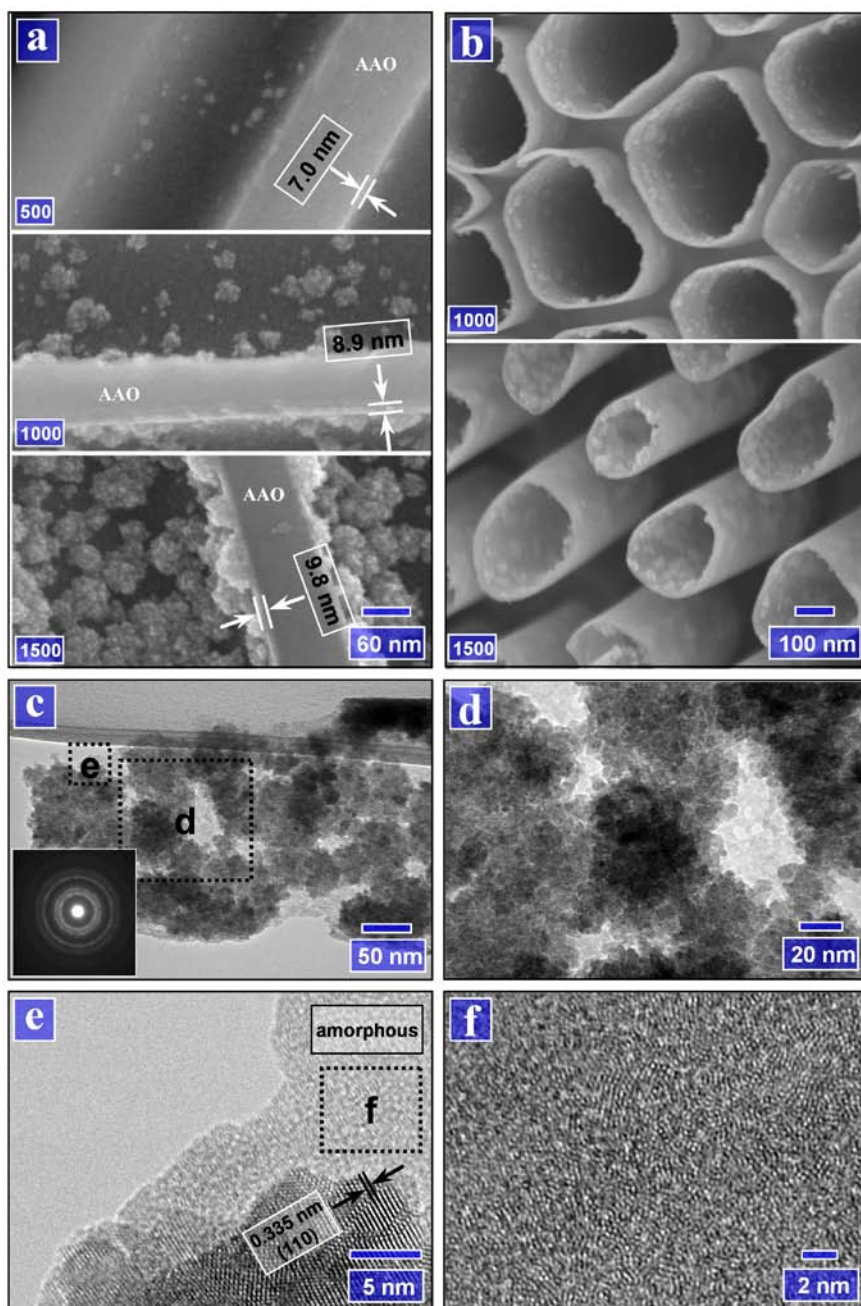


Figure 5.4. The growth characteristics of ALD-SnO₂ at 200 °C. (a) SEM side views of AAO pores after 500, 1000, and 1500 cycles of ALD-SnO₂; (b) the received nanotube arrays of ALD-SnO₂ of 1000 and 1500 cycles after AAO templates were etched away; (c) TEM image for a piece of debris of the deposited SnO₂ after 1500-cycle ALD-SnO₂ (inset: SAED patterns); (d) high-magnification TEM image for a local area as indicated in (c); (e) HRTEM image for a local area as indicated in (c); and (f) HRTEM image for a local area of the beneath layer as indicated in (e).

debris for the deposited materials of 1500 cycles, and the selected area electron diffraction (SAED, the inset of figure 5.4(c)) patterns disclose the polycrystalline character. A higher magnification TEM image (figure 5.4(d)) on a local area (as marked by “d” in figure 5.4(c)) confirms that the clusters consist of numerous nanoparticles of around 5 nm, consistent to the wide XRD peaks of figure 5.2(b). Figure 5.4(e) reveals the HRTEM observation on another local area in figure 5.4(c), consisting of a part of beneath layer and a part of a cluster. It reveals that the beneath layer by nature is amorphous while the cluster is crystalline in structure. As denoted in figure 5.4(e), the inter-plane spacing of 0.335 nm is identifiable for some nanoparticles, which is consistent to the (110) planes of rutile SnO₂ (JCPDS PDF No. 41-1445). Furthermore, the amorphous area was further examined with higher magnification, as shown in figure 5.4(f). It is disclosed that the beneath layer is arranged in a disordered manner, but there are uncountable tiny nuclei of 1 - 2 nm formed. Obviously, the ALD-SnO₂ at 200 °C proceeded in a layer-by-cluster (or particle) growth mode, in which the growth of the amorphous layer is preferable before the clusters takes predominance. In comparison to the case of ALD-SnO₂ at 150 °C, the layer growth at 200 °C is much faster in the first 500 cycles (figure 5.4(a)) but hindered by the increasing advent of nanoparticle clusters in the following ALD processes.

Figure 5.5 illustrates the ALD-SnO₂ growth characteristics due to the increased temperature of 300 °C. Figure 5.5(a) shows five SEM images of the side views of AAO pores, corresponding to the ALD-SnO₂ of 200, 400, 600, 800, and 1000 cycles in a sequence from top to bottom, respectively. The cycling number is indicated on the left-bottom corner of each image as well. It is obvious that there were more and more nanoparticles deposited in the pores while they were growing larger from 15 to 40 nm with increased cycles. In addition, it is also observable from the images that there is also a thin layer underneath the particles (see also figure SI-5.1 in Supporting Information). Upon 1000 cycles, it is noticeable that the growing particles have squished into each other and completely covered the inner walls. In figure 5.5(b), it is shown that the ALD-SnO₂ formed a series of nanotubes. The nanotubes are featured by smooth outer surfaces and nanoparticle-decorated inner surfaces. In particular, the nanoparticles are tunable in both size and amount by simply adjusting ALD cycles. It is also noticed that the beneath

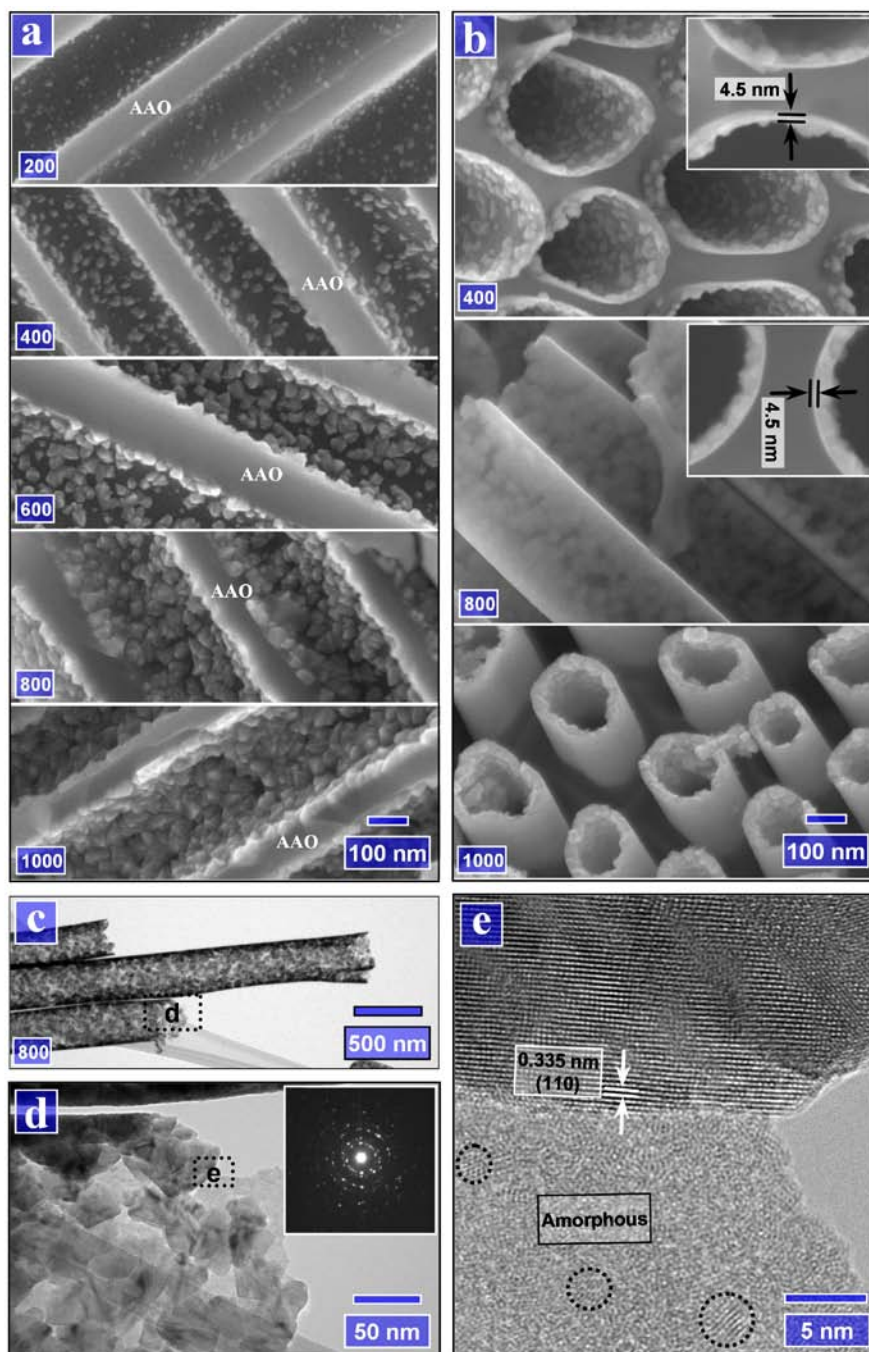


Figure 5.5 The growth characteristics of ALD-SnO₂ at 300 °C. (a) SEM side views of AAO pores coated with the ALD-SnO₂ of 200, 400, 600, 800, and 1000 cycles (as marked on the left-bottom corner of each case); (b) SEM images for the received SnO₂ nanotubes after 400, 800, and 1000 ALD-cycles (insets: top-views on ALD-SnO₂ of 400 and 800 cycles); (c) the TEM image for the SnO₂ nanotubes of 800 ALD-cycles; (d) the high magnification TEM image for a part of a SnO₂ nanotube in (c) (inset: SAED patterns); (e) the HRTEM image for a local area in (d).

layer is uniform with a thickness of 4.5 nm after 200 ALD-cycles and the thickness remains constant in the following ALD processes (see the insets in figure 5.5(b) as well as figure SI-5.1 in Supporting Information). In figure 5.5(c), the received SnO₂ nanotubes of 800 ALD-cycles are shown by a TEM image and one local area is enlarged in figure 5.5(d). The inset of figure 5.5(d) indicates the polycrystalline nature of the nanotubes by SAED patterns. Furthermore, figure 5.5(e) discloses that the particles are crystalline while the beneath layer is amorphous. In particular, the characteristic planes of (110) are observed with some nanoparticles, showing an inter-plane distance of 0.335 nm. In addition, it is also observed that there are numerous tiny nuclei (as circled for some in figure 5.5(e)) appearing on the amorphous layer, accounting for the increased amount of crystalline particles with increased cycles. Thus, the ALD-SnO₂ at 300 °C also experienced a layer-by-particle growth mode, in which the amorphous layer grew first before the growth of the crystalline nanoparticles took the predominance. Apparently, the deposited crystalline SnO₂ nanoparticles are responsible for the XRD peaks of figure 5.2(c).

Obviously, the information from figure 5.4 and 5.5 jointly disclosed a layer-by-particle growth mode, where the layers are amorphous and the particles are crystalline. This novel growth mode prompted our further investigation on the effects of temperatures. As a consequence, it was also found that the layer-by-particle growth still occurred at the temperatures of 250 and 350 °C. The results for the two cases are included in figure SI-5.2 and SI-5.3 in Supporting Information, respectively. It was observed that there is an amorphous layer of 6.2 nm for ALD-SnO₂ at 250 °C, but at the case of 350 °C the layer is too thin to quantify (in spite of its observable existence). In addition, it can also be observed that crystalline particles appear much earlier and grow faster with increased temperatures, accounting for an average GPC of 0.24 and 0.3 Å/cycle for 300 and 350 °C, respectively. Thus, it is reasonable to conclude that temperatures have evident effects on the evolution of the layer-by-particle mode. In other words, the higher the temperature is, the thinner the amorphous layer can develop but the faster the crystalline particles can grow. This was also confirmed by XRD patterns of 200-cycle ALD-SnO₂ at different temperatures (see figure SI-5.4 in Supporting Information). There are no peaks observed

for the cases of 200 and 250 °C, but peaks begin to appear at 300 °C and then become stronger and easier for identification in the cases of 350 and 400 °C. Thus, temperatures are essential for adjusting the double-layered amorphous-crystalline SnO₂ nanotubes. In return, various double-layered SnO₂ nanotubes were developed, featuring adjustable amorphous layers and crystalline particles, as shown in [figure 5.4](#) and [5.5](#), as well as in [figure SI-5.1](#) to [5.3](#).

As the temperature was increased up to 400 °C, however, the growth of ALD-SnO₂ exhibited some new characteristics, as illustrated in [figure 5.6](#). [Figure 5.6\(a\)](#) shows four SEM images of the side views of AAO pores, corresponding to the ALD-SnO₂ of 400, 600, 800, and 1000 cycles, respectively. The cycling number is indicated on the left-bottom corner of each image. It is clearly shown in [figure 5.6\(a\)](#) that the ALD-SnO₂ deposited only nanoparticles on the inner walls of AAO pores and that there is a sharp boundary between the nanoparticles and the inner surfaces. In other words, the beneath amorphous layers as observed in the range 200 to 350 °C is unobservable at the case of 400 °C. In addition, it is noticed from [figure 5.6\(a\)](#) that nanoparticles stopped lateral growth but continue their growth upwards along radial orientations after 600 ALD-cycles. Correspondingly, [figure 5.6\(b\)](#) shows the received SnO₂ nanotubes after different cycles. It is found that the as-deposited nanotubes of 400 ALD-cycles are evidently porous and the porosity decreases with increased cycles. In the case of 1000 ALD-cycles, the arrays of dense SnO₂ nanotubes are produced with an average GPC of 0.46 Å/cycle. Obviously, the fabrication of the nanotubes at 400 °C seems a sintering process of separate nanoparticles, in which the growing nanoparticles squished each other and thereby formed nanotubes. A few of 600-cycle nanotubes were further examined with TEM, as shown in [figure 5.6\(c\)](#), and one end of a nanotube is enlarged in [figure 5.6\(d\)](#). The inset of [figure 5.6\(d\)](#) exposes the polycrystalline nature of the nanotubes by the SEAD patterns. In addition, two local areas in [figure 5.6\(d\)](#) were examined with HRTEM and both commonly disclose the crystalline characteristics of nanoparticles in [figure 5.6\(e\)](#) and [\(f\)](#). [Figure 5.6\(e\)](#) shows the characteristic planes of (110) with the inter-plane distance of 0.335 nm while [figure 5.6\(f\)](#) reveals the characteristic planes of (101) with the inter-plane distance of 0.264 nm. Obviously, the ALD-SnO₂ at 400 °C is distinguishable with a

growth mode of evolutionary particles.

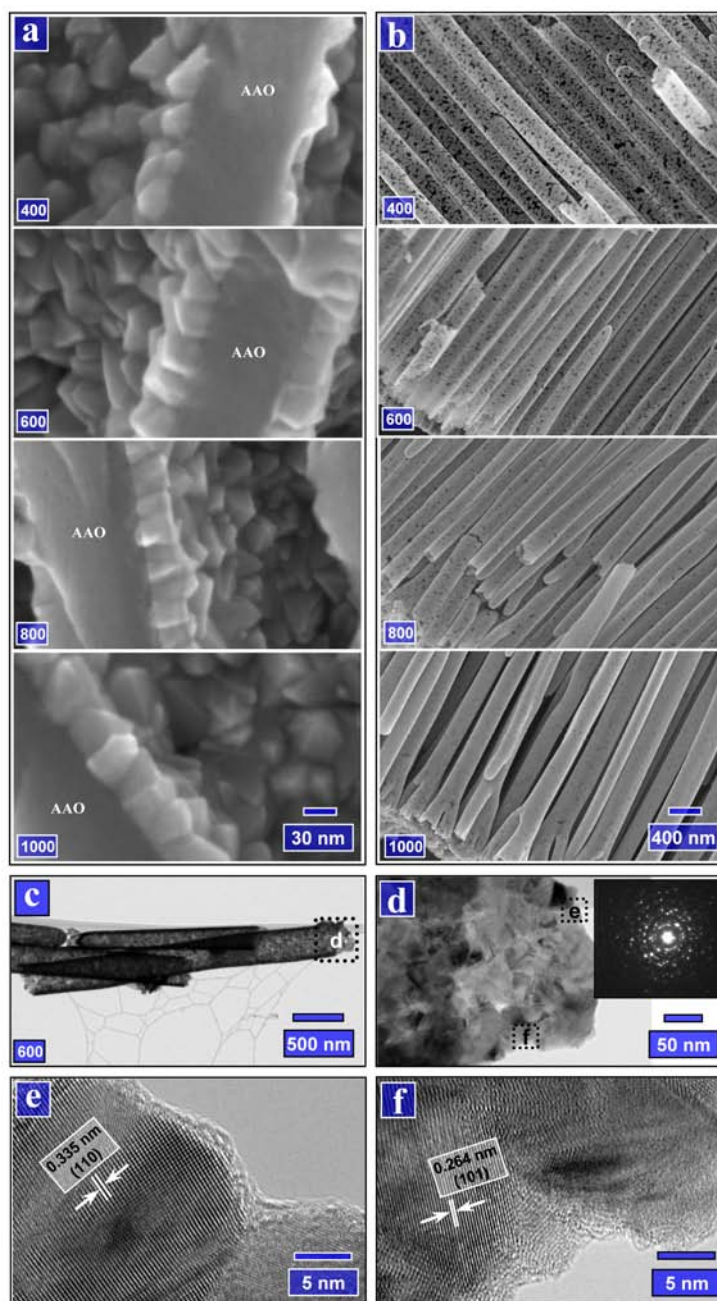


Figure 5.6 The growth characteristics of ALD-SnO₂ at 400 °C. (a) SEM side views of AAO pores coated with the ALD-SnO₂ of 400, 600, 800, and 1000 cycles (as marked on the left-bottom corner of each case); (b) SEM images for the received SnO₂ nanotubes after 400, 600, 800, and 1000 ALD-cycles; (c) the TEM image for the SnO₂ nanotubes of 600 ALD-cycles; (d) the high magnification TEM image for one end of a SnO₂ nanotube in (c) (inset: SAED patterns); (e) and (f) the HRTEM images for two local areas in (d).

Based on the above-disclosed results, it is remarkable that the synthesis of SnO₂ nanotube arrays by the template-directed ALD revealed three temperature-dependent growth modes, i.e., layer-by-layer ($T < 200$ °C), layer-by-particle ($200 \leq T < 400$ °C), and evolutionary particles ($T \geq 400$ °C), in which the layers are exclusively amorphous while the particles are commonly crystalline. In addition, it is also very apparent that the resultant nanotubes are highly structure-tunable with controllable phases and transferable morphologies. Thus, it is of great interest to explore the underlying mechanisms, especially the effects of temperatures for the intriguing results in order to gain a better understanding. On these interesting results, we will make a detailed discussion in the following sections.

5.3.2 Discussion

5.3.2.1 Effects of temperatures

In general, there are typically three key parameters in ALD processes, i.e., precursors, substrates, and temperatures [23]. The three parameters combine to determine the growth characteristics of a certain material. Of the exposed precursors to date, metal chlorides and water are among the widely used pairs in ALD practice for depositing binary metal oxides. In ALD processes, substrates play two main roles: one is to shape the deposited materials in a certain form (e.g., 0D, 1D, or 2D structures [24]) and another is to initiate the deposition on their surface. A prerequisite for the latter role is that the surface of a substrate should be with reactive sites in order to chemisorb the molecules of one precursor and thereby to initiate an ALD process for a certain material. In return, the peculiarities of a substrate (e.g., their structural characters as well as surface conditions) exert some influence on the growth characteristics as well as the properties of the resultant materials. However, the knowledge in this way is still very limited. With reference to temperatures, ALD requires that they should not be so high that precursors decompose, for any decomposition leads to a CVD process other than an ALD process. Even for the temperatures in the range suitable for an ALD process, it was observed that they may still result in some difference in the growth of a certain material, such as on GPC and the properties of that material [23]. Thus, growth temperatures are critical for an

ALD process when its precursors and substrate are determined.

In this study, we used SnCl_4 and water as the precursors for the ALD- SnO_2 on AAO in order to produce nanotube arrays. Earlier studies [25-29] mainly employed them on flat substrates (e.g., glass, silicon, and α -alumina) to deposit 2D thin films. Although the researchers noticed to some extent the occurrence of phase-transition with increased temperatures, the underlying mechanisms were hardly touched. It was demonstrated [29] that SnCl_4 and water are stable under the temperatures up to 600 °C. Thus, the temperatures of 150 – 400 °C in this study met the requirements of ALD processes. In particular, as revealed above, the characters of the as-synthesized nanotubes show an evident dependence on their growth temperatures in this study. Thus, it is of our great curiosity to explore the effects of temperatures as well as the underlying mechanisms. Based on reviewing earlier studies, we noticed that increased temperatures might have taken effect on the other two parameters, i.e., AAO and the precursors, and thereby result in different growth behaviors, consequently leading to the highly structure-tunable nanotubes. Thus, the effects of increased temperatures deserve a special discussion, as detailed below.

(A) On AAO template

As stated above, the surface nature of a substrate is crucial for ALD processes and it should be reactive to at least one precursor. In this study, the amorphous AAO template was used as the substrate for synthesizing SnO_2 nanotubes. Thus, its surface, especially the characters and coverage of reactive sites on the inner surfaces of AAO pores, is critical for the initiation and the subsequent growth of ALD- SnO_2 . Previous studies revealed that, no matter whatever the fabrication method was, AAO is commonly covered by hydroxyl groups as well as water molecules [30-32]. There are many types of hydroxyl groups identified, such as isolated and hydrogen-bonded ones [30,33-38]. Correspondingly, it was also experimentally [30,33-35] and theoretically [36-38] demonstrated that all types of hydroxyl groups as well as oxygen bridges are among the candidate groups to react with metal chlorides. In addition, a recent study showed that

water coverage of a surface also has important influence on surface reactions in ALD processes [38].

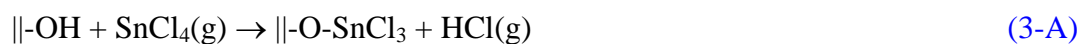
With increased temperatures, it was observed that the substrate surface generally experiences some change. It was previously demonstrated that, for example, the hydrogen-bonded hydroxyl groups and water coverage decrease in amount with increased temperatures, resulting in the isolated hydroxyl groups available as principal bonding sites [30,32,33,35,38]. A mechanism for the decrease of hydrogen-bonded hydroxyl groups is the dehydroxylation of adjacent hydroxyl groups [39]:



where the symbol || denotes the substrate surface and (g) refers to gas phase species. As a consequence, this dehydroxylation causes the appearance of oxygen bridges on the surface while it reduces the number of hydroxyl groups. Thus, increased temperatures tend to change the functional groups (either types or amounts, or the both) on the substrate surface.

(B) On surface reactions

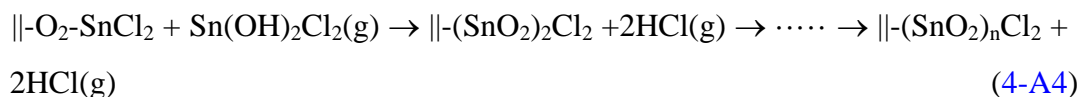
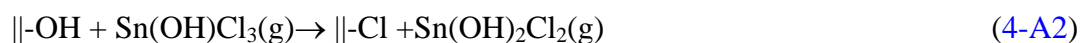
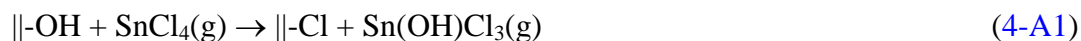
Besides the influences on the surface conditions of AAO templates, increased temperatures are also inclined to affect ALD processes as well. As is well-known, as a surface-controlled process, ALD proceeds via two alternating self-saturating surface reactions and each precursor induces a half-reaction. Thus, increased temperatures can take effect on the precursors by changing their corresponding surface reactions and thereby result in different growth characteristics. In the case of the ALD-SnO₂, there are two surface reactions suggested previously [40]:



The half-reaction (reaction 3-A) due to a pulse of SnCl₄ and the half-reaction (reaction 3-B) due to a pulse of H₂O consist of one typical “A-B” cycle to deposit SnO₂ in the ALD-SnO₂ process. As a result, the “A-B” cycling builds up SnO₂ films in AAO pores. Apparently, this surface chemistry is applicable to explain the growth of the amorphous

layers in [figure 5.3-5.5](#). However, it is evidently incompetent to address the growth of the nanoparticles (clusters) in [figure 5.4-5.6](#), for it betrayed the layer-by-layer nature of ALD processes. Thus, increased temperatures might have changed one or both of the aforementioned surface reactions in the [reaction 3-A](#) and [3-B](#), and thereby led to other mechanisms. To address this issue, other researchers conducted lots of inspiring work, though the answer was not fixed to date due to its complication.

The growth of crystalline particles, in addition to the cases discussed in this study, was also observed in the ALD processes of TiO_2 [41] and ZrO_2 [33] when growth temperatures are higher than $300\text{ }^\circ\text{C}$. In particular, the aforementioned studies commonly used metal chlorides and water as precursors. Many experimental efforts [30,34,35] were dedicated to investigate the behind stories and proposed various mechanisms. Unfortunately, none of the mechanisms could account for the experimental observations of crystalline particle formation. Also unsuccessful was the efforts from simulations [36-38]. This kind of phenomena is so intriguing that Puurunen [42] made a special review attempted to provide a comprehensive explanation. Based on the examinations on earlier studies, Puurunen claimed that ligand exchange (as shown in [reaction 3-A](#) and [3-B](#)) is the most prevalent mechanism for amorphization at low temperature ($< 300\text{ }^\circ\text{C}$) whereas a prominent two-step chlorination in the pulses of metal chlorides underlies the growth of crystallize particles at high temperature ($> 300\text{ }^\circ\text{C}$). In particular, the two mechanisms compete for dominance with temperatures. Thus, there are two different rules for ALD processes of using metal chlorides and water as precursors, and their predominance is determined by temperatures. Thanks to Puurunen's contributions, it becomes possible to explicate the growth of crystalline particles and amorphous layers. In the case of ALD- SnO_2 of using SnCl_4 and water, the following reactions might be induced in the pulses of SnCl_4 when temperatures were increased [43,44]:



In the above reactions, SnCl₄ first chlorinates the surface hydroxyl groups and form an intermediate hydroxychloride molecule (Sn(OH)₂Cl₂) by two steps, as shown in the [reaction 4-A1 and 4-A2](#). Then the hydroxychloride reacts with the surface chlorine groups through its hydroxyl groups, as shown in the [reaction 4-A3](#). In particular, the chlorine groups on the right side of the former [reaction 4-A3](#) might further react with hydroxychloride and result in a chain of reactions, as shown in the [reaction 4-A4](#). Thus, surface reactions in the pulses of SnCl₄ could contribute a formation of multilayer under high temperatures. As a consequence, nanoparticles could grow more quickly at high temperatures than at low temperatures after a same number of ALD cycles, for high temperatures should be more favorable for the [reaction 4-A4](#). This is consistent to our results, as disclosed in [figure 5.4-5.6](#) as well as in [figure SI-5.1 to 5.3](#) in [Supporting Information](#). In addition, the above reactions also provide the answers for the size-varied nanoparticles and the continuously newly-appeared nanoparticles on the inner surfaces of AAO pores, for some sites might be involved in a chain of reactions (as shown in the [reaction 4-A4](#)) while others might not. With reference to the reaction happened in the pulses of water, it was suggested [42] to be still ligand exchange, as shown in the following reaction 4-B:



To summarize the above discussion, it is clear that there are two different mechanisms for the growth of amorphous layers and crystalline particles. In particular, the two compete for dominance with increased temperatures. Previous studies [30,33-35,41] observed the particle growth when the temperature is higher than 300 °C. However, as clearly demonstrated in this study, crystalline particles appeared to grow when the temperatures reached 200 °C or higher. This is likely due to lower cycles studied by previous studies, for they mainly worked on the first several cycles. As a whole, the three growth modes appeared in our work provide evidence for the two mechanisms.

Obviously, the above discussion is exclusively based on hydroxyl groups. As stated before, increased temperatures may reduce hydrogen-bonded hydroxyl groups and induce more oxygen bridges. Thus, it is necessary to address their effects on ALD-SnO₂. In

contrast to a general acceptance on the roles of hydroxyl groups, there is a debate on the effects of oxygen bridges, as detailed by Puurunen [42]. Some earlier studies [33,41] suggested that metal chlorides can attack oxygen bridges via dissociation. However, some later studies [34,35] questioned its validity and Puurunen [42] even excluded the possibility for oxygen bridges to participate the growth of crystalline particles. Recent simulations [36-38] suggested that oxygen bridges are possible to react with metal precursors. However, their reaction rates are much lower than the ones for hydroxyl groups [37] while their adsorption energy and reaction opportunity highly depend on water coverage [38]. Remarkably, the issue on oxygen bridges is far from giving a clearly defined answer in this work and it deserves a further investigation in future. Even so, we would still suggest the reaction between SnCl₄ and oxygen bridges as follows, based on previous studies [33,36-39,41]:



Apparently, the above reaction chlorinates oxygen bridges via a cleavage. In a following interaction between water and the produced chlorine groups, the resultant reactions are still via ligand exchange [36-38], similar to the ones stated in the reaction 3-B or 4-B, and they create new hydroxyl groups. Thus, oxygen bridges may contribute to the growth of crystalline particles with increasing ALD cycles at elevated temperatures as well, for the created hydroxyl groups can also initiate reactions as stated in the reactions 4-A1 to 4-A4.

5.3.2.2 Three growth models

In the above section, it was discussed that temperatures could influence the growth of ALD-SnO₂ by changing the surface nature of AAO as well as surface reactions of ALD processes. In terms of surface chemistry, it is disclosed that there are different mechanism for the growth of amorphous layers and crystalline particles, which can well explain our results. Based on the afore-discussion and in order to better illustrate the three growth modes revealed in our study, we schematically demonstrate them with three models in figure 5.7.

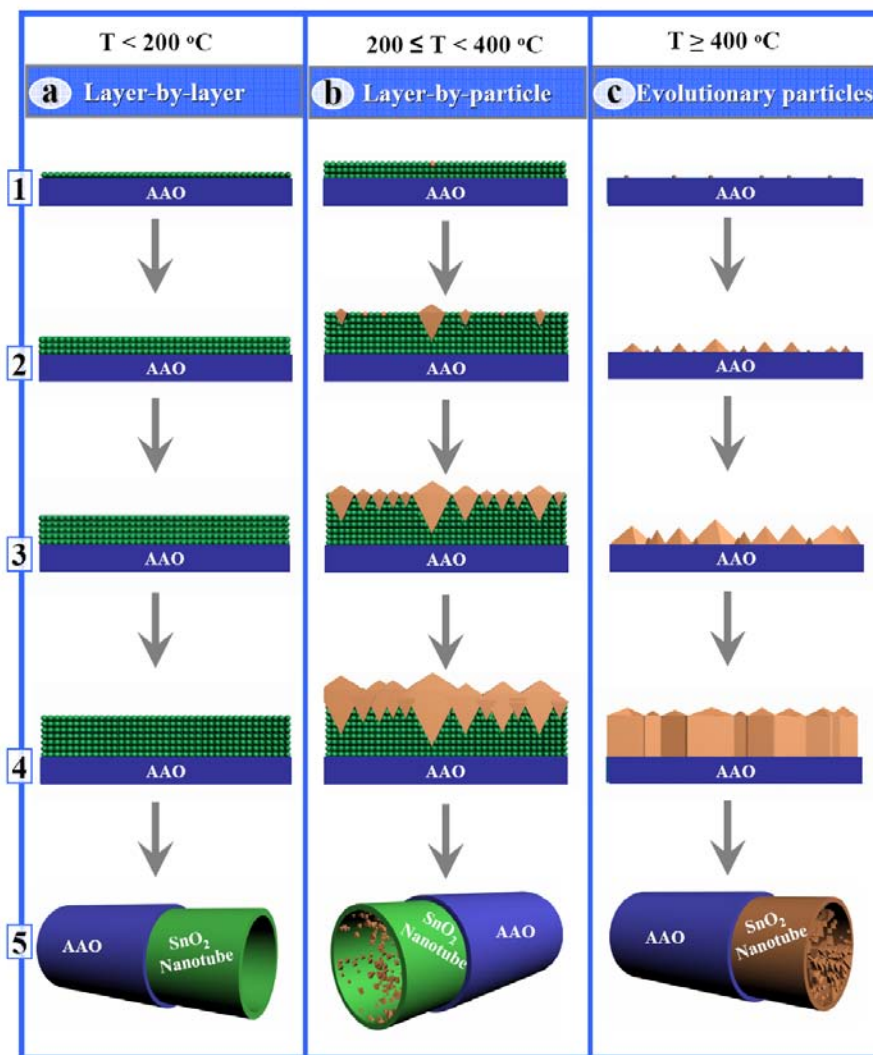


Figure 5.7 Three growth models for ALD-SnO₂ nanotube arrays. At a temperature lower than 200 °C, the ALD-SnO₂ was built up in AAO pores in a mode of **(a)** layer-by-layer growth, as schematically shown in **(a1-4)** with uniform films of increasing thickness; in the range 200-400 °C, the ALD-SnO₂ experienced a mode of **(b)** layer-by-particle growth: **(b1)** amorphous layers prevailed at the initial stage but random nucleation happened with increased films, **(b2)** crystals grew laterally and radially while new nuclei appeared with increased films, **(b3)** crystals saturated on the surface and amorphous layers stopped growing, **(b4)** crystals stopped their lateral growth and competed with each other for their radial growth; at a temperature no less than 400 °C, the ALD-SnO₂ transferred to a mode of **(c)** evolutionary particle: **(c1)** nuclei formed immediately on the substrate surface at the starting of the ALD process, **(c2)** crystals grew quickly with increased ALD-cycles, **(c3)** crystals saturated on the substrate surface, **(c4)** crystals grew predominantly in their radial direction. In **(a5)**, **(b5)**, and **(c5)**, the produced nanotubes were schematically illustrated.

Figure 5.7(a) provides the model for layer-by-layer growth. As is disclosed above, this growth is predominant with low temperatures (< 200 °C, see figure 5.3). In this case, the surface of AAO pores suffers less change in its reactive sites. Consequently, abundant hydroxyl groups as well as possible high water coverage are preferable for SnCl_4 to interact with multiple adsorption sites [38]. The ALD- SnO_2 initiates on the AAO surface by ligand exchange, as described in the reactions of 3-A and 3-B. In the following SnCl_4 and water pulses, ligand exchange proceeds and contributes a layer-by-layer growth. As illustrated by figure 5.7(a1) to (a4) in side views of AAO pores, increased ALD-cycles contribute to the increase in film thickness. In this case, the GPC (as disclosed in figure 5.3) is pretty low, for surface reactivity is very limited under low temperatures. Figure 5.7(a5) shows a resultant SnO_2 nanotube with a well-controlled amorphous wall.

Figure 5.7(b) illustrates the layer-by-particle growth in the temperature range 200 to 400 °C. In this temperature range, results (see figure 5.4, 5.5, as well as figure SI-5.1 to SI-5.3 in Supporting Information) revealed that the dominant growth changes from amorphous layers to crystalline particles. It was also disclosed that the ultimate thickness of amorphous layers is constant for a certain temperature and decreases with increased temperatures. Contrary to the reducing layers, however, the particles grow faster with temperatures. The mechanisms lie in the competing effects between ligand exchange and chlorination, i.e., lower temperatures are favorable for ligand exchange while higher temperatures prompt chlorination [42]. In this kind of growth, the AAO surface nature is exposed to a higher possibility for change, depending on the adopted temperature. Meanwhile, increased temperatures may also improve surface reactivity and induce some reactions which do not occur at lower temperatures [23]. As illustrated by figure 5.7(b1), a side view on AAO pores shows that amorphous layers take the priority to deposit, probably due to the favorable surface nature of AAO and its amorphous structure. With the increasing layers, however, nucleation events (illustrated by orange dots) happen randomly on the layers and the layers may be also favorable for the growth of nuclei, for they have different nature with respect to AAO. Further increased ALD-cycles, as illustrated in figure 5.7(b2), prompt the crystals to grow in both lateral and radial directions. At the same time, more nucleation events take place while the amorphous

layers grow thicker. To a certain point, as illustrated in [figure 5.7\(b3\)](#), the growing crystals and new-born nuclei saturate the growing surface. Since then, as illustrated in [figure 5.7\(b4\)](#), the amorphous layers stop to grow and only crystalline particles compete for available space in AAO pores. In the competitive growth of crystalline particles, they stop the growth in literal direction while continue the one along radial direction. As a result, the double-layered amorphous-crystalline SnO₂ nanotubes (see [figure 5.7\(b5\)](#)) are produced. In particular, this type of nanotubes is highly tunable in structure, for the layers and particles are controllable with temperatures.

[Figure 5.7\(c\)](#) illustrates the third grow mode, evolutionary particle, under a temperature no less than 400 °C. In this case, the AAO surface may be modified to a large extent, resulting in a considerable reduction of hydroxyl groups and water coverage but an increase of oxygen bridges. In particular, at the high temperatures chlorination becomes the only mechanism for ALD-SnO₂. As a result, the modified surface conditions of AAO and the unique chlorination may combine to lead to the exclusive growth mode of crystalline particles. [Figure 5.7\(c1\)](#) shows in a side view on the AAO pores that nuclei appear at the right beginning of the ALD-SnO₂. With increased ALD-cycles (see [figure 5.7\(c2\)](#)), the nuclei grow into crystals and more nuclei appear at the same time. While the nuclei crystallize, the crystals grow in both lateral and radial directions. To a certain point, the AAO surface is saturated with crystals and nuclei (see [figure 5.7\(c3\)](#)). Since then, the crystals begin a competitive process in which they fight each other for available space. The survived crystals obtain the opportunities to grow only in radial orientation. Similar competitive processes were ever studied in other areas where they are named as evolutionary selection [45,46]. The resultant crystalline SnO₂ nanotube is shown in [figure 5.7\(c5\)](#).

In summary, three temperature-dependent growth modes (i.e., layer-by-layer, layer-by-particle, and evolutionary particles) were revealed for the synthesis of SnO₂ nanotubes by the template-directed ALD strategy, leading to a series of highly structure-tunable SnO₂ nanotubes. Aiming at exploring the underlying mechanisms, a detailed discussion on the effects of temperatures was conducted. It is believed that two different mechanisms of

surface chemistry are responsible for the growth of amorphous layers and crystalline particles, respectively, and the two compete for dominance with temperatures. To further demonstrate the transformations of different growth modes, three growth models were proposed and schematically demonstrated. Thus, this work is helpful not only for manipulating the fabrication of novel SnO₂ nanotubes but also for scientific insights.

5.4 Conclusions

This work presented a template-directed ALD strategy to synthesize SnO₂ nanotubes. Using SnCl₄ and water as precursors, the fulfillment of ALD-SnO₂ on AAO template revealed that this strategy features its capabilities in highly tuning the synthesized SnO₂ nanotubes. It was disclosed that the growth of SnO₂ nanotubes take three different modes, i.e., layer-by-layer, layer-by-particle, and evolutionary particles, in which the layers are amorphous while the particles are crystalline. Thus, this strategy can precisely control both phases and morphologies of SnO₂ nanotube by simply adjusting temperatures. These intriguing results prompted our exploration on the underlying mechanisms and, based on reviewing earlier studies, the effects of temperatures were discussed. In particular, two different principles were clarified for the occurrence of amorphous layers and crystalline particles during the growth of SnO₂ nanotubes. Furthermore, three growth models were suggested to illustrate the evolutions between different growth modes with temperatures. Thus, this work would be important for manipulating the synthesis of SnO₂ nanotubes and it is also helpful to meet scientific curiosities with insightful views. In addition, it is believed that the synthesized SnO₂ nanotubes would be promising as components in many applications, such as batteries, sensors, solar cells, and field emission, etc.

Acknowledgements

This research was supported by the Natural Science and Engineering Research Council of Canada (NSERC), Canada Research Chair (CRC) Program, Canadian Foundation for Innovation (CFI), Ontario Research Fund (ORF), Early Researcher Award (ERA) and the

University of Western Ontario.

References

- [1] A. S. Aricò, P. Bruce, B. Scrosati, J. M. Tarascon, and W. V. Schalkwijk, Nanostructured materials for advanced energy conversion and storage devices, *Nat. Mater.*, 2005, **4**, 366-377.
- [2] J. Weber, R. Singhal, S. Zekri, and A. Kumar, One-dimensional nanostructures: fabrication, characterisation and applications, *Int. Mater. Rev.*, 2008, **53**, 235-255.
- [3] M. Lee, T. W. Kim, C. Bae, H. Shin, and J. Kim, Fabrication and applications of metal-oxide nanotubes, *JOM*, 2010, **62**, 44-49.
- [4] M. Batzill, and U. Diebold, The surface and materials science of tin oxide, *Prog. Surf. Sci.*, 2005, **79**, 47-154.
- [5] M. Batzill, Surface science studies of gas sensing materials: SnO₂, *Sensors*, 2006, **6**, 1345-1366.
- [6] D. Deng, M. G. Kim, J. Y. Lee, and J. Cho, Green energy storage materials: nanostructured TiO₂ and Sn-based anodes for lithium-ion batteries, *Energy Environ. Sci.*, 2009, **2**, 818-837.
- [7] H. J. Snaith, and C. Ducati, SnO₂-based dye-sensitized hybrid solar cells exhibiting near unity absorbed photon-to-electron conversion efficiency, *Nano Lett.*, 2010, **10**, 1259-1265.
- [8] J. H. He, T. H. Wu, C. L. Hsin, K. M. Li, L. J. Chen, Y. L. Chueh, L. J. Chou, and Z. L. Wang, Beaklike SnO₂ nanorods with strong photoluminescent and field-emission properties, *Small*, 2006, **2**, 116-120.
- [9] Y. Wang, J. Y. Lee, and H. C. Zeng, Polycrystalline SnO₂ nanotubes prepared via infiltration casting of nanocrystallites and their electrochemical application, *Chem. Mater.*, 2005, **17**, 3899-3903.
- [10] W. Zhu, W. Wang, H. Xu, and J. Shi, Fabrication of ordered SnO₂ nanotube arrays via a template route, *Mater. Chem. Phys.*, 2006, **99**, 127-130.
- [11] M. Lai, J. A. Gonzalez Martinez, M. Grätzel, and D. J. Riley, Preparation of tin dioxide nanotubes via electrosynthesis in a template, *J. Mater. Chem.*, 2006, **16**, 2843-2845.
- [12] M. Lai, J. H. Lim, S. Mubeen, Y. Rheem, A. Mulchandani, M. A. Deshusses, and N.

V. Myung, Size-controlled electrochemical synthesis and properties of SnO₂ nanotubes, *Nanotechnology*, 2009, **20**, 185602.

[13] G. X. Wang, J. S. Park, M. S. Park, and X. L. Gou, *Sens. Actuators B*, 2008, **131**, 313-317.

[14] Y. Wang, M. Wu, Z. Jiao, and J. Y. Lee, One-dimensional SnO₂ nanostructures: facile morphology tuning and lithium storage properties, *Nanotechnology*, 2009, **20**, 345704.

[15] N. Wang, X. Cao, and L. Guo, Facile one-pot solution synthesis of SnO₂ nanotubes, *J. Phys. Chem. C*, 2008, **112**, 12616-12622.

[16] S. L. Chou, J. Z. Wang, H. K. Liu, and S. X. Dou, SnO₂ meso-scale tubes: one-step, room temperature electrodeposition synthesis and kinetic investigation for lithium storage, *Electrochem. Commun.*, 2009, **11**, 242-246.

[17] Z. R. Dai, J. L. Gole, J. D. Stout, and Z. L. Wang, Tin oxide nanowires, nanoribbons, and nanotubes, *J. Phys. Chem. B*, 2002, **106**, 1274-1279.

[18] Y. Liu, and M. Liu, Growth of aligned square-shaped SnO₂ tube arrays, *Adv. Funct. Mater.*, 2005, **15**, 57-62.

[19] J. Duan, Q. Cao, S. Yang, H. Huang, X. Zhao, R. Zhang, and G. Cheng, Preparation and characterization of rectangular tin dioxide microtubes, *J. Cryst. Growth*, 2006, **289**, 164-167.

[20] M. Salehi, B. Janfeshan, and S. K. Sadrnezhad, Growth of tin oxide nanotubes by aerial carbothermal evaporation, *Appl. Phys. A*, 2009, **97**, 361-364.

[21] Z. Li, H. Wang, P. Liu, B. Zhao, and Y. Zhang, Synthesis and field-emission of aligned SnO₂ nanotubes arrays, *Appl. Surf. Sci.*, 2009, **255**, 4470-4473.

[22] S. M. George, Atomic layer deposition: an overview, *Chem. Rev.*, 2010, **110**, 111-131.

[23] R. L. Puurunen, Surface chemistry of atomic layer deposition: a case study for the trimethylaluminum/water process, *J. Appl. Phys.*, 2005, **97**, 121301.

[24] M. Knez, K. Nielsch, and L. Niinistö, Synthesis and surface engineering of complex nanostructures by atomic layer deposition, *Adv. Mater.* 2007, **19**, 3425-3438.

- [25] A. Rosental, A. Tarre, A. Gerst, T. Uustare, and V. Sammelselg, Atomic-layer chemical vapor deposition of SnO₂ for gas-sensing applications, *Sens. Actuators B*, 2001, **77**, 297-300.
- [26] A. Tarre, A. Rosental, V. Sammelselg, T. Uustare, Comparative study of low-temperature chloride atomic-layer chemical vapor deposition of TiO₂ and SnO₂, *Appl. Surf. Sci.*, 2001, **175-176**, 111-116.
- [27] T. Takeuchi, K. Shoji, T. Tadano, I. Doteshta, and S. Onodera, Preparation of sub-nanometer thickness-controlled tin dioxide films by pulsed atomic-layer CVD, *Thin Solid Films*, 2003, **442**, 98-101.
- [28] T. Takeuchi, I. Doteshta, and S. Asami, Expitaxial growth of sub-nanometer thick tin dioxide films on sapphire substrates by pulsed atomic layer chemical vapour deposition, *Surf. Interface Anal.*, 2004, **36**, 1133-1135.
- [29] J. Lu, J. Sundqvist, M. Ottosson, A. Tarre, A. Rosental, J. Aarik, and A. Harsta, Microstructure characterisation of ALD-grown expitaxial SnO₂ thin films, *J. Cryst. Growth*, 2004, **260**, 191-200.
- [30] A. Kytökivi, and M. Lindblad, IR and ¹H NMR studies on the adsorption of gaseous hydrogen chloride on γ -alumina, *J. Chem. Soc. Faraday Trans.*, 1995, **91**, 941-948.
- [31] J. W. Diggle, T. C. Downie, and C. W. Goulding, Anodic oxide films on aluminum, *Chem. Rev.*, 1969, **69**, 365-405.
- [32] G. D. Parfitt, Surface chemistry of oxides, *Pure Appl. Chem.*, 1976, **48**, 415-418.
- [33] A. Kytökivi, E.-L. Lakomaa, and A. Root, Controlled formation of ZrO₂ in the reaction of ZrCl₄ vapor with porous silica and γ -alumina surfaces, *Langmuir*, 1996, **12**, 4395-4403.
- [34] S. Haukka, E.-L. Lakomaa, O. Jylhä, J. Vilhunen, and S. Hornytzkyj, Dispersion and distribution of titanium species bound to silica from TiCl₄, *Langmuir*, 1993, **9**, 3497-3506.
- [35] S. Haukka, E.-L. Lakomaa, and A. Root, An IR and NMR study of the chemisorption of TiCl₄ on silica, *J. Phys. Chem.*, 1993, **97**, 5085-5094.
- [36] Z. Hu, and C. H. Turner, Initial surface reactions of TiO₂ atomic layer deposition onto SiO₂ surfaces: density functional theory calculations, *J. Phys. Chem. B*, 2006, **110**, 8337-8347.
- [37] Z. Hu, and C. H. Turner, Atomic layer deposition of TiO₂ from TiI₄ and H₂O onto

SiO₂ surfaces: ab initio calculations of the initial reaction mechanisms, *J. Am. Chem. Soc.*, 2007, **129**, 3863-3878.

[38] A. B. Mukhopadhyay, C. B. Musgrave, and J. F. Sanz, Atomic layer deposition of hafnium oxide from hafnium chloride and water, *J. Am. Chem. Soc.*, 2008, **130**, 11996-12006.

[39] J. Aarik, A. Aidla, V. Sammelselg, H. Siimon, and T. Uustare, Control of thin film structure by reactant pressure in atomic layer deposition of TiO₂, *J. Cryst. Growth*, 1996, **169**, 496-502.

[40] X. Du, Y. Du, S. M. George, In situ examination of tin oxide atomic layer deposition using quartz crystal microbalance and Fourier transform infrared techniques, *J. Vac. Sci. Technol. A*, 2005, **23**, 581-588.

[41] M. Ritala, and M. Leskelä, Growth of titanium-dioxide thin-films by atomic layer epitaxy, *Thin Solid Films*, 1993, **225**, 288-295.

[42] R. L. Puurunen, Formation of metal oxide particles in atomic layer deposition during the chemisorption of metal chlorides: a review, *Chem. Vap. Deposition*, 2005, **11**, 79-90.

[43] X. Meng, D. Geng, J. Liu, M. N. Banis, Y. Zhang, R. Li, and X. Sun, Non-aqueous approach to synthesize amorphous/crystalline metal oxide-graphene nanosheet hybrid composites, *J. Phys. Chem. C*, 2010, **114**, 18330-18337.

[44] X. Meng, Y. Zhong, Y. Sun, M. N. Banis, R. Li, and X. Sun, Nitrogen-doped carbon nanotubes coated by atomic layer deposited SnO₂ with controlled morphology and phase, *Carbon*, 2011, **49**, 1133-1144.

[45] A. van der Drift, Evolutionary selection, a principle governing growth orientation in vapour-deposited layers, *Philips. Res. Repts.*, 1967, **22**, 267-288.

[46] A. B. Rodriguez-Navarro, Model of texture development in polycrystalline films growing on amorphous substrates with different topographies, *Thin Solid Films*, 2001, **389**, 288-295.

Supporting Information

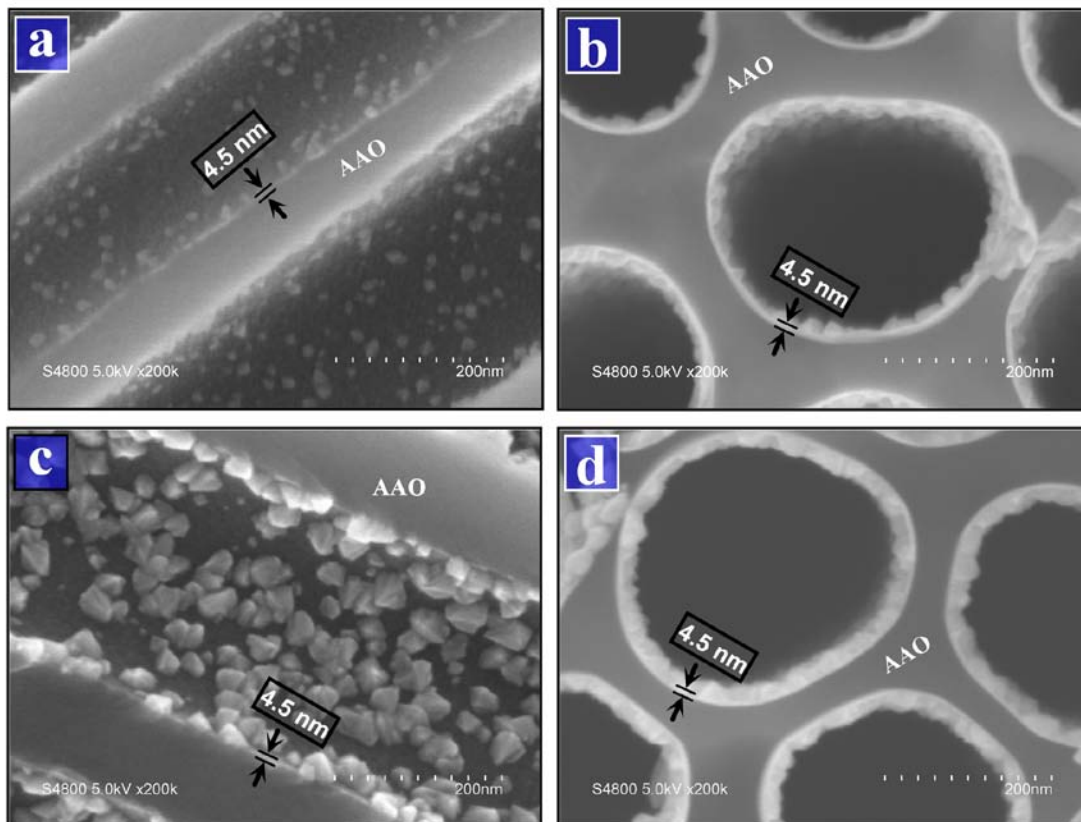


Figure SI-5.1 ALD-SnO₂ at 300 °C. SEM images of side-views of AAO pores after (a) 200, and (c) 600 ALD-SnO₂ cycles; and SEM images of top-views of AAO pores after (b) 400, and (d) 600 ALD-SnO₂ cycles.

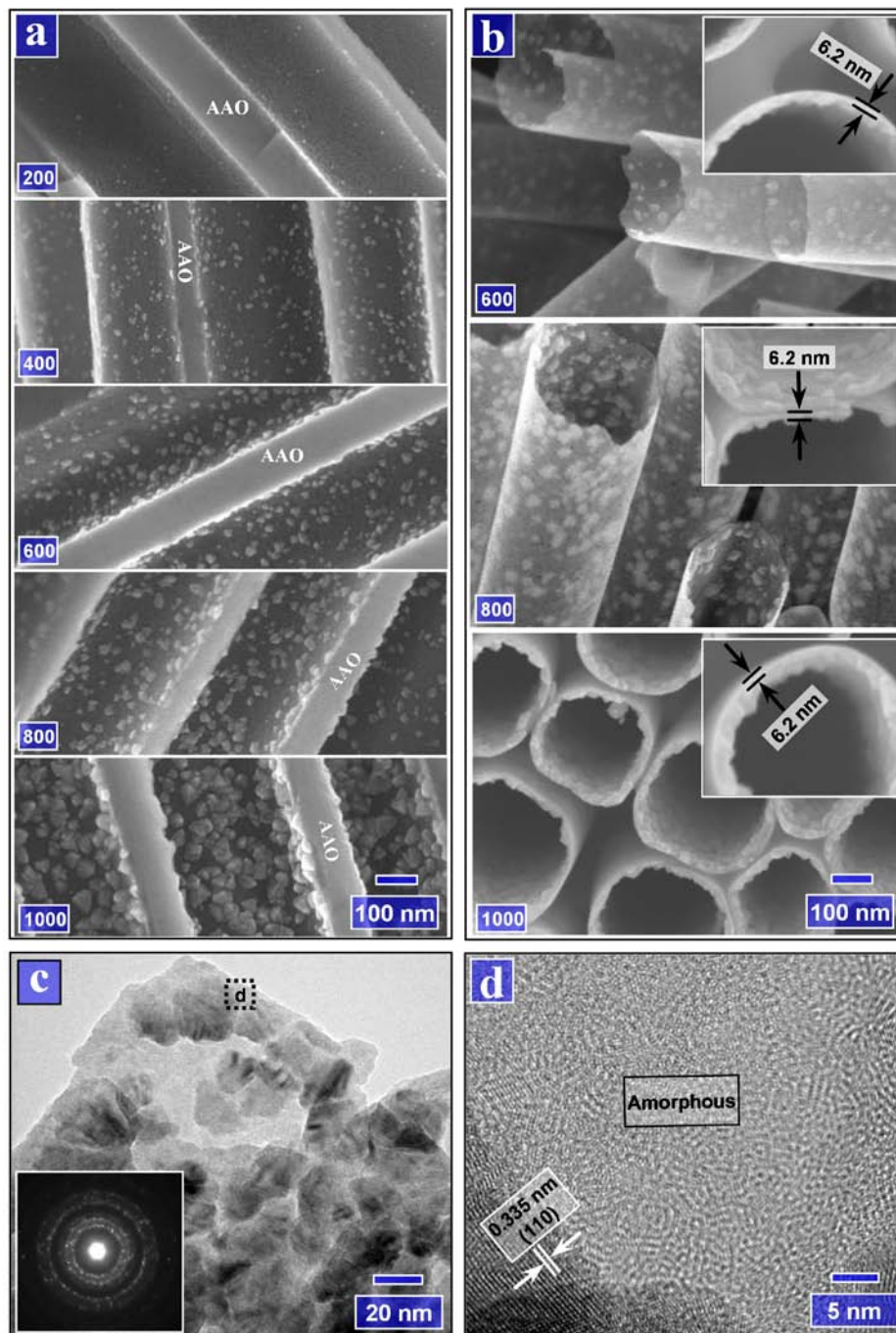


Figure SI-5.2 The growth characteristics of ALD-SnO₂ at 250 °C. (a) SEM side views of AAO pores coated with the ALD-SnO₂ of 200, 400, 600, 800, and 1000 cycles (as marked on the left-bottom corner of each case); (b) SEM images for the received SnO₂ nanotubes after 600, 800, and 1000 ALD-cycles; (c) the TEM image for the SnO₂ nanotubes of 800 ALD-cycles (inset: SAED patterns); (d) the HRTEM image for a local area in (c).

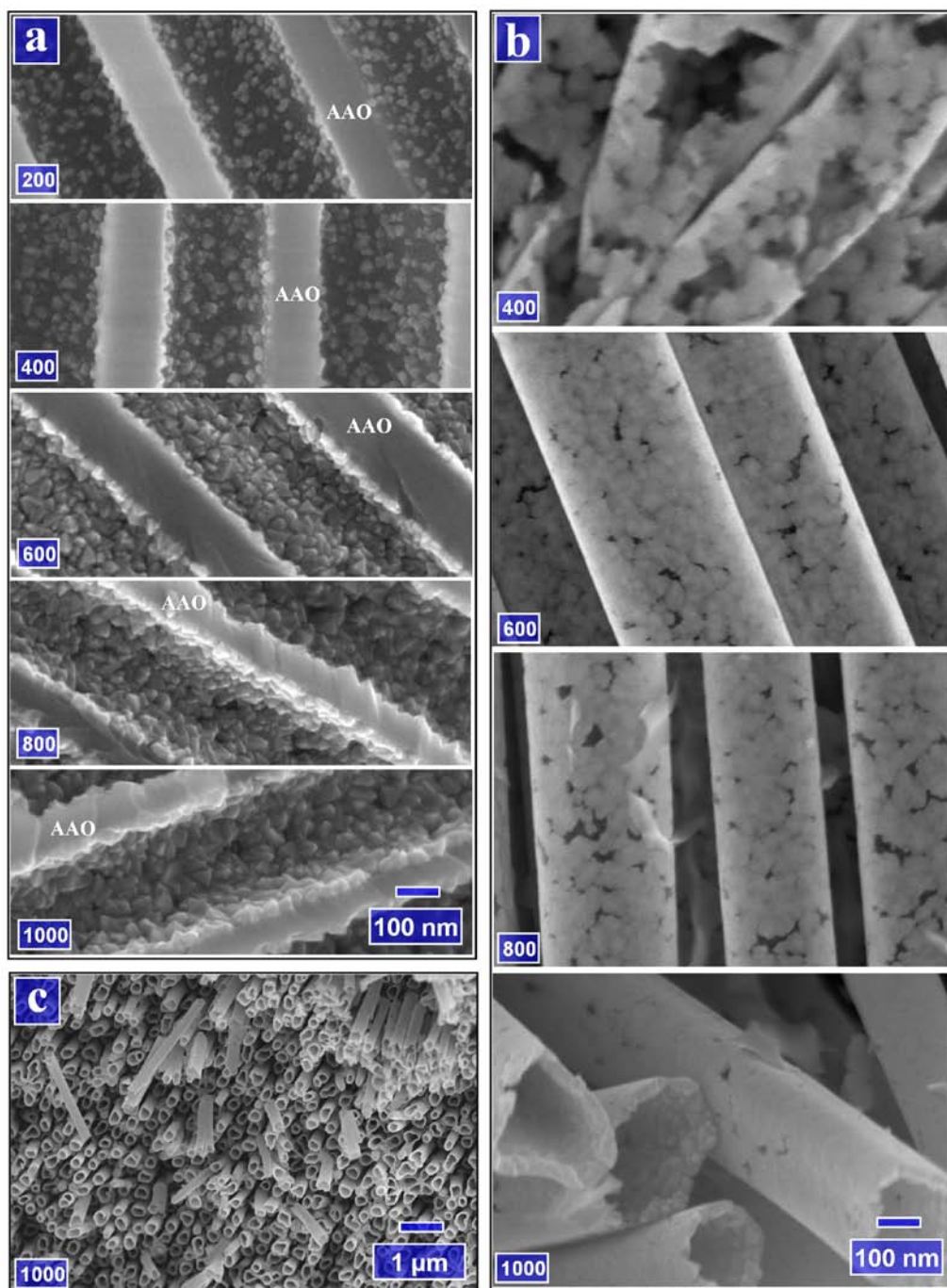


Figure SI-5.3 The growth characteristics of ALD-SnO₂ at 350 °C. (a) SEM side views of AAO pores coated with the ALD-SnO₂ of 200, 400, 600, 800, and 1000 cycles (as marked on the left-bottom corner of each case); (b) SEM images for the received SnO₂ nanotubes after 400, 600, 800, and 1000 ALD-cycles; (c) the arrays of SnO₂ nanotubes of 1000 ALD-cycles.

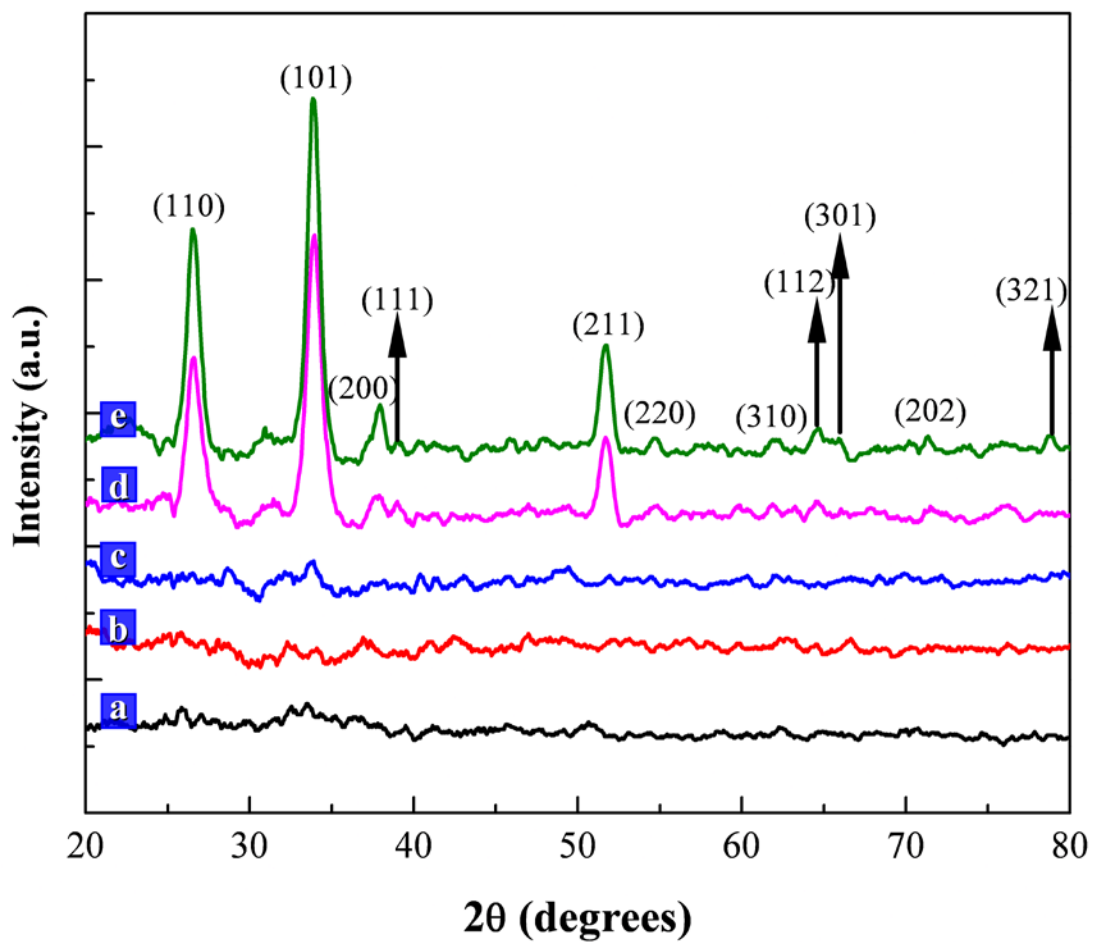


Figure SI-5.4. XRD spectra of 200-cycle ALD-SnO₂ at different growth temperatures: (a) 200, (b) 250, (c) 300, (d) 350, and (e) 400 °C.

CHAPTER 6

NITROGEN-DOPED CARBON NANOTUBES COATED BY ATOMIC LAYER DEPOSITED SnO₂ WITH CONTROLLED MORPHOLOGY AND PHASE

A version of this chapter has been published in *Carbon*, 2011, 49, 1133-1144.

Atomic layer deposition (ALD) was used to synthesize metal oxide-carbon nanotube (MO-CNT) hybrid materials by coating nitrogen-doped CNTs (N-CNTs). SnO₂-CNT hybrids were produced using SnCl₄ and water as precursors and exhibited many unique features. It was demonstrated that the use of N-CNTs was beneficial for directly initiating the ALD of SnO₂ (ALD-SnO₂) and that adjustable ALD parameters were favorable for controlling the morphology and phase of the deposited SnO₂. The cyclic and surface-controlled nature of ALD contributed to the morphologies of SnO₂ tunable from nanoparticles to nanofilms, and the temperature-dependent characteristics of the ALD-SnO₂ rendered the phases of SnO₂ controllable with amorphous, crystalline, or a mixed phase by the former two. Furthermore, this study also explored the underlying mechanisms for the controlled synthesis of SnO₂-CNT hybrid materials.

Keywords: *Atomic layer deposition, Nitrogen-doped carbon nanotubes, Metal oxides, Tin dioxide, Nanocomposites*

6.1 Introduction

There was a long history for the discoveries of carbon nanotubes (CNTs) [1], but only after Iijima's work [2] was an extensive investigation boosted with many findings on their exceptional properties and significant applications [3]. A primary approach for applications was to incorporate CNTs with other materials, and the resultant hybrid materials in general exhibited improved properties. Of them, CNT-based metal oxide (MO-CNT) hybrids represent an important class and are very promising as functional materials, such as in lithium-ion batteries (LIBs) and supercapacitors [4].

Tin (IV) dioxide (SnO_2) is among the most investigated nanoscale MOs, ascribing to its distinctive properties very useful in many areas (e.g., field emission [5,6], gas sensors [7], and LIBs [8-10]). In comparison, CNT-based SnO_2 (SnO_2 -CNT) hybrids are much superior to their pure SnO_2 tubular counterparts, e.g., exhibiting higher sensitivity as gas sensors [11,12], as well as increased specific mass capacity and extended durability as anodes of LIBs [13-20]. Thus, a large amount of effort has previously devoted to develop SnO_2 -CNT hybrids using various methods including arc-discharge [13], chemical vapor deposition (CVD) [14], different chemical-solution routes [15-20], etc. However, the used CNTs required a pretreatment process to modify their inert surface nature before a deposition of SnO_2 was performed. This could be realized either by acid oxidation [14-19] or by surfactants [20]. Unfavorably, the two functionalization methodologies of CNTs commonly needed wet chemical treatment, while the former one further risked CNTs to some damages in their inherent properties. As a consequence, the previous methods [13-20] were confined with a limited flexibility and they exclusively produced polycrystalline nanoparticles of SnO_2 on functionalized CNTs.

To bypass the drawbacks suffered by earlier studies, we recently developed an alternative strategy to synthesize MO-CNT hybrids, in which the technique of atomic layer deposition (ALD) was used to coat nitrogen-doped CNTs (N-CNTs) directly. As a consequence, it was demonstrated that the ALD route as well as the use of N-CNTs brought many unique advantages. First of all, N-CNTs by nature are chemically active

[21] and thereby can directly induce the following ALD of SnO₂ (ALD-SnO₂). Furthermore, ALD is a surface-controlled and layer-by-layer process, relying on two sequential self-terminating half-reactions [22-24]. Thus, ALD is superior in deposition with high flexibility and preciseness. As for ALD-SnO₂, some earlier efforts practiced the deposition on flat substrates and nanoparticles using different precursors [25-35]. However, there were no cases to date reported on the ALD-SnO₂ on CNTs. In this study, we attempted to achieve this goal using N-CNTs as substrates, as well as SnCl₄ and water as precursors. In essence, the reaction between SnCl₄ and H₂O is fairly straightforward with the product of SnO₂, as described in the following [Reaction 1](#).



In ALD-SnO₂, the above reaction was previously interpreted by two half-reactions [33]:



where “||” indicates the substrate surface, and “(g)” denotes the vapor species. With the fulfillment of ALD-SnO₂ on N-CNTs, it was found in this study that the deposited SnO₂ is controllable in morphology as well as structural phase. In particular, it was also revealed that the ALD-SnO₂ is highly temperature-dependent. Thus, besides the aforementioned two half-reactions, other underlying mechanisms for ALD-SnO₂ were developed as well. In summary, there are three features induced by the proposed strategy (i.e., ALD-SnO₂ on N-CNTs): (i) the N-CNTs are free of external functionalization; (ii) the deposited SnO₂ materials are tunable in morphology from nanoparticles to nanofilms; (iii) the deposited SnO₂ materials are controllable in structural phase from amorphous to crystalline or a mixed phase by the former two. Thus, this work opened an avenue for highly precise synthesis of CNT-based hybrids and provided multiple candidates for many important applications, such as gas sensors, and LIBs, etc.

6.2 Experimental

6.2.1 Synthesis of N-CNTs

A thermal CVD method was applied to grow N-CNTs on substrates (carbon papers or Si wafers). The substrates were initially coated with a buffer layer of 30 nm thick aluminum and a catalyst layer of 5 nm thick iron. In the presence of Ar, the pyrolysis of melamine ($C_3H_6N_6$) at 800 °C induced the growth of N-CNTs on the substrates. The synthesized N-CNTs were structurally multi-walled and bamboo-like, presenting a typical N content of over 10 at.%. More details were described in a previous work [36].

6.2.2 ALD-SnO₂

ALD-SnO₂ was performed on the synthesized N-CNTs through supplying tin (IV) chloride (99% SnCl₄, Sigma-Aldrich) and deionized water into a commercial ALD reactor (Savannah 100, Cambridge Nanotechnology Inc., USA) in an alternating manner. The temperature of the ALD reactor was in a range 200 - 400 °C. Nitrogen was used as the carrier gas with a flow rate of 20 sccm, and the ALD reactor was sustained at a low level of base pressure (typically 0.4 Torr) by a vacuum pump (Pascal 2005 I, Adixon). The ALD procedures were set as follows: (1) a 0.5 s supply of SnCl₄; (2) a 3 s extended exposure of SnCl₄ to N-CNTs; (3) a 10 s purge of oversupplied SnCl₄ and any by-products; (4) a 1 s supply of water vapor; (5) a 3 s extended exposure of water to N-CNTs; (6) a 10 s purge of oversupplied water and any by-products. The aforementioned six-step sequence constituted one ALD-SnO₂ cycle and the ALD processes could differ in the number of cycles.

6.2.3 Characterization

The synthesized N-CNTs and SnO₂-CNT hybrid materials were characterized using a field-emission scanning electron microscope (FE-SEM, Hitachi 4800S) equipped with energy dispersive X-ray spectroscopy (EDS), transmission electron microscope (TEM,

Philips CM10), high-resolution TEM (HRTEM, JEOL 2010 FEG), micro X-ray diffractometer (XRD, Bruker D8, CuK α radiation, $\lambda = 1.5406 \text{ \AA}$), and X-ray photoelectron spectrometer (XPS, Kratos Axis Ultra Al K(alpha)).

6.3 Results and Discussion

6.3.1 Results

In [figure 6.1\(a\)](#) and [\(b\)](#), the synthesized N-CNTs are shown by SEM images of low and high magnification, respectively. [Figure 6.1\(a\)](#) reveals that the N-NCTs were grown on carbon papers with high density, and [figure 6.1\(b\)](#) shows that they are morphologically bamboo-like with diameters in the range 40 – 80 nm. [Figure 6.1\(c\)](#) presents the XRD spectra of two samples coated by ALD-SnO₂ at 200 and 400 °C. The two samples commonly exhibit two strong peaks at 26.38° and 54.54°, consistent with those reference values of crystalline graphite (JCPDS PDF No. 41-1487). The two peaks are apparently induced by pristine N-CNTs and marked as Graphite(002) and Graphite(004), respectively. To further identify the information of SnO₂, the XRD spectra between 30° and 55° are magnified in the [insert of figure 6.1\(c\)](#). It is found that the sample coated at 400 °C (marked with a solid square) presents several characteristic peaks of crystalline SnO₂ (JCPDS PDF No. 41-1445) at 33.89°, 42.63°, and 51.78°, corresponding to the (101), (210), and (211) plane, respectively. Another sample coated at 200 °C (marked with a solid triangle) has no observable peaks in the range 30° - 55°, implying an amorphous state of the deposited SnO₂. Furthermore, EDS spectra in [figure 6.1\(d\)](#) confirm the presence of Sn and O element with the sample coated at 200 °C. As for other elements, C is attributed to N-CNTs, both Al and Fe are from the coatings of carbon papers, and Cl is due to some remaining Cl ligands. Thus, it is reasonable to conclude that growth temperatures are determinant for the phases of the deposited SnO₂.

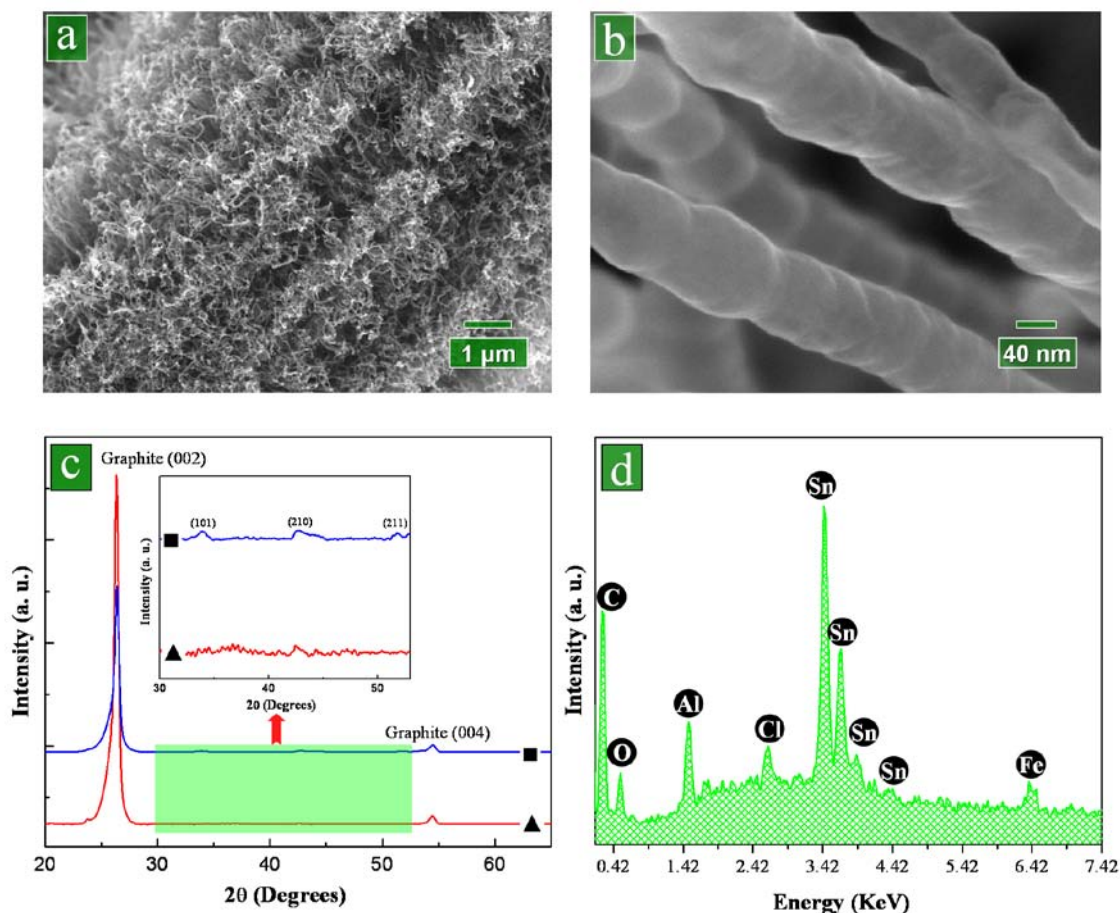


Figure 6.1 SEM images of N-CNTs with (a) low magnification, and (b) high magnification; (c) XRD spectra of N-CNTs coated with 200-cycle ALD-SnO₂ at (▲) 200 °C and (■) 400 °C; (d) EDS spectra of N-CNTs coated with 200-cycle ALD-SnO₂ at 200 °C.

To further characterize the synthesized SnO₂-CNT hybrid materials, we applied SEM, TEM, and HRTEM. **Figure 6.2** shows the SnO₂-CNT hybrids synthesized at 200 °C. SEM images of **figure 6.2(a)**, **(c)**, and **(e)** correspond to the ALD-SnO₂ of 50, 100, and 200 cycles, respectively. They commonly reveal that, in comparison to pristine N-CNTs illustrated in **figure 6.1(b)**, the surface of N-CNTs becomes rougher with a coating of some external material. According to **Reactions 1-A** and **1-B**, the material deposited

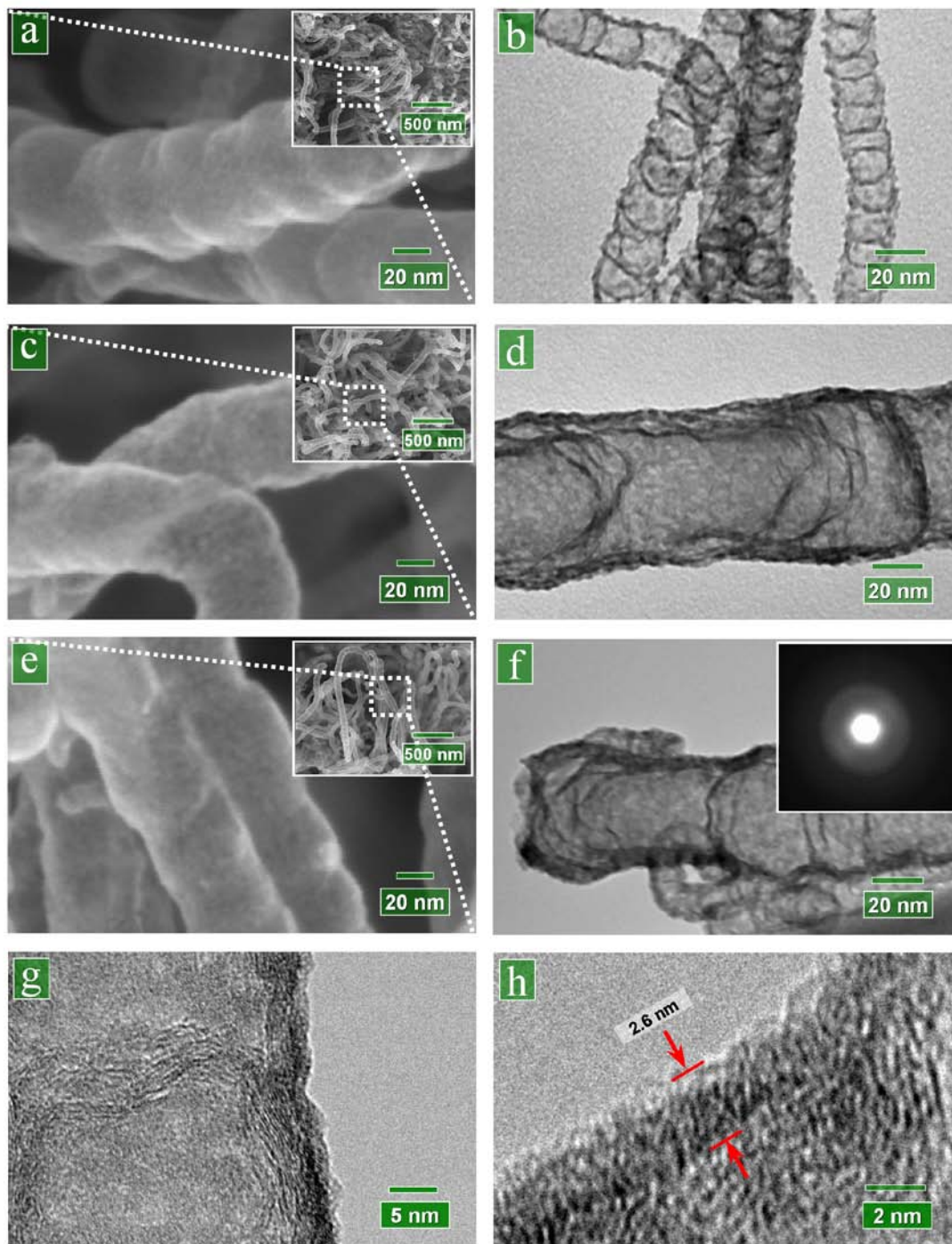


Figure 6.2 ALD-SnO₂ on N-CNTs at 200 °C. SEM images after (a) 50, (c) 100, and (e) 200 ALD cycles; TEM images after (b) 50, (d) 100, and (f) 200 ALD cycles (insert: SAED patterns); (g and h) HRTEM images of 200-cycle ALD-SnO₂.

externally should be SnO₂ and the information from figure 6.1(c) and (d) discloses the deposited SnO₂ in an amorphous state. Furthermore, the corresponding TEM images in figure 6.2(b), (d), and (f) jointly reveal that the morphological evolution of SnO₂ experienced three stages: separated nanoparticles (3 - 5 nm, figure 6.2(b)), coalescence of nanoparticles (figure 2(d)), and formation of a coaxial nanofilm (figure 2(f)). In particular, the patterns of selected area electron diffraction (SAED, insert of figure 2(f)) show the disordered nature of the hybrid material, which confirms the amorphous nature of the deposited SnO₂. Additionally, the case of 200-cycle ALD-SnO₂ was further analyzed by HRTEM, as shown in figure 6.2(g) and (h). Figure 6.2(g) shows that, besides the graphene layers of N-CNTs, there is no crystalline structure with the deposited SnO₂. Figure 6.2(h) also reveals the amorphous nature of the deposited SnO₂ and exposes a uniform film thickness of around 2.6 nm. As a consequence, the amorphous SnO₂ reached an average growth of around 0.13 Å/cycle at the temperature of 200 °C.

Following up the synthesis of SnO₂-CNT hybrid materials at 200 °C, a high temperature of 400 °C was applied to continue the synthesis and the main results are included in figure 6.3. As disclosed by the SEM image of figure 6.3(a), a 50-cycle ALD-SnO₂ seemingly produced only nanoparticles of around 10 nm on N-CNTs. Further increasing ALD-SnO₂ to 100 (figure 6.3(b)), 200 (figure 6.3(c)), and 400 cycles (figure 6.3(d)) prompted the growth of nanoparticles in size (up to 50 nm) and density but there were no films formed on N-CNTs. The TEM image (figure 6.3(e)) for the case of 100-cycle ALD-SnO₂ confirms that, besides nanoparticles, there were no others deposited on N-CNTs. SAED discloses a polycrystalline nature of the deposited nanoparticles, consistent to the XRD result in figure 6.1(c). The HRTEM images in figure 6.3(f) and (g) show clearly the crystalline structures of both SnO₂ and N-CNTs. It is noteworthy that, besides some big nanoparticles (around 20 nm) as disclosed in figure 6.3(e), a large amount of tiny nanoparticles of less than 5 nm are exposed in figure 6.3(f) and (g), as red-circled in the images. In particular, it is noted that the deposited nanoparticles are predominately located in the interlinked areas of N-CNTs. Thus, it is apparent that nanoparticles did not grow with a same rate. Furthermore, as indicated in figure 6.3(f) and (g), there are two kinds of lattice planes identified with the nanoparticles. The inter-plane spacing of 0.335

nm corresponds to the (110) plane, while the one of 0.264 nm corresponds to the (101) plane of SnO₂. It is worth noting that the (110) plane of SnO₂ has not been identified in XRD spectrum (figure 6.1(c)), for its characteristic position at 26.61° is very close to that of Graphite(002).

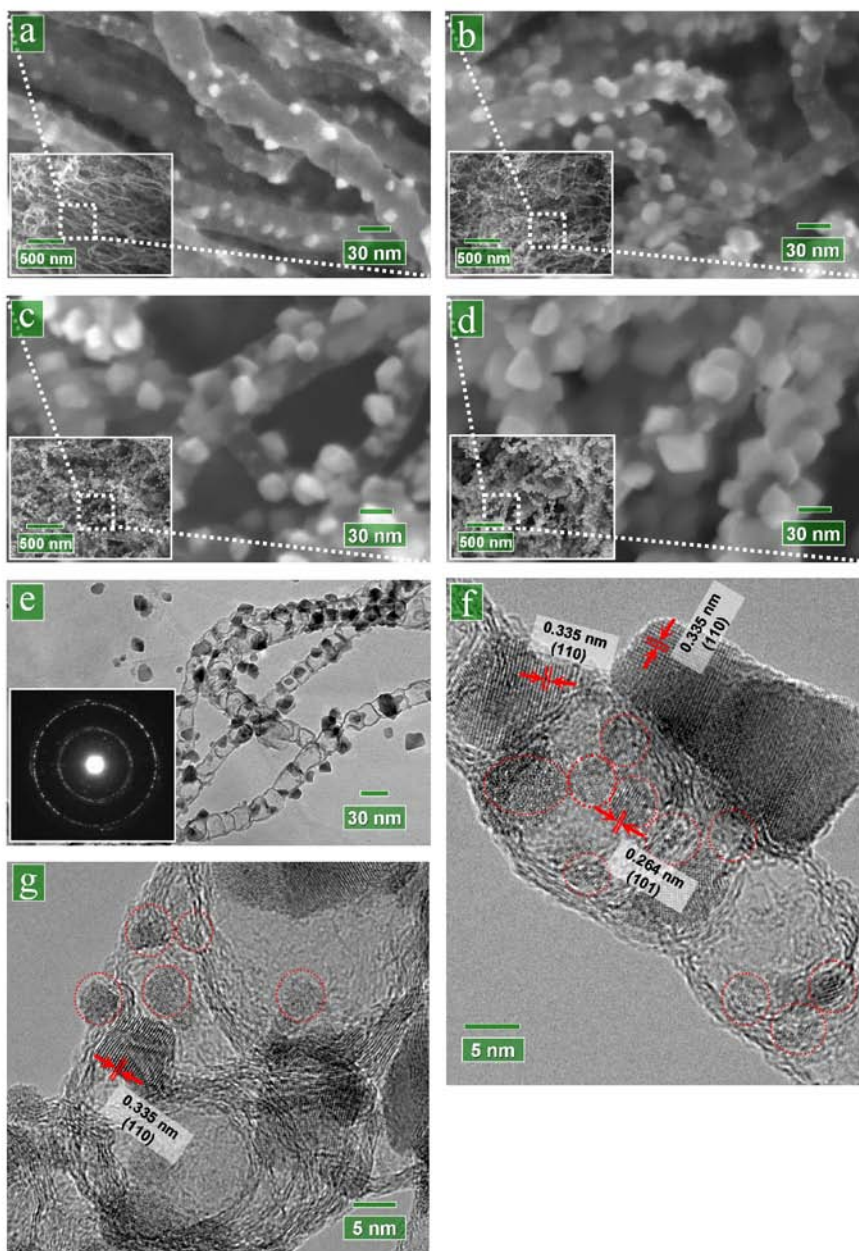


Figure 6.3 ALD-SnO₂ on N-CNTs at 400 °C. SEM images after (a) 50, (b) 100, (c) 200, (d) 400 ALD cycles; (e) TEM image of 100-cycle ALD-SnO₂ (insert: SAED patterns); (f and g) HRTEM images of 100-cycle ALD-SnO₂.

Based on the above-disclosed results, it is evident that growth temperatures are crucial for ALD-SnO₂ on N-CNTs. To further investigate the effects of growth temperature, an intermediate temperature of 300 °C was used to synthesize SnO₂-CNT hybrids, and the resultant results are illustrated in figure 6.4. Along with the increasing ALD-SnO₂ from 50 (figure 6.4(a)), 100 (figure 6.4(b)) to 200 cycles (figure 6.4(c)), one can observe numerous nanoparticles deposited on N-CNTs with increased sizes, accounting for 3 - 5 nm, 3 - 7 nm, to 5 - 15 nm, respectively. However, besides nanoparticles presenting white and bright spots in the images, the intervals between nanoparticles seem also covered with a continuous layer. Figure 6.4(d) shows the TEM image for the case of 200-cycle ALD-SnO₂, and the corresponding SAED patterns in the inset of figure 6.4(d) disclose that the deposited SnO₂ presents polycrystalline characteristics. Under the HRTEM examination (figure 6.4(e) and (f)), it is worth noting that a 2.6 nm thick amorphous nanofilm and many crystalline nanoparticles are observed. The nanoparticles show clearly an inter-plane of 0.335 nm, corresponding to the (110) plane of SnO₂. Obviously, the crystalline nanoparticles are responsible for the polycrystalline nature of the SAED patterns (the inset of figure 6.4(d)). Thus, an intermediate growth temperature prompted a covering of heterogeneous structural phases, i.e., an amorphous film embellished with crystalline nanoparticles.

Upon this point, it was clearly demonstrated that the proposed strategy shows a strong capability in synthesizing SnO₂-CNT hybrids as well as in controlling the deposited SnO₂ with different phases and morphologies. To summarize, there are three main features exhibited by the synthesized SnO₂-CNTs hybrids: (i) direct initiation of ALD-SnO₂ on N-CNTs; (ii) controllable phases of the deposited SnO₂ with temperature, showing amorphous (figure 6.2), crystalline (figure 6.3), or even a mixed amorphous-crystalline phase (figure 6.4); (iii) tunable morphologies of the deposited SnO₂, exhibiting nanoparticles (figure 6.2 and 6.3), nanofilms (figure 6.2), or a mixture of nanofilms and nanoparticles (figure 6.4). To understand these interesting results, it is believed that both the effects of N-CNTs and the underlying mechanisms of ALD-SnO₂ are essential. In particular, their distinctive dependence on temperature should be clarified. Thus, we investigated them and will discuss in the following sections.

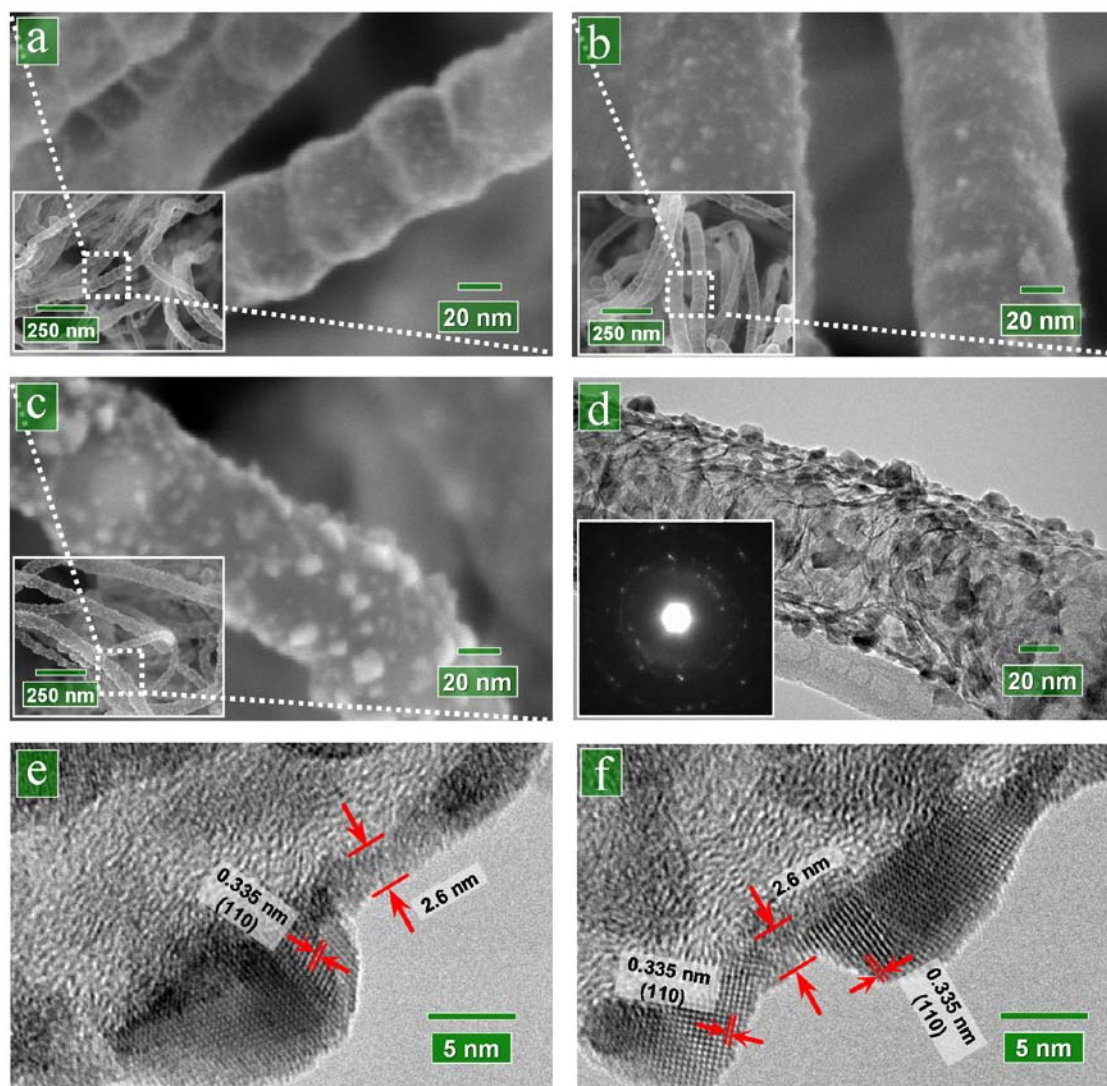


Figure 6.4 ALD-SnO₂ on N-CNTs at 300 °C. SEM images after (a) 50, (b) 100, and (c) 200 ALD cycles; (d) TEM image of 200-cycle ALD-SnO₂ (insert: SAED patterns); (e and f) HRTEM images of 200-cycle ALD-SnO₂.

6.3.2 Discussion

6.3.2.1 The effects of N-doping

As stated above, one feature with this study is the use of N-CNTs which initiated ALD-SnO₂ directly. As a surface-controlled process, ALD initiates on a substrate via an interaction between the molecules of one precursor and the reactive sites of the substrate. This kind of interaction contributes to an irreversible adsorption of one precursor and is restricted to chemisorption [37]. In comparison to pure (undoped) CNTs used in previous studies [14-20], the difference of N-CNTs lies in their N-doping. Therefore, the N-doping is responsible for the reactivity of N-CNTs and thereby for the initiation of ALD-SnO₂. In this case, an investigation on the effects of N-doping is crucial for a better understanding of the ALD-SnO₂ on N-CNTs.

Of the two precursors (SnCl₄ and H₂O) used in this study, H₂O could only be possible to physically adsorb on the N-CNTs and the adsorption of these molecules can be reversed easily [38]. In this case, SnCl₄ holds as the only candidate to chemically bond with N-related defective sites and to initiate the ALD-SnO₂ on N-CNTs. Evidence from earlier studies [39-41] demonstrated that metal atoms could bond with N-related defective sites and thereby induce the growth of metal nanoparticles or nanowires on N-CNTs. In addition, they also disclosed that the effects of N-doping are closely related with the doped-N configurations, for different doped-N configurations have distinctive mechanisms to adsorb metal atoms. Thus, it would be better to investigate the effects of N-doping according to their configurations. As for the configurations of the doped-N atoms, there are several ones identified to date, including gaseous N₂, nitric oxides, pyridine-like nitrogen, graphite-like nitrogen, and pyrrolic nitrogen [42,43]. Although these doped-N configurations might not appear concurrently [44], there are two primary ones commonly exposed in N-CNTs, i.e., graphite-like (in which a nitrogen atom replaces a graphitic carbon atom) and pyridine-like N configuration (in which a nitrogen atom bonds with two carbon atoms). Furthermore, it was also experimentally [39-41] and theoretically [40,45,46] demonstrated that the two are the main factors for the surface

reactivity of N-CNTs and they induce chemical activeness via different mechanisms. In comparison, the pyridine-like N configuration can induce a stronger binding energy to the adsorption of metal atoms [40,46]. In addition, it was also demonstrated that CN bonds are thermally stable [44,47,48] and the two primary configurations can stand an annealing of up to 800 °C [44].

Upon this point, it is clear that the initiation of ALD-SnO₂ was likely induced by the interaction of SnCl₄ with N-related defects and the two main doped-N configurations should be exempt from structural changes during ALD-SnO₂ as well, where growth temperatures of less than 400 °C were applied. In this case, it will be insightful to investigate the effects of N-doping by differentiating their configurations and changes. To fulfill this goal, we applied XPS to study three samples of N-CNTs grown on Si wafers. One control sample consists of pristine (uncoated) N-CNTs, and two comparative samples consist of N-CNTs coated with 100-cycle SnO₂ at 200 and 400 °C, respectively. Figure 6.5 shows the XPS surveys of the three samples. The XPS spectrum of the uncoated N-CNTs (figure 6.5(a)) displays two characteristic peaks around 285 and 399 eV, corresponding to C 1s and N 1s, respectively. In addition, there are relatively weak peaks for O 1s, Fe 2p, and Si 2s as well, attributing to the Si wafer covered by a layer of native SiO₂ as well as a layer of iron catalyst. The XPS spectra for the two coated samples are shown in figure 6.5(b) and (c). In comparison, the N 1s peaks of the coated samples are significantly reduced while their C 1s peaks remain at a comparable level. Due to ALD-SnO₂, the coated samples show the newly appeared peaks of Sn and Cl, as well as some increase in the O 1s peaks. The weak Cl peaks are due to unreacted Cl ligands in ALD-SnO₂. In terms of a full width of at half-maximum (FWHM), it is found that the value for C 1s slightly decreases from 2.95 eV (figure 6.5(a)) to 2.87 eV (figure 6.5(b)) and 2.92 eV (figure 6.5(c)), while the value for N 1s significantly increases from 3.23 eV (figure 6.5(a)) to 3.86 eV (figure 6.5(b)) and 5.38 eV (figure 6.5(c)). As the indicators for the main compositions of N-CNTs, the narrowing C 1s and broadening N 1s peaks are essential for understanding the effects of N-doping and therefore deserve a further investigation with their high resolution spectra.

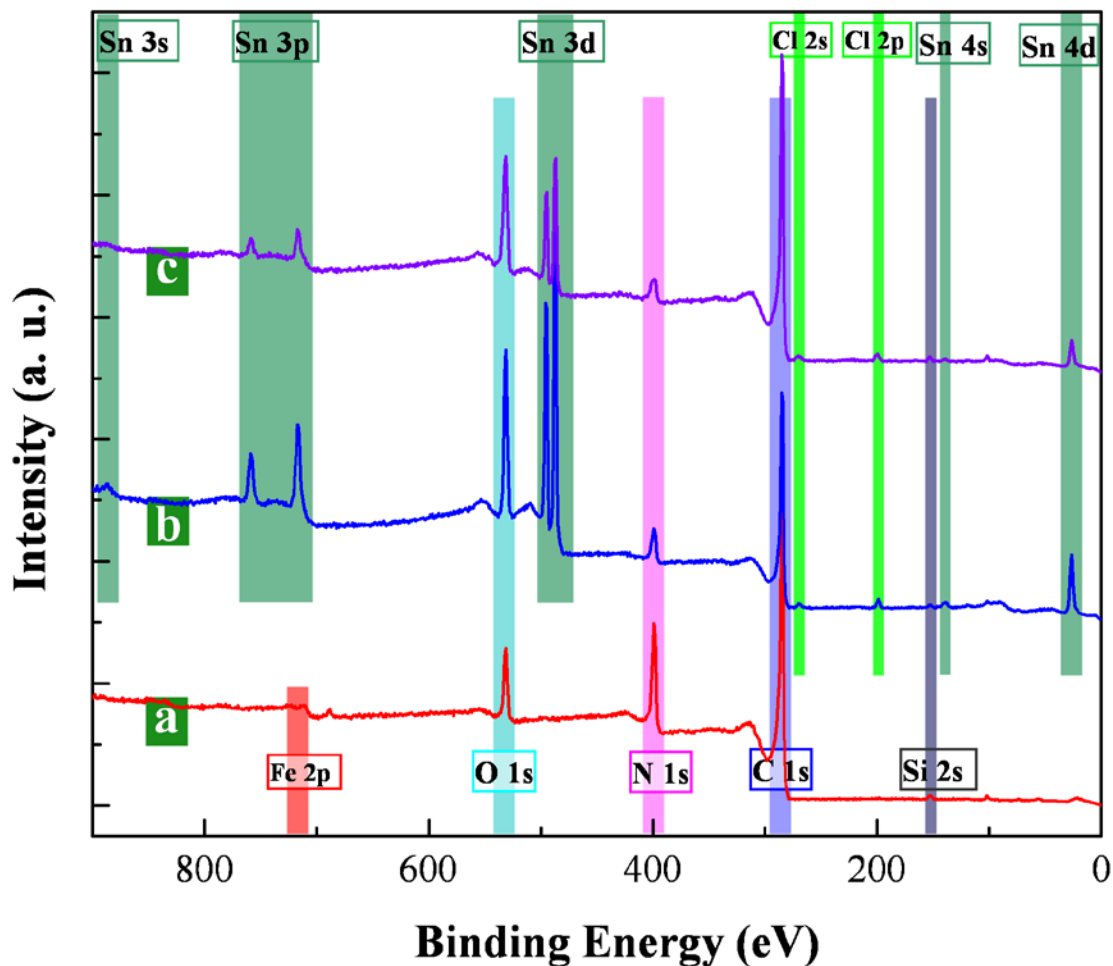


Figure 6.5 Survey scans of XPS spectra for (a) pristine N-CNTs, as well as N-CNTs coated with 100-cycle ALD-SnO₂ at (b) 200 °C and (c) 400 °C.

The high resolution C 1s spectra of the three samples are shown in figure 6.6(a) – (c), in which the dashed lines represent raw data and the solid lines are the corresponding fittings. The asymmetric C 1s spectra are commonly deconvoluted into five sub-peaks: PC1 (284.6 eV) [49] for the C-C bonds of graphite showing a peculiar dissymmetric shape, PC2 – PC4 (285.5-289 eV) [50,51] for overlapping defective carbon structures due

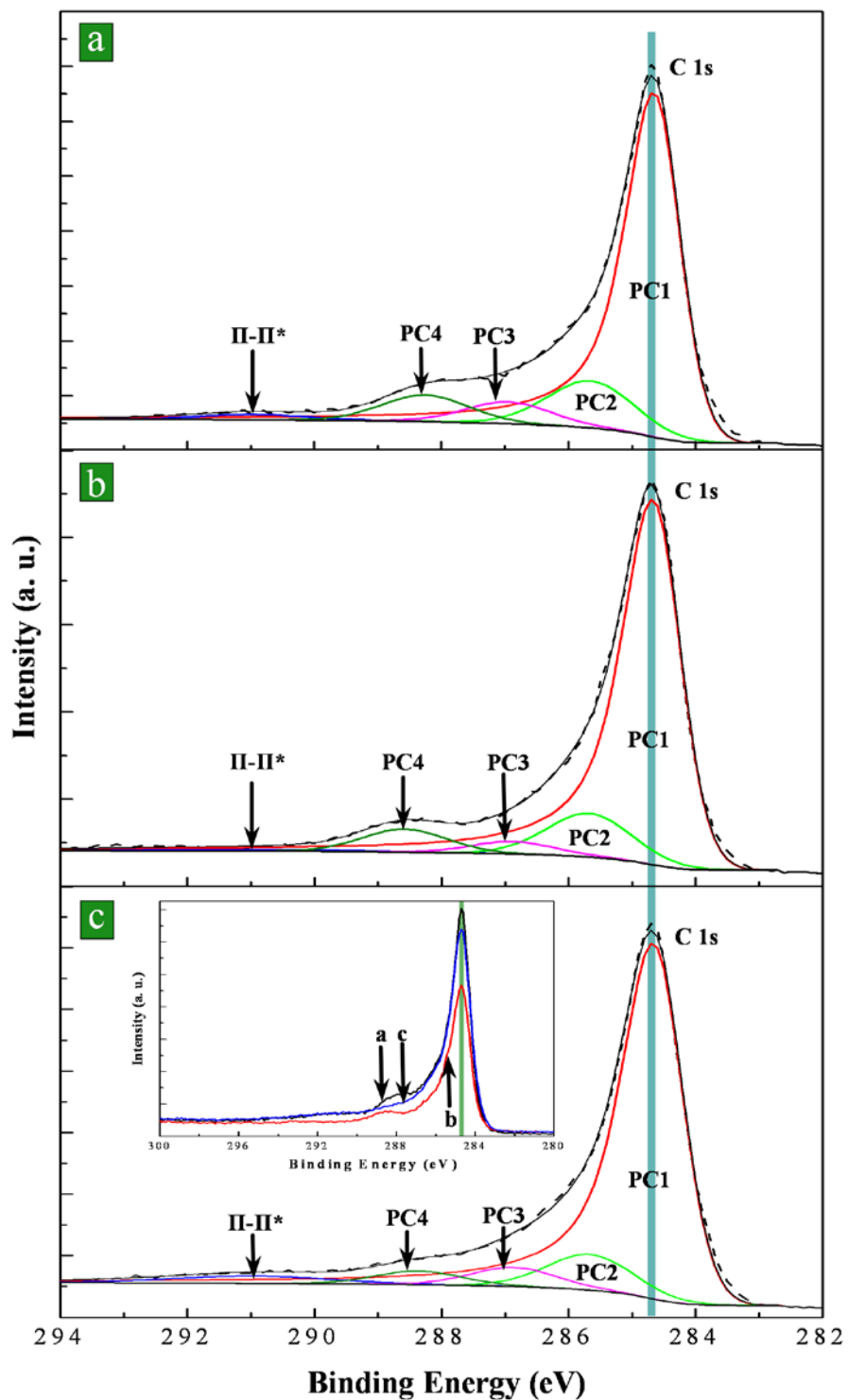


Figure 6.6 High-resolution XPS spectra of C 1s peak for (a) pristine N-CNTs as well as for N-CNTs coated with 100-cycle ALD-SnO₂ at (b) 200 °C and (c) 400 °C (insert: comparison of C 1s peaks).

to C-N and C-O bonds, and π - π^* transition (291 eV) [49], respectively. In comparison to the uncoated sample (figure 6.6(a)), it is observed that the defective sub-peaks (PC2 - PC4) of the two coated samples (figure 6.6(b) and (c)) show some decrease. Quantitatively, the areal ratio between the areal addition of PC2 - PC4 and the area of PC1 is 0.47, 0.34, and 0.29 for the uncoated sample and the two samples coated at 200 and 400 °C, respectively. The reducing areal ratio accounts for a decreasing area of the defective peaks and suggests that ALD-SnO₂ preferentially happened on the defective sites, for the deposited SnO₂ could lead to a block effect on XPS measurements of the defective sites. In a much clearer view, the three C 1s peaks are compared in the insert of figure 6.6(c). In comparison to the uncoated sample (marked as “a”), the C 1s peak for the sample coated at 200 °C (marked as “b”) becomes narrower and weaker. This should be incurred by the uniform deposition of SnO₂ nanoparticles (as shown in figure 6.2(c) and (d)). On the other hand, the C 1s peak for the sample coated at 400 °C (marked as “c”) only shows a slight decrease along the centered line while there is an evident reduction in the defective area. These changes are consistent with the selective deposition of SnO₂ nanoparticles at 400 °C (as shown in figure 6.3(b)), in which some defective sites must have been preferentially covered. Based on the above discussion, it is reasonable to conclude that N-related defective sites are responsible for the deposition of SnO₂.

To further clarify the roles of different doped-N configurations, figure 6.7(a) – (c) show the N 1s spectra of the three samples with high resolution, in which the dashed lines represent raw data and the solid lines are the corresponding fittings. The N 1s spectrum of the uncoated sample (figure 6.7(a), a N content of 14.8 at.%) was deconvoluted into four peaks: PN1 (398.7 eV) [44,52] ascribed to the pyridine-like N configuration, PN2 (400.8 eV) [44,52] corresponding to the graphite-like N configuration, as well as PN3 (403.5 eV) and PN4 (405.6 eV) [36] both attributing to nitrogen oxides. As for the two coated samples, it is observed from figure 6.7(b) and (c) that the PN1 peak reduces more evidently than PN2 peak in both cases. The areal ratio between PN1 and PN2 is 4.56, 2.27, and 2.00 for the uncoated sample and the two samples coated at 200 and 400 °C, respectively. The reducing areal ratio strongly suggests that SnO₂ were deposited on the defective sites of the two types but the deposition was more preferential for the pyridine-

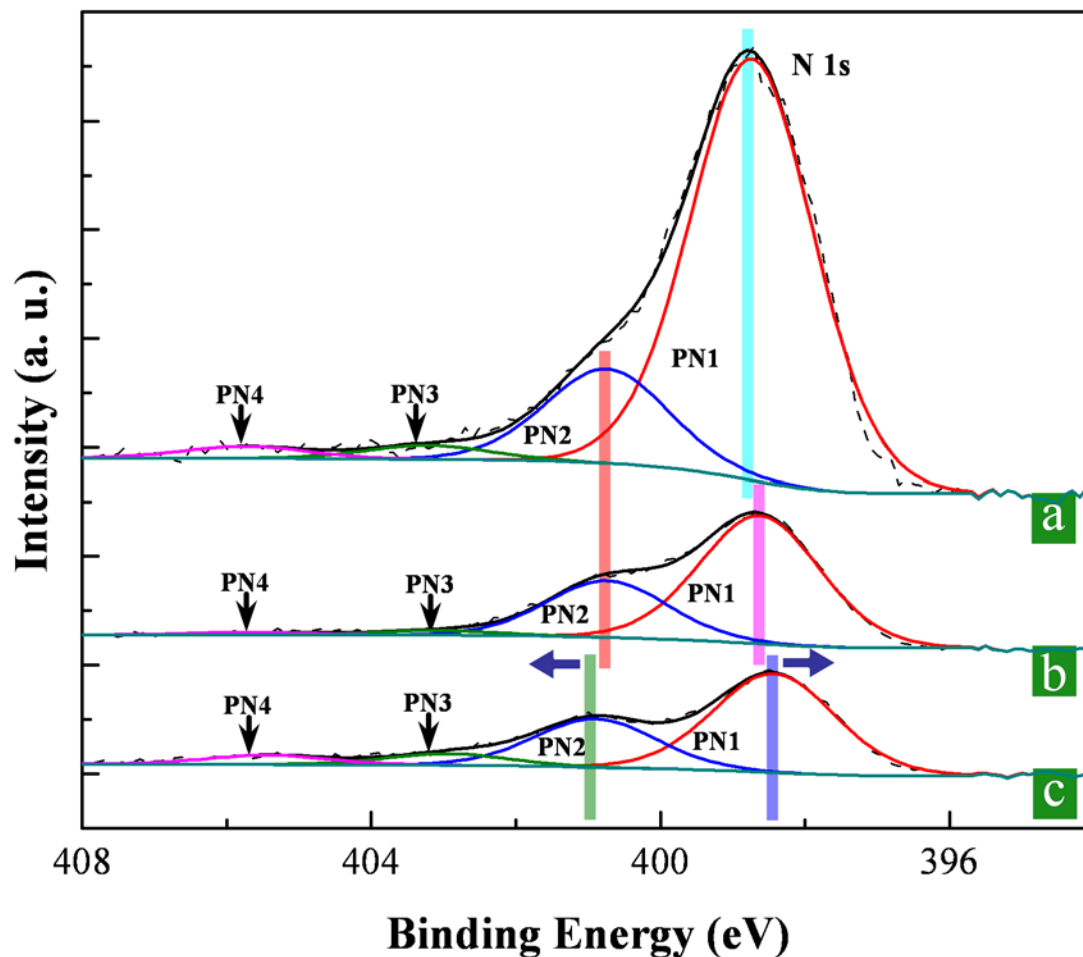


Figure 6.7 High-resolution XPS spectra of N 1s peak for (a) pristine N-CNTs as well as for N-CNTs coated with 100-cycle ALD-SnO₂ at (b) 200 °C and (c) 400 °C.

like N configuration. The selectiveness becomes stronger with growth temperature. In addition, it is also observed from [figure 6.7](#) that the PN1 centered lines of the coated samples move towards the low energy region (right-shifting), implying that the deposited SnO₂ chemically bonded to pyridine-like N configurations. In particular, the energy right-shifting is much larger with the sample coated with crystalline SnO₂ at 400 °C ([figure 6.7\(c\)](#)). On the other hand, it is also noted that there is a shift with the PN2 centered line

of the sample coated at 400 °C (figure 6.7(c)), moving towards the high energy region (left-shifting). The energy left-shifting as well as the larger energy right-shifting with the sample coated at 400 °C suggests that crystalline SnO₂ must have induced stronger interactions to both the pyridine-like and graphite-like N configuration than those incurred by amorphous SnO₂ deposited at 200 °C. The opposite shifting of PN1 and PN2 is evidence to the previous claim [40,46]: pyridine-like and graphite-like N configuration take effect on deposition with different mechanisms. In pyridine-like N configurations, the N atoms could directly bond with metal atoms; in graphite-like N configurations, the N atoms could not bond with metal atoms directly but mediated their neighboring C atoms to bond with metal atoms [40,46]. It is also worth noting that for a given coated sample its pyridine-like N atoms shifted more in binding energy than its graphite-like N atoms. This is in well agreement with the earlier claim that the pyridine-like N configuration induces a stronger binding energy to metal atoms than the graphite-like N one. In addition, it needs to mention that nitrogen oxides (PN3 and PN4) are not counted as main factors in this discussion, due to their low compositions. If one would compare figure 6.7(c) with (a), it is not difficult to observe that nitrogen oxides have little change after ALD-SnO₂. The reduction of nitrogen oxides in figure 6.7(b) may be due to a full coverage of SnO₂ on N-CNTs (see figure 6.2(d)), which induced some block to XPS measurements.

Based on the above discussion, it is reasonable to conclude that defective sites induced by N-doping are responsible for the initiation of ALD-SnO₂. Of the doped-N configurations, the pyridine-like and graphite-like ones are the main forces for ALD-SnO₂. In comparison, the pyridine-like N atoms took the predominant roles, for they provided higher binding energies to certain precursor atoms. This predominance became more evident with an increased growth temperature, for the adsorption of atoms needs a higher binding energy under a higher temperature. As revealed in figure 6.3(f) and (g), there are more SnO₂ nanoparticles deposited in the regions of the interlinked nodes at 400 °C. These regions are dominated by the pyridine-like N configuration [53], and consequently higher binding energies provided by the pyridine-like N atoms led more SnO₂

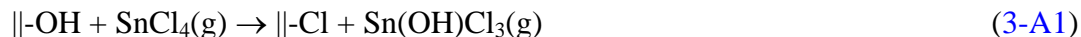
nanoparticles to deposit in the interlinked nodes. Thus, this also explained why the coverage of SnO₂ decreased at 400 °C, in comparison to the cases at 200 °C and 300 °C.

6.3.2.2. The characteristics of surface chemistry

In addition to the above investigation on the effects of N-doping on ALD-SnO₂, we also explored the underlying mechanisms responsible for the growth characteristics of ALD-SnO₂. As revealed in [Section 3.1](#), the ALD-SnO₂ showed a strong dependence on growth temperatures, resulting in amorphous nanoparticles/films ([figure 6.2](#)) at 200 °C, crystalline nanoparticles ([figure 6.3](#)) at 400 °C, and amorphous films embellished with crystalline nanoparticles ([figure 6.4](#)) at 300 °C. Obviously, there existed phase-transition in ALD-SnO₂ processes. To understand the temperature-dependent phase-transition, one view from surface chemistry will be helpful, for surface reactions are crucial and possible to change with temperature in ALD processes.

Earlier studies [[54-56](#)] noticed that the ALD processes of using metal chlorides and water as precursors always produced crystalline nanoparticles (e.g., TiO₂ or ZrO₂) on silica or alumina substrates when a threshold temperature (300 °C) was reached. Otherwise, amorphous films were formed at lower temperatures. More importantly, Puurunen [[57](#)] reviewed this sort of ALD processes, and further investigated the underlying mechanisms from a view of surface chemistry. It was suggested that the phase-transition of a deposited material is due to the changing ALD surface reactions with temperature, especially in the pulse of a metal chloride. This researcher postulated that ligand exchange (as described in [Reaction 2-A](#)) dominates surface reactions at a growth temperature lower than 300 °C, while chlorination becomes predominant at a growth temperature higher than 300 °C. Ligand exchange competes against chlorination in ALD processes, and their dominance highly depends on the growth temperature. Based on Puurunen's work, we proposed both ligand exchange and chlorination for ALD-SnO₂ in this study. For a low growth temperature, the dominant ligand exchange happens in both the pulse of SnCl₄ and H₂O, as shown in [Reaction 2-A](#) and [2-B](#), respectively. As a consequence, ligand exchange contributes to a layer-by-layer growth of SnO₂, as

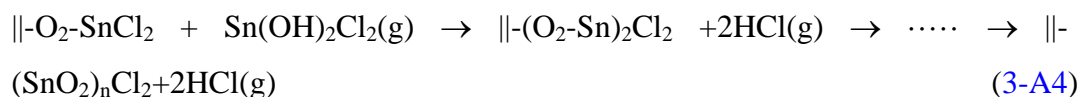
demonstrated in [figure 2](#). For a high growth temperature, the dominant chlorination happens in the pulse of SnCl₄ as follows:



First, SnCl₄ chlorinates the surface hydroxyl groups and form an intermediate hydroxychloride molecule (Sn(OH)₂Cl₂) in a two-step reaction, as shown by [Reaction 3-A1](#) and [3-A2](#). Then, the hydroxychlorides further react with surface chlorine groups via their hydroxyl groups, as shown in [Reaction 3-A3](#) as follows:



In particular, the chlorine groups on the right side of the above [Reaction 3-A3](#) further react with hydroxychlorides in a chain of reactions, as shown in the following [Reaction 3-A4](#):



As a consequence, a multilayer of SnO₂ is formed in one pulse of SnCl₄, accounting for a quicker growth of nanoparticles at a high temperature (e.g., 400 °C) than the one at a low temperature (e.g., 200 °C) after a same number of cycles. Additionally, it is worth noting that crystalline nanoparticles (shown in [figure 6.3](#) and [figure 6.4](#)) varied in sizes, i.e., they did not nucleate at the same time and with a same rate. It is ascribed to the exposure variances of local sites in the pulse of SnCl₄. A sufficient exposure of SnCl₄ contributes to big nanoparticles grown on some sites while a deficient exposure of SnCl₄ leads to small nanoparticles grown on other sites. However, in a pulse of H₂O the surface reaction is the same as described in [Reaction 2-B](#), and rewritten as:



It is obvious that chlorination leads to a non-uniform growth of SnO₂, as demonstrated in [figure 6.3](#). Furthermore, the case of ALD-SnO₂ at 300 °C ([figure 6.4](#)) provides a strong support to the competing behavior between ligand exchange and chlorination, resulting in amorphous films embellished with crystalline nanoparticles. Thus, it is reasonable to conclude that growth temperatures determined the phase-transition of SnO₂, at which different surface reactions are dominant. As for the limited coverage of SnO₂ at 400 °C, besides the reason due to the difference between different doped-N configurations (as

discussed in the section of 3.2.1), another reason is the deficient exposure of SnCl_4 to some local defective sites.

Furthermore, it is noteworthy that the ALD- SnO_2 at 200 °C experienced an island-like growth in the first 100 cycles before a layer of SnO_2 film was formed by the coalescence of nanoparticles. However, the island-like growth mode at 200 °C is different from the growth of crystalline nanoparticles at 400 °C in mechanism. The former one is determined by the reactive nature of the N-CNT surface (mainly due to density of functional groups) and presents a substrate-inhibited characteristic, while the latter one is mainly due to the chlorination as discussed above.

To further help form a better understanding on this study, we schematically summarized the characteristics of the ALD- SnO_2 on N-CNTs in figure 6.8. Figure 6.8(a) emphasizes the effects of N-doping. Figure 6.8(a1) shows two main doped-N (pyridine-like and graphite-like) configurations in pristine N-CNTs. In the first ALD cycle, SnCl_4 is chemically adsorbed on the surface of N-CNTs via N-related defects (figure 6.8(a2)), and then chlorine (Cl) groups are replaced by hydroxyl (OH) groups in the following reaction (figure 6.8(a3)). According to our findings in this study, growth temperature took important influences on ALD- SnO_2 . As shown in figure 6.8(b), the influences of temperature are clarified. First, the coverage of OH groups on N-CNTs changes with temperature (figure 6.8(b1)): there are more OH groups around interlinked nodes (indicated by blue rings on N-CNTs) at a high (H: 400 °C) temperature while the distribution of OH groups is uniform at a low (L) and an intermediate (I) temperature. In a following SnCl_4 pulse, the surface reactions are temperature-dependent. In figure 6.8(b2), ligand exchange (L column) and chlorination (H column) are dominant at a low and high temperature, respectively. For an intermediate temperature (I column), the two reactions compete and coexist with each other. In a following H_2O pulse (figure 6.8(b3)), however, ligand exchange is dominant for all the temperatures. Repeating ALD- SnO_2 with m -cycles (≤ 100) (figure 6.8(b4)), the deposited SnO_2 presents amorphous (L column), crystalline (H column), and coexisting amorphous-crystalline nanoparticles (I column) for different temperatures. In addition, the coverage is mainly dependent on the

initial distribution of OH groups (figure 6.8(b1)). With increased k-cycles (> 100) (figure 6.8(b5)), coaxial films are formed on N-CNTs at a low (L column) and an intermediate temperature (I column), but the latter is decorated with some growing crystalline nanoparticles. At a high temperature (H column), only crystalline nanoparticles are deposited and grow with a tendency to coalesce.

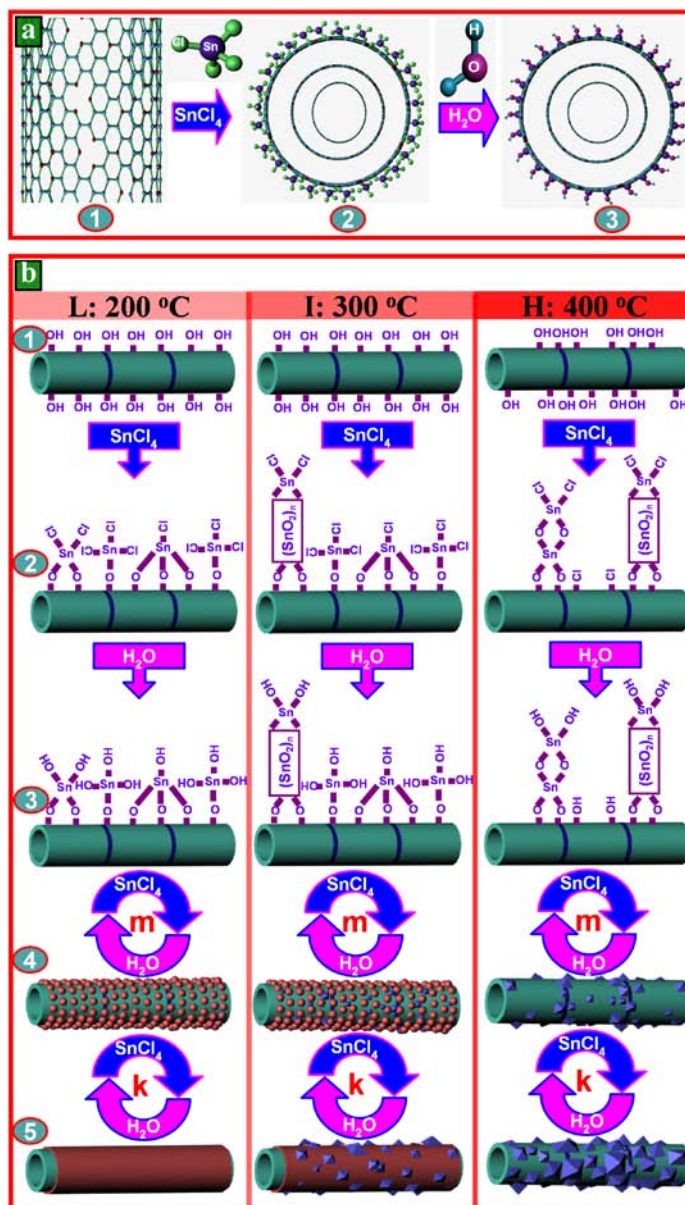


Figure 6.8 Schematic diagram of ALD- SnO_2 on N-CNTs. (a) The first ALD- SnO_2 cycle functionalized the surface of N-CNTs: (1) pristine N-CNTs decorated by N-doping defects, (2) SnCl_4 chemically adsorbed on N-CNTs in the first ALD half reaction induced by N-doping defects, and (3) OH functional groups

generated in the second ALD half reaction induced by H₂O. (b) The temperature-dependent ALD-SnO₂ on N-CNTs: (1) N-CNTs (blue rings indicating interlinked nodes) uniformly covered by OH groups at low (L: 200 °C) and intermediate (I: 300 °C) temperature, but with more OH groups around interlinked nodes at high (H: 400 °C) temperature; (2) the half-reaction of SnCl₄ dominated by ligand exchange (L), chlorination (H), as well as a competition (I) between the two, respectively; (3) the half-reaction of H₂O dominated by ligand exchange in all the cases (L, I, and H); (4) N-CNTs deposited with tiny amorphous (L), crystalline (H), as well as coexisting amorphous-crystalline nanoparticles (I) after m-cycles ($m \leq 100$) of ALD-SnO₂; (5) N-CNTs deposited with coaxial amorphous film (L), coalesced crystalline nanoparticles (H), as well as coaxial amorphous film decorated with crystalline nanoparticles (I) after k-cycles ($k > 100$) of ALD-SnO₂.

In summary, the ALD-SnO₂ on N-CNTs is temperature-dependent via two routes: (i) the adsorption of the tin source precursor (SnCl₄) on the surface of N-CNTs was reduced with an increased growth temperature, owing to the variances of different doped-N configurations to chemically adsorb precursor molecules; (ii) the inherent surface reactions changed with growth temperature and there was a competition between ligand exchange and chlorination for dominance. Consequently, the synthesized hybrid nanostructures present controllable phases: amorphous (dominated by ligand exchange), crystalline (dominated by chlorination), as well as a coexisting amorphous-crystalline phase (dominated by the competition between ligand exchange and chlorination). In addition, the morphologies of the deposited SnO₂ are also controllable, presenting coaxial nanoparticles or nanofilms.

6.4 Conclusions

In this paper, we demonstrated a strategy to synthesize a series of novel SnO₂-CNT hybrid materials in a highly controllable means. This strategy was featured by applying ALD-SnO₂ directly on N-CNTs and exhibited some unique advantages. First of all, the N-CNTs could initiate the following ALD-SnO₂ directly, exempt from any pretreatment as widely used for undoped CNTs. In addition, ALD benefited the deposited SnO₂ with tunable morphologies from nanoparticles to nanofilms. Furthermore, the temperature-

dependent nature of surface reactions contributed the deposited SnO₂ to controllable phases from amorphous to crystalline or a coexisting amorphous-crystalline phase. In order to get a better understanding on the role of N-CNTs and the temperature-dependent nature of ALD-SnO₂, we also explored the underlying mechanisms. Using XPS, we first investigated the effects of N-doping on the initiation of ALD-SnO₂. It was revealed that N-related defects were crucial, especially the graphite-like and pyridine-like N configuration. In comparison, pyridine-like N configuration played a more important role in ALD-SnO₂. As for the controllable phases with growth temperature, it was suggested that different growth temperatures induced different surface reactions in ALD-SnO₂ and thereby determined the phase of the deposited SnO₂. It is believed that ligand exchange was dominant at low temperatures while chlorination was paramount at high temperatures. The former led to amorphous SnO₂ deposited at 200 °C while the latter was responsible for crystalline SnO₂ deposited at 400 °C. The two competed with each other with temperature, and led to a coexisting amorphous-crystalline phase of SnO₂ deposited at 300 °C. As a consequence, this work not only fulfilled a new strategy for synthesizing SnO₂-CNT hybrid materials but provided the underlying mechanisms for a better understanding as well. In particular, these novel SnO₂-CNT hybrids have great potential applications in many important areas, such as lithium-ion batteries, and gas-sensors, etc.

Acknowledgements

This research was supported by the Natural Science and Engineering Research Council of Canada (NSERC), Canada Research Chair (CRC) Program, Canadian Foundation for Innovation (CFI), Ontario Research Fund (ORF), Early Researcher Award (ERA) and the University of Western Ontario. In addition, the authors would like to appreciate Mr. Mark Biesinger at Surface Science Western and Mr. Fred Pearson at McMaster University.

References

- [1] M. Monthieux and V. L. Kuznetsov, Who should be given the credit for the discovery of carbon nanotubes, *Carbon*, 2006, **44**, 1621-1623.
- [2] S. Iijima, Helical microtubules of graphitic carbon, *Nature*, 1991, **354**, 56-58.
- [3] H. Dai, Carbon nanotubes: synthesis, integration, and properties, *Acc. Chem. Res.*, 2002, **35**, 1035-1044.
- [4] H. Zhang, G. Cao, and Y. Yang, Carbon nanotube arrays and their composites for electrochemical capacitors and lithium-ion batteries, *Energy Environ. Sci.*, 2009, **2**, 932-943.
- [5] Z. Li, H. Wang, P. Liu, B. Zhao, and Y. Zhang, Synthesis and field-emission of aligned SnO₂ nanotubes arrays, *Appl. Surf. Sci.*, 2009, **255**, 4470-4473.
- [6] L. A. Ma and T. L. Guo, Synthesis and field emission properties of needle-shaped SnO₂ nanostructures with rectangular cross-section, *Mater. Lett.*, 2009, **63**, 295-297.
- [7] M. Batzill, Surface science studies of gas sensing materials: SnO₂, *Sensors*, 2006, **6**, 1345-66.
- [8] Y. Idota, T. Kubota, A. Matsufuji, Y. Maekawa, and T. Miyasaka, Tin-based amorphous oxide: a high-capacity lithium-ion-storage material, *Science*, 1997, **276**, 1395-1397.
- [9] N. Zhao, L. Fu, L. Yang, T. Zhang, G. Wang, Y. Wu, et al., Nanostructured anode materials for Li-ion batteries, *Pure Appl. Chem.*, 2008, **80**, 2283-2295.
- [10] F. Cheng, Z. Tao, J. Liang, and J. Chen, Template-directed materials for rechargeable lithium-ion batteries, *Chem. Mater.*, 2008, **20**, 667-681.
- [11] A. Yang, X. Tao, R. Wang, S. Lee, and C. Surya, Room temperature gas sensing properties of SnO₂/multiwall-carbon-nanotube composite nanofibers, *Appl. Phys. Lett.*, 2007, **91**, 133110.
- [12] J. Gong, J. Sun, and Q. Chen, Micromachined sol-gel carbon nanotube/SnO₂ nanocomposite hydrogen sensor, *Sens. Actuators B*, 2008, **130**, 829-835.
- [13] N. D. Hoa, N. V. Quy, H. Song, Y. Kang, Y. Cho, and D. Kim D, Tin oxide nanotube structures synthesized on a template of single-walled carbon nanotubes, *J. Crystal Growth*, 2009, **311**, 657-661.

- [14] Q. Kuang, S. F. Li, Z. X. Xie, S. C. Lin, X. H. Zhang, S. Y. Xie, et al., Controllable fabrication of SnO₂-coated multiwalled carbon nanotubes by chemical vapour deposition, *Carbon*, 2006, **44**, 1166-1172.
- [15] W. Q. Han and A. Zettl, Coating single-walled carbon nanotubes with tin oxide, *Nano Lett.*, 2003, **3**, 681-683.
- [16] Z. Wen, Q. Wang, Q. Zhang, and J. Li, In situ growth of mesoporous SnO₂ on multiwalled carbon nanotubes: a novel composite with porous-tube structure as anode for lithium batteries, *Adv. Funct. Mater.*, 2007, **17**, 2772-2778.
- [17] H. X. Zhang, C. Feng, Y. C. Zhai, K. L. Jiang, Q. Q. Li, and S. S. Fan, Cross-stacked carbon nanotube sheets uniformly loaded with SnO₂ nanoparticles: a novel binder-free and high-capacity anode material for lithium-ion batteries, *Adv. Mater.*, 2009, **21**, 2299-2304.
- [18] Y. Myung, D. M. Jang, Y. J. Cho, H. S. Kim, J. Park, J. U. Kim, et al., Nonenzymatic amperometric glucose sensing of platinum, copper sulphide, and tin oxide nanoparticle-carbon nanotube hybride nanostructures, *J. Phys. Chem. C*, 2009, **113**, 1251-1259.
- [19] G. Chen, Z. Wang, and D. Xia, One-pot synthesis of carbon nanotube@SnO₂-Au coaxial nanocable for lithium-ion batteries with high-rate capability, *Chem. Mater.*, 2008, **20**, 6951-6956.
- [20] N. Du, H. Zhang, B. Chen, X. Ma, X. Huang, J. Tu, et al., Synthesis of polycrystalline SnO₂ nanotubes on carbon nanotube template for anode material of lithium-ion battery, *Mater. Res. Bull.*, 2009, **44**, 211-215.
- [21] M. Terrones, A. Jorio, M. Endo, A. M. Rao, Y. A. Kim, T. Hayashi, et al., New direction in nanotube science, *Materials Today*, 2004, **7**, 30-45.
- [22] S. M. Georgem, Atomic layer deposition: an overview, *Chem. Rev.*, 2010, **110**, 111-131.
- [23] M. Knez, K. Nielsch, and L. Niinistö, Synthesis and surface engineering of complex nanostructures by atomic layer deposition, *Adv. Mater.*, 2007, **19**, 3425-3438.
- [24] H. Kim, H. B. R. Lee, and W. J. Maeng, Applications of atomic layer deposition to nanofabrication and emerging nanodevices, *Thin Solid Films*, 2008, **517**, 2563-2580.
- [25] A. Rosental, A. Tarre, A. Gerst, T. Uustare, and V. Sammelselg, Atomic-layer

chemical vapor deposition of SnO₂ for gas-sensing applications, *Sens Actuators B*, 2001, **77**, 297-300.

[26] A. Tarre, A. Rosental, V. Sammelseg, and T. Uustare, Comparative study of low-temperature chloride atomic-layer chemical vapor deposition of TiO₂ and SnO₂, *Appl. Surf. Sci.*, 2001, **175**, 111-116.

[27] A. Tarre, A. Rosental, A. Aidla, J. Aarik, J. Sundqvist, and A. Hårsta, New routes to SnO₂ heteroepitaxy, *Vacuum*, 2002, **67**, 571-575.

[28] T. Takeuchi, K. Shoji, T. Tadano, I. Doteshta, and S. Onodera, Preparation of sub-nanometer thickness-controlled thin dioxide films by pulsed atomic-layer CVD, *Thin Solid Films*, 2003, **442**, 98-101.

[29] A. Rosental, A. Tarre, A. Gerst, J. Sundqvist, A. Hårsta, A. Aidla, et al., Gas sensing properties of epitaxial SnO₂ thin films prepared by atomic layer deposition, *Sens Actuators B*, 2003, **93**, 552-555.

[30] T. Takeuchi, I. Doteshta, and S. Asami, Epitaxial growth of sub-nanometre thick thin dioxide films on sapphire substrates by pulsed atomic layer chemical vapour deposition, *Surf. Interface Anal.*, 2004, **36**, 1133-1135.

[31] J. Lu, J. Sundqvist, M. Ottosson, A. Tarre, A. Rosental, J. Aarik, et al., Microstructure characterisation of ALD-grown epitaxial SnO₂ thin films, *J. Crystal Growth*, 2004, **260**, 191-200.

[32] G. Natarajan and D. C. Cameron, Influence of oxygen depletion layer on the properties of tin oxide gas-sensing films fabricated by atomic layer deposition, *Appl. Phys. A*, 2009, **95**, 621-627.

[33] X. Du, Y. Du, and S. M. George, In situ examination of tin oxide atomic layer deposition using quartz crystal microbalance and Fourier transform infrared techniques, *J. Vac. Sci. Technol. A*, 2005, **23**, 581-588.

[34] J. D. Ferguson, K. J. Buechler, A. W. Weimer, and S. M. George, SnO₂ atomic layer deposition on ZrO₂ and Al nanoparticles: pathway to enhanced thermite materials, *Powder Technol.*, 2005, **156**, 154-163.

[35] X. Du, Y. Du, and S. M. George, CO gas sensing by ultrathin tin oxide films grown by atomic layer deposition using transmission FTIR spectroscopy, *J. Phys. Chem. A*, 2008, **112**, 9211-9219.

- [36] Y. Zhong, M. Jaidann, Y. Zhang, G. Zhang, H. Liu, M. I. Ionescu, et al., Synthesis of high nitrogen doping of carbon nanotubes and modeling the stabilization of filled DAATO@CNTs (10,10) for nanoenergetic materials, *J. Phys. Chem. Solids*, 2010, **71**, 134-139.
- [37] R. L. Puurunen, Surface chemistry of atomic layer deposition: a case study for the trimethylaluminum/water process, *J. Appl. Phys.*, 2005, **97**, 121301.
- [38] S. Peng and K. Cho, Ab initio study of doped carbon nanotube sensors, *Nano Lett.*, 2003, **3**, 513-517.
- [39] C. L. Sun, L. C. Chen, M. C. Su, L. S. Hong, O. Chyan, C. Y. Hsu, et al., Ultrafine platinum nanoparticles uniformly dispersed on arrayed CN_x nanotubes with high electrochemical activity, *Chem. Mater.*, 2005, **17**, 3749-3753.
- [40] S. H. Yang, W. H. Shin, J. W. Lee, H. S. Kim, J. K. Kang, and Y. K. Kim, Nitrogen-mediated fabrication of transition metal-carbon nanotube hybrid materials, *Appl. Phys. Lett.*, 2007, **90**, 013103.
- [41] S. Sun, G. Zhang, Y. Zhong, H. Liu, R. Li, X. Zhou, et al., Ultrathin single crystal Pt nanowires grown on N-doped carbon nanotubes, *Chem. Comm.*, 2009, **45**, 7048-7050.
- [42] H. C. Choi, J. Park, and B. Kim, Distribution and structure of N atoms in multiwalled carbon nanotubes using variable-energy X-ray photoelectron spectroscopy, *J. Phys. Chem. B*, 2005, **109**, 4333-4340.
- [43] S. H. Yang, W. H. Shin, and J. K. Kang, The nature of graphite- and pyridinelike nitrogen configurations in carbon nitride nanotubes: dependence on diameter and helicity, *Small*, 2008, **4**, 437-4341.
- [44] H. C. Choi, S. Y. Bae, W. S. Jang, J. Park, H. J. Song, H. J. Shin, et al., Release of N₂ from the carbon nanotubes via high-temperature annealing, *J. Phys. Chem. B*, 2005, **109**, 1683-1688.
- [45] S. Stafström, Reactivity of curved and planar carbon-nitride structures, *Appl. Phys. Lett.*, 2000, **77**, 3941-3943.
- [46] Y. H. Li, T. H. Hung, and C. W. Chen, A first-principles study of nitrogen- and boron-assisted platinum adsorption on carbon nanotubes, *Carbon*, 2009, **47**, 850-855.

- [47] J. J. Li, W. T. Zheng, H. H. Wu, L. Sun, G. G. Gu, H. J. Bian, et al., Compositional and structural modifications of amorphous carbon nitride films induced by thermal annealing, *J. Phys. D Appl. Phys.*, 2003, **36**, 2001-2005.
- [48] J. J. Li, W. T. Zheng, Z. S. Jin, T. X. Gai, G. R. Gu, H. J. Bian, et al., Thermal stability of magnetron sputtering amorphous carbon nitride films, *Vacuum*, 2004, **72**, 233-239.
- [49] H. Estrade-Szwarckopf, XPS photoemission in carbonaceous materials: a “defect” peak beside the graphitic asymmetric peak, *Carbon*, 2004, **42**, 1713-1721.
- [50] D. Marton, K. J. Boyd, A. H. Al-Bayati, S. S. Todorov, and J. W. Rabalais, Carbon nitride deposited using energetic species: a two-phase system, *Phys. Rev. Lett.*, 1994, **73**, 118-121.
- [51] L. H. Chan, K. H. Hong, D. Q. Xiao, T. C. Lin, S. H. Lai, W. J. Hsieh, et al., Resolution of the binding configuration in nitrogen-doped carbon nanotubes, *Phys. Rev. B*, 2004, **70**, 125408.
- [52] S. Maldonado, S. Morin, and K. J. Stevenson, Structure, composition, and chemical reactivity of carbon nanotubes by selective nitrogen doping, *Carbon*, 2006, **44**, 1429-1437.
- [53] M. Terrones, P. M. Ajayan, F. Banhart, X. Blase, D. L. Carroll, J. C. Charlier, et al., N-doping and coalescence of carbon nanotubes: synthesis and electronic properties, *Appl. Phys. A*, 2002, **74**, 355-361.
- [54] S. Haukka, E. L. Lakomaa, and A. Root, An IR and NMR study of the chemisorption of TiCl_4 on silica, *J. Phys. Chem.*, 1993, **97**, 5085-5094.
- [55] S. Haukka, E. L. Lakomaa, O. Jylhä, J. Vilhunen, and S. Hornytzkyj, Dispersion and distribution of titanium species bound to silica from TiCl_4 , *Langmuir*, 1993, **9**, 3497-3506.
- [56] A. Kytökivi, E. L. Lakomaa, and A. Root, Controlled formation of ZrO_2 in the reaction of ZrCl_4 vapor with porous silica and γ -alumina surfaces, *Langmuir*, 1996, **12**, 4395-4403.
- [57] R. L. Puurunen, Formation of metal oxide particles in atomic layer deposition during the chemisorption of metal chlorides: a review, *Chem. Vap. Deposition*, 2005;**11**, 79-90.

CHAPTER 7

NON-AQUEOUS APPROACH TO SYNTHESIZE AMORPHOUS/CRYSTALLINE METAL OXIDE- GRAPHENE NANOSHEET HYBRID COMPOSITES

A version of this chapter has been published in *Journal of Physical Chemistry C*, 2010, 114, 18330-18337.

Nowadays there is a dramatically increasing interest in developing graphene-supported nanocomposites, due to their unprecedented properties. Different from the methods exposed in previous studies, this article presents a non-aqueous approach of using atomic layer deposition (ALD) to constitute novel metal oxide-graphene hybrid nanocomposites based on graphene nanosheet (GNS) powders. It is demonstrated that this gas-solid strategy exhibits many unique benefits. It reports for the first time that the as-prepared SnO₂-GNS nanocomposites are featured with not only tunable morphologies but controllable amorphous and crystalline phases of SnO₂ component as well, using SnCl₄ and H₂O as the ALD precursors. Furthermore, the determinant factors and underlying mechanisms were outlined and discussed in this work. As a consequence, besides the demonstration of ALD being an important approach for nanoarchitecturing novel metal oxide-GNS composites, the as-synthesized SnO₂-GNS hybrid nanocomposites provide more choices for many important applications, such as lithium-ion batteries, solar cells, and gas sensing.

Keywords: *Atomic layer deposition, Graphene, Metal oxide, Tin dioxide, Nanocomposites*

7.1 Introduction

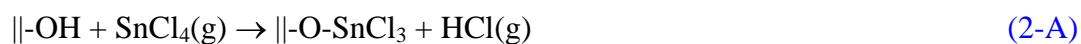
Interest on nanocomposites is ever-growing, ascribed to their peculiarities in combining desirable properties of hybrid nanosized building blocks for a given application. On this way, carbon nanotubes (CNTs) being an excellent one-dimensional (1D) candidate have been extensively incorporated in a wide range of nanocomposites for many applications [1-4]. Nowadays, following up CNTs, graphene being a 2D nanoscale building block is attracting more and more efforts on developing novel nanoarchitected composites since its discovery [5] in 2004. To date, graphene (or graphene stacks, a few layers of graphene) has been reported to incorporate with three main types of materials: polymers [6-9], metals [10-13], and metal oxides [14-20], covering a series of applications (including field emitters, photocatalysis, conductors, supercapacitors, fuel cells, and batteries, etc.) with improved mechanical, electrical, optical, or electrochemical properties. For metal oxide-graphene nanocomposites (MO-GNCs), however, only limited cases were exposed in literature and they were prominently synthesized in aqueous solutions via two routes: wet chemical deposition [15-19] and solution-based mechanical mixing [20]. The former route was generally carried out with a complicated and tedious process, accounting for several tens of hours [15-19]. As an alternative, the latter one was simply performed through mechanically mixing available metal oxide nanoparticles with graphene dispersions [20], having less manipulation on metal oxide nanoparticles and thereby lacking of flexibility and precision as a synthesis strategy. Commonly, the aqueous solution-based methods exposed in literature show inability to precisely control the morphologies and structures of metal oxides.

With attempts to circumvent the above-mentioned issues, recently we successfully fulfilled the synthesis of MO-GNCs via a non-aqueous approach and the first case will be reported in this article. This strategy is featured by applying the technique of atomic layer deposition (ALD) to deposit metal oxides on graphene nanosheet (GNS) powders. Our studies demonstrated that this approach can provide a precise fabrication of MO-GNCs with more benefits, opening a potential avenue for mass production. Characteristically, ALD is a surface-controlled gas-solid process and uniquely performed by two

sequentially cyclic half-reactions [21]. In comparison to wet chemical routes as well as traditional chemical and physical vapor deposition, ALD contributes to a controllable, uniform, and conformal deposition at the atomic level [21], and is going into a fashion in nanotechnology to synthesize novel nanostructures and nanodevices [22,23]. In addition, ALD has capability to deposit both inorganic (metals and metal oxides) [24] and organic materials (polymers) [21]. In the case of SnO₂, it has mainly been performed on flat substrates (e.g., quartz glass) via ALD [25-27] using SnCl₄ and H₂O as well as other precursors. The reaction between SnCl₄ and H₂O is fairly straightforward with the product of SnO₂, as described in the following [Reaction 1](#).



In the ALD of SnO₂ (ALD-SnO₂), however, [Reaction 1](#) was replaced with two sequential half-reactions as suggested as follows [28]:



where the symbol || denotes the substrate surface, and (g) refers to gas phase species. One “A” pulse of SnCl₄ ([Reaction 2-A](#)) and one following “B” pulse of H₂O ([Reaction 2-B](#)) consist of one typical “A-B” cycle in ALD process, and the cycling of “A-B” half-reactions can build up SnO₂ films increasing with accuracy at the atomic level. In this article, we deduce this ALD strategy through exemplifying the synthesis of SnO₂-GNS composites, using SnCl₄ and H₂O as the ALD precursors.

The successful demonstration of ALD-SnO₂ on GNS produced 3-D nanoarchitected networks of SnO₂-GNS composites. More importantly, the composites are featured with tunable morphologies and controllable phases of the SnO₂ component. It was found that the SnO₂ component can present amorphous and crystalline phase through suitably adjusting the growth temperature. In addition, due to the cycling nature of ALD, the synthesis of SnO₂-GNS nanocomposites also showed a characteristic on precisely controlling the morphologies of as-deposited SnO₂. Thus, this article is significant with three main outcomes: (i) ALD was for the first time suggested and successfully demonstrated as an efficient strategy to synthesize MO-GNCs; (2) the as-synthesized nanocomposites of SnO₂-GNS presented fine-tuned morphologies, and (3) well-

controlled structural phases from amorphous to crystalline SnO₂. To highlight the outcomes from this non-aqueous approach, we used a schematic illustration to help readers understand, as shown in [figure 7.1](#). The ALD-SnO₂, as illustrated by [figure 7.1\(a\)](#), is fulfilled by two sequential half reactions induced by SnCl₄ and H₂O, respectively. At a low growth temperature (200 °C), amorphous SnO₂ nanoparticles ([figure 7.1\(b\)](#)) were uniformly formed on GNS in initial ALD cycles. The nanoparticles grew bigger and finally coalesced into a thin film ([figure 7.1\(c\)](#)) with increased ALD cycles. At a high temperature (400 °C), on the other hand, crystalline SnO₂ nanoparticles were deposited on GNS and grew from small sizes ([figure 7.1\(d\)](#)) to large ones ([figure 7.1\(e\)](#)) with increased ALD cycles. Furthermore, the underlying mechanisms responsible for controllable structural phases of SnO₂ were also explored in this work based on surface chemistry.

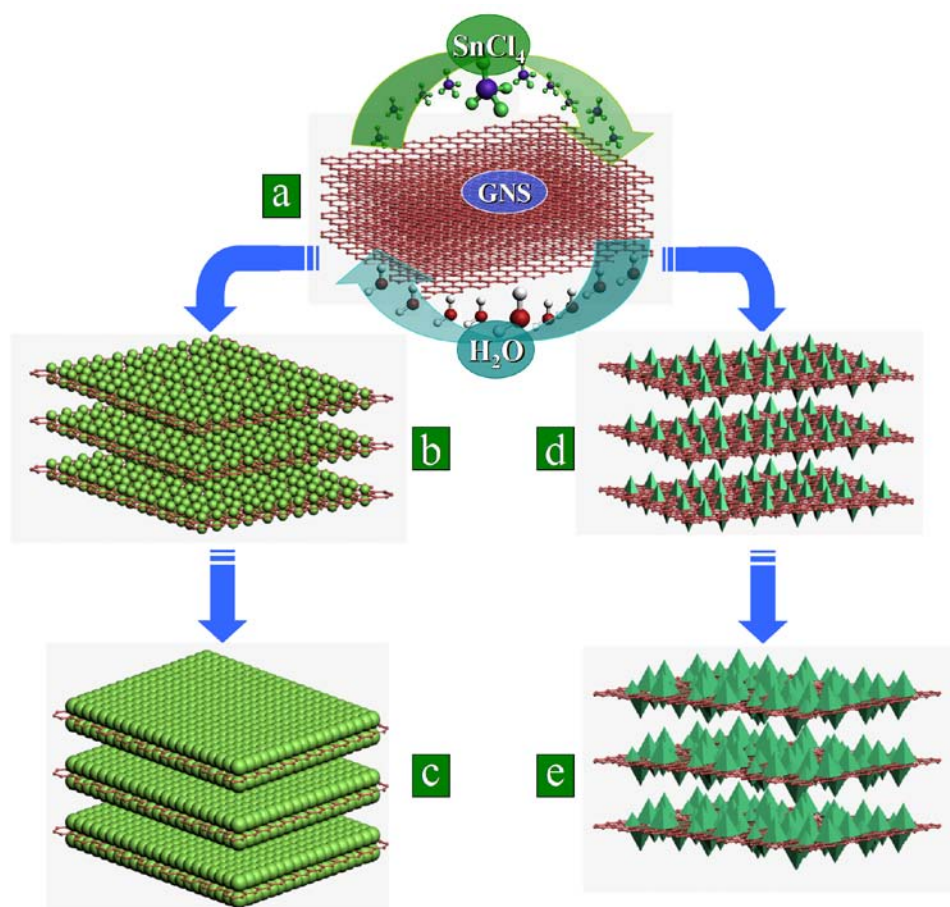


Figure 7.1 Schematic illustration of the precise approach to tune the morphology and amorphous-crystalline phases via atomic layer deposition technique (ALD). (a) ALD-SnO₂ process employed on graphene nanosheets (GNS) using SnCl₄ and H₂O as the two precursors to form amorphous/crystalline SnO₂-GNS nanocomposites; (b) uniformly distributed amorphous SnO₂ nanoparticles on GNS surface and (c) amorphous SnO₂ thin film formed on GNS surface by growing nanoparticles; (d) small crystalline SnO₂ nanoparticles uniformly distributed on GNS surface and (e) large SnO₂ nanoparticles uniformly distributed on GNS surface with higher density.

7.2 Experimental

7.2.1 Preparation of GNS

For preparation of GNS, we first oxidized natural graphite powder (45 μm, 99.99%, Sigma-Aldrich as shown in [figure SI-7.1\(a\)](#) and [\(b\)](#), [Supporting Information](#)) using a modified Hummers method [29]. In detail, graphite powder (1 g) was first stirred in concentrated sulphuric acid (23 ml) with a following addition of sodium nitrate (0.5 g) at room temperature. The stirring lasted for 16 h, and then the mixture was cooled down to 0 °C. Thereafter, potassium permanganate (3 g) was added to form a new mixture. Two hours later, the mixture formed a green slurry around 35 °C, and it was stirred for another 3 h. Then, water (46 ml) was slowly added into the paste with an increased temperature around 98 °C. The suspension was remained at this temperature for 30 minutes before it was further diluted with another addition of water and hydrogen peroxide (140 ml). In the following, the suspension was filtered and washed until the pH value of the filtrate was neutral. The as-received slurry is the so-called graphite oxide (GO, [figure SI-7.1\(c\)](#) and [\(d\)](#), [Supporting Information](#)), which was further dried in a vacuum oven at 60 °C. To prepare GNS, the as-synthesized GO was first flushed by Ar for 20 min in a quartz tube. Then, the quartz tube was promptly moved into a Lindberg tube furnace with a preheated temperature around 1050 °C. After 30 s thermal treatment, GO was reduced into expanded GNS powders as illustrated in [figure 7.2\(a\)](#).

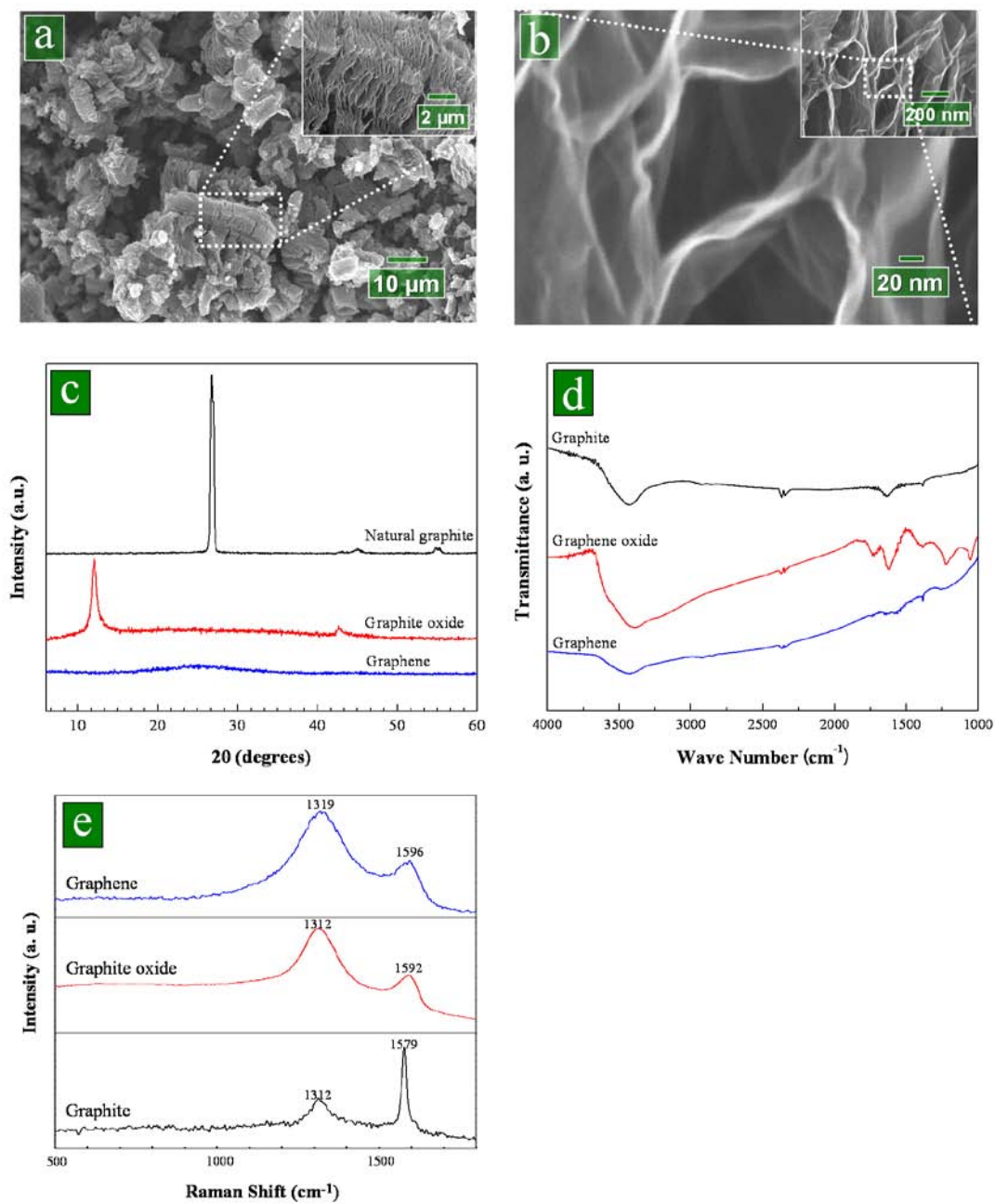


Figure 7.2 Characteristics of GNS: SEM images of (a) low magnification, and (b) high magnification; (c) XRD, (d) FTIR, and (e) Raman spectra.

7.2.2 ALD-SnO₂

The as-synthesized GNS powder was first loaded into a commercial ALD reactor (Savannah 100, Cambridge Nanotechnology Inc., USA) preheated to a preset growth temperature. In this study, two growth temperatures were applied, i.e., 200 and 400 °C. The following ALD-SnO₂ was performed through introducing tin (IV) chloride (99% SnCl₄, Sigma-Aldrich) and deionized water (DI H₂O) into the ALD reactor in an alternating manner. In the ALD processes, nitrogen was selected in this study as the carrier gas with a flow rate of 20 sccm, and the ALD reactor was sustained at a low level of pressure (typically 0.4 Torr) with a vacuum pump (Pascal 2005 I, Adixon). The ALD procedures were set as follows: (1) a 0.5 s supply of SnCl₄; (2) a 3 s extended exposure of SnCl₄ to GNS; (3) a 10 s purge of oversupplied SnCl₄ and any by-products; (4) a 1 s supply of water vapor; (5) a 3 s extended exposure of water vapor to GNS; (6) a 10 s purge of oversupplied water and any by-products. The aforementioned six-step sequence constituted one ALD-SnO₂ cycle and the ALD processes were adjusted with different cycling numbers.

7.2.3 Characterization

To characterize our samples' morphologies, structures, and compositions, we used field emission scanning electron spectrometry (FE-SEM, Hitachi 4800S) coupled with energy dispersive spectroscopy (EDS), transmission electron microscope (TEM, Philips CM10), high-resolution transmission electron microscope (HRTEM, JEOL 2010 FEG), X-ray diffractometer (XRD, Inel multi-purpose diffractometer), Raman spectrometry (RXN1-785, Kaiser Optical Systems InCo.), Fourier transform infrared spectroscopy (FTIR, Bruker Tensor 27), and the results are elucidated in the following sections.

7.3 Results and Discussion

The GNS powders employed in our study were made from natural graphite powders via a series of processes. During the preparation, graphite powders were first oxidized using Hummers method [29] with the product of graphite oxide (GO). Thereafter, GO was reduced via a rapid thermal expansion [30] which separated the layered GO into partially functionalized GNS. The as-synthesized GNS powders were characterized by SEM, XRD, FTIR, and Raman, as illustrated in figure 7.2. In contrast to the natural graphite and GO (figure SI-7.1, Supporting Information), the GNS powders (figure 7.2(a) and insert) present a fluffy worm-like porous structure [31]. The porous “worms” are featured by numerous honeycombs (inset of figure 7.2(b)) surrounded by wrinkles of typically less than 3 nm in thickness (figure 7.2(b)). XRD spectra patterns (figure 7.2(c)) clearly distinguished the as-synthesized GNS from the natural graphite as well as GO. Graphite has the strongest (002) peak at 26.8° as well as three weak peaks of (100), (101), and (004) at 43° , 45° and 55° , respectively. In comparison, GO shows a very strong (001) diffraction peak at 12° , suggesting that the interlayer distance increases and the structure is modified due to oxygenated groups [32], as well as a weak (100) diffraction peak around 43° . In contrast, the GNS received a broad diffraction (002) peak shifted back to 26.8° , implying that GO was reduced via the rapid thermal expansion and the extensive conjugated sp^2 carbon network (i.e., the ordered crystal structure) was restored [33]. FTIR spectra (figure 7.2(d)) further clarified their differences in functional groups. It is easy to observe that the natural graphite mainly shows the stretching vibrations of hydroxyl (-OH) groups (3420 cm^{-1}) and C=C (1586 cm^{-1}), while GO has been added with the stretching vibrations of C=O (1736 cm^{-1}), carboxy C-O (1414 cm^{-1}), epoxy C-O (1220 cm^{-1}), and C-O (1100 cm^{-1}) [34-36]. In comparison, GNS mainly shows the stretching vibrations of hydroxyl (-OH) groups and C=C [34-36]. The FTIR results imply that GNS was significantly reduced, and this is consistent to XRD results. Peaks below 900 cm^{-1} are usually not interpreted for they represent too complex a structural signature [32]. Furthermore, the samples were examined by Raman spectroscopy, an essential tool to characterize graphene [37]. As illustrated in figure 7.2(e), the Raman spectra underwent changes along the graphite-GO-GNS process, similar to those observed in the

graphite to amorphous carbon transition [38]. The Raman spectra of the graphite show the in-phase vibration of the graphite lattice (G band) at 1579 cm^{-1} and a weak D band at 1312 cm^{-1} . The Raman spectra for GO present a broadened G band at 1592 cm^{-1} , owing to the presence of isolated double bonds that resonate at higher frequencies than the G band of graphite [39]. The D band of GO becomes evident and keeps at 1312 cm^{-1} , indicating the reduction in size of the in-plane sp^2 domains due to the extensive oxidation [40]. As for the Raman spectra of GNS, the G and D band are located at and 1596 cm^{-1} and 1319 cm^{-1} , respectively. Besides the similarities of Raman spectra between GO and GNS, it is noteworthy that the D/G intensity ratio of GNS (0.82) is, in comparison with the value (0.78) of graphite, increased, indicating a decrease in the size of the in-plane sp^2 domains and a partially ordered crystalline structure of GNS [38].

The GNS powders were thereafter used to prepare metal oxide-GNS nanocomposites via ALD- SnO_2 under different cycles. The samples after 300-cycle ALD- SnO_2 at $200\text{ }^\circ\text{C}$ and $400\text{ }^\circ\text{C}$ were characterized by XRD, and their XRD spectra were compared with those of the pristine GNS, illustrated in figure 7.3(a). The XRD results show that, in comparison to the pristine GNS, the sample produced at $200\text{ }^\circ\text{C}$ shows no observable change while many characteristic peaks were with the sample produced at $400\text{ }^\circ\text{C}$. To confirm the formation of ALD- SnO_2 at $200\text{ }^\circ\text{C}$, the sample was examined by EDS equipped on FE-SEM, and EDS results (figure 7.3(b)) revealed the presence of Sn, O, and C elements with the sample. The Al peak is resulted from the sample holder for EDS measurement. In addition, there is some Cl element resulting from unreacted functional groups. Thus, combined with the results disclosed by XRD, it was believed that amorphous SnO_2 has been deposited on GNS. On the other hand, the XRD peaks with the sample produced at $400\text{ }^\circ\text{C}$ were identified in the standard card and consistent with those reference values of crystalline SnO_2 (Joint Committee on Powder Diffraction Standards (JCPDS) powder diffraction file (PDF) No. 41-1445). Thus, the ALD approach produced two different types of nanocomposites through simply adjusting growth temperatures: amorphous and crystalline SnO_2 -GNS composites at $200\text{ }^\circ\text{C}$ and $400\text{ }^\circ\text{C}$, respectively.

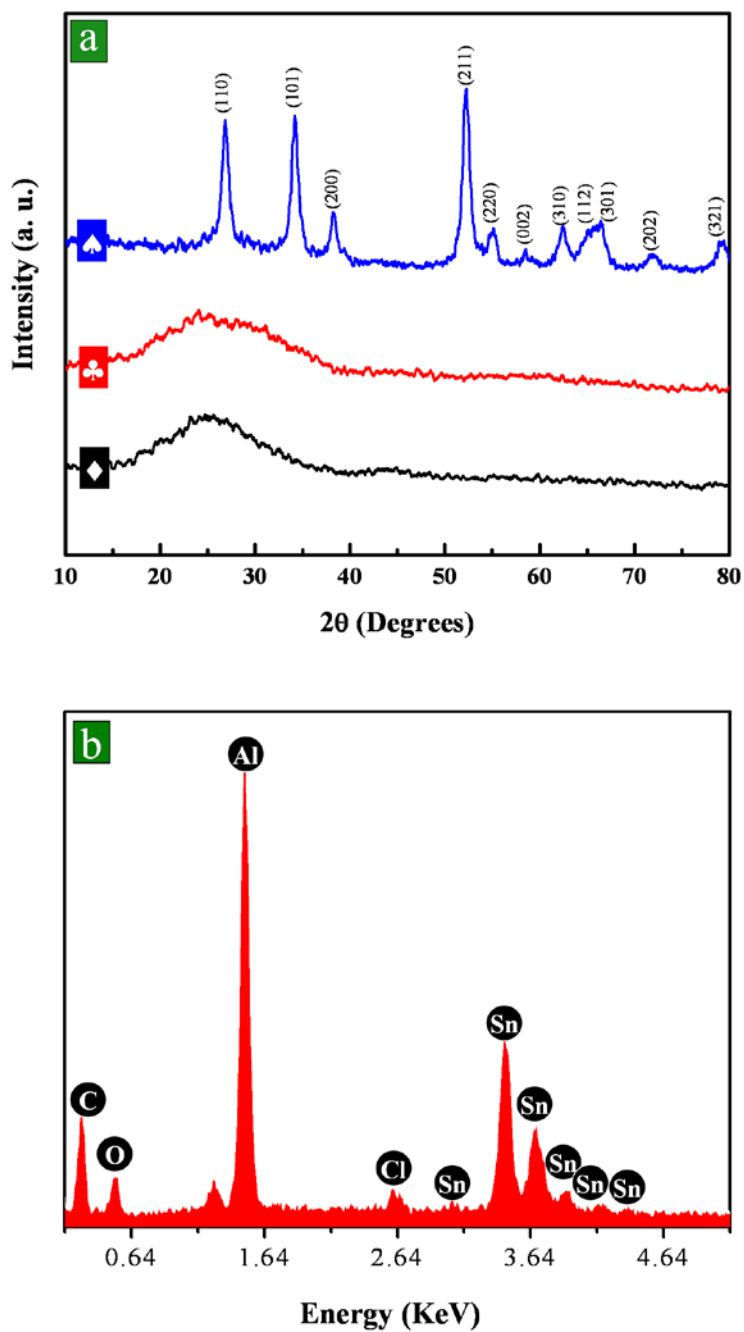


Figure 7.3 (a) XRD spectra of (♦) GNS, (♣) SnO₂-GNS nanocomposites synthesized at 200 °C, and (♠) SnO₂-GNS nanocomposites synthesized at 400 °C; (b) EDS spectra for SnO₂-GNS nanocomposites synthesized at 200 °C.

To further unveil the characteristics of the two types of nanocomposites produced at different temperatures, they were commonly examined by SEM and TEM. As shown in [figure 7.4](#), ALD-SnO₂ on GNS at 200 °C was performed with various ALD cycles. The SEM image for 100 cycles of ALD-SnO₂ ([figure 7.4\(a\)](#)) shows that GNS was covered with tiny nanoparticles (~ 3 nm, [figure SI-7.2\(b\), Supporting Information](#)), which were confirmed by TEM ([insert of figure 7.4\(a\)](#)). Upon 200 ALD cycles ([figure 7.4\(b\)](#)), it was observed that GNS surface has been totally covered by SnO₂ nanoparticles (~ 5 nm, [figure SI-7.2\(d\), Supporting Information](#)) of high density, and the as-synthesized SnO₂-GNS composite remains the porous structure. In the case of 300 ALD cycles, as shown in [figure 7.4\(c\)](#) by SEM image, we observed a thin film formed on GNS. Obviously, the ALD-SnO₂ on GNS surface experienced an island-like growth in the first 200 ALD cycles at a growth temperature of 200 °C before the growing nanoparticles coalesced into a uniform layer. Additionally, it is also noteworthy that the ALD-SnO₂ was deposited equally on both sides of a single graphene (as disclosed in [figure 7.4\(b\) and \(c\)](#)). The sample after 300-cycle ALD-SnO₂ was further examined by TEM, as shown in [figure 7.4\(d\)-\(f\)](#). We can observe from [figure 7.4\(d\)](#) that the nanocomposite retains the morphologies of GNS with numerous wrinkles. In addition, two local areas, as blue-circled as “e” and “f”, were further shown in [figure 7.4\(e\)](#) and [\(f\)](#), respectively. With an increased magnification TEM image in [figure 7.4\(e\)](#), it is worth noting that GNS was uniformly coated, and selected area electron diffraction (SAED, [insert of figure 7.4\(e\)](#)) only shows the disordered nature of the composite. The HRTEM image in [figure 7.4\(f\)](#) further confirmed no crystalline structure with SnO₂, but it is easy to observe the graphene stacked with 5-6 layers and the interlayer spacing keeps at 0.34 nm ([insert of figure 7.4\(f\)](#)). Based on the above-discussed results, we can clearly conclude that amorphous SnO₂-GNS nanocomposites were synthesized at a growth temperature of 200 °C, exhibiting tunable morphologies of SnO₂ component and unchangeable morphologies of GNS.

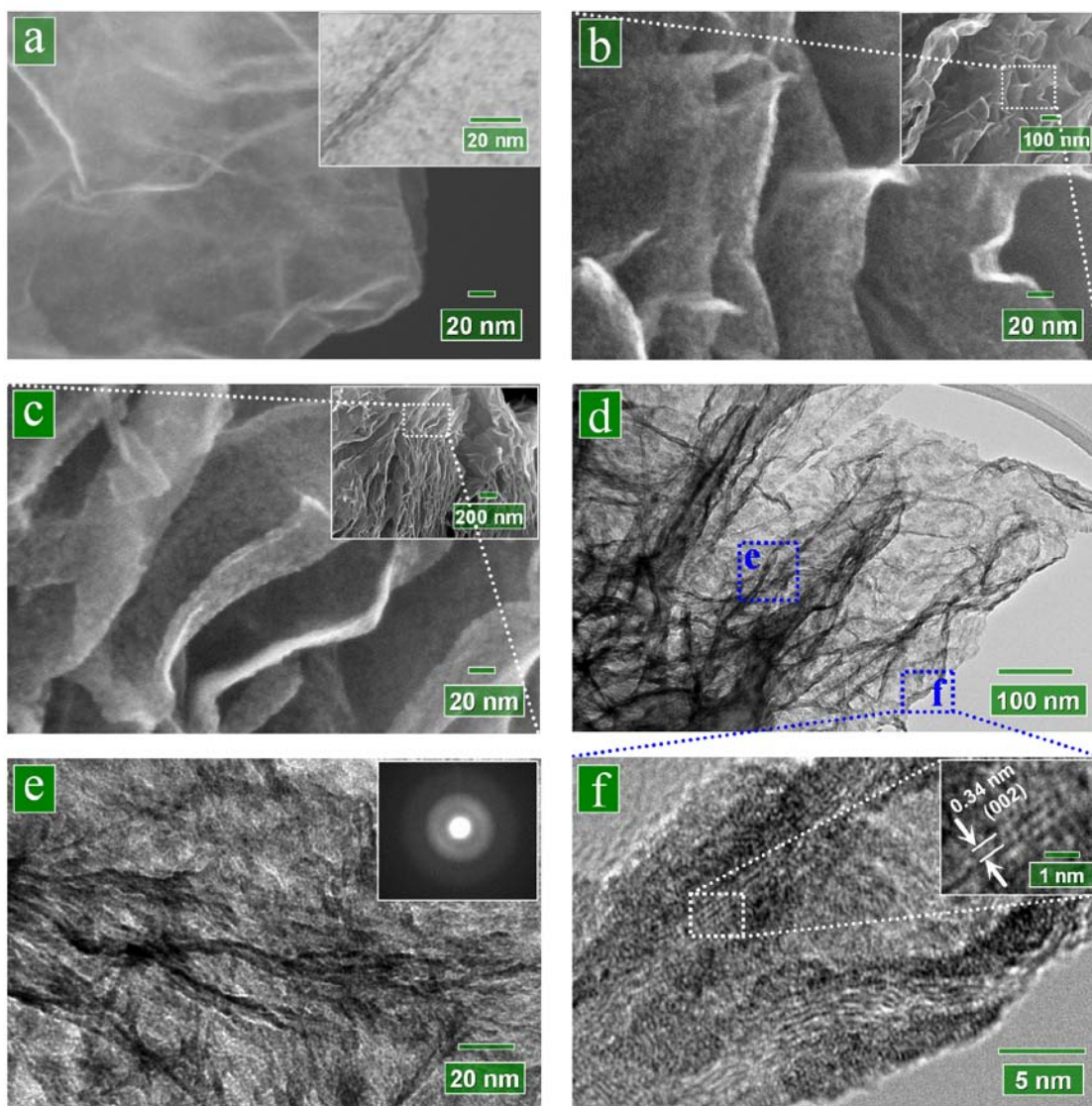


Figure 7.4 Amorphous SnO₂-GNS nanocomposites: (a) 100 ALD cycles of SnO₂; (b) 200 ALD cycles of SnO₂; (c) 300 ALD cycles of SnO₂; (d) low magnification TEM image of 300-cycle SnO₂; (e) and (f) HRTEM images of 300-cycle SnO₂.

Following the results of amorphous SnO₂-GNS nanocomposites prepared at 200 °C, the results of crystalline SnO₂-GNS nanocomposites prepared at 400 °C are shown in [figure 7.5](#). After an initial 100-cycle ALD-SnO₂, the sample in [figure 7.5\(a\)](#) shows that GNS surface was deposited uniformly with numerous nanoparticles varying in the range of 10 - 20 nm. An averaging on 100 nanoparticles accounts for a value of ~13 nm for the nanoparticle size. [Figure 7.5\(b\)](#) shows nanoparticles growing bigger with an average size of ~27 nm after 200 ALD cycles, and [figure 7.5\(c\)](#) shows ever-growing nanoparticles having an average size of ~33 nm after 300 ALD cycles. Thus, we observed a non-linear growth with nanoparticles. In addition, it is noteworthy that, at each stage of different ALD cycles, there were always some tiny particles newly appeared and the density of nanoparticles showed an increasing tendency, implying that SnO₂ nanoparticles might not all nucleate at the same time. The underlying reason could be attributed to deficient exposure of some local surface areas to precursors during ALD processes, and then these sites nucleated later and experienced fewer ALD-SnO₂ cycles. In particular, we observed that, besides the nanoparticles sitting on top of the graphene surface, there are also numerous nanoparticles encapsulated inside GNS, as some are red-circled in [figure 7.5\(a\)-\(c\)](#). The aforementioned results have three important implications: (1) the porous structure of GNS provided space for precursors to enter and thereby to deposit; (2) GNS consisted of only a few layers of graphene were functionalized in both sides; (3) as a gas-solid reaction system, ALD can provide well-controlled deposition through adjusting the number of ALD cycles. Furthermore, the sample after 300-cycle ALD-SnO₂ was further examined using TEM. [Figure 7.5\(d\)](#) revealed similar information as [figure 7.5\(c\)](#), and a blue-circled part marked with “e” was enlarged in [figure 7.5\(e\)](#). Clearly we can observe the nanoparticles located on the upside and downside of GNS. The [insert of figure 7.5\(e\)](#) disclosed that the SnO₂ nanoparticles are crystalline and were further examined by HRTEM in [figure 7.5\(f\)](#). It was clearly shown that the SnO₂ nanoparticles are with characteristic lattice fringe of (101). Combined with XRD spectra ([figure 7.2\(a\)](#)), we can conclude that the SnO₂-GNS nanocomposites produced at 400 °C are with a crystalline SnO₂ component, and SnO₂ nanoparticles are tunable in size as well.

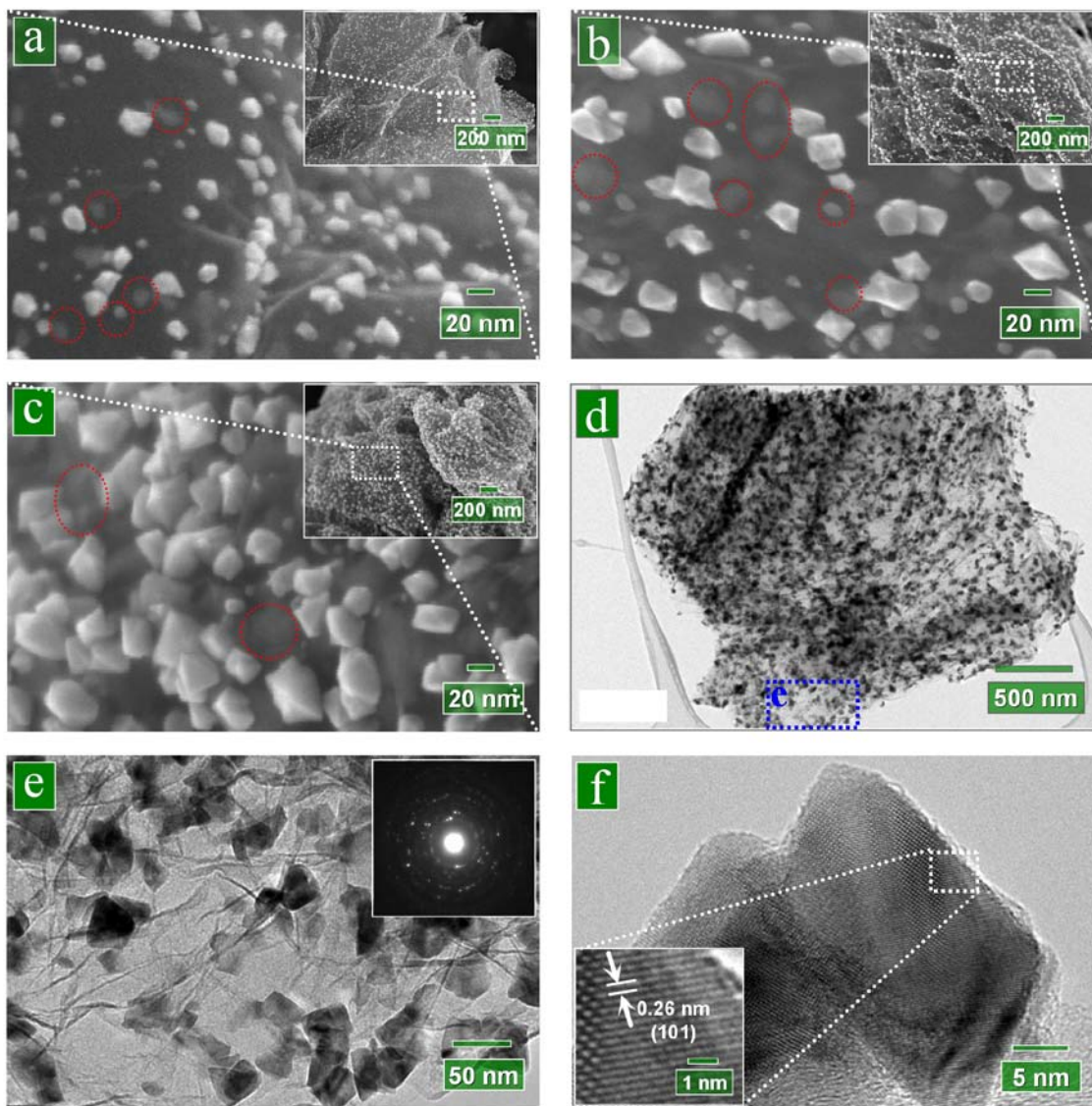
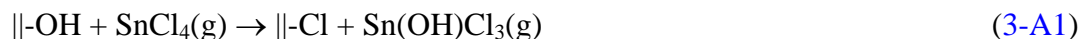


Figure 7.5 Crystalline SnO₂-GNS nanocomposites: (a) 100 ALD cycles of SnO₂; (b) 200 ALD cycles of SnO₂; (c) 300 ALD cycles of SnO₂; (d) low magnification TEM image of 300-cycle SnO₂; (e) and (f) HRTEM images of 300-cycle SnO₂.

In the above-discussed results, we deduced that the ALD strategy is a facile approach to synthesize SnO₂-GNS hybrid composites with controllable amorphous/crystalline phase as well as tunable morphologies of SnO₂ component. It is worth noting that growth

temperature plays an important role in determining the structural phases of SnO₂, i.e., a low temperature contributes to amorphous phase while a high temperature is responsible for crystalline phase. Thus, it is necessary to explore the underlying mechanisms for a better understanding and manipulating the synthesis process. On this way, we explained the phenomena by applying the knowledge of surface chemistry and it is believed that surface reactions are temperature-dependent.

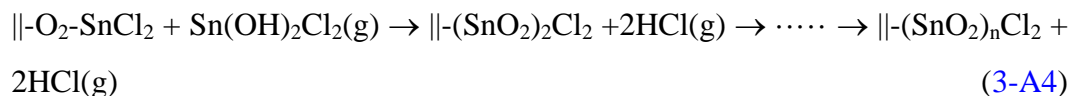
As stated above, ALD is a surface-controlled process. So, the initiation of an ALD process is highly dependent on the functional groups carried by pristine samples. As disclosed by FTIR spectra (figure 7.2(d)), the as-synthesized GNS samples were dominantly attached with hydroxyl (-OH) groups. Thus, the hydroxyl groups guaranteed the initiation of ALD-SnO₂, as described in Reaction 2-A. To explain controllable structural phases of SnO₂, however, we noticed that the corresponding surface reactions are temperature-dependent in nature. On this way, Puurunen [41] made an excellent review on ALD processes of using metal chlorides and water as the precursors, and noticed that this sort of ALD processes (e.g., TiO₂, and ZrO₂) experienced a phase-transition from amorphous films to crystalline nanoparticles when a threshold temperature (300 °C) was achieved. Furthermore, Puurunen proposed different underlying mechanisms for them: (a) ligand exchange (as shown in Reaction 2-A and 2-B) is the most prevalent mechanism responsible for amorphization at low temperature (< 300 °C); (b) a prominent two-step chlorination in the pulse of a metal chloride is responsible for crystallization at high temperature (> 300 °C). To address the two-step chlorination potentially happened in ALD-SnO₂, we proposed and described it for ALD-SnO₂ in the following reactions:



First, SnCl₄ chlorinates the surface hydroxyl groups and form an intermediate hydroxychloride molecule (Sn(OH)₂Cl₂) in two steps, as shown in Reaction 3-A1 and 3-A2. Then the hydroxychloride reacts with surface chlorine groups through its hydroxyl groups, as shown in Reaction 3-A3 as follows:



In particular, the chlorine groups on the right side of the former [Reaction 3-A3](#) would still potentially react with hydroxychloride in a chain of reactions, as shown in the following [Reaction 3-A4](#):



Thus, surface reactions at high temperature in a pulse of SnCl_4 could contribute a formation of multilayer. It explained why the nanoparticles grew more quickly at high temperature than at low temperature after a same number of ALD cycles. In addition, it also provided the answers to the size-varied nanoparticles and the continuously newly-appeared nanoparticles with a non-linear growth mode, for some sites might be involved in reactions in a chain (as shown in [Reaction 3-A4](#)) while others were not in a certain pulse of SnCl_4 . On the other hand, the surface reaction happened in a pulse of H_2O is still simple ligand exchange, which is the same as shown by [Reaction 2-B](#):



To compare the differences in surface reactions incurred by different temperatures, it is believed that the half reactions occurred in the pulse of H_2O are independent of temperature, as commonly indicated by [Reaction 2-B](#) and [3-B](#). However, the half reactions occurred in the pulse of SnCl_4 are temperature-dependent, as described in [Reaction 2-A](#) for low temperature ($200\text{ }^\circ\text{C}$) and in [Reaction 3-A1](#) to [3-A4](#) for high temperature ($400\text{ }^\circ\text{C}$). To further understand the different mechanisms incurred by growth temperature, we schematically illustrated the growth mechanisms in the following [figure 7.6](#). On the left side of [figure 7.6](#), surface reactions were illustrated for amorphization of deposited materials based on ligand exchange, and they are self-limiting in nature. On the right side of [figure 7.6](#) for crystallization, however, the surface reactions (as stated in above [Reaction 3-A1](#) to [3-A4](#)) are not self-limiting in the pulse of SnCl_4 while the ones are self-limiting in the pulse of H_2O , leading to the formation of multilayers dependent on reactive sites in one ALD cycle. In particular, as noticed by Puurunen [41], the transition between ligand exchange and chlorination might happen suddenly when the growth temperature is over a certain threshold, which is suggested around $300\text{ }^\circ\text{C}$. Obviously, it is growth temperature that influences the structural phases of deposited SnO_2 via surface chemistry.

7.4 Conclusions

In conclusion, in this article we applied a non-aqueous ALD approach for synthesis of MO-GNCs, which was successfully exemplified with the preparation of SnO₂-GNS hybrid composites using SnCl₄ and H₂O as the ALD precursors. This strategy exhibited many unique advantages in synthesizing MO-GNCs. First of all, it is a facile vapor route, which needs no further post-treatment (such as, filtration, washing, and annealing) widely used in solution-based methods [15-19]. Second, the ALD approach can well tune and control the deposited metal oxide on both morphologies and structural phases. As demonstrated in this work, the as-deposited SnO₂ was shown with nanoparticles/films as well as in form of amorphous/crystalline phases through adjusting the ALD cycling numbers and suitable growth temperatures. It has not been reported that both amorphous and crystalline SnO₂ have been synthesized with a single method in earlier studies. Third, this ALD approach has the potential for mass production. As reported earlier by George's group [43,44], ALD can be combined with fluidization technology [43] or rotary devices [44] for coating nanopartilces of large quantities. Thus, it is reasonable to believe that MO-GNCs can be produced in large quantities with this ALD route. Specifically, the as-synthesized SnO₂-GNS hybrid nanocomposites can be important candidates for many applications, such as Li-ion batteries [18-20], gas-sensing [45], as well as solar cells [46]. The controllable amorphous/crystalline phase of SnO₂ would provide more choices for seeking a better performance of the aforementioned applications and is also potentially appealing for academic curiosity.

Acknowledgements

This research was supported by the Natural Science and Engineering Research Council of Canada (NSERC), Canada Research Chair (CRC) Program, Canadian Foundation for Innovation (CFI), Ontario Research Fund (ORF), Early Researcher Award (ERA) and the University of Western Ontario.

References

- [1] D. S. Su and R. Schlögl, Nanostructured carbon and carbon nanocomposites for electrochemical energy storage applications, *ChemSusChem*, 2010, **3**, 136-168.
- [2] Z. Spitalsky, D. Tasis, K. Papagelis, and C. Galiotis, Carbon nanotube-polymer composites: chemistry, processing, mechanical and electrical properties, *Prog. Polym. Sci.*, 2010, **35**, 357-401.
- [3] L. Sun, R. F. Gibson, F. Gordaninejad, and J. Suhr, Energy absorption capability of nanocomposites: a review, *Compos. Sci. Technol.*, 2009, **69**, 2392-2409.
- [4] Z. Zeng, X. Zhou, X. Huang, Z. Wang, Y. Yang, Q. Zhang, F. Boey, and H. Zhang, Electrochemical deposition of Pt nanoparticles on carbon nanotube patterns for glucose detection, *Analyst*, 2010, **135**, 1726-1730.
- [5] K. S. Novoselov, A. K. Geim, S. V. Morozov, D. Jiang, Y. Zhang, S. V. Dubonos, I. V. Grigorieva, and A. A. Firsov, Electric field effect in atomically thin carbon films, *Science*, 2004, **306**, 666-669.
- [6] S. Stankovich, D. A. Dikin, G. H. B. Dommett, K. M. Kohlhaas, E. J. Zimney, E. A. Stach, R. D. Piner, S. T. Nguyen, and R. S. Ruoff, Graphene-based composite materials, *Nature*, 2006, **442**, 282-286.
- [7] G. Eda, H. E. Unalan, N. Rupesinghe, G. A. J. Amaratunga, and M. Chhowalla, Field emission from graphene based composite thin films, *Appl. Phys. Lett.*, 2008, **93**, 233502.
- [8] T. Wei, G. Luo, Z. Fan, C. Zheng, J. Yan, C. Yao, W. Li, and C. Zhang, Preparation of graphene nanosheet/polymer composites using in situ reduction-extractive dispersion, *Carbon*, 2009, **47**, 2290-2299.
- [9] X. Qi, K.-Y. Pu, X. Zhou, H. Li, B. Liu, F. Boey, W. Huang, H. Zhang, Conjugated-polyelectrolyte-functionalized reduced graphene oxide with excellent solubility and stability in polar solvents, *Small*, 2010, **6**, 663-669.
- [10] Y. Li, W. Gao, L. Ci, C. Wang, P. M. Ajayan, Catalytic performance of Pt nanoparticles on reduced graphene oxide for methanol electro-oxidation, *Carbon* **2010**, **48**, 1124-1130.
- [11] X. Zhou, X. Huang, X. Qi, S. Wu, C. Xue, F. Y. C. Boey, Q. Yan, P. Chen, and H. Zhang, In situ synthesis of metal nanoparticles on single-layer graphene oxide and

- reduced graphene oxide surfaces, *J. Phys. Chem. C*, 2009, **113**, 10842-10846.
- [12] S. Guo, S. Dong, and E. Wang, Three-dimensional Pt-on-Pd dimetallic nanodendrites supported on graphene nanosheet: facile synthesis and used as an advanced nanoelectrocatalyst for methanol oxidation, *ACS Nano*, 2010, **4**, 547-555.
- [13] X. Huang, X. Zhou, S. Wu, Y. Wei, X. Qi, J. Zhang, F. Boey, and H. Zhang, Reduced graphene oxide-templated photochemical synthesis and in situ assembly of Au nanodots to orderly patterned Au nanodot chains, *Small*, 2010, **6**, 513.
- [14] G. Williams, B. Seger, and P. V. Kamat, TiO₂-graphene nanocomposites. UV-assisted photocatalytic reduction of graphene oxide, *ACS Nano*, 2008, **2**, 1487-1491.
- [15] D. Wang, D. Choi, J. Li, Z. Yang, Z. Nie, R. Kou, D. Hu, C. Wang, L. V. Saraf, J. Zhang, I. A. Aksay, and J. Liu, Self-assembled TiO₂-graphene hybrid nanostructures for enhanced Li-ion insertion, *ACS Nano*, 2009, **3**, 907-914.
- [16] J. M. Lee, Y. B. Pyun, J. Yi, J. W. Choung, and W. I. Park, ZnO nanorod-graphene hybrid architectures for multifunctional conductors, *J. Phys. Chem. C*, 2009, **113**, 19134-19138.
- [17] J. Wu, X. Shen, L. Jiang, K. Wang, and K. Chen, Solvothermal synthesis and characterization of sandwich-like/ZnO nanocomposites, *Appl. Surf. Sci.*, 2010, **256**, 2826-2830.
- [18] J. Yao, X. Shen, B. Wang, H. Liu, and G. Wang, In situ chemical synthesis of SnO₂-graphene nanocomposites as anode materials for lithium-ion batteries, *Electrochem. Comm.*, 2009, **11**, 1849-1852.
- [19] D. Wang, R. Kou, D. Choi, Z. Yang, Z. Nie, J. Li, L. V. Saraf, D. Hu, J. Zhang, G. L. Graff, J. Liu, M. A. Pope, and I. A. Aksay, Ternary self-assembly of ordered metal oxide-graphene nanocomposites for electrochemical energy storage, *ACS Nano*, 2010, **4**, 1587-1595.
- [20] S. M. Paek, E. Yoo, and I. Honma, Enhanced cyclic performance and lithium storage capacity of SnO₂/graphene nanoporous electrodes with three-dimensionally delaminated flexible structure, *Nano Lett.*, 2009, **9**, 72-75.
- [21] S. M. George, Atomic layer deposition: an overview, *Chem. Rev.*, 2010, **110**, 111-131.
- [22] M. Knez, K. Nielsch, and L. Niinistö, Synthesis and surface engineering of complex

- nanostructures by atomic layer deposition, *Adv. Mater.*, 2007, **19**, 3425-3438.
- [23] H. Kim, H. B. R. Lee, W. J. Maeng, Application of atomic layer deposition to nanofabrication and emerging nanodevices, *Thin Solid Films*, 2008, **517**, 2563-2580.
- [24] Z. Li, S. T. Barry, and R. G. Gordon, Synthesis and characterization of copper(I) amidinates as precursors for atomic layer deposition (ALD) of copper metal, *Inorg. Chem.*, 2005, **44**, 1728-1735.
- [25] A. Rosental, A. Tarre, A. Gerst, T. Uustare, and V. Sammelseg, Atomic-layer chemical vapor deposition of SnO₂ for gas-sensing applications, *Sens. Actuators B*, 2001, **77**, 297-300.
- [26] T. Takeuchi, K. Shoji, T. Tadano, I. Doteshita, and S. Onodera, Preparation of sub-nanometer thickness-controlled tin dioxide films by pulsed atomic-layer CVD, *Thin Solid Films*, 2003, **442**, 98-101.
- [27] A. Rosental, A. Tarre, A. Gerst, J. Sundqvist, A. Hårsta, A. Aidla, J. Aarik, V. Sammelseg, and T. Uustare, Gas sensing properties of epitaxial SnO₂ thin films prepared by atomic layer deposition, *Sens. Actuators B*, 2003, **93**, 552-555.
- [28] X. Du, Y. Du, and S. M. George, In situ examination of tin oxide atomic layer deposition using quartz crystal microbalance and Fourier transform infrared techniques, *J. Vac. Sci. Technol. A*, 2005, **23**, 581-588.
- [29] W. S. Hummers and R. E. Offeman, Preparation of graphitic oxide, *J. Am. Chem. Soc.*, 1958, **80**, 1339.
- [30] H. C. Schniepp, J. L. Li, M. J. McAllister, H. Sai, M. Herrera-Alonso, D. H. Adamson, R. K. Prud'homme, R. Car, D. A. Saville, and I. A. Aksay, Functionalized single graphene sheets derived from splitting graphite oxide, *J. Phys. Chem. B*, 2006, **110**, 8535-8539.
- [31] A. Celzard, J. F. Mareche, and G. Furdin, Modelling of exfoliated graphite, *Prog. Mater. Sci.*, 2005, **50**, 93-179.
- [32] D. W. Lee, L. D. L. Santos V., J. W. Seo, L. L. Felix, A. Bustamante D., J. M. Cole, and C. H. W. Barnes, The structure of graphite oxide: investigate of its surface chemical groups, *J. Phys. Chem. B*, 2010, **114**, 5723-5728.
- [33] L. Tang, Y. Wang, Y. Li, H. Feng, J. Lu, and J. Li, Preparation, structure, and electrochemical properties of reduced graphene sheet films, *Adv. Funct. Mater.*, 2009, **19**,

2782-2789.

[34] W. Chen, L. Yan, and P. R. Bangal, Preparation of graphene by the rapid and mild thermal reduction of graphene oxide induced by microwaves, *Carbon*, 2010, **48**, 1146-1152.

[35] V. K. Singh, M. K. Patra, M. Manoth, G. S. Gowd, S. R. Vadera, and N. Kumar, In situ synthesis of graphene oxide and its composites with iron oxide, *New Carbon Mater.*, 2009, **24**, 147-152.

[36] C. Nethravathi, T. Nisha, N. Ravishankar, C. Shivakumara, M. Rajamathi, Graphene-nanocrystalline metal sulphide composites produced by a one-pot reaction starting from graphite oxide, *Carbon*, 2009, **47**, 2054-2059.

[37] C. N. R. Rao, K. Biswas, K. S. Subrahmanyam, and A. Govindaraj, Graphene, the new nanocarbon, *J. Mater. Chem.*, 2009, **19**, 2457-2469.

[38] A. C. Ferrari and J. Robertson, Interpretation of Raman spectra of disordered and amorphous carbon, *Phys. Rev. B*, 2000, **61**, 14095-14107.

[39] K. N. Kudin, B. Ozbas, H. C. Schniepp, R. K. Prud'homme, I. A. Aksay, and R. Car, Raman spectra of graphite oxide and functionalized graphene sheets, *Nano Lett.*, 2008, **8**, 36-41.

[40] S. Stankovich, D. A. Dikin, R. D. Piner, K. A. Kohlhaas, A. Kleinhammes, Y. Jia, Y. Wu, S. T. Nguyen, and R. S. Ruoff, Synthesis of graphene-based nanosheets via chemical reduction of exfoliated graphite oxide, *Carbon*, 2007, **45**, 1558-1565.

[41] R. L. Puurunen, Formation of metal oxide particles in atomic layer deposition during the chemisorption of metal chlorides: a review, *Chem. Vap. Deposition*, 2005, **11**, 79-90.

[42] R. L. Puurunen and W. Vandervorst, Island growth as a growth mode in atomic layer deposition: a phenomenological model, *J. Appl. Phys.*, 2004, **96**, 7686-7695.

[43] L. F. Hakim, S. M. George, and A. W. Weimer, Conformal nanocoating of zirconia nanoparticles by atomic layer deposition in a fluidized bed reactor, *Nanotechnology*, 2005, **16**, S375-S381.

[44] A. S. Cavanagh, C. A. Wilson, A. W. Weimer, and S. M. George, Atomic layer deposition on gram quantities of multi-walled carbon nanotubes, *Nanotechnology*, 2009, **20**, 255602.

[45] M. Batzill, Surface science studies of gas sensing materials: SnO₂, *Sensors*, 2006, **6**,

1345-1366.

[46] H. J. Snaith and C. Ducati, SnO₂-based dye-sensitized hybrid solar cells exhibiting near unity absorbed photon-to-electron conversion efficiency, *Nano Lett.*, 2010, **10**, 1259-1265.

Supporting Information

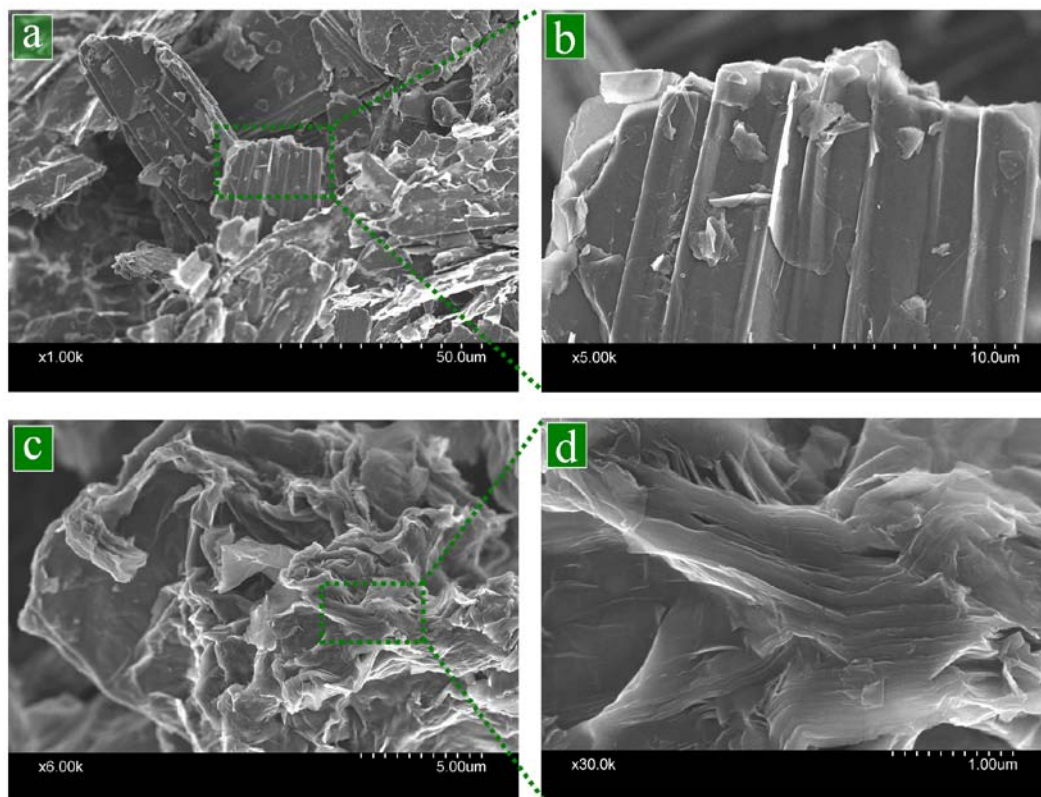


Figure SI-7.1 SEM images for natural graphite of (a) lower magnification and (b) higher magnification, as well as graphite oxide of (c) lower magnification and (d) higher magnification.

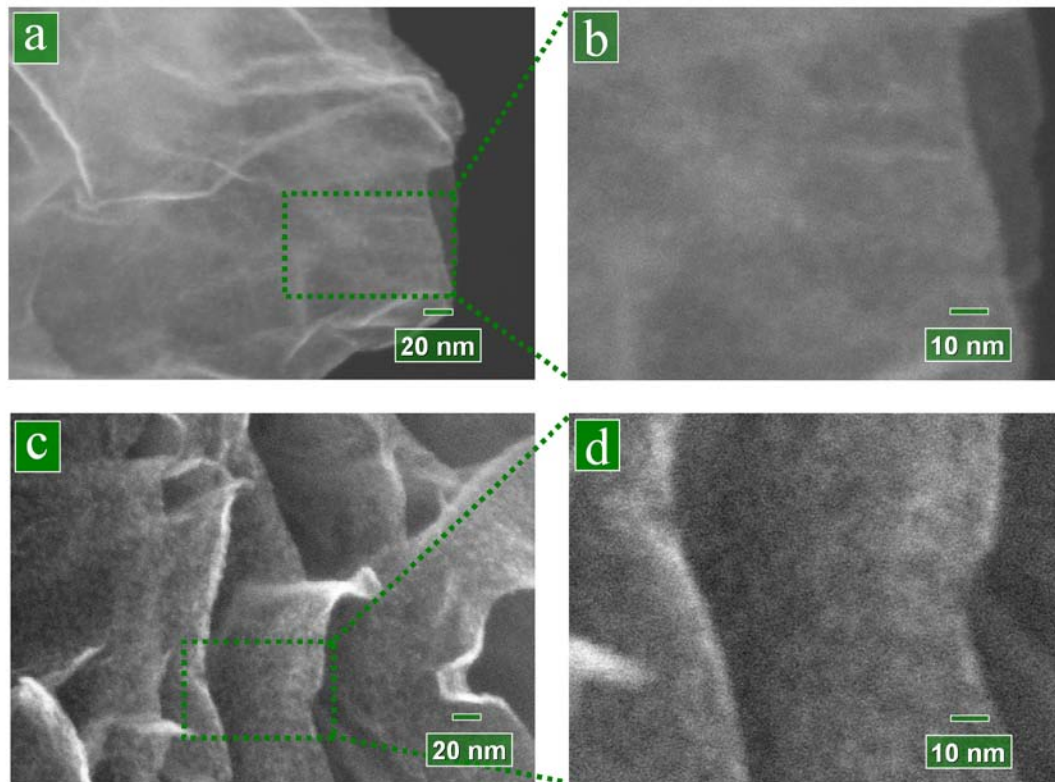


Figure SI-7.2 SEM images for amorphous SnO₂-GNS nanocomposites: 100 ALD cycles of SnO₂ with (a) lower magnification and (b) higher magnification of SEM image; 200 ALD cycles of SnO₂ with (c) lower magnification and (d) higher magnification of SEM image.

CHAPTER 8

CONTROLLABLE ATOMIC LAYER DEPOSITION OF ONE-DIMENSIONAL NANOSTRUCTURED TiO₂

A version of this chapter will be submitted for publishing. This work is related to a National Defense project about “*Nanostructured photocatalysts for water splitting and hydrogen production*”.

This study aimed at synthesizing one-dimensional (1D) nanostructures of TiO₂ using atomic layer deposition (ALD) on anodic aluminum oxide (AAO) templates and carbon nanotubes (CNTs). The precursors are titanium isopropoxide (TTIP, Ti(OCH(CH₃)₂)₄) and deionized water. It was found that the morphologies and structural phases of as-deposited TiO₂ are tunable through adjusting cycling numbers of ALD and growth temperatures. The low temperature (150 °C) produced amorphous TiO₂ while the high temperature (250 °C) led to crystalline anatase TiO₂. In addition, it was revealed that the deposition of TiO₂ on CNTs experienced island growth first before a film formed. The wall thickness of TiO₂ nanotubes in AAO could be precisely controlled. The synthesized 1D nanostructures of TiO₂ are important candidates in many applications, such as water splitting, solar cells, lithium-ion batteries, and gas sensors.

Keywords: *Atomic layer deposition, Anodic aluminum oxide templates, Carbon nanotubes, Metal oxides, Titanium dioxide, Nanotubes, Core-shell structures, Nanocomposites*

8.1 Introduction

Growing environmental concerns related to the extensive use of non-sustainable fossil fuels (oil, natural gas, and coal) and a constantly increasing energy demand are forcing mankind to develop clean and sustainable sources of energy [1]. Photocatalysis is expected to make a great contribution to both environment treatment (emission cleaning and water purification) and renewable energy. Hydrogen (H_2) is widely considered to be the future clean energy carrier in many applications, such as environmentally friendly vehicles, domestic heating, and stationary power generation. Photocatalytic hydrogen production from water is one of the most promising ways to realize a hydrogen economy for three reasons: (1) this technology is based on photon (or solar) energy, which is a clean, perpetual source of energy, and mainly water, which is a renewable resource; (2) it is an environmentally safe technology without undesirable by-products and pollutants; and (3) the photochemical conversion of solar energy into a storable form of energy, i.e., hydrogen, allows one to deal with the intermittent character and seasonal variation of the solar influx. However, it has proven difficult to find an ideal photocatalyst, which meets all the requirements (chemical stability, corrosion resistance, visible light harvesting, and suitable band edges) that would render photocatalytic hydrogen production a viable alternative. Fortunately, nanoscience and nanotechnology have boosted the modification of existing photocatalysts and the discovery and development of new candidate materials. Photocatalysts are typically made of metal oxides, metal sulfides, oxysulfides, oxynitrides, and composites thereof. In comparison, TiO_2 has received more attention because it is stable, corrosion-resistant, non-toxic, abundant, and cheap [1]. It was pointed out that the morphology of TiO_2 plays a very important role in the efficiency of photocatalysis for hydrogen production. One-dimensional (1D) TiO_2 (nanowires, nanorods, nanotubes, and nanofibers) has attracted more and more attention [1]. Compared to spherical particles, 1D TiO_2 nanostructures could provide a high surface area and a high interfacial charge transfer rate [1]. The carriers are free to move throughout the length of these nanostructures, which is expected to reduce the e^-/h^+ recombination probability. To date, 1D TiO_2 nanotubes has been synthesized by many routes, such as anodization [2-18], hydrothermal [19-23], and template-directed methods [24-27]. For gaining improved

properties, in addition, carbon nanotubes (CNTs) as supports were also used for synthesizing 1D TiO₂ nanocomposites [28-32]. In particular, the aforementioned studies also disclosed that, besides for the application of water splitting, 1D TiO₂ nanostructures are also important candidates for solar cells, lithium-ion batteries, gas sensors, and self-cleaning.

The above review clearly demonstrates that 1D TiO₂ nanotubes and CNT-based TiO₂ hybrids attracted extensive investigation. Of the applied methods, atomic layer deposition (ALD) as a route was also fulfilled based on porous templates [25-27]. As disclosed in these studies, ALD is capable of precise tuning the wall thickness, due to its layer-by-layer character. In this study, therefore, we attempted to fabricate 1D TiO₂ nanotubular structures using both porous anodic aluminum oxide (AAO) templates and CNTs as substrates. The precursors are titanium isopropoxide (TTIP, Ti(OCH(CH₃)₂)₄) and deionized water.

8.2 Experimental

8.2.1 ALD-TiO₂

In ALD-TiO₂ processes, commercial AAO (Whatman, Anodisc, 60 μm in thickness and 13 mm in diameter) and multi-walled CNTs (MWCNTs, Shenzhen Nanotech Port Co., Ltd., China) were first loaded into a commercial ALD reactor (Savannah 100, Cambridge Nanotechnology Inc., USA) preheated to a certain temperature. Then, TTIP (98%, Sigma-Aldrich) and deionized water (DI H₂O) were introduced into the ALD reactor in an alternating sequence to perform ALD-TiO₂. TTIP was heated to 70 °C while water was kept at room temperature in order to provide sufficient vapors for ALD-TiO₂ processes. Additionally, the delivery lines were heated to 150 °C in order to prevent the precursors from condensation. Nitrogen was used as the carrier gas with a flow rate of 20 sccm and the ALD reactor was sustained at a low level of pressure (typically 0.4 Torr) with a vacuum pump (Pascal 2005 I, Adixon). The ALD procedures were set as follows: (1) a

1.0-s supply of TTIP; (2) a 3.0-s extended exposure of TTIP to AAO and CNTs; (3) a 10.0-s purge of oversupplied TTIP and any by-products; (4) a 2.0-s supply of water vapor; (5) a 3.0-s extended exposure of water vapor to AAO and CNTs; (6) a 10.0-s purge of oversupplied water and any by-products. The aforementioned six-step sequence constituted one ALD-TiO₂ cycle and the ALD processes could be adjustable with different cycling numbers and growth temperatures. In this study, two growth temperatures were employed for ALD-TiO₂ processes, i.e., 150 and 250 °C.

8.2.2 Functionalization of substrates

As is well-known, any ALD process requires functional groups with substrate in order to initiate the following deposition of target materials. Of the two substrates (AAO and CNTs), AAO as an oxide is generally covered by various functional groups [33] whereas CNTs are typically free of reactive sites due to their structural perfectness [34]. Therefore, CNTs were first functionalized by oxidization before they were applied for ALD-TiO₂. A general strategy for oxidization is to reflux CNTs in nitric acid [35]. In this study, the oxidization of CNTs was fulfilled using concentrated nitric acid (70% HNO₃) and CNTs were refluxed in nitric acid for 1 or 2 h at 100 °C. After cooling to room temperature, the received dispersions were vacuum-filtered through a 0.2 μm membrane and washed with deionized water until a neutral pH value of the filtrate. The oxidized CNTs were dried in an oven at 100 °C overnight.

The commercial AAO is with nominal pore size of 200 nm while CNTs (Shenzhen) are nominally 60 nm in nominal diameter. However, observation of using scanning electron spectrometry disclosed that the CNTs range widely from around 10 to over 100 nm, as shown by [figure SI-8.1\(a\)](#) and [\(b\)](#) in Supporting Information. In addition, it was found that acid treatment produced no observable change on the morphologies of CNTs ([figure SI-8.1\(c\)-\(e\)](#)).

8.2.3 Characterization

To characterize the morphologies, structures, and compositions of various samples, we used field emission scanning electron spectrometry (FE-SEM, Hitachi 4800S) coupled with energy dispersive spectroscopy (EDS), high-resolution TEM (HR-TEM, JEOL 2010 FEG), and X-ray diffractometer (XRD, Inel multi-purpose diffractometer).

8.3 Results and Discussions

8.3.1 Results

8.3.1.1 1D TiO₂ nanotubes

Figure 8.1(a) shows the XRD patterns for two ALD-coated AAO templates after 500 cycles under 150 (as marked with “A”) and 250 °C (as marked with “B”). Apparently, the one at 150 °C displays no XRD peaks while the one at 250 °C exhibits many sharp XRD peaks which are consistent to the reference values for the crystalline TiO₂ of anatase phase (JCPDS PDF No. 21-1272). The XRD patterns imply that temperatures took effect on the growth characteristics of TiO₂ and the ALD-TiO₂ at 150 °C might have produced the amorphous phase. To confirm the success of ALD-TiO₂ at 150 °C, EDS was employed to probe elemental composition of partially etched an ALD-coated AAO template, as shown in figure 8.1(b). It was disclosed that there is a plenty of Ti, as well as O, Na, and Al. The oxygen element may be partially ascribed to AAO or ALD processes at 150 °C. Al is due to the Al sample holder while Na must be induced by the etching of NaOH. Obviously, temperatures played critical roles in ALD-TiO₂, and the induced growth characteristics need to further address.

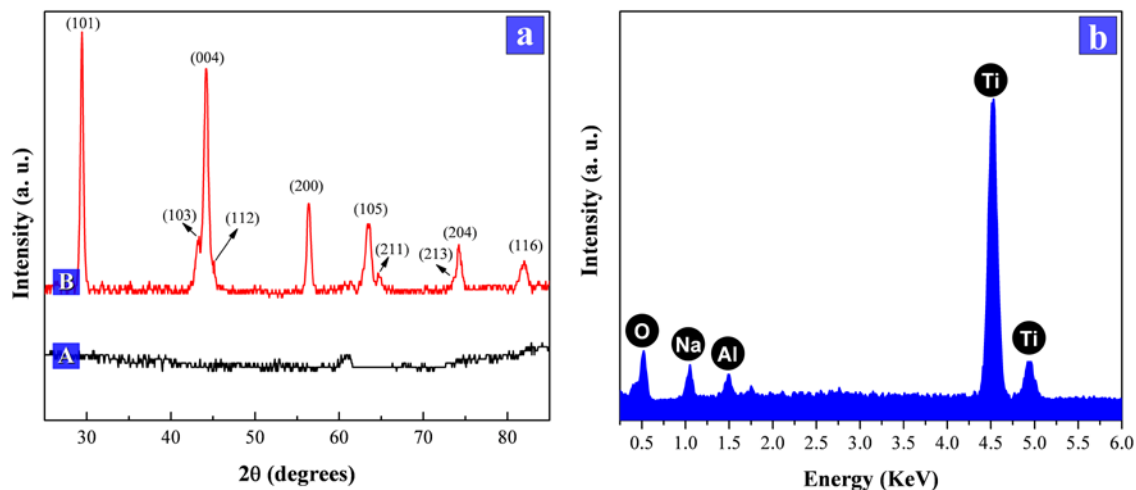


Figure 8.1 (a) XRD patterns induced by ALD-TiO₂ at 150 (A) and 250 °C (B). (b) EDS spectrum of ALD-TiO₂ at 150 °C.

Figure 8.2(a) and (b) shows the cross section of 500- and 600-cycle coated AAO using SEM image, respectively. Corresponding, each of them reveals a smooth and uniform layer of around 16.7 and 20.5 nm deposited in AAO nanopores. Through etching AAO with the 0.5 M NaOH solution, nanotube arrays were received for each case, i.e. 500- (figure 8.2(c)) and 600-cycle (figure 8.2(d)) ALD-TiO₂, respectively. It was noticed that the received nanotubes exhibit fluffy structures in their inner surfaces, as signified by red arrows in figure 8.2(d) and inset of figure 8.2(d). We postulated that it might be due to the amorphous nature of the nanotubes vulnerable to the NaOH solution, leading to the deposited material to partially peel off in the forms of thin strips. Figure 8.2(e) shows the TEM image of received nanotubes and reveals some fluctuation in wall thickness along the tubes. It further confirmed that the amorphous phase is easily subject to the influence of etching processes. The inset of figure 8.2(e) (the pattern of selected area electron diffraction, SAED) displays the disordered nature of the deposited material, consistent to the XRD data in figure 8.1. The HR-TEM image in figure 8.2(f) also discloses the amorphous nature of a local area (as denoted in figure 8.2(e) with “f”).

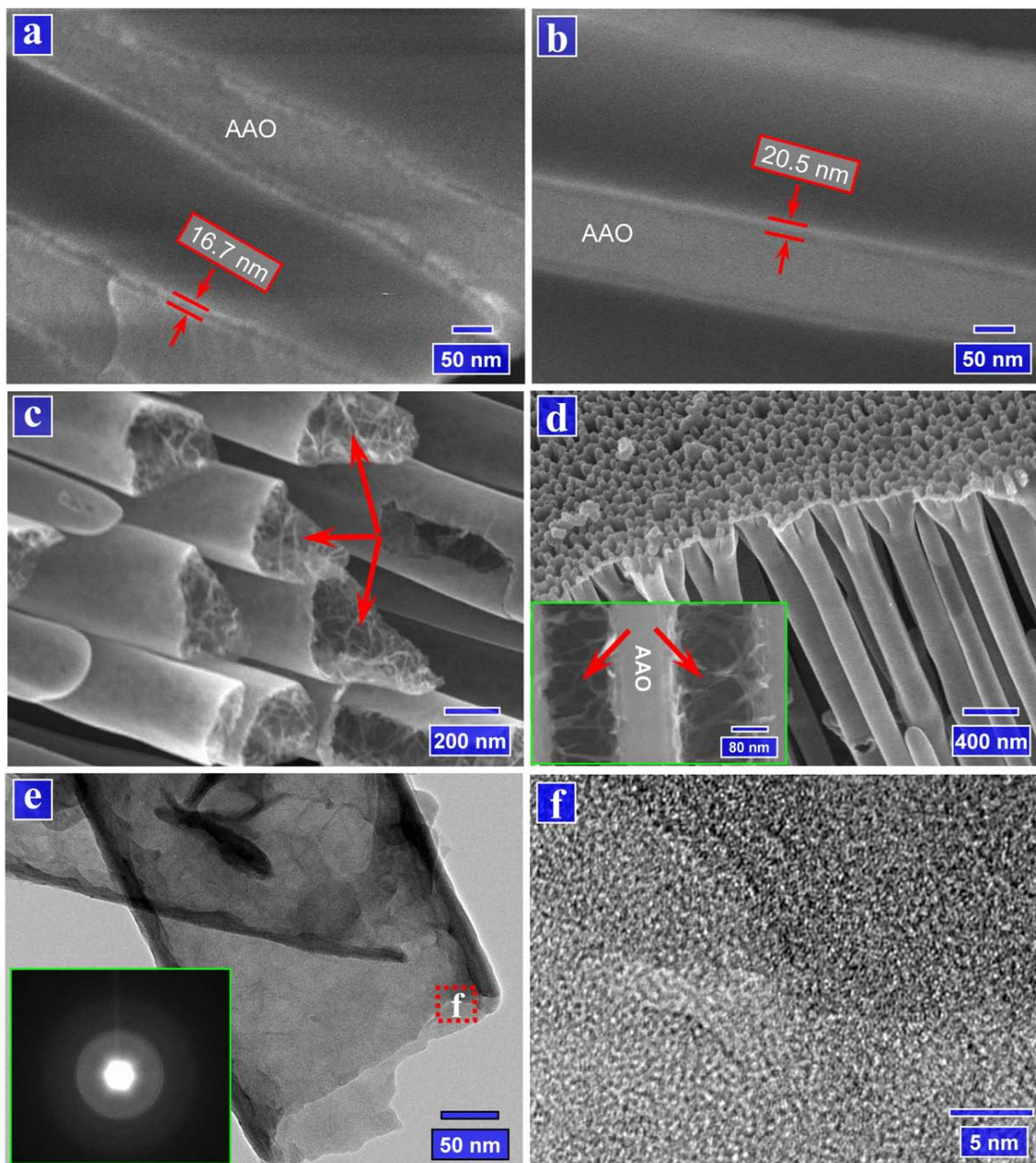


Figure 8.2 Template-directed ALD-TiO₂ at 150 °C. SEM images showing AAO templates deposited with (a) 500- and (b) 600-cycle ALD-TiO₂, and SEM images showing the received nanotubes arrays after (c) 500- and (d) 600-cycle ALD-TiO₂. (e) TEM image of the received nanotubes (inset: SAED pattern). (f) HR-TEM image of a local area as marked with “f” in (e).

Figure 8.3 shows the growth characteristics of ALD-TiO₂ at 250 °C. Figure 8.3(a) - (c) jointly disclose that the wall thickness increases from 8.7 to 17.9 and 35.3 nm with increasing ALD-cycles from 200 (figure 8.3(a)), to 300 (figure 8.3(b)) and 500 (figure 8.3(c)). It was noticed that the inner surfaces of the received nanotubes are smooth and free of fluffy structures as observed in figure 8.2. Figure 8.3(d) presents the SEM image of some bunches of the received nanotubes. In figure 8.3(e), the received nanotubes are displayed by a TEM image and the SAED inset reveals their polycrystalline nature by SAED. Figure 8.3(f) unveils the structural characteristics of the nanotube walls (the inset indicates the examined place of the nanotube) with a HR-TEM image, clearly showing the lattices of anatase TiO₂. The inter-plane distances of 0.352 and 0.243 nm correspond to the characteristic planes of (101) and (104) of anatase TiO₂, respectively.

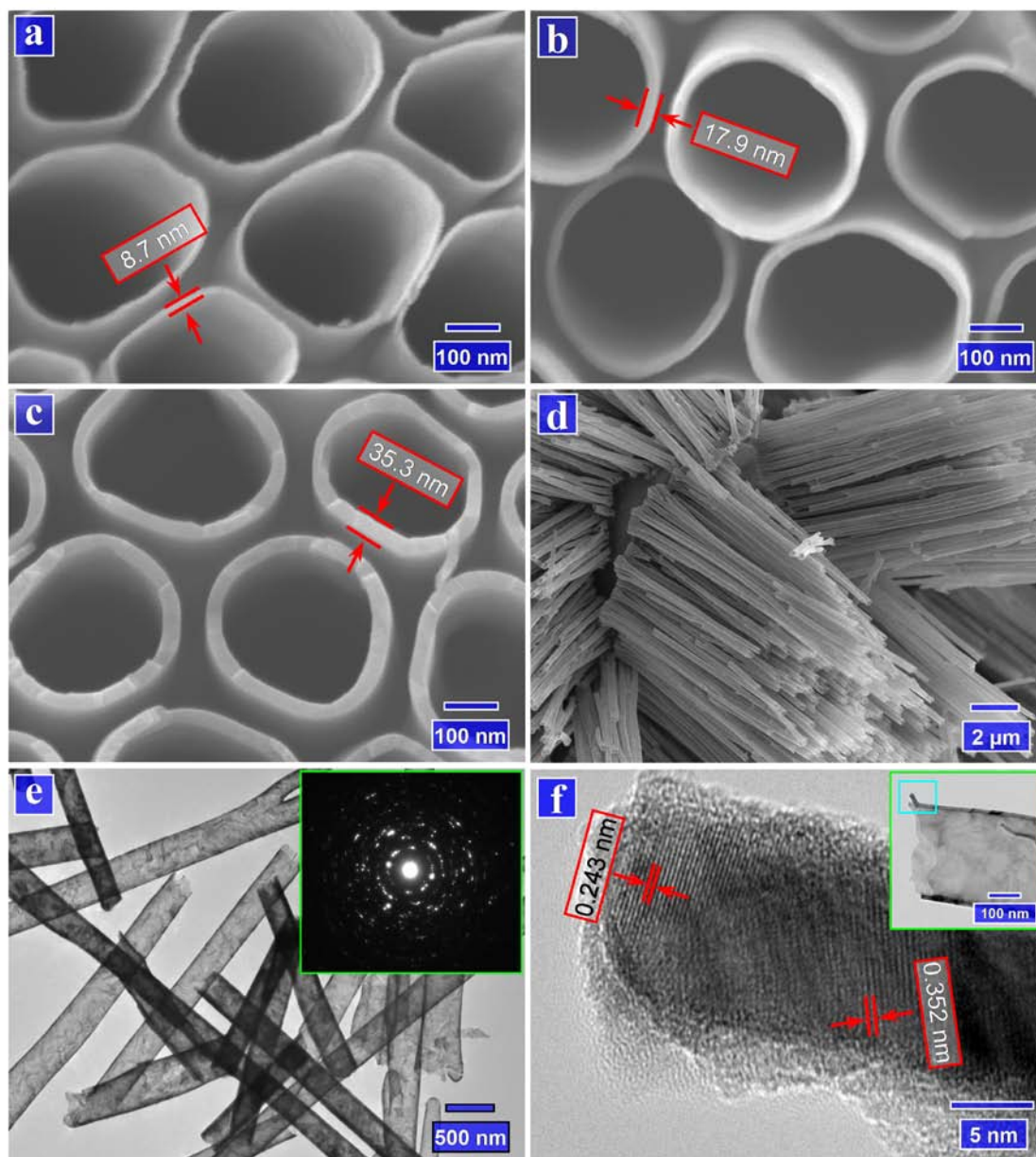


Figure 8.3 Template-directed ALD-TiO₂ at 250 °C. SEM images showing AAO templates deposited with (a) 200- (b) 300-, and (c) 500-cycle ALD-TiO₂. The received nanotubes shown by (d) SEM, (e) TEM (inset: SAED pattern), and (f) HR-TEM image (inset: the position for the piece examined by HR-TEM).

8.3.1.2. 1D CNT-TiO₂ core-shell nanostructures

In the above section, we demonstrate the growth characteristics of AAO template-directed ALD-TiO₂. As another route, CNT-based ALD-TiO₂ will be revealed in this section. First, [figure 8.4](#) discloses the XRD characteristics of CNTs (as marked with “A”), ALD-coated CNTs at 150 °C (as marked with “B”) and 250 °C (as marked with “C”). Compared to the XRD pattern (A) of CNTs, the pattern of ALD-TiO₂ coated CNTs at 150 °C (B) shows no difference, implying the amorphous nature of deposited TiO₂. In contrast, the ALD-coated CNTs at 250 °C (C) display many XRD peaks consistent to the reference values for the crystalline TiO₂ of anatase phase (JCPDS PDF No. 21-1272). Again, it was confirmed that growth temperatures took part in determining the growth characteristics of ALD-TiO₂, as revealed in the [section 8.3.1](#).

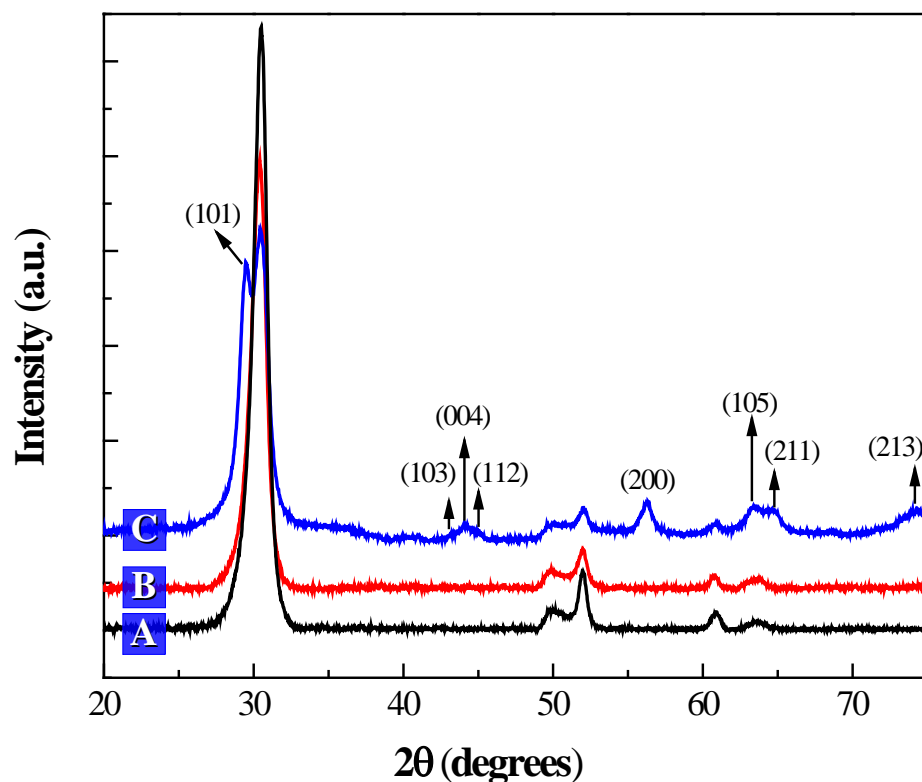


Figure 8.4 XRD patterns of (A) pristine CNTs, and 300-cycle ALD-TiO₂ on CNTs at (B) 150 and (C) 250 °C.

The ALD-TiO₂ on CNTs at 150 °C is shown in [figure 8.5](#). After 100 cycles, SEM ([figure 8.5\(a\)](#)) and TEM ([figure 8.5\(b\)](#)) image jointly disclose that some tiny particles of less than 10 nm were deposited on CNTs. Increasing the cycling number to 200 cycles, [figure 8.5\(c\)](#) and [\(d\)](#) combine to reveal that a very thin layer of around 4.5 nm was deposited on CNTs. Further increasing the cycling number to 300 cycles, it was found that the deposited film became thicker. As shown by the SEM image of [figure 8.5\(e\)](#), the broken part (as circled by yellow dashed line) exposed that a uniform film covered CNTs and the TEM image of [figure 8.5\(f\)](#) determined that the film thickness is 8.6 nm. Furthermore, a CNT sample coated with 100-cycle TiO₂ was examined by HR-TEM, as shown in [figure 8.5\(g\)](#). [Figure 8.5\(g\)](#) clearly shows the graphitic lattices of CNT walls, accounting for an inter-plane distance of 0.34 nm. In addition, as circled by yellow dashed lines, the disordered nature of the deposited material is displayed.

[Figure 8.6](#) illustrates the growth characteristics of ALD-TiO₂ on CNTs at 250 °C. The morphological changes due to 100-, 200-, and 300-cycle ALD-TiO₂ are shown by SEM images in [figure 8.6\(a\)](#), [\(c\)](#), and [\(e\)](#), respectively. They jointly disclose that the surface of CNTs got rougher with increased deposition of TiO₂. [Figure 8.6\(b\)](#) exposes that there are numerous nanoparticles of around 10 nm deposited on CNTs and the growing nanoparticles were going to coalesce. The inset of [figure 8.6\(b\)](#) further reveals that the nanoparticles are crystalline with identified lattices, as marked for the planes of (200). Upon the finishing of 200 cycles, [figure 8.6\(d\)](#) shows that nanoparticles coalesced into an average 7.7 nm thick film. As shown by [figure 8.6\(f\)](#), the films grew thickened to 12.1 nm after 300 cycles.

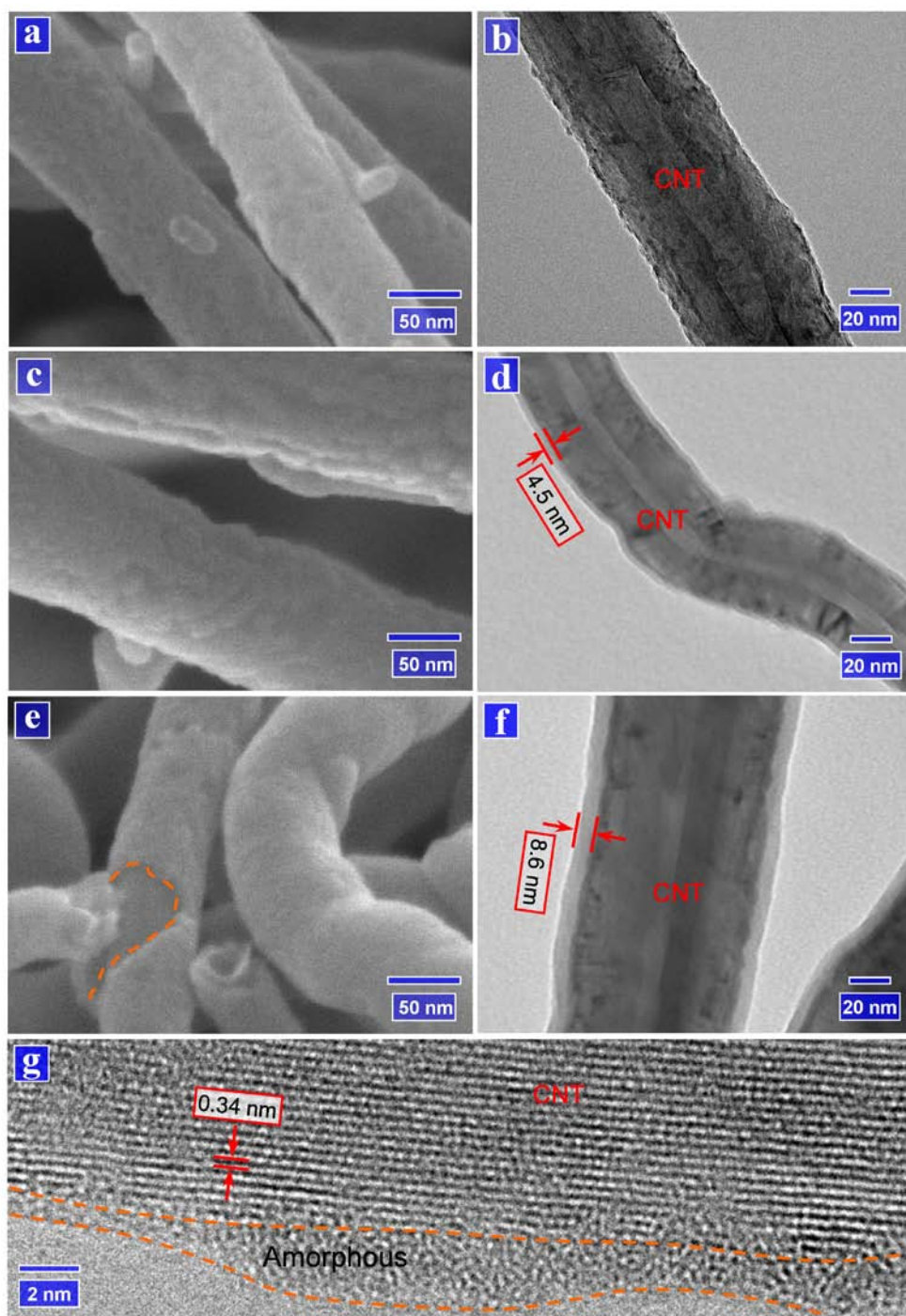


Figure 8.5 ALD-TiO₂ on CNTs at 150 °C. SEM images of (a) 100, (c) 200, and (e) 300 cycles of ALD-TiO₂. TEM images of (b) 100, (d) 200, and (f) 300 cycles of ALD-TiO₂. (g) HR-TEM image of 100-cycle ALD-TiO₂.

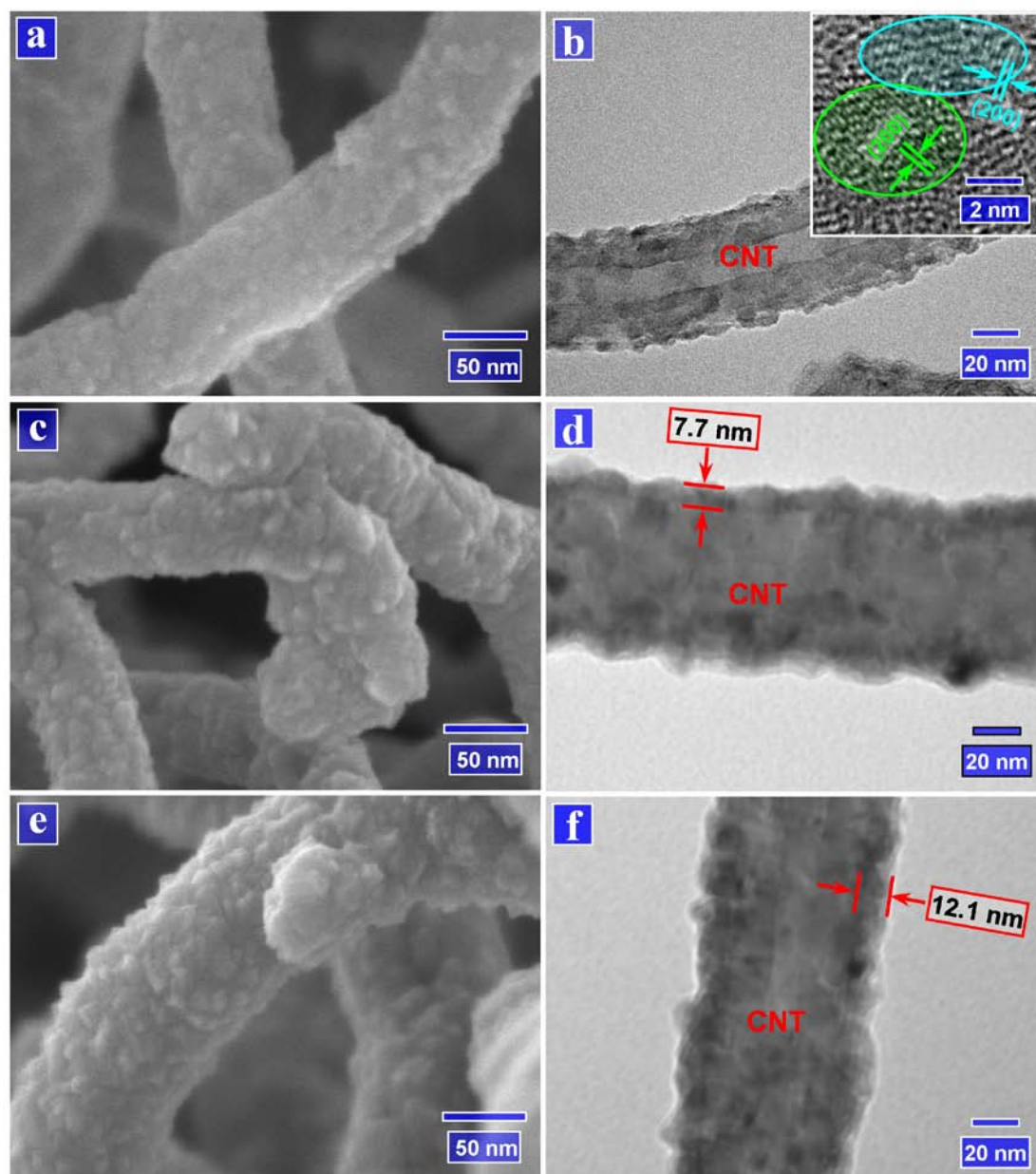


Figure 8.6 ALD-TiO₂ on CNTs at 250 °C. SEM images of (a) 100, (c) 200, and (e) 300 cycles of ALD-TiO₂. TEM images of (b) 100 (inset: HR-TEM image of nanoparticles), (d) 200, and (f) 300 cycles of ALD-TiO₂.

8.3.2 Discussion

Based on the above results, it is reasonable to conclude that the temperatures, i.e., 150 and 250 °C, exerted influence on ALD-TiO₂. The effects can be summarized into two points, i.e., the influence on shaping the structural phases of deposited TiO₂, and the influence on the growth rate per cycle. As for the former one, it is apparent that the ALD-TiO₂ is amorphous at the low temperature of 150 °C while crystalline at the high temperature of 250 °C, no matter which one of the two substrates was employed in this study. A possible explanation for this fact is that a higher temperature (250 °C) should be kinetically favorable for the ordering of the structure with minimum energy [36], for the intermediates might be able to migrate easily and enable the Ti and/or O ions to occupy the positions corresponding to the lowest free energy of the crystal.

On the other hand, it is obvious that the growth rate per cycle (GPC) at a certain temperature is different when the substrates are different. At 150 °C, the average GPC is 0.34 and 0.29 Å/cycle on AAO and CNTs, respectively. At 250 °C, the average GPC is 0.71 and 0.40 Å/cycle on AAO and CNTs, respectively. Obviously, the growth on AAO is higher than the one on CNTs, and the substrates played influence on GPC. The reason is probably due to the higher density of reactive sites with AAO in comparison to CNTs. In addition, it is also noticed that the GPC increased with temperature. The potential mechanism may lie in the improved reactivity due to the increased temperature. Aarik et al [37] revealed that water has a low reactivity towards TTIP in the ALD-TiO₂, but an increase on growth temperature could improve the reactivity of water, activate some reactions, and thereby improve the growth rate of ALD-TiO₂.

In summary, in this work we demonstrated two routes to synthesize 1D nanostructures of TiO₂ using ALD. In particular, the synthesized nanostructures exhibit tunable morphologies and phases, ascribed to cyclic operation of ALD and adopted temperatures, respectively.

8.4 Conclusions

In this article, we attempt to fabricate 1D nanotubes and CNT-based core-shell structures of TiO_2 . It was demonstrated that ALD is a highly tunable technique in controlling the deposited TiO_2 in different morphologies and phases. As a result, the pure nanotubes and CNT-based core-shell structures of TiO_2 commonly show amorphous or crystalline phase, depending on the adopted temperatures. Furthermore, the wall thickness of the TiO_2 nanotube via the AAO route is also precisely controllable and the deposited TiO_2 on CNTs can be tuned from nanoparticles to tubular films, depending on the ALD cycles for the two cases. Thus, ALD is versatile in synthesizing 1D nanostructures, and the synthesized nanostructures are useful for many applications.

Acknowledgements

This research was supported by the Natural Science and Engineering Research Council of Canada (NSERC), Canada Research Chair (CRC) Program, Canadian Foundation for Innovation (CFI), Ontario Research Fund (ORF), Early Researcher Award (ERA) and the University of Western Ontario. In addition, the authors would like to appreciate the help from Mr. Fred Pearson on HRTEM analysis at Canadian Center for Electron Microscopy, McMaster University.

References

- [1] J. Zhu, and M. Zäch, Nanostructured materials for photocatalytic hydrogen production, *Current Opinion in Colloid & Interface Science*, 2009, **14**, 260-269.
- [2] E. Y. Kim, J. H. Park, and G. Y. Han, Design of TiO₂ nanotubes array-based water splitting reactor for hydrogen generation, *J. Power Source*, 2008, **184**, 284-287.
- [3] A. Ghicov and P. Schmuki, Self-ordering electrochemistry: a review on growth and functionality of TiO₂ nanotubes and other self-aligned MO_x structures, *Chem. Comm.*, 2009, **20**, 2791-2808.
- [4] J. Gong, Y. Lai, and C. Lin, Electrochemically multi-anodized TiO₂ nanotube arrays for enhancing hydrogen generation by photoelectrocatalytic water splitting, *Electrochimica Acta*, 2010, **55**, 4776-4782.
- [5] S. Sreekantan, K. A. Saharudin, Z. Lockman, and T. W. Tzu, Fast-rate formation of TiO₂ nanotube arrays in an organic bath and their applications in photocatalysis, *Nanotechnology*, 2010, **21**, 365603.
- [6] S. Palmas, A. M. Polcaro, J. Rodriguez Ruiz, A. Da Pozzo, M. Mascia, A. Vacca, TiO₂ photoanodes for electrically enhanced water splitting, *International Journal of Hydrogen Energy*, 2010, **35**, 6561-6570.
- [7] D. Wang, B. Yu, C. Wang, F. Zhou, and W. Liu, A novel protocol toward perfect alignment of anodized TiO₂ nanotubes, *Adv. Mater.*, 2009, **21**, 1964-1967.
- [8] K. Kant, and D. Losic, A simple approach for synthesis of TiO₂ nanotubes with through-hole morphology, *Phys. Status Solidi RRL*, 2009, **3**, 139-141.
- [9] S. Li, G. Zhang, D. Guo, L. Yu, and W. Zhang, Anodization fabrication of highly ordered TiO₂ nanotubes, *J. Phys. Chem. C*, 2009, **113**, 12759-12765.
- [10] D. R. Baker, and P. V. Kamat, Disassembly, reassembly, and photoelectrochemistry of etched TiO₂ nanotubes, *J. Phys. Chem. C*, 2009, **113**, 17967-17972.
- [11] T. Stergiopoulos, A. Valota, V. Likodimos, Th. Speliotis, D. Niarchos, P. Skeldon, G. E. Thompson, and P. Falaras, Dye-sensitization of self-assembled titania nanotubes prepared by galvanostatic anodization of Ti sputtered on conductive glass, *Nanotechnology*, 2009, **20**, 365601.
- [12] O. K. Varghese, M. Paulose, and C. A. Grimes, Long vertically aligned titania

nanotubes on transparent conducting oxide for highly efficient solar cells, *Nature Nanotech.*, 2009, **4**, 592-597.

[13] H. Y. Chang, W. J. Tzeng, and S. Y. Cheng, Modification of TiO₂ nanotube arrays by solution coating, *Solid State Ionics*, 2009, **180**, 817-821.

[14] S. Sreekantan, R. Hazan, Z. Lockman, Photoactivity of anatase-rutile TiO₂ nanotubes formed by anodization method, *Thin Solid Films*, 2009, **518**, 16-21.

[15] N. K. Allam, and C. A. Grimes, Room temperatures one-step polyol synthesis of anatase TiO₂ nanotube arrays: photoelectrochemical properties, *Langmuir*, 2009, **25**, 7234-7240.

[16] Y. Lai, H. Zhuang, L. Sun, Z. Chen, C. Lin, Self-organized TiO₂ nanotubes in mixed organic-inorganic electrolytes and their photoelectrochemical performance, *Electrochim. Acta*, 2009, **54**, 6536-6542.

[17] S. Bauer, J. Park, J. Faltenbacher, S. Berger, K. von der Mark, and P. Schmuki, Size selective behavior of mesenchymal stem cells on ZrO₂ and TiO₂ nanotube arrays, *Integr. Biol.*, **2009**, **1**, 525-532.

[18] D. Wang, Y. Liu, B. Yu, F. Zhou, and W. Liu, TiO₂ nanotubes with tunable morphology, diameter, and length: synthesis and photo-electrical/catalytic performance, *Chem. Mater.*, 2009, **21**, 1198-1206.

[19] S. K. Das, and A. J. Bhattacharyya, High-lithium storage in mixed crystallographic phase nanotubes of titania and carbon-titania, *J. Phys. Chem. C*, 2009, **113**, 17367-17371.

[20] P. Chen, L. Gu, X. Xue, M. Li, and X. Cao, Engineering the growth of TiO₂ nanotube arrays on flexible carbon fibre sheets, *Chem. Comm.*, 2010, **46**, 5906-5908.

[21] S. Nosheen, F. S. Galasso, and S. L. Suib, Role of Ti-O bonds in phase transitions of TiO₂, *Langmuir*, 2009, **25**, 7623-7630.

[22] D. Wang, B. Yu, F. Zhou, C. Wang, and W. Liu, Synthesis and characterization of anatase TiO₂ nanotubes and their use in dye-sensitized solar cells, *Mater. Chem. Phys.*, 2009, **113**, 602-606.

[23] A. V. Grigorieva, E. A. Goodilin, L. E. Derlyukova, T. A. Anufrieva, A. B. Tarasov, Y. A. Dobrovolskii, and Y. D. Tretyakov, Titania nanotubes supported platinum catalyst in CO oxidation process, *Appl. Catal. A General*, 2009, **362**, 20-25.

[24] B. Ma, G. K. L. Goh, T. S. Zhang, J. Ma, Hierarchically structured anatase

- nanotubes and membranes, *Microporous Mesoporous Mater.*, 2009, **124**, 162-168.
- [25] H. Shin, D. K. Jeong, J. Lee, M. M. Sung, and J. Kim, Formation of TiO₂ and ZrO₂ nanotubes using atomic layer deposition with ultraprecise control of the wall thickness, *Adv. Mater.*, 2004, **16**, 1197-1200.
- [26] C. J. W. Ng, H. Gao, and T. T. Y. Tan, Atomic layer deposition of TiO₂ nanostructures for self-cleaning applications, *Nanotechnology*, 2008, **19**, 445604.
- [27] C. Bae, Y. Yoon, H. Yoo, D. Han, J. Cho, B. H. Lee, M. M. Sung, M. Lee, J. Kim, and H. Shin, Controlled fabrication of multiwall anatase TiO₂ nanotubular architectures, *Chem. Mater.*, 2009, **21**, 2574-2576.
- [28] G. Szöllösi, Z. Németh, K. Hernádi, and M. Bartók, Preparation and characterization of TiO₂ coated multi-walled carbon nanotube-supported Pd and its catalytic performance in the asymmetric hydrogenation of α,β -unsaturated carboxylic acids, *Catal. Lett.*, 2009, **132**, 370-376.
- [29] T. Tsubota, A. Ono, N. Murakami, and T. Ohno, Characterization and photocatalytic performance of carbon nanotube material-modified TiO₂ synthesized by using the hot CVD process, *Appl. Catal. B Environmental*, 2009, **91**, 533-538.
- [30] S. Muduli, W. Lee, V. Dhas, S. Mujawar, M. Dubey, K. Vijayamohan, S. H. Han, and S. Ogale, Enhanced conversion efficiency in dye-sensitized solar cells based on hydrothermally synthesized TiO₂-MWCNT nanocomposites, *Appl. Mater. Interfaces*, 2009, **1**, 2030-2035.
- [31] T. Ueda, K. Takahashi, F. Mitsugi, and T. Ikegami, Preparation of single-walled carbon nanotube/TiO₂ hybrid atmospheric gas sensor operated at ambient temperature, *Diamond Relat. Mater.*, 2009, **18**, 493-496.
- [32] Y. Zhao, Y. Hu, Y. Li, H. Zhang, S. Zhang, L. Qu, G. Shi, and L. Dai, Super-long aligned TiO₂/carbon nanotube arrays, *Nanotechnology*, **2010**, 21, 505702.
- [33] J. W. Diggle, T. C. Downie, and C. W. Goulding, Anodic oxide films on aluminum, *Chem. Rev.*, **1969**, 69, 365-405.
- [34] X. Meng, M. Ionescu, M. N. Banis, Y. Zhong, H. Liu, Y. Zhang, S. Sun, R. Li, and X. Sun, Heterostructural coaxial nanotubes of CNT@Fe₂O₃ via atomic layer deposition: effects of surface functionalization and nitrogen-doping, *J. Nanopart. Res.*, 2011, **13**, 1207-1218.

- [35] Z. Wang, M. D. Shierley, S. T. Meikle, R. L. D. Whitby, S. V. Mikhalovsky, The surface acidity of acid oxidized multi-walled carbon nanotubes and the influence of in-situ generated fulvic acids on their stability in aqueous dispersions, *Carbon*, 2009, **47**, 73-79.
- [36] J. Aarik, A. Aidla, T. Uustare, and V. Sammelselg, Morphology and structure of TiO₂ thin films grown by atomic layer deposition, *J. Cryst. Growth*, 1995, **148**, 268-275.
- [37] J. Aarik, A. Aidla, T. Uustare, M. Ritala, M. Leskelä, Titanium isopropoxide as a precursor for atomic layer deposition: characterization of titanium dioxide growth process, *Appl. Surf. Sci.*, 2000, **161**, 385-395.

Supporting Information

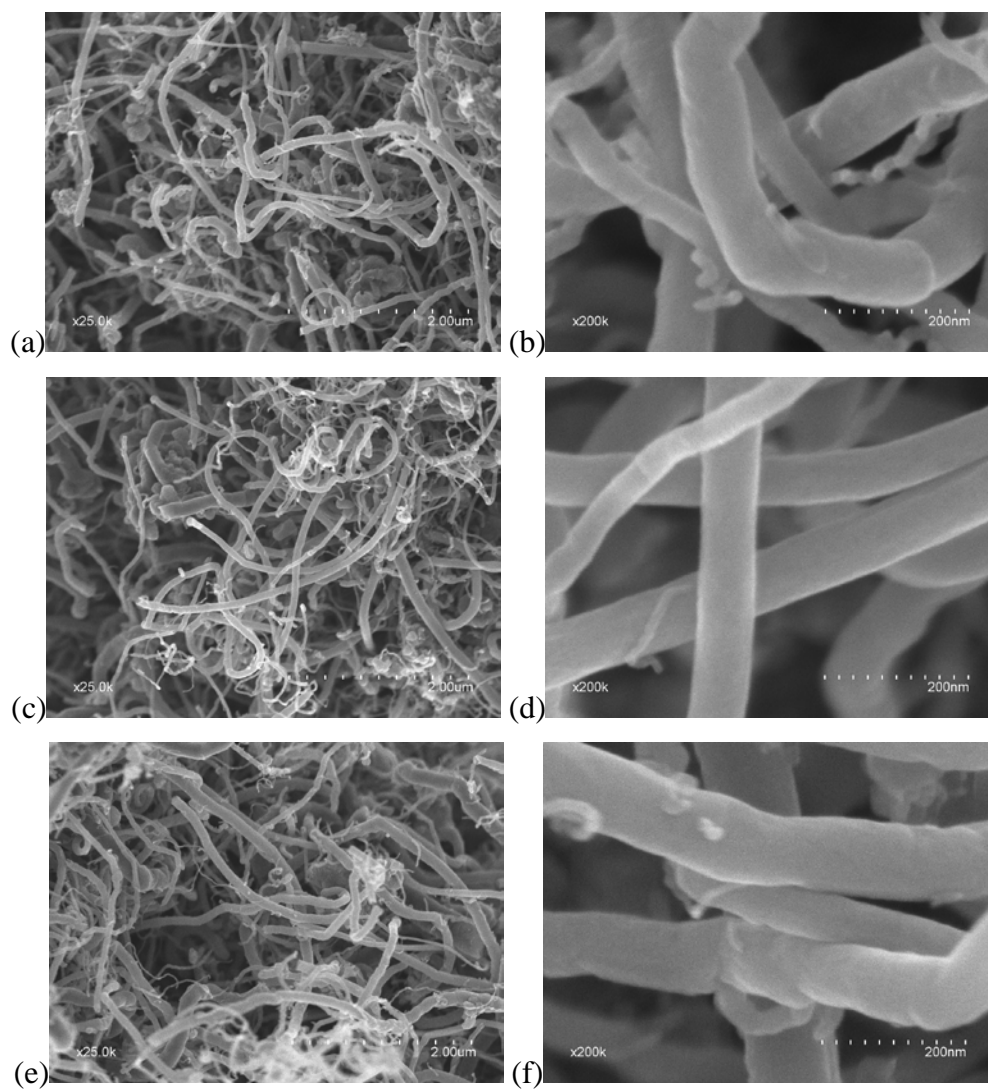


Figure SI-8.1 SEM images of (a,b) as-received, (c,d) 1h oxidized, and (e,f) 2h oxidized CNTs

CHAPTER 9

CONTROLLABLE SYNTHESIS OF GRAPHENE-BASED TITANIUM DIOXIDE NANOCOMPOSITES BY ATOMIC LAYER DEPOSITION

A version of this chapter has been published in *Nanotechnology*, 2011, 22, 165602, and featured by Cover Page.

Atomic layer deposition (ALD) was used to synthesize graphene-based metal oxide nanocomposites. This strategy was fulfilled on the preparation of TiO₂-graphene nanosheet (TiO₂-GNS) nanocomposites using titanium isopropoxide and water as precursors. The synthesized nanocomposites demonstrated that ALD exhibited many benefits in a controllable means. It was found that the as-deposited TiO₂ was not only tunable in its morphologies but also in its structural phases. As for the former one, TiO₂ was transferrable from nanoparticles to nanofilms with increased cycles. With regard to the latter one, TiO₂ was changeable from amorphous, to crystalline phase, and even a mixture of the two with increased growth temperatures (up to 250 °C). The underlying growth mechanisms were discussed and the resultant TiO₂-GNS nanocomposites have great potentials for many applications, such as photocatalysis, lithium-ion batteries, fuel cell, and sensors.

Keywords: *Atomic layer deposition, Nanocomposites, Graphene, Metal oxides, Titanium Dioxide*

9.1 Introduction

Since the discovery of graphene in 2004 [1], many exceptional properties have been reported to date, such as high values of Young's modulus ($\sim 1,100$ GPa) [2], fracture strength (125 GPa) [2], thermal conductivity ($\sim 5,000$ W/m·K) [3], mobility of charge carriers ($200,00$ cm²/V·s) [4], and specific surface area (2630 m²/g) [5]. As a consequence, a vast amount of research has been stimulated to explore its applications in recent years. One possible way to utilize these properties in applications would be to incorporate graphene in composite materials. In this way, recently there was an increasing interest in using graphenes as building blocks in various composites and this kind of nanocomposites exhibited many benefits due to the combination of desirable properties of different materials. So far, graphene (or graphene stacks, a few layers of graphene) has been reported in the incorporation with three main types of materials: polymers [6-8], metals [9-11], and metal oxides [12-23], covering a series of applications (including field emitters, photocatalysis, conductors, supercapacitors, solar cells, fuel cells, and batteries, etc.) with improved mechanical, electrical, optical, or electrochemical properties. Of the aforementioned cases, metal oxide-graphene nanocomposites (MO-GNCs) represent an important class, mainly synthesized via solution-based methods. Although the solution-based methods offer potentially low cost and scalability, they are also exposed with inflexibility in precisely manipulating the deposition of metal oxides.

To circumvent the inability of the solution-based methods in precise synthesis, we fulfilled the preparation of MO-GNCs via a non-aqueous strategy, atomic layer deposition (ALD) in our recent work. ALD as a gas-solid synthesis route is featured by two sequentially cyclic self-limiting half-reactions, and by nature it is a layer-by-layer technique. In particular, the self-limiting characteristic distinguishes itself from aqueous solution methods and other vapor deposition techniques (e.g., chemical and physical vapor deposition) in such ways: precise control in deposition at the atomic level, excellent uniformity and conformality of deposited materials. Since the beginning of the 21st century, ALD is going into a fashion for nanotechnology and expanding its uses from the deposition of simple two-dimensional (2D) planar films to the preparation of complex

nanostructures of various materials [24,25]. Additionally, ALD has the capability to deposit both inorganic (metals and metal oxides) and organic materials (polymers) [26]. Thus, ALD has potentials to provide many beneficial factors in synthesizing MO-GNCs by manipulating the deposition of MOs. Amongst the MO-GNCs reported in literature, TiO₂-graphene nanocomposites is probably the most intensively investigated one, exhibiting improved performance in lithium-ion batteries (LIBs) [18], photocatalysis [19, 20], and solar cells [21-23], etc. In earlier studies, ALD has prepared TiO₂ in the forms of 2D planar films [27-34], 1D nanotubes [35-40], 0D composite nanoparticles [41, 42], and other complicated nanostructures [43]. A variety of precursors were previously applied for various ALD-TiO₂ processes, but TiCl₄ and titanium isopropoxide (TTIP, Ti(OCH(CH₃)₂)₄) were two widely used titanium sources, and water was the most common oxygen source. In comparison, TTIP and water as the ALD precursors had one main advantage over the use of TiCl₄ and water: no release of the corrosive by-product HCl and no chlorine residues in the film [27,30].

To date, however, there was little effort in developing TiO₂-GNCs via ALD yet. Thus, in our recent attempts TiO₂ was chosen as the candidate and deposited on graphene nanosheet (GNS) powders (synthesized in our group) using TTIP and water as the ALD precursors. The success on the synthesis of TiO₂-GNS nanocomposites demonstrated that the ALD approach exhibited many advantages by controlling the deposition of TiO₂. First of all, different from the solution-based methods employed in reported work [18-23], the ALD method could synthesize the nanocomposites with the TiO₂ component precisely controlled in its morphologies as well as contents by changing ALD cycles. In addition, it was for the first time found that the as-deposited TiO₂ could be tuned in structures from amorphous to crystalline anatase phase by simply adjusting growth temperatures. In particular, the growth temperature for the deposited anatase TiO₂ is only around 250 °C, which has not been reported in earlier studies. Consequently, this work provided not only an alternative approach to synthesize MO-GNCs but multi-choices of MO-GNCs as well. The resultant nanocomposites have great potentials for many important applications.

9.2 Experimental

9.2.1 Preparation of GNS

For preparation of GNS, we first oxidized natural graphite (NG) powder (45 μm , 99.99%, Sigma-Aldrich, as shown in [figure SI-9.1\(a\), Supporting Information](#)) using a modified Hummers method [44]. In detail, graphite powder (1 g) was first stirred in concentrated sulphuric acid (23 ml) with a following addition of sodium nitrate (0.5 g) at room temperature. The stirring lasted for 16 h, and then the mixture was cooled down to 0 $^{\circ}\text{C}$. Thereafter, potassium permanganate (3 g) was added to form a new mixture. Two hours later, the mixture became a green paste at around 35 $^{\circ}\text{C}$ and was stirred for another 3 h. Then, water (46 ml) was slowly added into the paste and the temperature was increased to 98 $^{\circ}\text{C}$. The suspension was remained at this temperature for 30 minutes before it was further diluted with another addition of water and hydrogen peroxide (140 ml). In the following, the suspension was filtered and washed until the pH value of the filtrate was neutral. The as-received slurry is the so-called graphite oxide (GO, [figure SI-9.1\(b\), Supporting Information](#)), which was further dried in a vacuum oven at 60 $^{\circ}\text{C}$. Further, the as-synthesized GO was first flushed by Ar for 20 min in a quartz tube. Then, the quartz tube was promptly moved into a Lindberg tube furnace with a preheated temperature around 1050 $^{\circ}\text{C}$. After 30-s thermal treatment, GO was reduced into expanded GNS powders ([figure SI-9.1\(c\), Supporting Information](#)).

9.2.2 ALD-TiO₂

In ALD-TiO₂ processes, the as-prepared GNS powders were first loaded into a commercial ALD reactor (Savannah 100, Cambridge Nanotechnology Inc., USA) preheated to a certain temperature. Then, TTIP (98%, Sigma-Aldrich) and deionized water (DI H₂O) were introduced into the ALD reactor in an alternating sequence to perform ALD-TiO₂. TTIP was heated to 70 $^{\circ}\text{C}$ while water was kept at room temperature in order to provide sufficient vapors for ALD-TiO₂ processes. Additionally, the delivery lines were heated to 150 $^{\circ}\text{C}$ in order to prevent the precursors from condensation.

Nitrogen was used as the carrier gas with a flow rate of 20 sccm and the ALD reactor was sustained at a low level of pressure (typically 0.4 Torr) with a vacuum pump (Pascal 2005 I, Adixon). The ALD procedures were set as follows: (1) a 1.0-s supply of TTIP; (2) a 3.0-s extended exposure of TTIP to GNS; (3) a 10.0-s purge of oversupplied TTIP and any by-products; (4) a 2.0-s supply of water vapor; (5) a 3.0-s extended exposure of water vapor to GNS; (6) a 10.0-s purge of oversupplied water and any by-products. The aforementioned six-step sequence constituted one ALD-TiO₂ cycle and the ALD processes could be adjustable with different cycling numbers and growth temperatures. In this study, three growth temperatures were employed for ALD-TiO₂ processes: 150, 200, and 250 °C.

9.2.3 Characterization

To characterize the morphologies, structures, and compositions of various samples, we used field emission scanning electron spectrometry (FE-SEM, Hitachi 4800S) coupled with energy dispersive spectroscopy (EDS), transmission electron microscopy (TEM, Philips CM10), high-resolution TEM (HRTEM, JEOL 2010 FEG), X-ray diffractometer (XRD, Inel multi-purpose diffractometer), and Fourier transform infrared spectroscopy (FTIR, Bruker Tensor 27).

9.3 Results and Discussion

9.3.1 Results

As stated above, GNS was made from GO (the products of oxidized NG) and used as the building block in synthesizing MO-GNCs. The characteristics of GNS were characterized by employing SEM, TEM, XRD, and FTIR, as illustrated in [figure 9.1](#). In contrast to its starting materials: NG ([figure SI-9.1\(a\)](#)) and GO ([figure SI-9.1\(b\)](#)), GNS (the SEM image in [figure 9.1\(a\)](#)) presents a fluffy and porous structure [45] featured by numerous honeycombs. The honeycombs are surrounded by graphene wrinkles. TEM image in

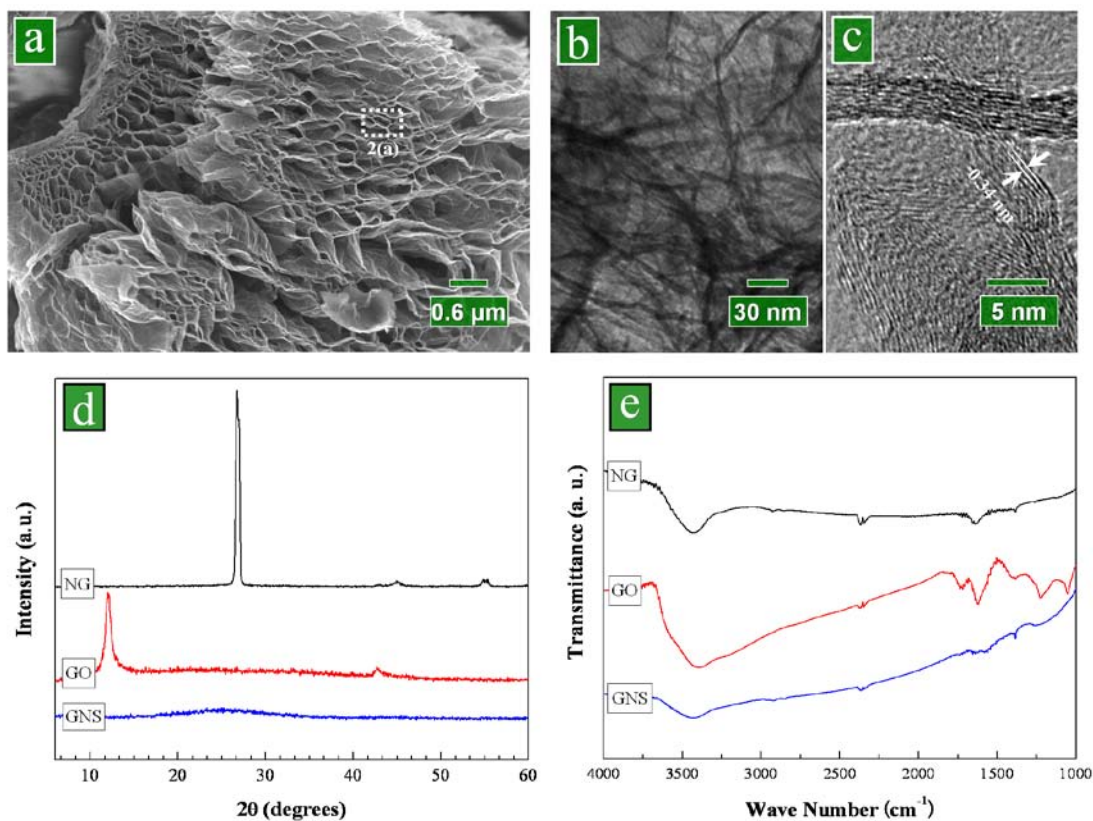


Figure 9.1 (a) SEM images of GNS; (b) TEM image, and (c) HRTEM image of GNS; (d) XRD and (e) FTIR spectra of NG, GO, and GNS.

figure 9.1(b) confirms the interlinked nature of the wrinkles. HRTEM image in figure 9.1(c) further reveals that the wrinkles are consisted of several graphene layers (typically less than 10 layers), i.e., graphene stacks. The interlayer distance is 0.34 nm. XRD spectra (figure 9.1(d)) clearly distinguish the as-synthesized GNS from its starting materials: NG and GO. NG has the strongest (002) peak at 26.8° , but GO shows the strongest (001) diffraction peak at 12° , suggesting that the interlayer distance increased and the structure was modified due to oxygenated groups [46]. In contrast, GNS receives a broad diffraction (002) peak shifted back to 26.8° , implying that GO was reduced via

the rapid thermal expansion and the extensive conjugated sp^2 carbon network (i.e., the ordered crystal structure) was restored [47]. FTIR spectra (figure 9.1(e)) further demonstrate the evolution of functional groups from NG to GO and GNS. NG mainly shows the stretching vibrations of hydroxyl (-OH) groups (3420 cm^{-1}) and C=C (1586 cm^{-1}) [48-50]. Besides the aforementioned groups, GO spectrum is added with the stretching vibrations of C=O (1736 cm^{-1}), carboxy C-O (1414 cm^{-1}), epoxy C-O (1220 cm^{-1}), and C-O (1100 cm^{-1}) [48-50]. In comparison, GNS is mainly with the stretching vibrations of hydroxyl groups and C=C [48-50]. The FTIR spectra imply that GNS was significantly reduced. Peaks below 900 cm^{-1} are usually not interpreted for they represent too complex a structural signature [46].

ALD-TiO₂ was performed on the as-prepared GNS powders with a series of cycles under three growth temperatures (150, 200, and 250 °C). The as-synthesized nanocomposites received from 300-cycle ALD-TiO₂ were characterized and compared, as shown in figure 9.2. It was found that growth temperature evidently influenced the natures of the as-synthesized nanocomposites. Figure 9.2(a) shows a high-magnification SEM image for a local area of GNS and its location is indicated in the inset of figure 9.2(a) as well as in figure 9.1(a). Obviously, the wrinkles are very thin (less than 3.4 nm in most cases, as disclosed in figure 9.1(c)). In contrast, a 300-cycle ALD-TiO₂ process changed the morphologies of GNS significantly, as shown in figure 9.2(b)-(d) and their insets with the same magnification. Remarkably, the wrinkles became thicker to around 15 nm (figure 9.2(b)), 29 nm (figure 9.2(c)), and 18 nm (figure 9.2(d)), corresponding to the growth temperature of 150, 200, and 250 °C, respectively. Obviously, ALD-TiO₂ deposited a layer of film on GNS in all the cases, which differed in thickness with temperature. Furthermore, if we suppose the pristine graphene wrinkles are around 3.4 nm with a conservative estimate, the average growth rates (or the growth per cycle, GPC) would be roughly evaluated as 0.19, 0.43, and 0.24 Å/cycle, respectively. The calculation of GPC is based on the homogeneous nature of ALD deposition on both sides of wrinkles and can be expressed by an equation: $GPC = (\text{the thickness of the coated wrinkles} - \text{the thickness of the pristine wrinkles}) / (2 \times \text{cycling numbers})$. Nevertheless, it was worth noting that the as-deposited TiO₂ is morphologically different under the three growth temperatures.

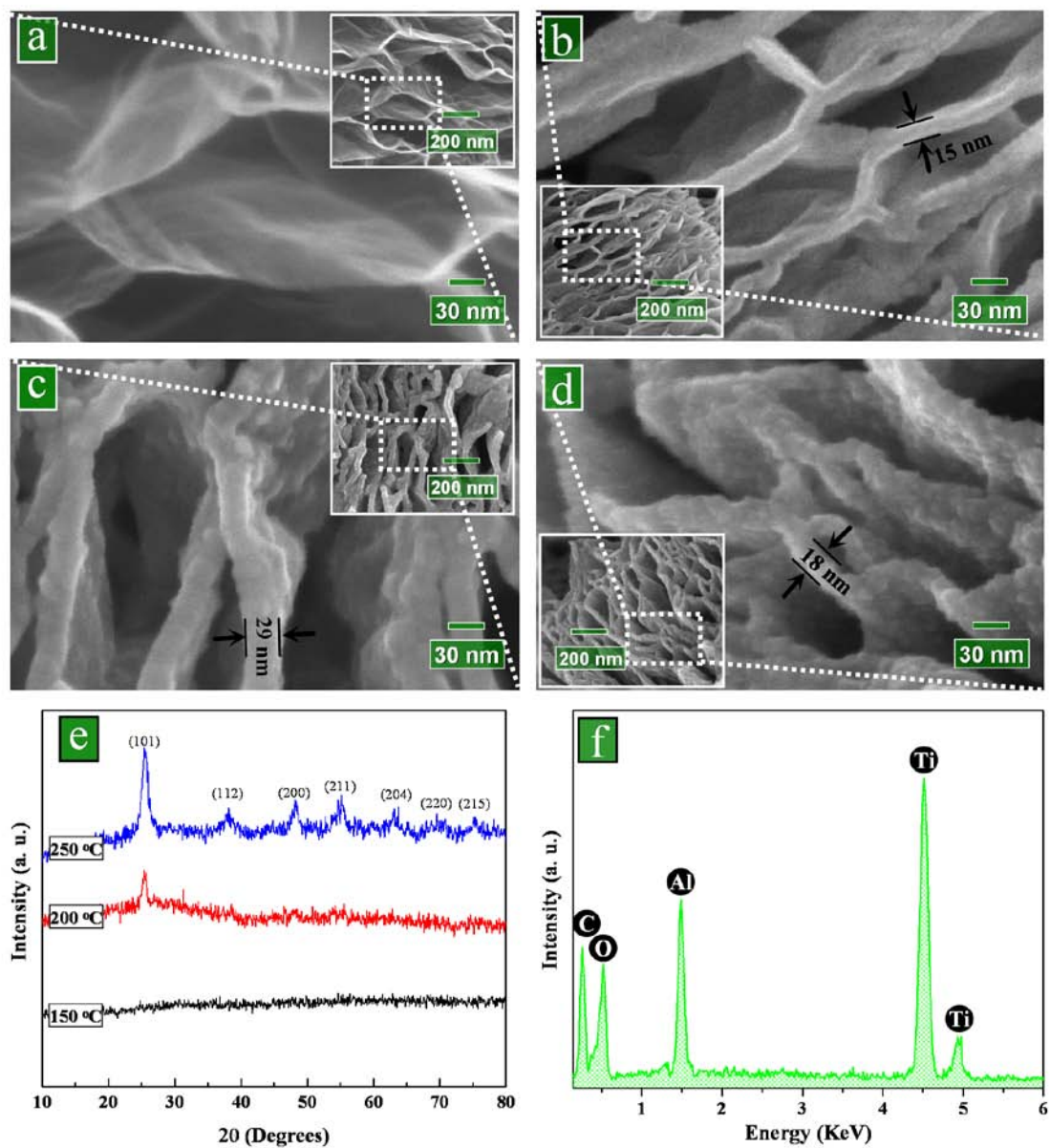


Figure 9.2 High-magnification SEM images of (a) pristine GNS, and 300-cycle ALD-TiO₂ on GNS at (b) 150 °C, (c) 200 °C as well as (d) 250 °C. Insets are low-magnification SEM images. (e) XRD spectra of 300-cycle ALD-TiO₂ on GNS at 150 °C, 200 °C, and 300 °C. (f) EDS spectra of 300-cycle ALD-TiO₂ on GNS at 150 °C.

In the case of 150 °C (figure 9.2(b)), the as-deposited layer is uniform and smooth; in the case of 200 °C (figure 9.2(c)), the deposited layer is mainly smooth except for some nanoparticles of around 15 nm which protrude from the film; in the case of 250 °C (figure 9.2(d)), however, the deposited layer becomes totally rough and bumpy. Thus, we postulated that growth temperature had influenced not only the deposition rates but the structures of the as-deposited TiO₂ as well. As for the latter one, XRD results illustrated in figure 9.2(e) provide the evidences. No peaks are identified with the sample deposited at 150 °C, suggesting that the as-deposited TiO₂ is amorphous. However, the sample grown at 200 °C exhibits a significant peak at 25.28° as well as two weak but uncertain peaks at 38.58° and 48.05°, corresponding to the (101), (112), and (200) plane of anatase TiO₂ (JCPDS PDF No. 21-1272), respectively. Furthermore, the XRD spectra of the sample grown at 250 °C present more peaks with increased intensities, corresponding to different characteristic planes of anatase TiO₂ (JCPDS PDF No. 21-1272) as denoted in figure 9.2(e). Obviously there existed phase transitions in the growth of ALD-TiO₂ with temperature. In addition, the compositions of the sample grown at 150 °C were further investigated using EDS, as shown in figure 9.2(f). Besides the confirmation on the presence of C, Ti, and O, figure 9.2(f) also shows some Al element contributed by the Al sample holder. Based on the information disclosed by figure 9.2, it is clearly shown that the growth temperatures influenced the structural phases, morphologies, and the deposition rates of the as-grown TiO₂. For more detailed growth characteristics, we examined the evolution of the ALD-TiO₂ with the increasing number of ALD cycles in each case.

Figure 9.3 reveals the growth of ALD-TiO₂ at 150 °C. A 50-cycle ALD-TiO₂ process (figure 9.3(a)) covered GNS with tiny nanoparticles of 2-3 nm uniformly and the nanoparticles grew to around 5 nm (the inset of figure 9.3(b)) with an additional 25 cycles (figure 9.3(b)). After a 100-cycle ALD-TiO₂ (figure 9.3(c)), a film was fully formed on GNS with a bit roughness and the wrinkles expose a thickness of around 7 nm. With another addition of 100 cycles (figure 9.3(d)), the film became smoother and much thicker. The wrinkles unveil a thickness of around 11 nm. Combined with the information of 300-cycle ALD-TiO₂ revealed in figure 9.2(b), we conclude that the ALD-TiO₂ at 150

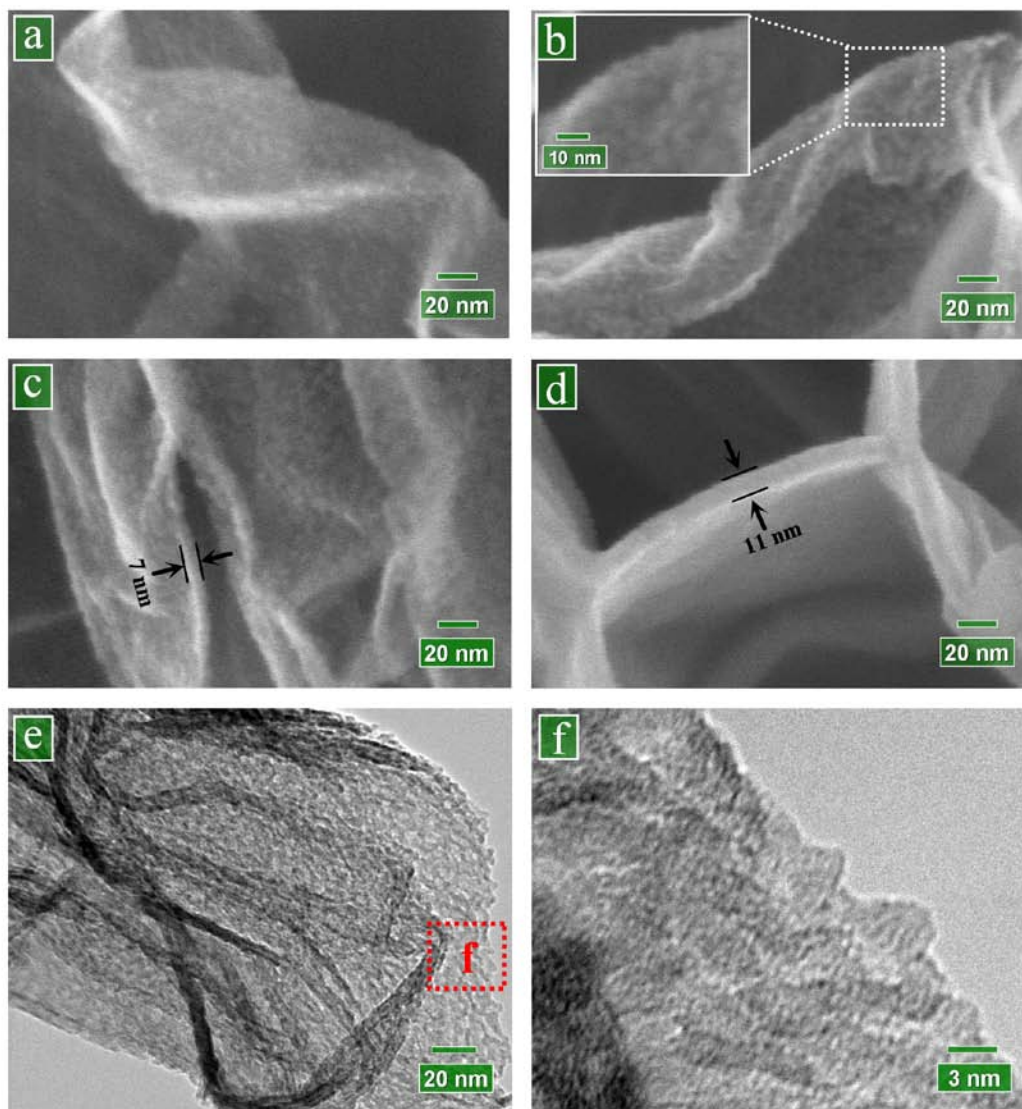


Figure 9.3 High-magnification SEM images of ALD-TiO₂ on GNS at 150 °C after (a) 50 cycles, (b) 75 cycles (inset for a higher magnification SEM image), (c) 100 cycles, and (d) 200 cycles. (e) TEM and (f) HRTEM image of 75-cycle ALD-TiO₂ on GNS at 150 °C.

°C experienced a slower growth in the first 100 cycles, accounting for about 0.18 Å/cycle; and the growth rate was increased to a consistent rate of 0.2 Å/cycle after the first 100 cycles. More information is included in [figure SI-9.2](#) in [Supporting Information](#). In

addition, TEM and HRTEM were applied to examine a sample coated by a 75-cycle ALD-TiO₂. In [figure 9.3\(e\)](#), TEM observation confirms the information disclosed by SEM in [figure 9.3\(b\)](#). Additionally, we noticed that nanoparticles were going to coalesce into a full layer. A local area as red-squared with a sign of “f” was further examined by HRTEM and shown in [figure 9.3\(f\)](#). The HRTEM image shows the disordered nature of the deposited TiO₂, providing additional evidence that the as-deposited TiO₂ was amorphous in structure. This is consistent with the XRD spectra for 150 °C in [figure 9.2\(e\)](#).

In [Figure 9.4](#), the growth of ALD-TiO₂ at 200 °C is illustrated. Similar to the case of 150 °C, GNS was mainly covered by nanoparticles after the first 50 and 75 cycles, as shown in [figure 9.4\(a\)](#) and [\(b\)](#), respectively. Upon the finishing of a 100-cycle ALD-TiO₂ ([figure 9.4\(c\)](#)), a significant change is observed from the thickness of wrinkles, accounting for 11 nm typically. It is also observed that a smooth film has been formed on GNS. In addition, it is noticed that some particles (around 5 nm) stand out of the film, as white-circled in [figure 9.4\(c\)](#). While the ALD-TiO₂ proceeded to 200 cycles ([figure 9.4\(d\)](#)), we can see that the GNS wrinkles increased to around 20 nm and the protruded particles became bigger in size to around 10 nm. Combined with the information of the 300-cycle ALD-TiO₂ revealed in [figure 9.2\(c\)](#), it is easy to conclude that the ALD-TiO₂ at 200 °C also experienced a slower growth in the first 100 cycles, accounting for about 0.38 Å /cycle; and the growth rate was increased to a constant rate of 0.45 Å/cycle after the first 100 cycles. More information is included in [figure SI-9.3](#) in [Supporting Information](#). Based on a sample with a 75-cycle ALD-TiO₂, TEM image in [figure 9.4\(e\)](#) reveals that the nanoparticles are around 10 nm and almost coalesce into a film. HRTEM observation on a local area, as red-squared with a sign of “f” in [figure 9.4\(e\)](#), is shown in [figure 9.4\(f\)](#). It is found that the as-deposited TiO₂ is mostly amorphous but decorated with some tiny crystalline nanoparticles of 2 - 3 nm which are partially indicated by the white-circled areas in [figure 9.4\(f\)](#). The crystalline particles are identified with an inter-plane spacing of 0.23 nm, corresponding to the (112) planes of anatase TiO₂. In addition, the graphene lattices are also observable, as marked with a 0.34-nm inter-plane spacing in [figure 9.4\(f\)](#). Based on the above discussion, we could further conclude that the particles protruded

from the films in [figure 9.4\(c\)](#) and [\(d\)](#) as well as in [figure 9.2\(c\)](#) are crystalline anatase while the films are mostly amorphous. Thus, we could know that the XRD spectra for 200 °C ([figure 9.2\(e\)](#)) resulted from the mixed amorphous and anatase phase of the as-deposited TiO₂. More specifically, the films are dominant by amorphous TiO₂ while the embellished anatase nanoparticles are responsible for the XRD characteristic peaks in [figure 9.2\(e\)](#).

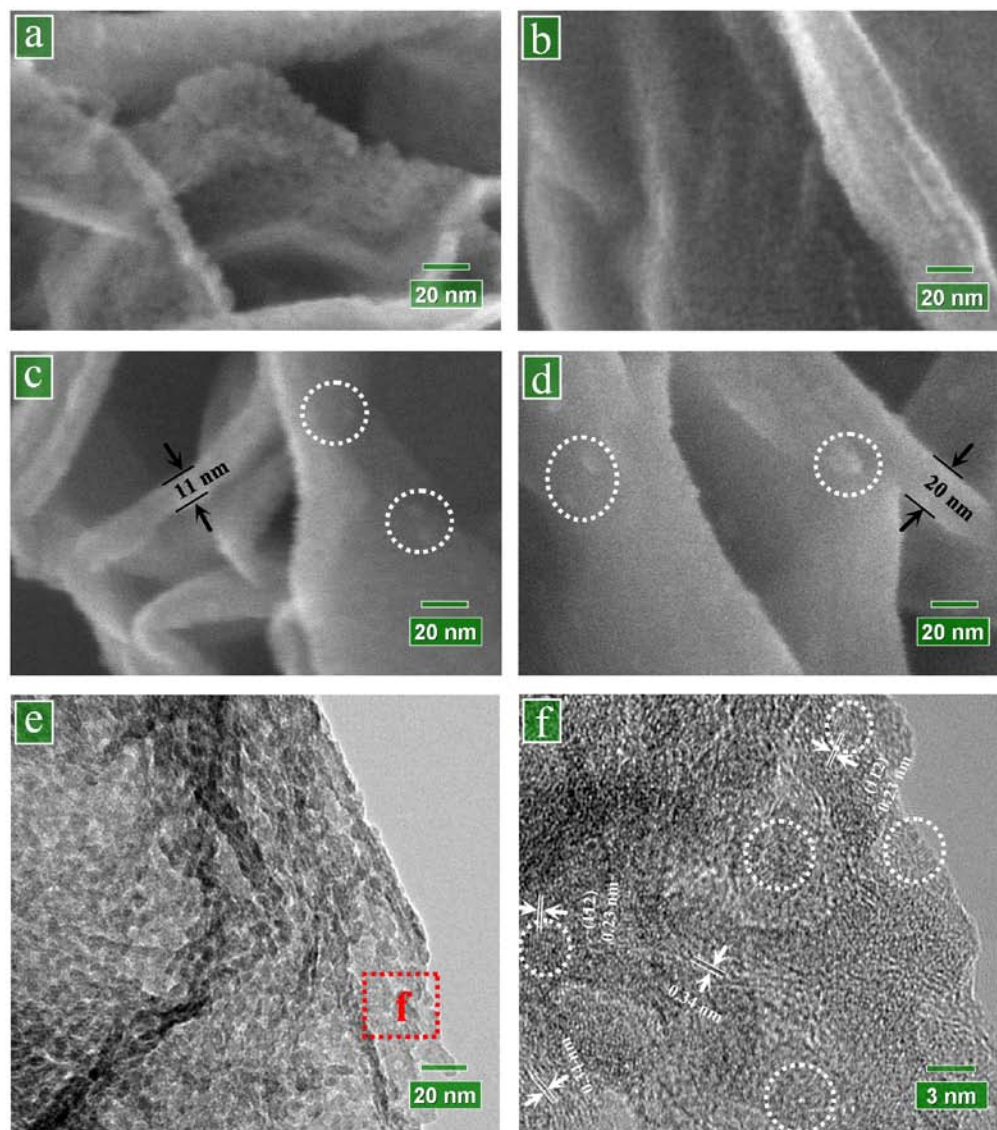


Figure 9.4 High-magnification SEM images of ALD-TiO₂ on GNS at 200 °C after (a) 50 cycles, (b) 75 cycles, (c) 100 cycles, and (d) 200 cycles. (e) TEM and (f) HRTEM image of 75-cycle ALD-TiO₂ on GNS at 200 °C.

Following the afore-discussed cases at 150 and 200 °C, we further demonstrate the growth of ALD-TiO₂ at 250 °C in [figure 9.5](#). Firstly, the ALD-TiO₂ deposited nanoparticles in the first several tens of cycles, growing bigger with increased cycles. In [figure 9.5\(a\)](#), the nanoparticles are less than 5 nm after a 50-cycle ALD-TiO₂. [Figure 9.5\(b\)](#) shows that the nanoparticles were significantly improved in their density while their sizes were increased to around 5 nm after a 75-cycle ALD-TiO₂. Upon the finishing of a 100-cycle ALD-TiO₂, SEM image in [figure 9.5\(c\)](#) presents a layer of a rough film due to the coalescence of the nanoparticles. At this stage, the wrinkles with the sample show a thickness of around 8 nm. Moreover, SEM image in [figure 9.5\(d\)](#) discloses that the wrinkles further grew in thickness to around 13 nm and the film retained some roughness. Combined with the information of the 300-cycle ALD-TiO₂ revealed in [figure 9.2\(d\)](#), it is obvious that ALD-TiO₂ at 250 °C experienced a slower growth of 0.23 Å/cycle in the first 100 cycles while almost remained a constant rate of 0.25 Å/cycle in the following cycles. More information is included in [figure SI-9.4](#) in [Supporting Information](#). Furthermore, based on a sample coated by a 75-cycle ALD-TiO₂, TEM image in [figure 9.5\(e\)](#) confirms that the as-deposited nanoparticles are around 5 nm and retain individually. HRTEM observation on a local area of [figure 9.5\(e\)](#) (as red-squared with a sign of “f”) is shown in [figure 9.5\(f\)](#). It reveals that all the as-deposited TiO₂ nanoparticles are crystalline and they mostly show an inter-plane spacing of 0.23 nm, corresponding to the (112) planes of anatase TiO₂. This is consistent to the XRD characteristic peak at 38.58° disclosed in [figure 9.2\(e\)](#) for 250 °C.

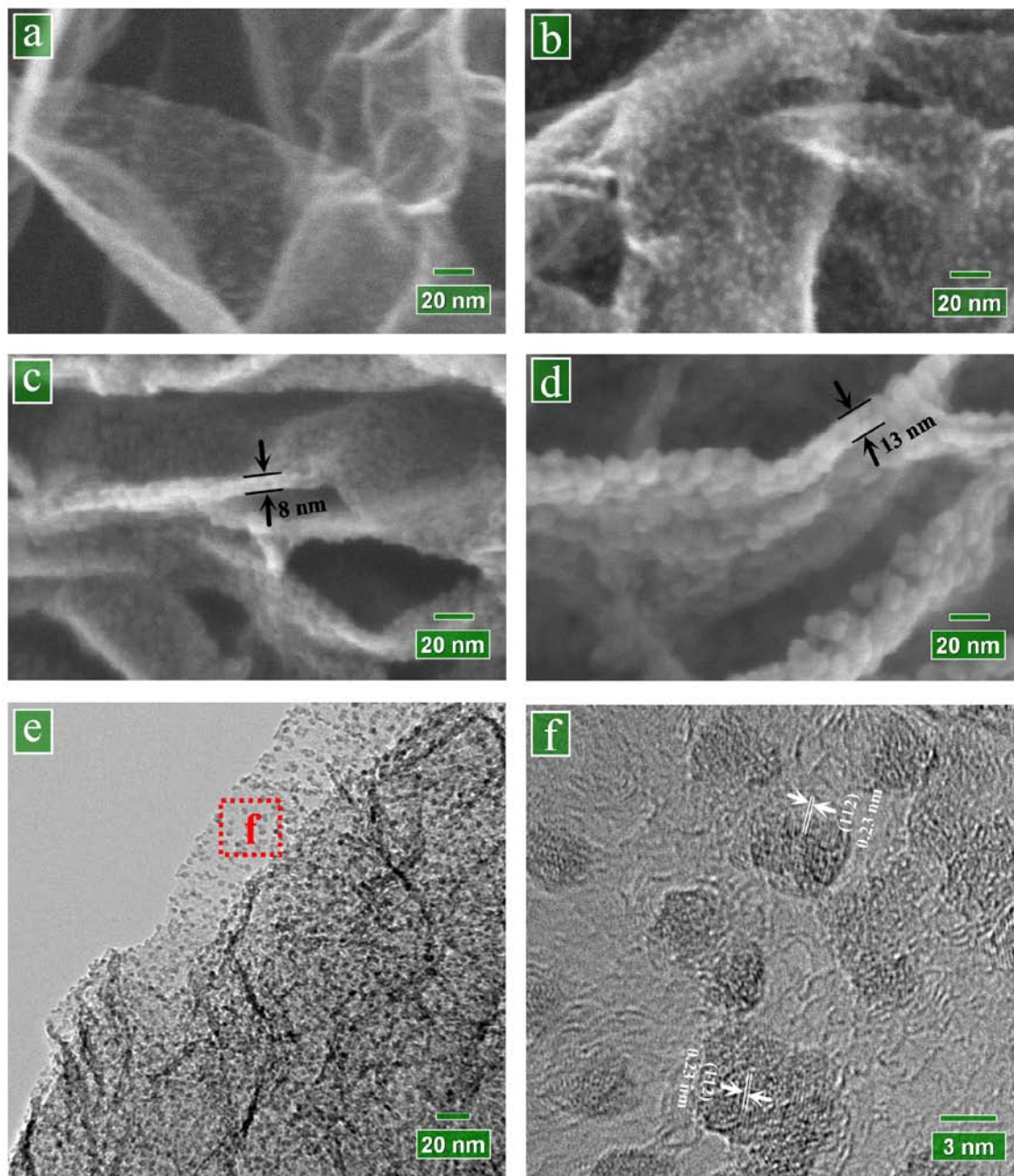


Figure 9.5 High-magnification SEM images of ALD-TiO₂ on GNS at 250 °C after (a) 50 cycles, (b) 75 cycles, (c) 100 cycles, and (d) 200 cycles. (e) TEM and (f) HRTEM image of 75-cycle ALD-TiO₂ on GNS at 250 °C.

9.3.2 Discussion

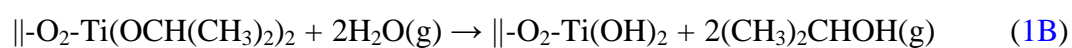
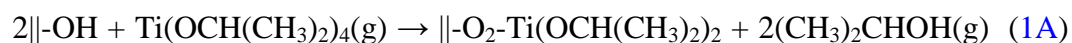
Based on the results disclosed above, one can easily learn that ALD as a strategy is flexible and precise in synthesizing MO-GNCs. In terms of the as-deposited TiO₂, its advantages are mainly exhibited in two ways: (1) tunable morphologies from nanoparticles to nanofilms; and (2) controllable structures from amorphous to crystalline anatase phase. The former is simply ascribed to its self-limiting and cyclic characters while the latter discloses the temperature-dependent nature of the ALD-TiO₂. To gain a better understanding, therefore, it is essential to clarify the determinant factors and to further explore the underlying mechanisms, which will be discussed in this section.

It is easy to understand that any result occurs only under some suitable conditions. In ALD processes, generally, there are three key parameters: the precursors, substrates and temperatures [51]. As stated in the beginning of this study, TTIP and water were the precursors and GNS was used as the substrate for ALD-TiO₂. As for the growth temperatures, we applied the ones not higher than 250 °C. On the choice of temperatures, it is in essence determined by the fundamentals of ALD as well as the properties of precursors. As a layer-by-layer deposition technique, ALD requires that the precursors will not decompose by themselves under a given growth temperature [27, 52]. Otherwise, the deposition will be a process of chemical vapor deposition (CVD), and destroy the self-limiting growth mechanism of ALD. Of the two precursors (TTIP and water), it is obvious that water being an oxygen source is not an issue for ALD-TiO₂ processes and it has been used under a temperature up to 600 °C [53]. The limit is mainly from TTIP. Some pioneer work conducted by Finish researchers [27-29] has disclosed that TTIP is only chemically stable for the temperatures not higher than 250 °C. Thus, any higher temperature would incur an increasing part of CVD growth of TiO₂ due to the decomposition of TTIP. Obviously, our experiments fell into a scope of temperatures being safe for the ALD processes of TiO₂.

In addition, in order to well fulfill the self-limiting layer-by-layer nature of the ALD technique, one needs to guarantee that there are sufficient vapors of the applied

precursors supplied during ALD processes. Otherwise, a slower but uncertain growth [51] as well as some unexpected structure [54] might be produced. Thus, to avoid these uncertainties, we investigated the suitable pulse lengths for the precursors of TTIP and water. It was found that a 0.8-s TTIP and 1.0-s water could provide sufficient vapors for an unchanged growth mode of the ALD-TiO₂. The evidences are included in [figure SI-9.5](#) and [9.6](#) in [Supporting Information](#). Therefore, the adopted pulses of 1.0-s TTIP and 2.0-s water in this study would always contribute a consistent deposition behavior of the ALD-TiO₂ for a certain temperature.

To further understand the findings disclosed in this study, one needs to know the roles played by the aforementioned parameters, which are associated with surface chemistry. It is well-known that ALD as a surface-controlled process relies on two alternating half-reactions to realize a layer-by-layer deposition. Ascribed to Rahtu and Ritala [29], the ALD process of using TTIP and water was described by two half-reactions as follows:



where the symbol “||” denotes the substrate surface and “(g)” refers to gas phase species. In particular, Rahtu and Ritala claimed that this mechanism is suitable for an ALD-TiO₂ with a temperature not higher than 250 °C. Obviously, the self-limiting nature of “A-B” determines the precise growth of TiO₂. Due to its surface-controlled character, ALD requires a substrate functionalized for its initiation. To meet this requirement, the FTIR spectra of [figure 9.1\(e\)](#) clearly reveal that the as-prepared GNS was decorated with hydroxyl groups, which could initiate an ALD-TiO₂ by following the reaction of [1A](#).

Based on the above discussion, we will first clarify the facts on the tunable morphologies of the as-deposited TiO₂. As we observed, the as-deposited TiO₂ differed in morphologies and growth rates between the stage of the first 100 cycles and the stage after the first 100 cycles. To facilitate the following discussion, we refer them to Stage-I and Stage-II, respectively. In the Stage-I, the as-deposited TiO₂ showed an island-like growth and appeared in the forms of nanoparticles with a lower growth rate; while in the Stage-II, the as-deposited TiO₂ coalesced into nanofilms with a higher and constant growth rate. These

serve for all the cases of different temperatures. As for the growth rates, we illustrated the values of GPC in [figure 9.6](#). According to earlier studies, there are two potential reasons for the occurrence of the Stage-I: steric hindrance of ligands and low density reactive surface sites [51]. Steric hindrance of ligands might cause the chemisorbed intermediates to shield part of the surface from being accessible to the precursors, highly depending on the sizes of the surface intermediates. In the case of TTIP, the effective diameter of a molecule is significantly larger than that of a Ti or O site [28]. On the other hand, the low density of reactive sites provides less “seats” than the numbers required for the precursors to bond and thereby to cover the surface. Thus, both could induce a low growth rate of TiO₂. While a film was fully formed on the surface of GNS (i.e., the cases occurred in the Stage-II), it is obvious that there would be more reactive sites. The increased reactive sites would promote the growth rates, as illustrated in [figure 9.6](#). Quite apparently, the ALD-TiO₂ on GNS experienced a substrate-inhibited growth of Type 1 [51]. Additionally, [figure 9.6](#) also shows that, besides the effect of the cycling numbers, the growth of ALD-TiO₂ is also highly temperature-dependent. In terms of the average GPC over the total 300 cycles, GPC increases with an increase in temperature from 150 to 200 °C whereas decreases with a further increase to 250 °C. To interpret this phenomenon, there are two factors for consideration: reactivity of precursors and density of reactive sites [51]. Aarik et al [28] revealed that water has a low reactivity towards TTIP in the ALD-TiO₂, but an increase on growth temperature could improve the reactivity of water, activate some reactions, and thereby improve the growth rate of ALD-TiO₂. However, the increased temperatures might incur an unfavorable effect at the same time: dehydroxylation of hydroxyl groups [55], whose occurrence would change the surface reactivity of GNS and thereby influence the following deposition of TiO₂ towards the chemisorbed TTIP molecules. The dehydroxylation is described as follows [54]:



Remarkably, this dehydroxylation would reduce the number of hydroxyl groups and thereby lead to a lower growth rate. Thus, an increased temperature might exert two contrary effects on the ALD-TiO₂. As a consequence, the highest GPC would achieve at a temperature at which a compromise could be reached between the two factors. It is easy to conclude that, as shown in [figure 9.6](#), the improved GPC with an increased temperature

from 150 to 200 °C was due to the predominance of the promoted reactivity of water while the reduced GPC with a further increase to 250 °C was induced by the dominant dehydroxylation. In addition, the evidences are also clearly shown in figure 9.3-9.5. For example, comparing figure 9.4(e) with 9.5(e), we can easily observe the reduced coverage due to dehydroxylation when the temperature was increased from 200 to 250 °C. Thus, the tunable morphologies of the as-deposited TiO₂ were commonly determined by both the surface nature of the substrate and the applied temperature.

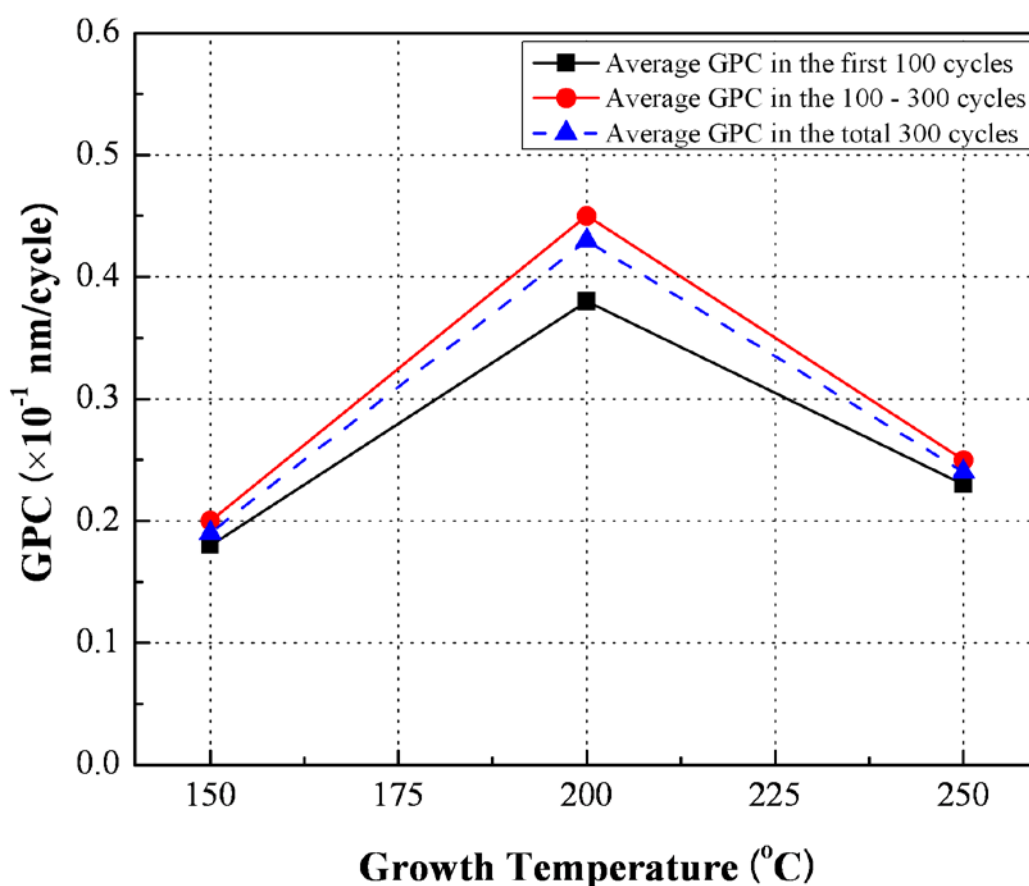


Figure 9.6 The growth rates (GPC) of ALD-TiO₂ with temperatures.

Besides tunable morphologies, it is of great interest to explain another main finding revealed in this study: the controllable structures of the as-deposited TiO_2 with growth temperature. In particular, this was rarely reported in literature of using TTIP and water as the precursors. In earlier studies, TTIP and water have been used to fulfill the ALD- TiO_2 on a series of substrates (soda lime glasses [27, 29], silica substrates [28], silicon substrates [28, 30], nanoporous templates [35-37], and nanoparticles [42]) for various nanostructures. All the efforts exclusively contributed the deposition of amorphous TiO_2 , except for a partial crystalline film grown on glasses at the temperature of 250 °C and at the higher ones [27]. It is worth noting that we reveal a pure crystalline TiO_2 deposited on GNS (as demonstrated in figure 9.2 and 9.5) at 250 °C. Thus, it is necessary to explore the bases for its occurrence. In this way, previous studies demonstrated that, in manipulating the phase-controllable growth of TiO_2 , both growth temperatures and substrates are important for the given precursors. Using TiCl_4 and water as ALD precursors, for example, amorphous TiO_2 films were grown on glasses while crystalline films were deposited on crystalline substrates at the same conditions [53]. Similarly, Schuisky et al also demonstrated that substrates could influence the structural phases of the as-deposited TiO_2 using TiI_4 and H_2O_2 as ALD precursors [56]. Nevertheless, Aarik et al [57] revealed that growth temperature is another important factor influencing the structural phases of TiO_2 using TiCl_4 and water as ALD precursors and higher temperatures are preferable to the growth of crystalline films on silicon substrates. Thus, it is reasonably believed that the characters of the as-prepared GNS and a relative high temperature (250 °C) jointly contributed the crystalline anatase TiO_2 deposited on GNS in this work. First, a higher temperature (250 °C) should be kinetically favorable for the ordering of the structure with minimum energy [57], for the intermediates might be able to migrate easily and enable the Ti and/or O ions to occupy the positions corresponding to the lowest free energy of the crystal. Furthermore, GNS is crystalline by nature and this might have prompted the deposition of the pure anatase TiO_2 as well, as demonstrated on crystalline substrates using TiCl_4 and water in literature [53]. In addition, a higher temperature (250 °C) might change the surface characters of GNS and the following deposition behaviors of the ALD- TiO_2 by modifying their reactive sites and natures. As a result, they might have been changed to be favorable for the preparation of the crystalline

TiO₂. Unfortunately, there is to date little knowledge to interpret the roles of substrates in literature and a further investigation on the growth mechanisms is needed. In comparison, two reasons might lead to previous fails in direct ALD-TiO₂ of crystalline structures using TTIP and water: low growth temperatures [35-37] or unfavorable substrates [27-30, 42]. As for the amorphous and mixed phases disclosed in figure 9.3 and 9.4 respectively, their lower temperatures (≤ 200 °C) should be the most dominant factor.

In summary, we produced a series of MO-GNCs via ALD-TiO₂ using TTIP and water as precursors in this work and the as-synthesized TiO₂-GNS nanocomposites exhibited many peculiarities in a controllable means. Besides the tunable morphologies, the as-deposited TiO₂ was also controllable in structures. In addition to the self-limiting and cyclic natures of ALD, the precursors, temperatures, and substrate (GNS) are believed to be among the main factors and their roles were discussed.

9.4 Conclusions

This work fulfilled and exemplified a non-aqueous approach to synthesize MO-GNCs. Based on powder-based GNS, TiO₂ was deposited on graphene (or graphene stacks) by ALD with a series of cycles under different temperatures. The results revealed that the as-synthesized TiO₂-GNS nanocomposites could be tuned in morphologies as well as structures. As for the controllable structures of TiO₂, it is found that a lower temperature (150 °C) contributed to amorphous TiO₂ while a higher temperature (250 °C) produced crystalline anatase TiO₂. In particular, a phase transition was observed with an intermediate temperature (200 °C). In all the cases, by adjusting their cycling numbers, the as-deposited TiO₂ could present nanoparticles or nanofilms on GNS. Furthermore, we discussed and explained the underlying mechanisms responsible for both the controllable structures and morphologies of the as-synthesized TiO₂-GNS nanocomposites. As a consequence, this article demonstrated that, in comparison to the solution-based methods exposed in literature, ALD contributed a precise and flexible route to prepare MO-GNCs. The as-synthesized hybrid TiO₂-GNS materials are potentially important candidates for

many important applications, such as lithium-ion batteries, solar cells, gas-sensing, and photocatalysis.

Acknowledgements

This research was supported by the Natural Science and Engineering Research Council of Canada (NSERC), Canada Research Chair (CRC) Program, Canadian Foundation for Innovation (CFI), Ontario Research Fund (ORF), Early Researcher Award (ERA) and the University of Western Ontario. In addition, the authors would like to appreciate the help from Mr. Fred Pearson on HRTEM analysis at Canadian Center for Electron Microscopy, McMaster University.

References

- [1] K. S. Novoselov, A. K. Geim, S. V. Morozov, D. Jiang, Y. Zhang, S. V. Dubonos, I. V. Grigorieva, and A. A. Firsov, Electric field effect in atomically thin carbon films, *Science*, 2004, **306**, 666-669.
- [2] C. Lee, X. Wei, J. W. Kysar, and J. Hone, Measurement of the elastic properties and intrinsic strength of monolayer graphene, *Science*, 2008, **321**, 385-388.
- [3] A. A. Balandin, S. Ghosh, W. Bao, I. Calizo, D. Teweldebrhan, F. Miao, and C. N. Lau, Superior thermal conductivity of single-layer graphene, *Nano Lett.*, 2008, **8**, 902-907.
- [4] K. I. Bolotin, K. J. Sikes, Z. Jiang, M. Klima, G. Fudenberg, J. Hone, P. Kim, and H. L. Stormer, Ultrahigh electron mobility in suspended graphene, *Solid State Commun.*, 2008, **146**, 351-355.
- [5] M. D. Stoller, S. Park, Y. Zhu, J. An, and R. S. Ruoff, Graphene-based ultracapacitors, *Nano Lett.*, 2008, **8**, 3498-3502.
- [6] S. Stankovich, D. A. Dikin, G. H. B. Dommett, K. M. Kohlhaas, E. J. Zimney, E. A. Stach, R. D. Piner, S. T. Nguyen, and R. S. Ruoff, Graphene-based composite materials, *Nature*, 2006, **442**, 282-286.
- [7] G. Eda, H. E. Unalan, N. Rupesinghe, G. A. J. Amaratunga, and M. Chhowalla, Field emission from graphene based composite thin films, *Appl. Phys. Lett.*, 2008, **93**, 233502.
- [8] T. Wei, G. Luo, Z. Fan, C. Zheng, J. Yan, C. Yao, W. Li, and C. Zhang, Preparation of graphene nanosheet/polymer composites using in situ reduction-extractive dispersion, *Carbon*, 2009, **47**, 2290-2299.
- [9] Y. Li, W. Gao, L. Ci, C. Wang, and P. M. Ajayan, Catalytic performance of Pt nanoparticles on reduced graphene oxide for methanol electro-oxidation, *Carbon*, 2010, **48**, 1124-1130.
- [10] X. Zhou, X. Huang, X. Qi, S. Wu, C. Xue, F. Y. C. Boey, Q. Yan, P. Chen, and H. Zhang, In situ synthesis of metal nanoparticles on single-layer graphene oxide and reduced graphene oxide surfaces, *J. Phys. Chem. C*, 2009, **113**, 10842-10846.
- [11] S. Guo, S. Dong, and E. Wang, Three-dimensional Pt-on-Pd dimetallic nanodendrites supported on graphene nanosheet: facile synthesis and used as an advanced

nanoelectrocatalyst for methanol oxidation, *ACS Nano*, 2010, **4**, 547-555.

[12] J. M. Lee, Y. B. Pyun, J. Yi, J. W. Choung, and W. I. Park, ZnO nanorod-graphene hybrid architectures for multifunctional conductors, *J. Phys. Chem. C*, 2009, **113**, 19134-19138.

[13] J. Wu, X. Shen, L. Jiang, K. Wang, and K. Chen, Solvothermal synthesis and characterization of sandwich-like/ZnO nanocomposites, *Appl. Surf. Sci.*, 2010, **256**, 2826-2830.

[14] J. Yao, X. Shen, B. Wang, H. Liu, and G. Wang, In situ chemical synthesis of SnO₂-graphene nanocomposites as anode materials for lithium-ion batteries, *Electrochem. Comm.*, 2009, **11**, 1849-1852.

[15] D. Wang, R. Kou, D. Choi, Z. Yang, Z. Nie, J. Li, L. V. Saraf, D. Hu, J. Zhang, G. L. Graff, J. Liu, M. A. Pope, and I. A. Aksay, Ternary self-assembly of ordered metal oxide-graphene nanocomposites for electrochemical energy storage, *ACS Nano*, 2010, **4**, 1587-1595.

[16] S. M. Paek, E. Yoo, and I. Honma, Enhanced cyclic performance and lithium storage capacity of SnO₂/graphene nanoporous electrodes with three-dimensionally delaminated flexible structure, *Nano Lett.*, 2009, **9**, 72-75.

[17] T. N. Lambert, C. A. Chavez, B. Hernandez-Sanchez, P. Lu, N. S. Bell, A. Ambrosini, T. Friedman, T. J. Boyle, D. R. Wheeler, and D. L. Huber, Synthesis and characterization of titania-graphene nanocomposites, *J. Phys. Chem. C*, 2009, **113**, 19812-19823.

[18] D. Wang, D. Choi, J. Li, Z. Yang, Z. Nie, R. Kou, D. Hu, C. Wang, L. V. Saraf, J. Zhang, I. A. Aksay, and J. Liu, Self-assembled TiO₂-graphene hybrid nanostructures for enhanced Li-ion insertion, *ACS Nano*, 2009, **3**, 907-914.

[19] G. Williams, B. Seger, and P. V. Kamat, TiO₂-graphene nanocomposites. UV-assisted photocatalytic reduction of graphene oxide, *ACS Nano*, 2008, **2**, 1487-1491.

[20] X. Y. Zhang, H. P. Li, X. L. Cui, and Y. Lin, Graphene/TiO₂ nanocomposites: synthesis, characterization and application in hydrogen evolution from water photocatalytic splitting, *J. Mater. Chem.*, 2010, **20**, 2801-2806.

[21] S. Sun, L. Gao, and Y. Liu, Enhanced dye-sensitized solar cell using graphene-TiO₂ photoanode prepared by heterogeneous coagulation, *Appl. Phys. Lett.*, 2010, **96**, 083113.

- [22] N. Yang, J. Zhai, D. Wang, Y. Chen, and L. Jiang, Two-dimensional graphene bridges enhanced photoinduced charge transport in dye-sensitized solar cell, *ACS Nano*, 2010, **4**, 887-894.
- [23] Y. B. Tang, C. S. Lee, J. Xu, Z. T. Liu, Z. H. Chen, Z. He, Y. L. Cao, G. Yuan, H. Song, L. Chen, L. Luo, H. M. Cheng, W. J. Zhang, I. Bello, and S. T. Lee, Incorporation of graphenes in nanostructured TiO₂ films via molecular grafting for dye-sensitized solar cell application, *ACS Nano*, 2010, **4**, 3482-3488.
- [24] M. Knez, K. Nielsch, and L. Niinistö, Synthesis and surface engineering of complex nanostructures by atomic layer deposition, *Adv. Mater.*, 2007, **19**, 3425-3438.
- [25] H. Kim, H. B. R. Lee, and W. J. Maeng, Application of atomic layer deposition to nanofabrication and emerging nanodevices, *Thin Solid Films*, 2008, **517**, 2563-2580.
- [26] S. M. George, Atomic layer deposition: an overview, *Chem. Rev.*, 2010, **110**, 111-131.
- [27] M. Ritala and M. Leskelä, Titanium isopropoxide as a precursor in atomic layer epitaxy of titanium dioxide thin films, *Chem. Mater.* 1993, **5**, 1174-1181.
- [28] J. Aarik, A. Aidla, T. Uustare, M. Ritala, and M. Leskelä, Titanium isopropoxide as a precursor for atomic layer deposition: characterization of titanium dioxide growth process, *Appl. Surf. Sci.*, 2000, **161**, 385-395.
- [29] A. Rahtu and M. Ritala, Reaction mechanism studies on titanium isopropoxide-water atomic layer deposition process, *Chem. Vap. Deposition*, 2002, **8**, 21-28.
- [30] Q. Xie, Y. L. Jiang, C. Detavernier, D. Deduytsche, R. L. Van Meirhaeghe, G. P. Ru, B. Z. Li, and X. P. Qu, Atomic layer deposition of TiO₂ from tetrakis-dimethyl-amido titanium or Ti isopropoxide precursors and H₂O, *J. Appl. Phys.*, 2007, **102**, 083521.
- [31] A. Suisalu, J. Aarik, H. Mändar, and I. Sildos, Spectroscopic study of nanocrystalline TiO₂ thin films grown by atomic layer deposition, *Thin Solid Films*, 1998, **336**, 295-298.
- [32] J. Aarik, A. Aidla, H. Mändar, and V. Sammelselg, Anomalous effect of temperature on atomic layer deposition of titanium dioxide, *J. Crystal Growth*, 2000, **220**, 531-537.
- [33] R. Matero, A. Rahtu, and M. Ritala, In situ quadrupole mass spectrometry and quartz crystal microbalance studies on the atomic layer deposition of titanium dioxide from titanium tetrachloride and water, *Chem. Mater.*, 2001, **13**, 4506-4511.

- [34] R. Methaapanon and S. F. Bent, Comparative study of titanium dioxide atomic layer deposition on silicon dioxide and hydrogen-terminated silicon, *J. Phys. Chem. C*, 2010, **114**, 10498-10504.
- [35] H. Shin, D.-K. Jeong, J. Lee, M. M. Sung, and J. Kim, Formation of TiO₂ and ZrO₂ nanotubes using atomic layer deposition with ultraprecise control of the wall thickness, *Adv. Mater.*, 2004, **16**, 1197-1200.
- [36] J. Lee, H. Ju, J. K. Lee, H. S. Kim, and J. Lee, Atomic layer deposition of TiO₂ nanotubes and its improved electrostatic capacitance, *Electrochem. Commun.*, 2010, **12**, 210-212.
- [37] G. M. Kim, S. M. Lee, G. H. Michler, H. Roggendorf, U. Gösele, and M. Knez, Nanostructured pure anatase titania tubes replicated from electrospun polymer fiber templates by atomic layer deposition, *Chem. Mater.*, 2008, **20**, 3085-3091.
- [38] M. S. Sander, M. J. Côté, W. Gu, B. M. Kile, and C. P. Tripp, Template-assisted fabrication of dense, aligned arrays of titania nanotubes with well-controlled dimensions on substrates, *Adv. Mater.*, 2004, **16**, 2052-2057.
- [39] C. J. W. Ng, H. Gao, and T. T. Y. Tan, Atomic layer deposition of TiO₂ nanostructures for self-cleaning applications, *Nanotechnology*, 2008, **19**, 445604.
- [40] L. K. Tan, M. A. S. Chong, and H. Gao, Free-standing porous anodic alumina templates for atomic layer deposition of highly ordered TiO₂ nanotube arrays on various substrates, *J. Phys. Chem. C*, 2008, **112**, 69-73.
- [41] J. D. Ferguson, A. R. Yoder, A. W. Weimer, and S. M. George, TiO₂ atomic layer deposition on ZrO₂ particles using alternating exposures of TiCl₄ and H₂O, *Appl. Surf. Sci.*, 2004, **226**, 393-404.
- [42] D. M. King, X. Liang, Y. Zhou, C. S. Carney, L. F. Hakim, P. Li, and A. W. Weimer, Atomic layer deposition of TiO₂ films on particles in a fluidized bed reactor, *Powder Technol.*, 2008, **183**, 356-363.
- [43] X. D. Wang, E. Graugnard, J. S. King, Z. L. Wang, and C. J. Summers, Large-scale fabrication of ordered nanobowl arrays, *Nano Lett.*, 2004, **4**, 2223-2226.
- [44] W. S. Hummers and R. E. Offeman, Preparation of graphitic oxide, *J. Am. Chem. Soc.*, 1958, **80**, 1339.
- [45] A. Celzard, J. F. Mareche, and G. Furdin, Modelling of exfoliated graphite, *Prog.*

Mater. Sci., 2005, **50**, 93-179.

[46] D. W. Lee, L. D. L. Santos V., J. W. Seo, L. L. Felix, A. Bustamante D., J. M. Cole, and C. H. W. Barnes, The structure of graphite oxide: investigate of its surface chemical groups, *J. Phys. Chem. B*, 2010, **114**, 5723-5728.

[47] L. Tang, Y. Wang, Y. Li, H. Feng, J. Lu, and J. Li, Preparation, structure, and electrochemical properties of reduced graphene sheet films, *Adv. Funct. Mater.*, 2009, **19**, 2782-2789.

[48] C. Nethravathi, T. Nisha, N. Ravishankar, C. Shivakumara, and M. Rajamathi, Graphene-nanocrystalline metal sulphide composites produced by a one-pot reaction starting from graphite oxide, *Carbon*, 2009, **47**, 2054-2059.

[49] W. Chen, L. Yan, and P. R. Bangal, Preparation of graphene by the rapid and mild thermal reduction of graphene oxide induced by microwaves, *Carbon*, 2010, **48**, 1146-1152.

[50] V. K. Singh, M. K. Patra, M. Manoth, G. S. Gowd, S. R. Vadera, and N. Kumar, In situ synthesis of graphene oxide and its composites with iron oxide, *New Carbon Mater.*, 2009, **24**, 147-152.

[51] R. L. Puurunen, Surface chemistry of atomic layer deposition: a case study for the trimethylaluminum/water process, *J. Appl. Phys.*, 2005, **97**, 121301.

[52] M. Leskelä and M. Ritala, Atomic layer deposition chemistry: recent developments and future challenges, *Angew. Chem. Int. Ed.*, 2003, **42**, 5548-5554.

[53] M. Ritala, M. Leskelä, E. Nykänen, P. Soininen, and L. Niinistö, Growth of titanium-dioxide thin-films by atomic layer epitaxy, *Thin Solid Films*, 1993, **225**, 288-295.

[54] G. D. Parfitt, The surface of titanium oxide, *Prog. Surf. Membr. Sci.*, 1976, **11**, 181-226.

[55] J. Aarik, A. Aidla, V. Sammelselg, H. Siimon, and T. Uustare, Control of thin film structure by reactant pressure in atomic layer deposition of TiO₂, *J. Cryst. Growth*, 1996, **169**, 496-502.

[56] M. Schuisky, A. Harsta, A. Aidla, K. Kukli, A. A. Kiisler, and J. Aarik, Atomic layer chemical vapor deposition of TiO₂--low temperature epitaxy of rutile and anatase, *J. Electrochem. Soc.*, 2000, **147**, 3319-3325.

[57] J. Aarik, A. Aidla, T. Uustare, and V. Sammelselg, Morphology and structure of TiO₂ thin films grown by atomic layer deposition, *J. Cryst. Growth*, 1995, **148**, 268-275.

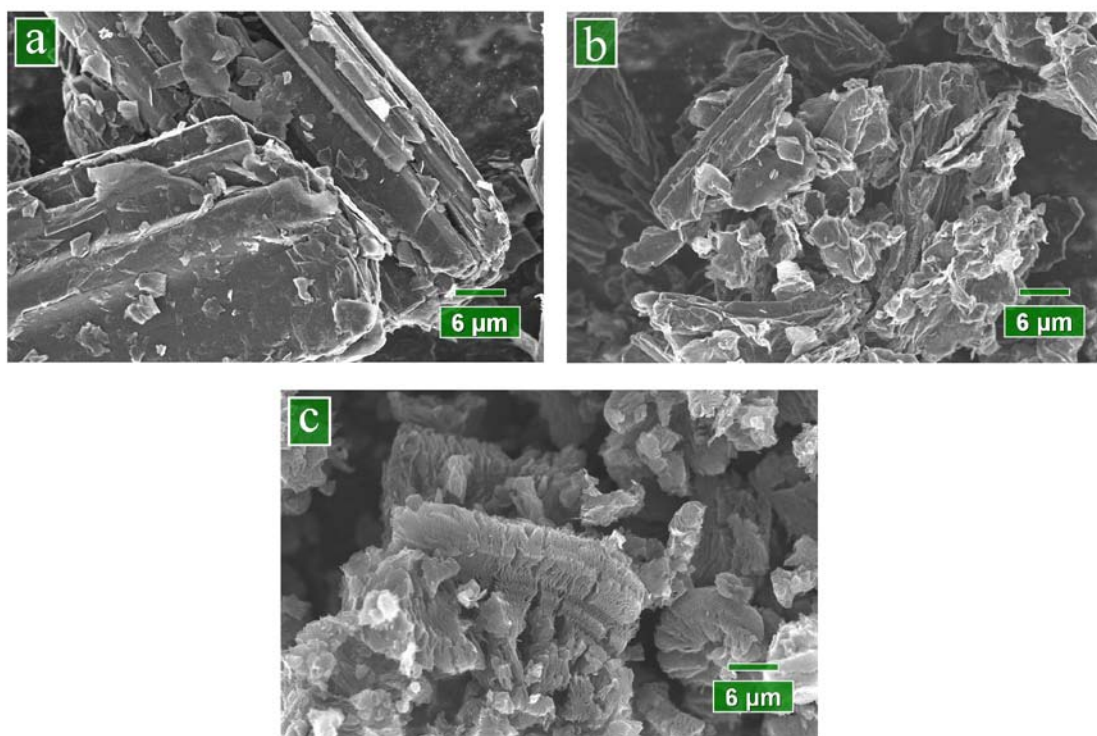
Supporting Information

Figure SI-9.1 SEM images of (a) NG, (b) GO, and (c) GNS powders.

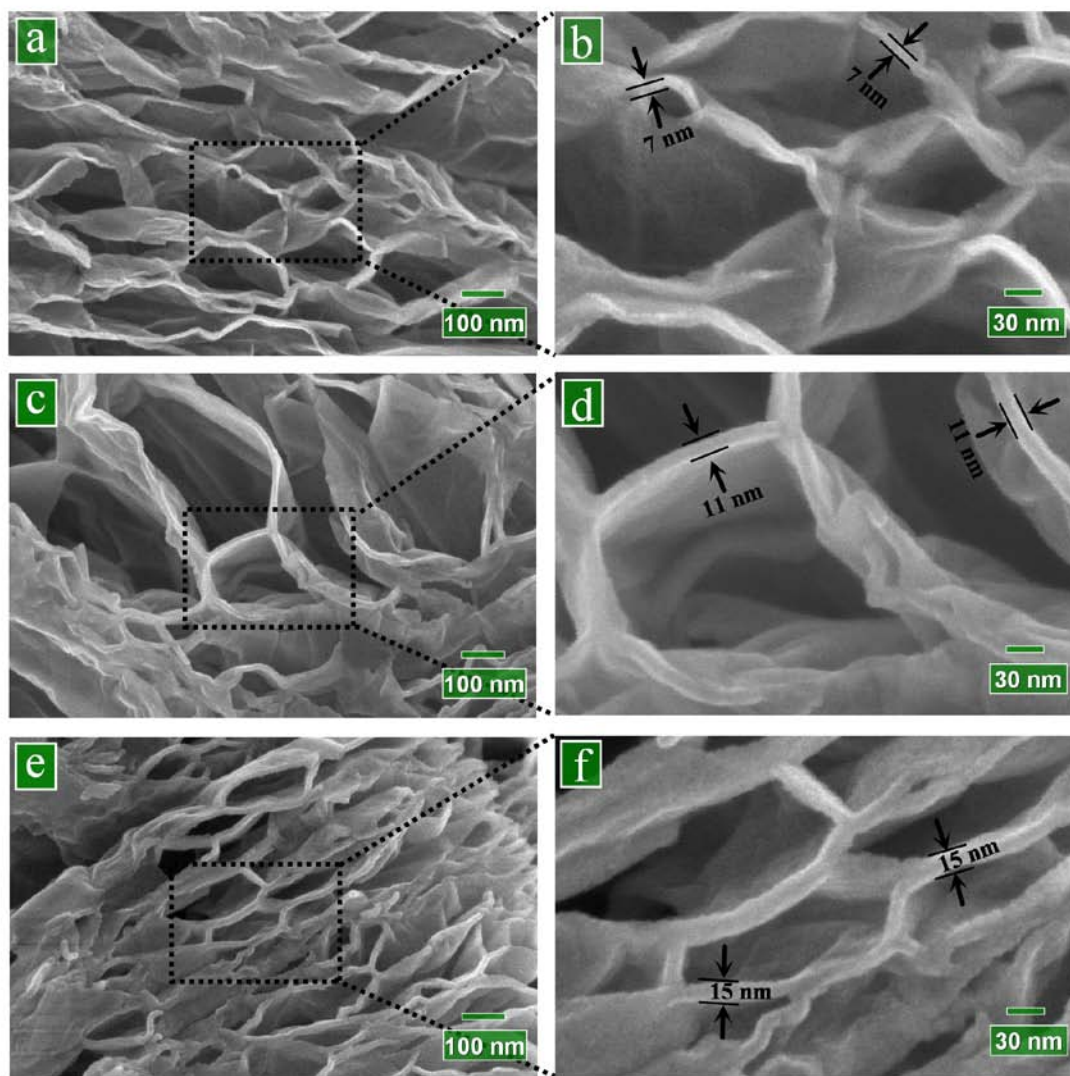


Figure SI-9.2 SEM images for ((a) and (b)) 100-cycle, ((c) and (d)) 200-cycle, and ((e) and (f)) 300-cycle ALD-TiO₂ on GNS at 150 °C under a supply of 1.0-s TTIP and 2.0-s water.

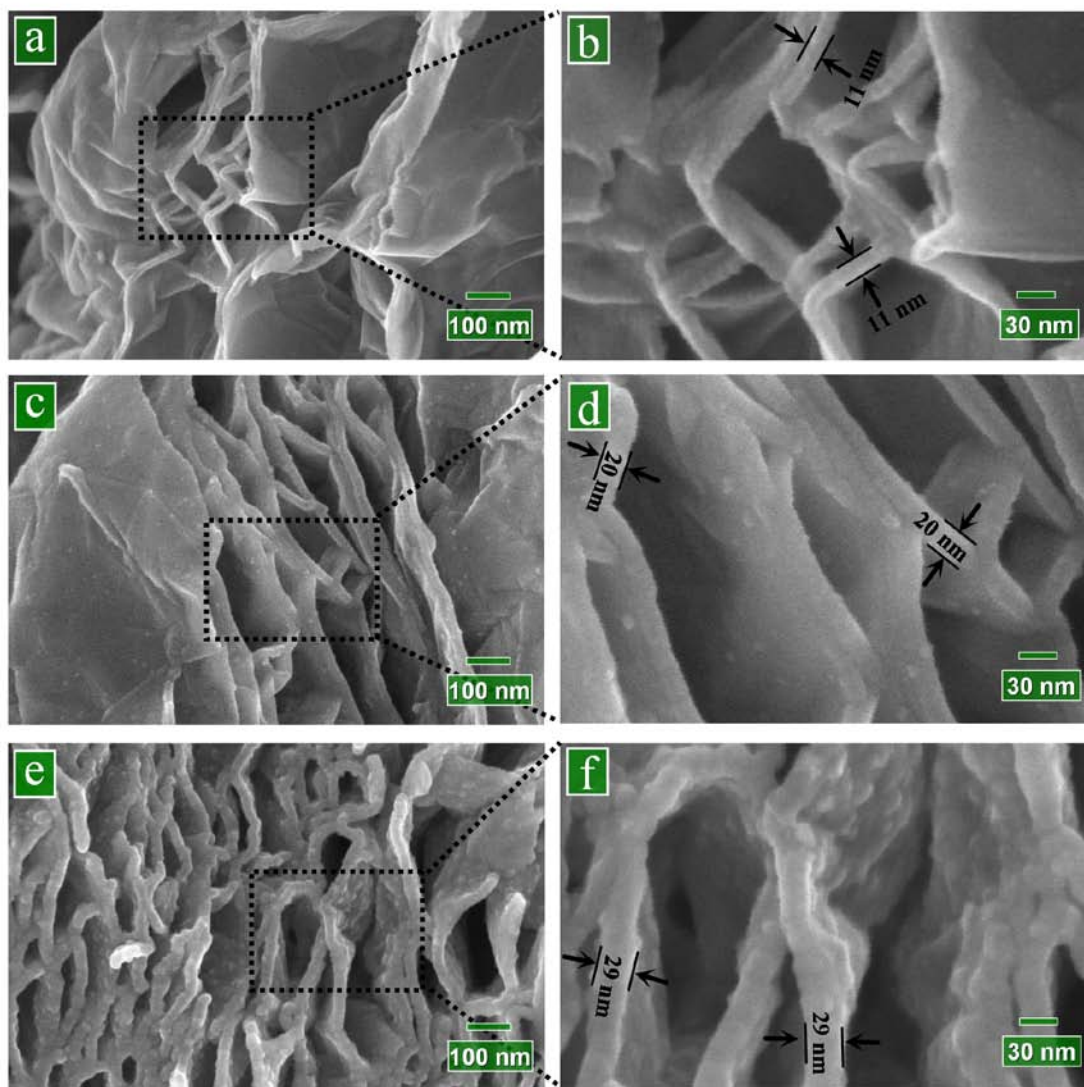


Figure SI-9.3 SEM images for ((a) and (b)) 100-cycle, ((c) and (d)) 200-cycle, and ((e) and (f)) 300-cycle ALD-TiO₂ on GNS at 200 °C under a supply of 1.0-s TTIP and 2.0-s water.

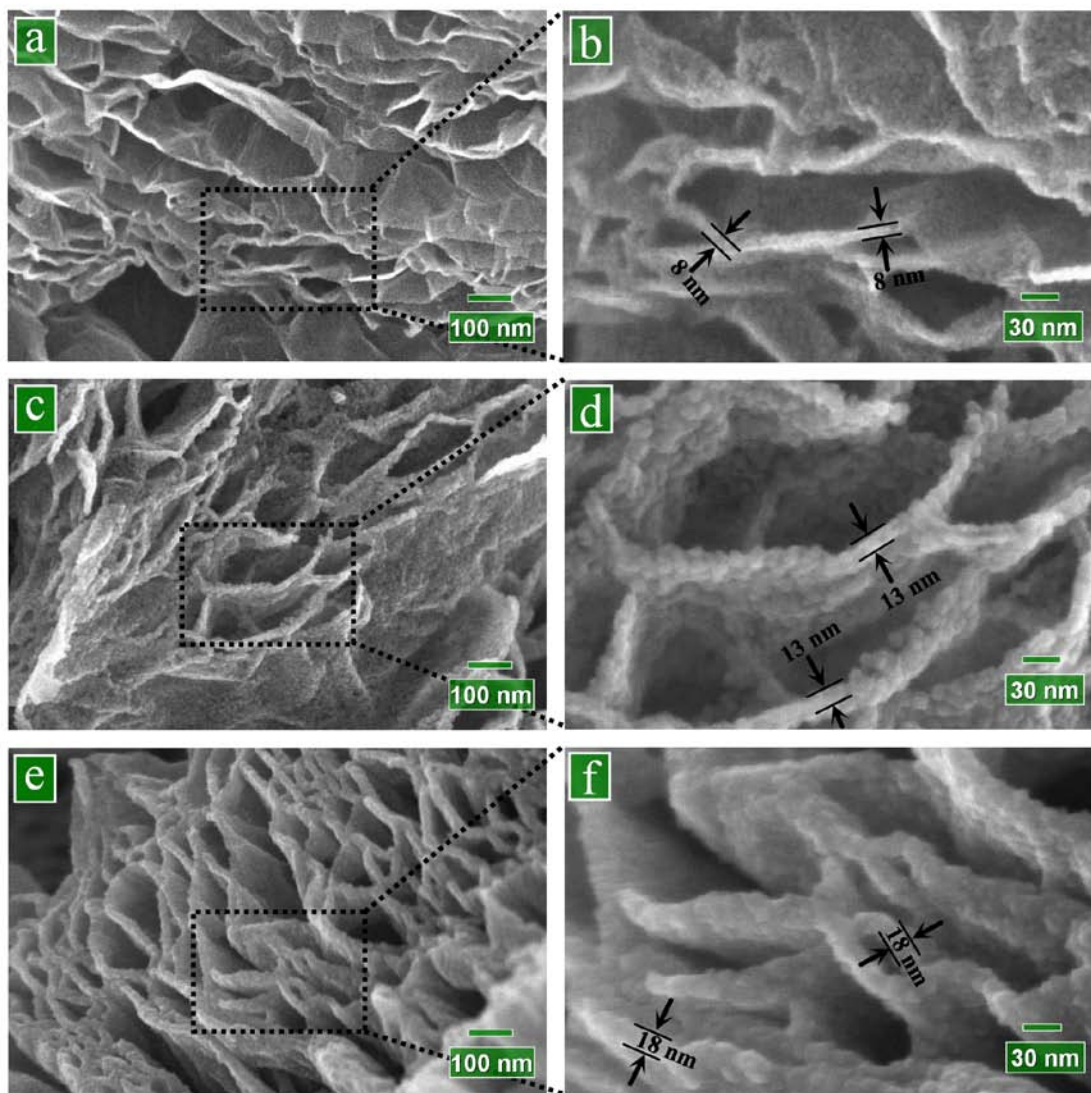


Figure SI-9.4 SEM images for ((a) and (b)) 100-cycle, ((c) and (d)) 200-cycle, and ((e) and (f)) 300-cycle ALD-TiO₂ on GNS at 250 °C under a supply of 1.0-s TTIP and 2.0-s water.

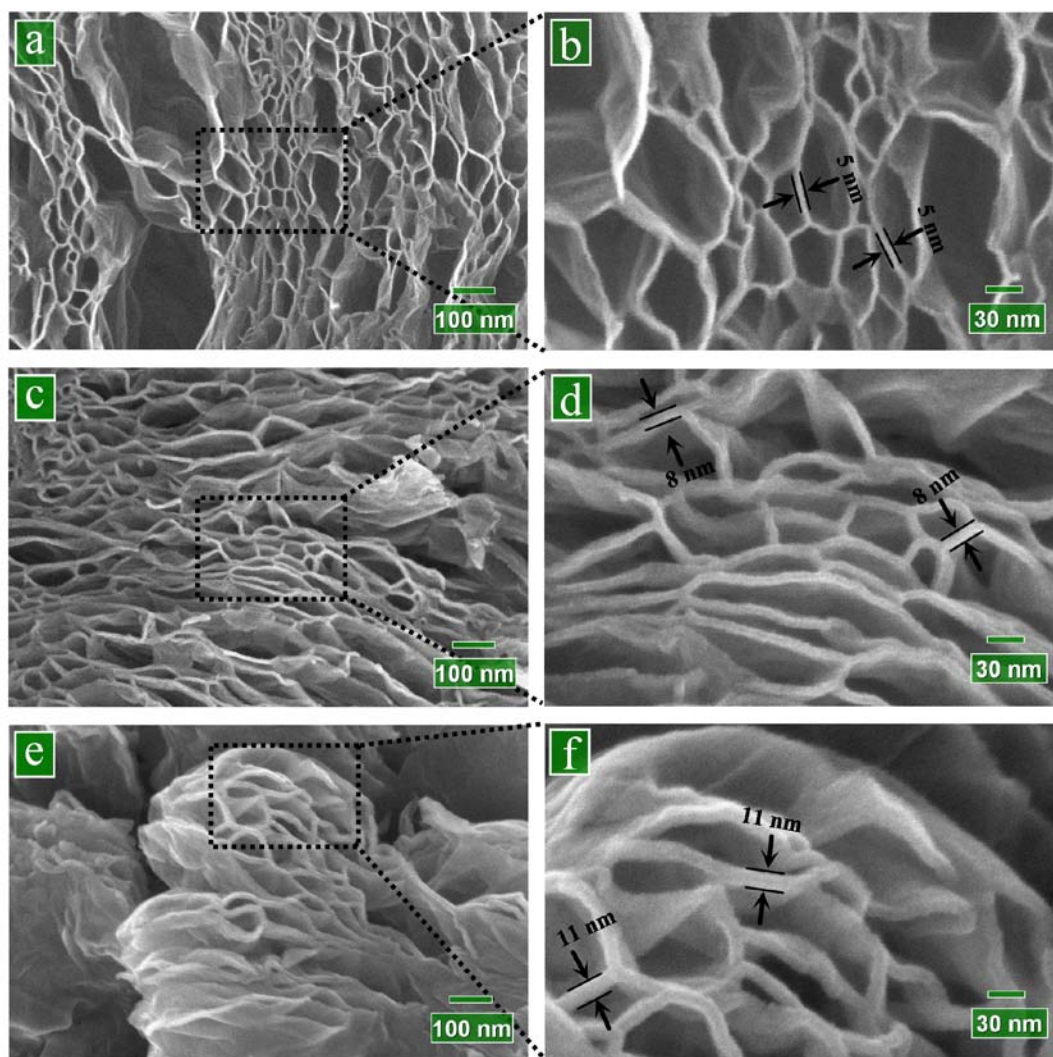


Figure SI-9.5 SEM images for ((a) and (b)) 100-cycle, ((c) and (d)) 200-cycle, and ((e) and (f)) 300-cycle ALD-TiO₂ on GNS at 150 °C under a supply of 0.5-s TTIP and 1.0-s water.

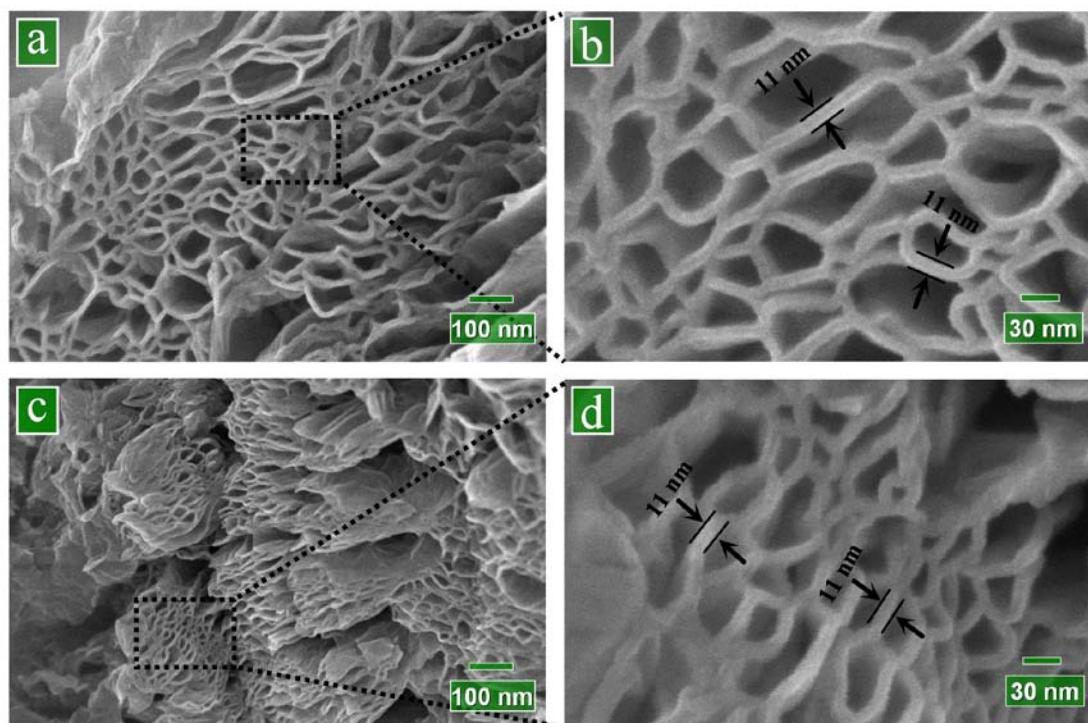


Figure SI-9.6 SEM images for 200-cycle ALD-TiO₂ on GNS at 150 °C under ((a) and (b)) a supply of 0.8-s TTIP and 1.0-s water as well as ((c) and (d)) a supply of 1.2-s TTIP and 2.5-s water.

CHAPTER 10

TUNABLE ATOMIC LAYER DEPOSITION OF CNT-BASED LITHIUM TITANIUM OXIDE NANOCOMPOSITE

A version of this chapter will be submitted for publishing.

This work presents the first effort using atomic layer deposition (ALD) to synthesize lithium titanium oxide (LTO) nanocomposite based on carbon nanotubes (CNTs). It was disclosed that, through combining a sub-ALD of lithium-containing deposition and a sub-ALD of titanium oxide, LTO can be synthesized by tuning the two sub-ALD systems. We believe that the synthesized CNT-based LTO nanocomposite will find promising applications as anodes in lithium-ion batteries.

Keywords: *Atomic layer deposition, Lithium-ion batteries, Carbon nanotubes, Lithium titanium oxide, Nanocomposites*

10.1 Introduction

As is well known, the investigation on alternative energy sources is becoming more and more intensive while fossil fuels as our main sources are depleting and causing a series of environmental issues. Of the potential alternatives, lithium-ion batteries (LIBs) are promising, for they can provide high energy and power density [1,2]. Although they are expected to supply energy for hybrid or pure electric vehicles (HEVs, or EVs), the technologies of LIBs are currently still facing some challenges in safety, cost, and service-life [3,4]. For example, carbon materials suffer from capacity degradation incurred by irreversible side reactions occurred between lithium ions and/or the solvent and the anode surface, leading to the formation of SEI during charge-discharge cycles [5,6]. As such, better alternative anode materials have been sought in the past decade. Among potential candidates, lithium titanium oxide ($\text{Li}_4\text{Ti}_5\text{O}_{12}$, LTO) are attractive, despite its relatively low specific capacity (175 mAh/g) and higher voltage level (1.2 – 2.0 V vs. Li^+/Li) [3,7]. The benefits include negligible volume change for improved cycleability, no electrolyte decomposition, and therefore no SEI formation and improved safety [3,7,8]. Due to the aforementioned advantages, many methods have been developed to synthesize LTO or its composite, such as sol-gel [9-11], solid-state [12,13], cellulose-assisted combustion [13-15], microwave [16], hydrothermal [17], solvothermal [18], spray pyrolysis [19], and molten salt processes [20]. Unfortunately, they are extensively exposed to some drawbacks and especially unable to design nanostructured LTO with ease.

In the past decade there was an increasing interest in employing atomic layer deposition (ALD) for synthesizing various nanostructures, as reviewed by Knez et al [21], Kim et al [22], and George [23]. ALD benefits the synthesis of nanostructured materials with a few unrivalled advantages such as atomic-scale control, excellent uniformity and conformality, low temperature, fine-tuned compositions. Additionally, ALD has extensively successes in depositing organic (e.g., polymer) and inorganic materials (e.g., metals and metal oxides) and widely choices on precursor [23,24]. In particular, recent studies [25,26] demonstrated that there exists suitable lithium precursors for depositing

lithium-containing thin films and even for complicated ternary compounds. Thus, we recently made the first attempt to investigate the possibility of ALD for nanostructured LTO. In this work, we will present our updated progress, featuring ALD-LTO on nitrogen-doped carbon nanotubes (N-CNTs). In return, the CNT-based LTO nanocomposites were fabricated for the first time and they are promising anode materials for LIBs and potential components for other applications.

10.2 Experimental

10.2.1 Synthesis of N-CNTs

N-CNTs were applied as substrates for ALD-LTO in this study. N-CNTs were grown on carbon papers by a floating catalyst chemical vapor deposition (FCCVD) method. Carbon papers were first coated with a 30 nm thick aluminum buffer layer by sputtering before the growth of N-CNTs. In a process of N-CNT synthesis, 2 g melamine ($C_3N_6H_6$) and 100 mg ferrocene ($Fe(C_5H_5)_2$) were supplied into a oven-heated quartz tube at 950 °C and the growth of N-CNTs occurred on carbon papers at the central area of the tube. For more details, readers can refer to our previous work published elsewhere [27]. The N contents of the synthesized N-CNTs are around 8.4 at.% as determined before.

10.2.2 ALD-LTO

ALD-LTO was designed to proceed with two sub-ALD systems, i.e., one for TiO_2 and another for a binary Li-containing compound. Through tuning and combining the two together with an optimal ratio, we expected to synthesize LTO in a well-controlled manner. As for ALD- TiO_2 , we used titanium isopropoxide (TTIP, $Ti(OCH(CH_3)_2)_4$) and deionized water (DI H_2O) as precursors. More details can be found in our previous work [28]. In regard to the ALD-lithium-containing compound, we performed with $Li(O^tBu)$ and water as precursors. In this work, we found that the ratio of 4:5 between ALD- TiO_2 and the ALD-lithium-containing compound is ideal for the ultimate ALD-LTO.

In ALD-LTO processes, N-CNTs were first loaded into a commercial ALD reactor (Savannah 100, Cambridge Nanotechnology Inc., USA) preheated to a certain temperature which was set 250 °C in this work. Then, the two sub-ALD systems were performed one by one. The first sub-ALD system is ALD-TiO₂ operated with 5 cycles. Following 5-cycle ALD-TiO₂, then another sub-ALD system of lithium-containing compound was initiated with 4 cycles. The two sub-ALD systems ran in an alternating manner and ALD-TiO₂ was conducted first. In more details, TTIP (98%, Sigma-Aldrich) and water were introduced into the ALD reactor in an alternating sequence to perform ALD-TiO₂. TTIP was heated to 70 °C while water was kept at room temperature in order to provide sufficient vapors for ALD-TiO₂ processes. The ALD procedures for ALD-TiO₂ were set as follows: (1) a 1.0-s supply of TTIP; (2) a 3.0-s extended exposure of TTIP to AAO and CNTs; (3) a 10.0-s purge of oversupplied TTIP and any by-products; (4) a 2.0-s supply of water vapor; (5) a 3.0-s extended exposure of water vapor to AAO and CNTs; (6) a 10.0-s purge of oversupplied water and any by-products. The aforementioned six-step sequence constituted one ALD-TiO₂ cycle and 5 cycles were performed before another sub-ALD. For ALD of lithium-containing compound, it is the same to ALD-TiO₂ in procedures, except for a preheated temperature of 170 °C for Li(O^tBu) to supply an efficient vapor and 4 cycles performed in series. Thus, 5-cycle ALD-TiO₂ and 4-cycle ALD-lithium-containing compound constituted an ALD-LTO cycle. Additionally, the delivery lines were heated to 150 °C in order to prevent the precursors from condensation. Nitrogen was used as the carrier gas with a flow rate of 20 sccm and the ALD reactor was sustained at a low level of pressure (typically 0.4 Torr) with a vacuum pump (Pascal 2005 I, Adixon).

10.2.3 Characterization

To characterize the morphologies, structures, and compositions of various samples, we mainly used field emission scanning electron spectrometry (FE-SEM, Hitachi 4800S) coupled with energy dispersive spectroscopy (EDS), and X-ray diffractometer (XRD, Inel multi-purpose diffractometer).

10.3 Results and Discussion

10.3.1 ALD of lithium-containing compound

Previous to the ALD-LTO on N-CNTs, we studied the ALD process induced by Li(O^tBu) and water. The two precursors have been applied in earlier studies by Aaltonen et al [26] and Cavanagh et al [29]. Aaltonen supposed that the resultant compound is LiOH or Li₂O but not confirmed. A later study conducted by Cavanagh et al [29] demonstrated that the resultant compound is LiOH, using in situ instruments. An important support is from in situ Fourier transform infrared spectroscopy (FTIR) which disclosed a characteristic peak around 3839 cm⁻¹, belonging to LiOH [30].

Based the above-discussed facts, we made efforts to investigate the ALD process resulted from Li(O^tBu) and water, using XRD and SEM. As shown in figure 10.1 are the XRD patterns for five different samples. Figure 10.1(a) presents the XRD pattern for a sample coated by 100 ALD-cycles at 250 °C. We can see that, aside from two strong peaks (as marked with Graphite (002) and (004)) induced by N-CNTs, the others are consistent to the reference values for Li₂CO₃ (JCPDS PDF No. 22-1141). Apparently, this result is contradictory to the claims made by Aaltonen et al [26] and Cavanagh et al [29]. It might be incurred by the exposure of the sample to air, for LiOH or Li₂O is easy to react with CO₂ [29,31,32]. In this case, we prepared a second sample coated with an extra layer of 100 ALD-TiO₂ at 150 °C after the coating as did for the first sample. The resultant TiO₂ is amorphous, as demonstrated in our previous work [28], and it is used to protect the lithium-containing film. However, as shown in figure 10.1(b), the XRD pattern of the second sample shows no difference compared to the one of the first sample. Figure 10.1(c) shows the XRD pattern of a sample deposited as the first sample but with an extended heat treatment of 250 °C. Again, there is no difference observed with respect to the first two samples. Figure 10.1(d) is the XRD pattern for a sample prepared like the third sample but further coated with an extra layer of 100-cycle ALD-TiO₂ at 150 °C. Still, we did not observe any change. The aforementioned four samples jointly demonstrated that only Li₂CO₃ was received in all the cases. The reason lies in the exposure to air or

inefficient protective layer of TiO_2 . There is another possibility, i.e., the resultant compound is in fact Li_2CO_3 . In any case, there is need for further investigation. The last sample is the first sample treated at $800\text{ }^\circ\text{C}$ for 3 h, as shown by [figure 10.1\(e\)](#). It is apparent that there is some change observed, consistent to the reference values of lithium formate hydrate ($\text{CHLi}_2\text{O}\cdot\text{H}_2\text{O}$) (JCPDS PDF #: 11-0826). In other words, high temperature induced phase transformation on Li_2CO_3 .

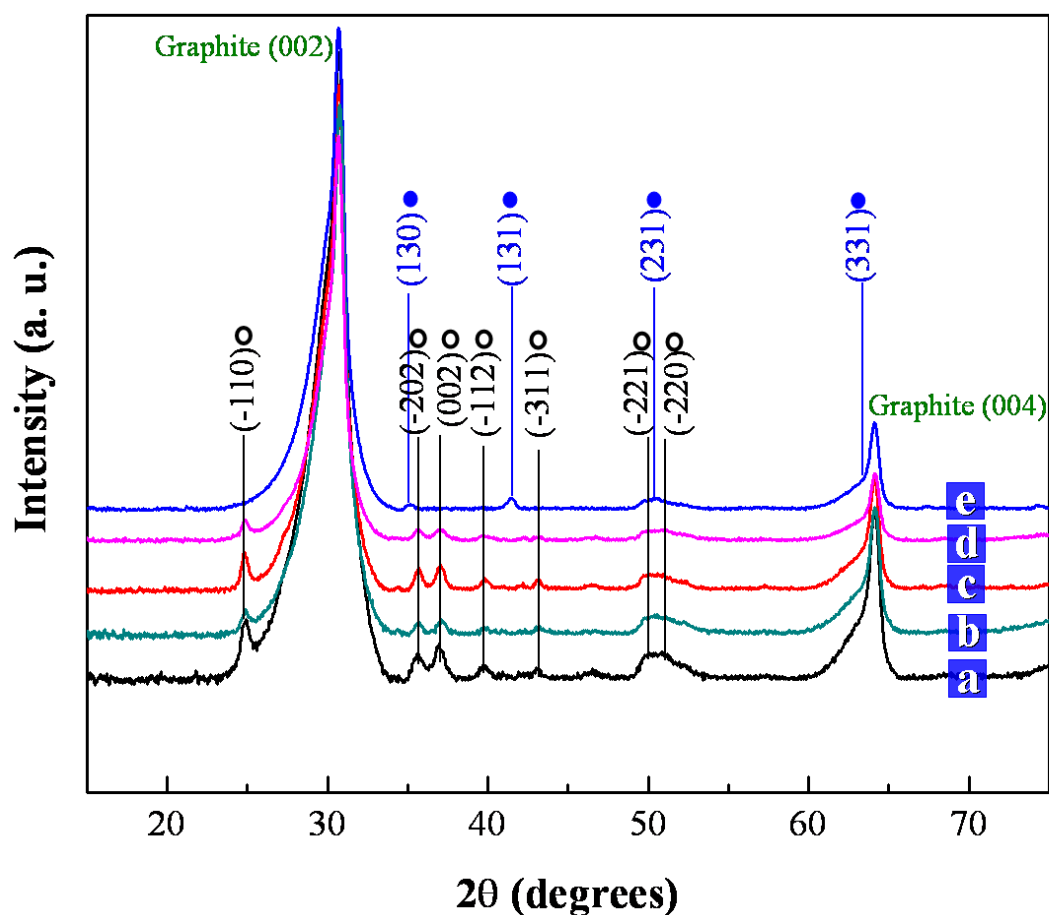


Figure 10.1 XRD patterns induced by the ALD of using $\text{Li}(\text{O}^i\text{Bu})$ and water: (a) a sample coated by a layer of 100-cycle lithium-containing film, (b) a sample coated by a layer of 100-cycle of lithium-containing film and an extra ALD- TiO_2 of 100 cycles, (c) a sample coated by a layer of 100-cycle lithium-containing film with 3 h extended heat treatment at $250\text{ }^\circ\text{C}$, (d) the former sample coated with an extra ALD- TiO_2 of 100 cycles, and (e) a sample coated by a layer of 100-cycle lithium-containing film but annealed at $800\text{ }^\circ\text{C}$ for 3 h. (○) is used to identify the peaks of Li_2CO_3 and (●) is used to identify the peaks of $\text{CHLi}_2\text{O}\cdot\text{H}_2\text{O}$.

Besides the XRD patterns shown above, we also applied SEM to observe the morphologies of the coated N-CNTs. Figure 10.2(a) display the N-CNTs coated by 50 cycles, showing non-uniform feather-like coatings. A phenomenon noticed during SEM observation is that the morphologies of the coated N-CNTs changed slowly from feather-like structures to smooth surfaces under electron bombardment in one minute, as illustrated in the inset of figure 10.2(a). Figure 10.2(b) discloses that the fluffy coatings became thicker with the ALD increased to 100 cycles. In particular, we further investigated the morphological change of this sample under electron bombardment. As compared by figure 10.2(c) and (d), the bombarded area (colored with red in figure 10.2(c)) was smoothened (colored with red in figure 10.2(d)), while the other areas (colored with blue in figure 10.2(c) and (d)) sustained their original looks. Obviously, electron bombardment took effect on the coatings. One possible reason is that the observed samples changed in composition and phase. Similar phenomenon was previously observed with a sample of LiOH changed into Li₂O under electron-irradiation of transmission electron microscope (TEM) in 2 min [33]. The researchers believed that the transformation is mainly induced by heating of electron bombardment. A potential result from our work is that Li₂CO₃ changed into CHLi₂O.H₂O due to the electron bombardment. On this point, future investigation is still needed.

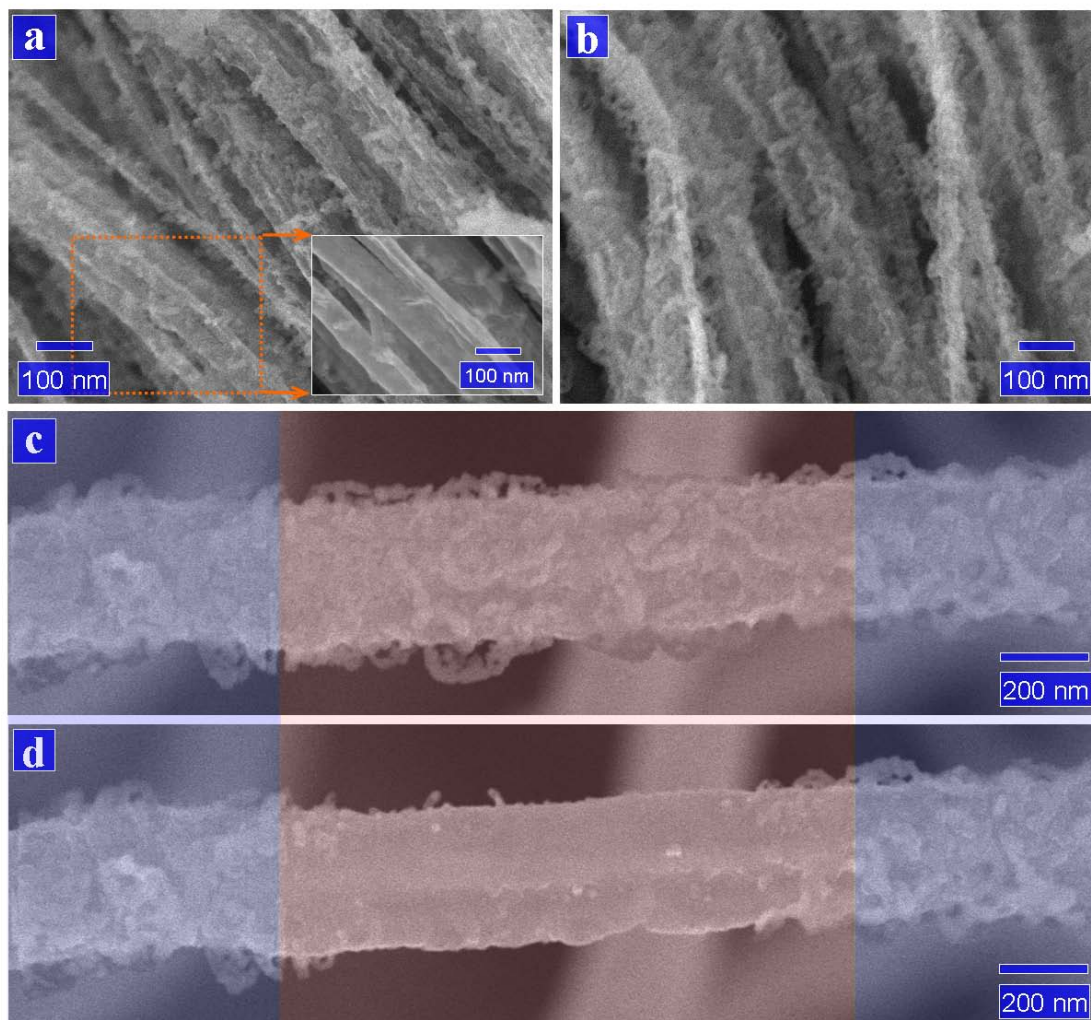


Figure 10.2 ALD-lithium-containing films using $\text{Li}(\text{O}^t\text{Bu})$ and water. SEM images for (a) 50 (inset: SEM image after 1 min electron bombardment) and (b) 100 ALD-cycles, and a comparison (c) before and (d) after 1 min electron bombardment on a 100-cycle deposited sample.

3.1.2. ALD-LTO

In spite of no definite answer received for the deposited compound from the ALD of using $\text{Li}(\text{O}^t\text{Bu})$ and water, it is clear that the deposited material is lithium-containing which is essential for LTO. As introduced in the section of Experimental, we designed the ALD of LTO through alternating two sub-ALD systems, i.e., TiO_2 and the above

lithium-containing film. We performed the ALD-LTO with different cycles, i.e., 20, 30, and 40 cycles. A coated sample after 40 cycles was examined by XRD and its XRD pattern was shown by figure 10.3(a). It is easy to know from figure 10.3(a) that, besides the characteristic peaks due to N-CNTs, there are several weak ones not belonging to LTO. We further annealed two 40-cycle coated samples under 850 (figure 10.3(c)) and 950 °C (figure 10.3(b)) for 3h in a vacuum system. It was found that they both exhibited evident characteristic LTO peaks (JCPDS PDF No. 49-0207) as well as some weak rutile TiO₂ peaks (JCPDS PDF No. 04-0551). Obviously, ALD is viable for synthesizing LTO in a controllable manner. We tried to remove the TiO₂ peaks with different methods, such as with extra coatings of lithium-containing films, but there was better results received. We examined the morphological changes before and after annealing, and the SEM results are illustrated in figure 10.4.

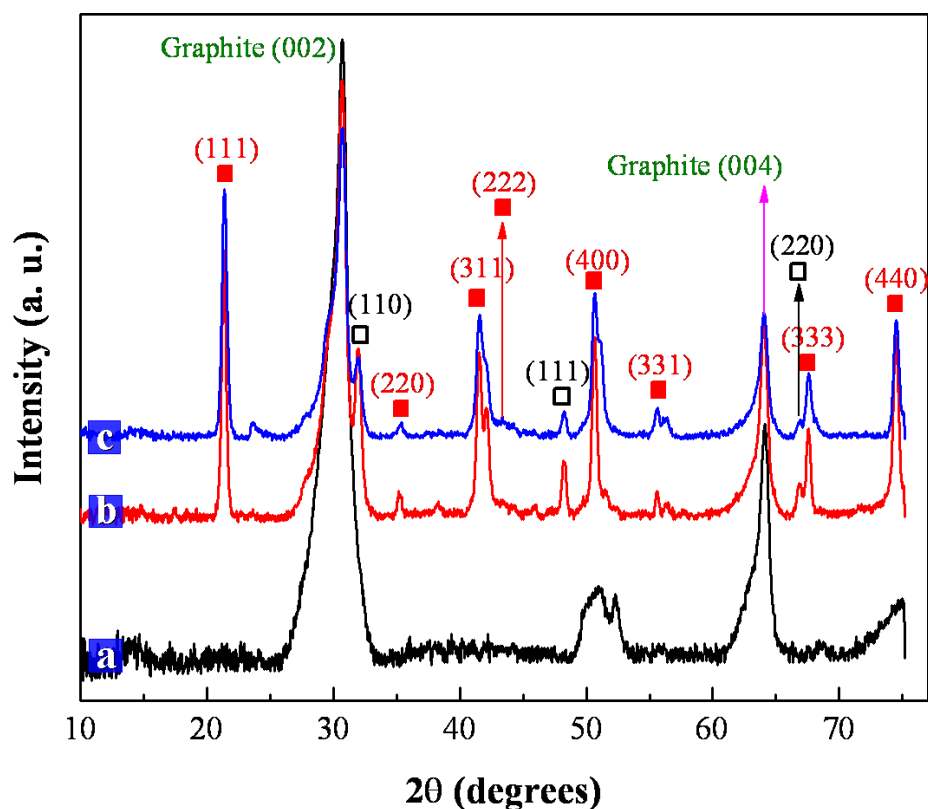


Figure 10.3 XRD patterns for ALD-LTO of 40 cycles: (a) directly deposited samples as well as annealed samples at (b) 950 and (c) 850 °C for 3 h. (□) is used to identify the peaks of TiO₂ and (■) is used to identify the peaks of Li₄Ti₅O₁₂.

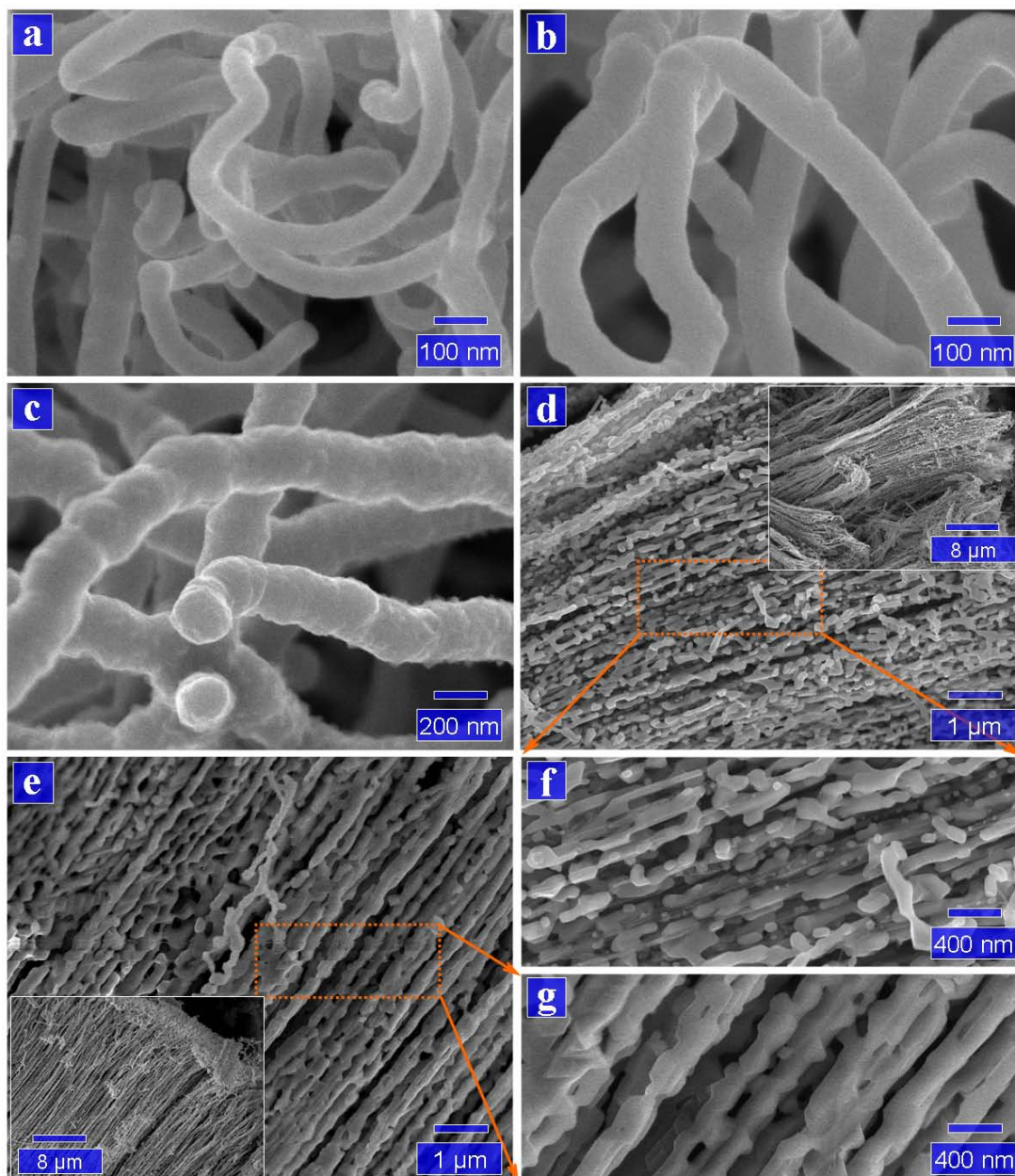


Figure 10.4 SEM images of ALD-LTO after (a) 20, (b) 30, and (c) 40 cycles at 250 °C, and SEM images of the 40-cycle samples annealed at (d, f) 850, and (e, g) 950 °C. The insets show the samples with lower magnification.

As shown in [figure 10.4\(a\)](#), [\(b\)](#), and [\(c\)](#), the SEM images disclose that ALD-LTO covered N-CNTs uniformly after 20, 30, and 40 cycles, respectively. The coverings

became thicker with increased cycles. [Figure 10.4\(d\)](#) reveals that the uniform coatings changed into bean-like chains after 3 h annealing at 850 °C. The inset shows a picture of several bunches of the coated N-CNTs after annealing. For a more clearer observation, a local area on the sample is magnified in [figure 10.4\(f\)](#). [Figure 10.4\(e\)](#) discloses the morphological change after 3 h annealing at 950 °C, showing a network structure consisting of coated N-CNTs. Again, [figure 10.4\(g\)](#) magnifies a local area of the sample and gives a clearer picture of the network structure. In comparison, annealing at different temperatures took some effect on the ultimate morphologies, probably due to different reaction rates resulted between TiO₂ and lithium-containing films. In summary, this work demonstrated that ALD is viable for developing LTO nanostructures and, in particular, it can be used to control the deposition with high precision.

10.4 Conclusions

This work represents a pioneered investigation on designing LTO nanostructures with ALD. The results demonstrated that ALD is viable and exhibits more advantages over previous methods. In addition, it was also disclosed that annealing could take effects on the ultimate nanostructures of LTO, probably by influencing the reaction rates between different components. For a full understanding of ALD-LTO, however, future studies are needed.

Acknowledgements

This research was supported by the Natural Science and Engineering Research Council of Canada (NSERC), Canada Research Chair (CRC) Program, Canadian Foundation for Innovation (CFI), Ontario Research Fund (ORF), Early Researcher Award (ERA) and the University of Western Ontario. In addition, the authors would like to appreciate the help from Mr. Fred Pearson on HRTEM analysis at Canadian Center for Electron Microscopy, McMaster University.

References

- [1] L.-X. Yuan, Z.-H. Wang, W.-X. Zhang, X.-L. Hu, J.-T. Chen, Y.-H. Huang, and J. B. Goodenough, Development and challenges of LiFePO_4 cathode material for lithium-ion batteries, *Energy Environ. Sci.*, 2011, **4**, 269-284.
- [2] M. R. Palacín, Recent advances in rechargeable battery materials: a chemist's perspective, *Chem. Soc. Rev.*, 2009, **38**, 2565-2575.
- [3] B. Scrosati, and J. Garche, Lithium batteries: status, prospects and future, *J. Power Sources*, 2010, **195**, 2419-2430.
- [4] J. B. Goodenough, and Y. Kim, Challenges for rechargeable Li batteries, *Chem. Mater.*, 2010, **22**, 587-603.
- [5] P. Arora, R. E. White, and M. Doyle, Capacity fade mechanisms and side reactions in lithium-ion batteries, *J. Electrochem. Soc.*, 1998, **145**, 3647-3667.
- [6] P. Verma, P. Maire, and P. Novák, A review of the features and analyses of the solid electrolyte interphase in Li-ion batteries, *Electrochim. Acta*, 2010, **55**, 6332-6341.
- [7] Z. Yang, J. Zhang, M. C. W. Kintner-Meyer, X. Lu, D. Choi, J. P. Lemmon, and J. Liu, Electrochemical energy storage for green grid, *Chem. Rev.*, 2011. DOI: 10.1021/cr100290v
- [8] D. Deng, M. G. Kim, J. Y. Lee, and J. Cho, Green storage materials: nanostructured TiO_2 and Sn-based anodes for lithium-ion batteries, *Energy Environ. Sci.*, 2009, **2**, 818-837.
- [9] N. A. Alias, M. Z. Kufian, L. P. Teo, S. R. Majid, and A. K. Arof, Synthesis and characterization of $\text{Li}_4\text{Ti}_5\text{O}_{12}$, *J. Alloys Compd.*, 2009, **486**, 645-648.
- [10] Z.-Q. He, L.-Z. Xiong, S. Chen, X.-M. Wu, W.-P. Liu, and K.-L. Huang, In situ polymerization preparation and characterization of $\text{Li}_4\text{Ti}_5\text{O}_{12}$ -polyaniline anode material, *Trans. Nonferrous Met. Soc. China*, 2010, **20**, s262-s266.
- [11] K. Naoi, S. Ishimoto, Y. Isobe, and S. Aoyagi, High-rate nano-crystalline $\text{Li}_4\text{Ti}_5\text{O}_{12}$ attached on carbon nano-fibers for hybrid supercapacitors, *J. Power Sources*, 2010, **195**, 6250-6254.

- [12] X. Li, M. Qu, and Z. Yu, Preparation and electrochemical performance of $\text{Li}_4\text{Ti}_5\text{O}_{12}$ /graphitized carbon nanotubes composite, *Solid State Ionics*, 2010, **181**, 635-639.
- [13] T. Yuan, R. Cai, R. Ran, Y. Zhou, and Z. Shao, A mechanism study of synthesis of $\text{Li}_4\text{Ti}_5\text{O}_{12}$ from TiO_2 anatase, *J. Alloys Compd.*, 2010, **505**, 367-373.
- [14] T. Yuan, R. Cai, P. Gu, and Z. Shao, Synthesis of lithium insertion material $\text{Li}_4\text{Ti}_5\text{O}_{12}$ from rutile TiO_2 via surface activation, *J. Power Sources*, 2010, **195**, 2882-2887.
- [15] T. Yuan, X. Yu, R. Cai, Y. Zhou, and Z. Shao, Synthesis of pristine and carbon-coated $\text{Li}_4\text{Ti}_5\text{O}_{12}$ and their low-temperature electrochemical performance, *J. Power Sources*, 2010, **195**, 4997-5004.
- [16] L. H. Yang, C. Dong, and J. Guo, Hybrid microwave synthesis and characterization of the compounds in the Li-Ti-O system, *J. Power Sources*, 2008, **175**, 575-580.
- [17] J. Chen, L. Yang, S. Fang, and Y. Tang, Synthesis of sawtooth-like $\text{Li}_4\text{Ti}_5\text{O}_{12}$ nanosheets as anode materials for Li-ion batteries, *Electrochem. Acta*, 2010, **55**, 6596-6600.
- [18] D. K. Lee, H.-W. Shim, J. S. An, C. M. Cho, I.-S. Cho, K. S. Hong, and D.-W. Kim, Synthesis of heterogeneous $\text{Li}_4\text{Ti}_5\text{O}_{12}$ nanostructured anodes with long-term cycle stability, *Nanoscale Res. Lett.*, 2010, **5**, 1585-1589.
- [19] S. H. Ju and Y. C. Kang, Effects of drying control chemical additive on properties of $\text{Li}_4\text{Ti}_5\text{O}_{12}$ negative powders prepared by spray pyrolysis, *J. Power Sources*, 2010, **195**, 4327-4331.
- [20] M. M. Rahman, J.-Z. Wang, M. F. Hassan, S. Chou, D. Wexler, and H.-K. Liu, Basic molten salt process—a new route for synthesis of nanocrystalline $\text{Li}_4\text{Ti}_5\text{O}_{12}$ - TiO_2 anode material for Li-ion batteries using eutectic mixture of LiNO_3 - LiOH - Li_2O_2 , *J. Power Sources*, 2010, **195**, 4297-4303.
- [21] M. Knez, K. Nielsch, and L. Niinistö, Synthesis and surface engineering of complex nanostructures by atomic layer deposition, *Adv. Mater.*, 2007, **19**, 3425-3438.
- [22] H. Kim, H.-B.-R. Lee, and W.-J. Maeng, Applications of atomic layer deposition to nanofabrication and emerging nanodevices, *Thin Solid Films*, 2009, **517**, 2563-2580.

- [23] S. M. George, Atomic layer deposition; an overview, *Chem. Rev.*, 2010, **110**, 111-131.
- [24] R. L. Puurunen, Surface chemistry of atomic layer deposition: a case study for the trimethylaluminum/water process, *J. Appl. Phys.*, 2005, **97**, 121301
- [25] M. Putkonen, T. Aaltonen, M. Alnes, T. Sajavaara, O. Nilsen, and H. Fjellvåg, Atomic layer deposition of lithium containing thin films, *J. Mater. Chem.*, 2009, **19**, 8767-8771.
- [26] T. Aaltonen, M. Alnes, O. Nisen, L. Costelle, and H. Fjellvåg, Lanthanum titanate and lithium lanthanum titanate thin films grown by atomic layer deposition, *J. Mater. Chem.*, 2010, **20**, 2877-2881.
- [27] H. Liu, Y. Zhang, R. Li, X. Sun, S. Désilets, H. Abou-Rachid, M. Jaidann, and L.-S. Lussier, Structural and morphological control of aligned nitrogen-doped carbon nanotubes, *Carbon*, 2010, **48**, 1498-1507.
- [28] X. Meng, D. Geng, J. Liu, R. Li, and X. Sun, Controllable synthesis of graphene-based titanium dioxide nanocomposites by atomic layer deposition, *Nanotechnology*, 2011, **22**, 165602.
- [29] A. S. Cavanagh, Y. Lee, B. Yoon, and S. M. George, Atomic layer deposition of LiOH and Li₂CO₃ using lithium t-butoxide as the lithium source, *ECS Transactions*, 2010, **33**, 223-229.
- [30] L. H. Jones, The infrared spectra and structure of LiOH, LiOH.H₂O and the deuterium species. Remark on fundamental frequency of OH⁻, *J. Chem. Phys.*, 1954, **22**, 217-219.
- [31] C. Naudin, J. L. Bruneel, M. Chami, B. Desbat, J. Grondin, J. C. Lassègues, and L. Servant, Characterization of the lithium surface by infrared and Raman spectroscopies, *J. Power Sources*, 2003, **124**, 518-525.
- [32] H. A. Mosqueda, C. Vazquez, P. Bosch, and H. Pfeiffer, Chemical sorption of carbon dioxide (CO₂) on lithium oxide (Li₂O), *Chem. Mater.*, 2006, **18**, 2307-2310.
- [33] Y. H. Hu, and E. Ruckenstein, Nano-structured Li₂O from LiOH by electron-irradiation, *Chem. Phys. Lett.*, 2006, **430**, 80-83.

CHAPTER 11

GENERAL DISCUSSION

This thesis focused on investigating the synthesis of various nanostructured metal oxides using ALD. The metal oxides include Fe_2O_3 , SnO_2 , TiO_2 , and $\text{Li}_4\text{Ti}_5\text{O}_{12}$. Through employing different substrates, i.e., AAO, CNTs, and GNS, the metal oxides can be fabricated into different nanostructures including nanotubes, CNT-based core-shell nanotubes, and GNS-based 3D architectures. In addition, the growth characteristics of the metal oxides were subject to the influences of three main parameters, i.e., precursors, substrates, and temperatures. Further, the surface chemistry of the substrates and their interactions with ALD precursors also were considered. As a consequence, the combinations of the aforementioned factors contributed to a series of novel nanostructured materials which are useful for energy-related devices such as LIBs and FCs.

First, it is apparent that the ultimate nanostructures of the metal oxides are dependent on the original structures of the employed substrates. This is destined by the unique mechanism of ALD and the resultant characteristics. The surface-controlled and self-limiting nature of ALD leads to the uniformity and conformality of ALD. Thus, the ALD-induced films can well keep the original structures of the substrates. For example, ALD deposits tubular films in the nanopores of AAO and thereby produce aligned nanotube arrays. Similarly, the ALD-induced coverings on CNTs and GNS resulted in CNT-based core-shell nanostructures and GNS-based 3D architectures, respectively. Thus, it is reasonable to believe that ALD can create more complicated nanostructures if suitable substrates are applied.

In addition, ALD benefits the deposited materials with tunable morphologies and structural phases. A distinguished advantage of ALD is its preciseness on deposition, ascribed to its self-limiting and cyclic characters. In return, it is widely observed that the deposition of the metal oxides experienced morphological evolution from nanoparticles to nanofilms. There are two potential reasons responsible for the initial formation of nanoparticles. One is related with the volume of the applied precursors, leading to steric hindrance. Another is the density of reactive sites on substrates, for surface reactions only occur at reactive sites. The morphological evolution of the deposited materials is

particularly beneficial for designing nanomaterials with controlled manners. On the other hand, ALD also offers tunability in the structural characteristics of the deposited materials. As disclosed by ALD-SnO₂ and ALD-TiO₂, the deposited SnO₂ and TiO₂ present both amorphous and crystalline phase depending on the growth temperatures. Apparently, ALD offers a facile route to design the deposited materials with a preferable phase. This advantage has been demonstrated by their applications in LIBs and FCs. For example, amorphous SnO₂-GNS composites exhibit more stable and higher capacity in LIBs while crystalline SnO₂-CNTs composites perform better in FCs.

The third one for discussion is the capability of ALD in synthesizing ternary or more complicated compounds. The successes of ALD on binary compound have been extensive reported. In comparison, the cases in ternary or more complicated compounds are relatively rare. In this thesis, the synthesis of LTO via ALD is exposed for the first time. It demonstrated that, through suitably adjusting the ratio between two sub-ALD systems, LTO can be fabricated in a more controlled manner. The study implies that ALD is a versatile tool to synthesize other complicated compounds. This character will greatly prompt future development of nanomaterials.

It needs to further emphasize that the above-discussed advantages commonly contributes to a common merit, i.e., ALD is a highly controlled technique for nanostructured materials. This character is particularly beneficial to produce materials with optimized structure, composition, and phase. The resultant materials will therefore be able to improve the performance of energy-related devices to the largest extent.

In conclusion, this thesis extensively investigated the synthesis of nanostructured metal oxides using ALD by applying various nanoscale templates. Further, ALD growth mechanisms have been studied by exploring surface chemistry and interactions with various substrates. The adopted synthesis strategies and the resultant materials are not only useful for energy-related devices but important for understanding the characteristics of ALD as well.

CHAPTER 12

CONCLUSIONS AND SUGGESTIONS

12.1 Conclusions

A series of experiments was conducted in this study to synthesize novel nanostructured metal oxides using ALD. In addition, the growth characteristics of the metal oxides and their underlying mechanisms were also investigated and explored. Thus, this study mainly worked on three ways: nanostructures, growth characteristics, and underlying mechanisms for metal oxides.

1D CNT-Fe₂O₃ core-shell nanotubes were synthesized using ferrocene and oxygen as ALD precursors. This work compared the effects of undoped CNTs and N-CNTs on the ALD-Fe₂O₃. It was disclosed that N-CNTs are beneficial for ALD-Fe₂O₃ while undoped CNTs require either covalent or non-covalent functionalization pretreatment for ALD-Fe₂O₃. This work for the first time demonstrated that the N-doped configurations provide reactive sites for ALD processes.

1D SnO₂ nanotubes were fabricated via AAO template-directed ALD route using SnCl₄ and water precursors. This work systematically investigated the effects of growth temperatures on ALD-SnO₂. As a consequence, it was revealed that there are three growth modes with the synthesized SnO₂ nanotubes, named as layer-by-layer, layer-by-particle, and evolutionary particles. In particular, the layers are amorphous while the particles are crystalline rutile. In addition, it is believed that there are two different underlying mechanisms responsible for the growth of the layers and the particles. As a consequence, the synthesized nanotubes present highly structure-controllable characteristics and can be amorphous, double amorphous-crystalline, and crystalline phase.

1D SnO₂-CNT core-shell nanotubes were produced using SnCl₄ and water precursors. N-CNTs were used as substrates. In this work, the effects of N-doped configurations were explored using XPS. It was demonstrated that different N-related defects, especially graphite-like and pyridine-like N configuration, play important roles for initiating ALD-SnO₂ on N-CNTs. In comparison, the pyridine-like configuration is more important.

Furthermore, it was also observed that the phases of the deposited SnO₂ are controllable from amorphous to crystalline. It was suggested that there are different mechanisms for the growth of the amorphous and crystalline SnO₂, mainly induced by growth temperatures.

3D SnO₂-GNS architectures were realized by ALD using SnCl₄ and water as precursors. The 3D architected GNS-based composites feature the deposited SnO₂ with controlled morphology and phase. The former contributes to the morphological evolution from nanoparticles to nanofilms, favored by the surface-controlled and cyclic nature of ALD. The latter results in the phase transformation from amorphous to crystalline phase, dominated by different temperature-dependent surface reactions.

1D nanostructures of TiO₂ were fulfilled via two ALD strategies, i.e., AAO-based and CNTs-based, using TTIP and water as precursors. The former leads to TiO₂ nanotubes in the form of aligned arrays while the latter renders the coaxial CNT-TiO₂ core-shell nanotubes. The two routes jointly demonstrated that the deposited TiO₂ are tunable from amorphous to crystalline anatase phase with increased temperatures while from nanoparticles to tubular nanofilms with increased cycles. It was believed that higher temperatures are kinetically favorable for the ordering of Ti and O atom with the structure of minimum energy, i.e., anatase crystals.

3D TiO₂-GNS architectures were prepared by ALD using TTIP and water as precursors. The architectures feature the deposited TiO₂ in forms of amorphous or crystalline anatase phase, depending on growth temperatures. In addition, the deposited TiO₂ experiences a morphological evolution from nanoparticles to nanofilms with increased cycles. In addition, there is a transition phase observed with an intermediate temperature, in which amorphous TiO₂ nanofilms are decorated with crystalline nanoparticles. As a result, this work contributes to tunable 3D TiO₂-GNS nanocomposites.

A pioneered work was conducted via ALD to develop 1D LTO-CNT nanocomposites. This work was fulfilled by two sub-ALD systems, TiO₂ and a lithium-containing

compound. The sub-ALD for TiO_2 adopted TTIP and water as precursors while the lithium-containing compound used lithium tert-butoxide and water. It was demonstrated that, through suitably adjusting the ratio between the two sub-ALD systems, LTO were successfully prepared on CNTs after high-temperature annealing. This work provides a facile but highly controllable route to synthesize ternary or even more complicated compound via ALD.

12.2 Suggestions

Despite ALD being a facile route for novel nanostructured materials, as demonstrated in this thesis, ALD as a special area deserves more extensive and intensive investigation, especially on the exact mechanisms of different materials. Based on the author's experience with ALD, there are also some suggestions for future studies of fellow researchers:

- This thesis provides several successes on controlling structural phases of metal oxides deposited by ALD. However, their exact mechanisms are still unclear. For a better understanding and therefore for a better control on ALD processes, more fundamental investigation is required. This topic will remain a challenge.
- This thesis exploited the deposition of a ternary compound LTO via ALD. However, the lithium-containing compound deposited by lithium tert-butoxide and water is not determined, for it requires an inert atmosphere to avoid potential disturbances from air.
- This thesis mainly worked on lab-scale substrates in various ALD processes. For energy-related applications, however, they require that a technique can fabricate and provide materials in a relatively large amount. On this way, ALD is still facing a lot of challenges. It merits future studies to find solutions which enable to combine ALD with other technologies for mass production.

- This thesis demonstrated that ALD is a feasible route to coat complex structures with controllable and uniform films. This is extremely important for developing 3D microbatteries. Besides the successes for binary electrode materials of LIBs, the precise control of ALD on ternary compounds such as LTO also implies another opportunity for all-solid-state microbatteries, i.e., ALD being also a promising method to exploit solid electrolytes which usually consist of multi-elements. Thus, it is reasonable to believe that researchers can solely rely on ALD to directly develop 3D all-solid-state microbatteries with high performance. This will be also very challenging but deserves our expectation in the coming studies.

APPENDICES

**APPENDIX I: PERMISSION FROM AMERICAN CHEMICAL SOCIETY (ACS)
FOR PUBLISHED ARTICLE**

Published article: Non-Aqueous Approach to Synthesize Amorphous/Crystalline Metal Oxide-Graphene Nanosheet Hybrid Composites, *Journal of Physical Chemistry C*, 2010, 114, 18330-18337

ACS Journal Publishing Agreement (<http://pubs.acs.org/page/copyright/journals/faqs.html>):

*The current ACS Journal Publishing Agreement covers several permitted uses by authors. Permitted uses are subject to certain conditions and may vary according to the version of the paper in production. **Permitted uses of all versions include:***

- **Use in theses and collections of your own work**
- *Teaching and training*
- *Presentations at conferences and seminars*
- *Sharing with colleagues*
- *Posting on websites and repositories*
- *Sharing links to free eprints of the published work*
- *Use and authorizing the use of Supporting Information*
- *Other permitted uses by authors that are delineated in the Agreement*

APPENDIX II: PERMISSION FROM ELSEVIER FOR PUBLISHED ARTICLE

Published article: Nitrogen-doped carbon nanotubes coated by atomic layer deposited SnO₂ with controlled morphology and phase, *Carbon*, 2011, 49, 1133-1144.

Elsevier Copyright Policy (<http://www.elsevier.com/wps/find/authorshome.authors/copyright>):

*As a journal author, you retain rights for a large number of author uses, including use by your employing institute or company. **These rights are retained and permitted without the need to obtain specific permission from Elsevier. These include:***

- *the right to make copies (print or electronic) of the journal article for your own personal use, including for your own classroom teaching use;*
- *the right to make copies and distribute copies (including via e-mail) of the journal article to research colleagues, for personal use by such colleagues for scholarly purposes*;*
- *the right to post a pre-print version of the journal article on Internet web sites including electronic pre-print servers, and to retain indefinitely such version on such servers or sites for scholarly purposes* (with some exceptions such as The Lancet and Cell Press. See also our information on electronic preprints for a more detailed discussion on these points);*
- *the right to post a revised personal version of the text of the final journal article (to reflect changes made in the peer review process) on your personal or institutional web site or server for scholarly purposes*, incorporating the complete citation and with a link to the Digital Object Identifier (DOI) of the article (but not in subject-oriented or centralized repositories or institutional repositories with mandates for systematic postings unless there is a specific agreement with the publisher- see www.elsevier.com/fundingbody agreements for further information]);*
- *the right to present the journal article at a meeting or conference and to distribute copies of such paper or article to the delegates attending the meeting;*
- *for your employer, if the journal article is a 'work for hire', made within the scope of the author's employment, the right to use all or part of the information in (any version of) the journal article for other intra-company use (e.g. training);*
- *patent and trademark rights and rights to any process or procedure described in the journal article;*
- ***the right to include the journal article, in full or in part, in a thesis or dissertation;***
- *the right to use the journal article or any part thereof in a printed compilation of your works, such as collected writings or lecture notes (subsequent to publication of the article in the journal); and*
- *the right to prepare other derivative works, to extend the journal article into book-length form, or to otherwise re-use portions or excerpts in other works, with full acknowledgement of its original publication in the journal.*

**APPENDIX III: PERMISSION FROM INSTITUTE OF PHYSICS (IOP) FOR
PUBLISHED ARTICLE**

Published article: Controllable Synthesis of Graphene-based Titanium Dioxide Nanocomposites by Atomic Layer Deposition, *Nanotechnology*, 2011, 22, 165602.



To:
Cc:
Bcc:
Subject: Fw: Requesting Permission
From: Danny Turner/Journals/IOPP - Monday 11/07/2011 07:35

From: xiangbo meng
To:
Cc:
Date: 04/07/2011 16:47
Subject: Requesting Permission

Dear Editor,

I am writing you to secure the permission for a paper entitled "*Controllable Synthesis of Graphene-based Titanium Dioxide Nanocomposites by Atomic Layer Deposition (Nanotechnology, 2011, 22, 165602)*". As its first author, I am planning to include this paper in my PhD thesis. Herein I am requesting you to assist me with a permission for my aforementioned use.

Thanks in advance and look forward to your reply!

Best regards,

Xiangbo Meng

Department of Mechanical & Materials Engineering
The University of Western Ontario
ON, Canada
N6A 5B8

PERMISSION TO REPRODUCE AS REQUESTED IS GIVEN PROVIDED THAT:

~~(a) the consent of the author(s) is obtained~~

(b) the source of the material including author, title of article, title of journal, volume number, issue number (if relevant), page range (or first page if this is the only information available), date and publisher is acknowledged.

(c) for material being published electronically, a link back to the original article should be provided (via DOI).

IOP Publishing Ltd
Dirac House
Temple Back
BRISTOL
BS1 6BE

11/7/2011
Date

Rights & Permissions

**APPENDIX IV: PERMISSION FROM ROYAL SOCIETY OF CHEMISTRY (RSC)
FOR PUBLISHED ARTICLE**

Published article: Three Growth Modes and Mechanisms for Highly Structure-tunable SnO₂ Nanotube Arrays of Template-directed Atomic Layer Deposition, *Journal of Materials Chemistry*, 2011, DOI: 10.1039/c1jm11511a.

RSC Copyright Policy

(<http://www.rsc.org/AboutUs/Copyright/RightsRetainedbyJournalsauthors.asp>):

When the author signs the exclusive Licence to Publish for a journal article, he/she retains certain rights that may be exercised without reference to the RSC. He/she may:

- ***Reproduce/republish portions of the article (including the abstract)***
- *Photocopy the article and distribute such photocopies and distribute copies of the PDF of the article that the RSC makes available to the corresponding author of the article upon publication of the article for personal or professional use only, provided that any such copies are not offered for sale.*

APPENDIX V: PERMISSION FROM SPRINGER FOR PUBLISHED ARTICLE

Published article: Heterostructural Coaxial Nanotubes of CNT@Fe₂O₃ via Atomic Layer Deposition: Effects of Surface Functionalization and Nitrogen-doping, *Journal of Nanoparticle Research*, 2011, **13**, 1207-1218.

SPRINGER LICENSE TERMS AND CONDITIONS

Jul 12, 2011

This is a License Agreement between Xiangbo Meng ("You") and Springer ("Springer") provided by Copyright Clearance Center ("CCC"). The license consists of your order details, the terms and conditions provided by Springer, and the payment terms and conditions.

All payments must be made in full to CCC. For payment instructions, please see information listed at the bottom of this form.

License Number	2706530745253
License date	Jul 12, 2011
Licensed content publisher	Springer
Licensed content publication	Journal of Nanoparticle Research
Licensed content title	Heterostructural coaxial nanotubes of CNT@Fe ₂ O ₃ via atomic layer deposition: effects of surface functionalization and nitrogen-doping
Licensed content author	Xiangbo Meng
Licensed content date	Jan 1, 2010
Volume number	13
Issue number	3
Type of Use	Thesis/Dissertation
Portion	Full text
Number of copies	1
Author of this Springer article	Yes and you are the sole author of the new work
Order reference number	
Title of your thesis / dissertation	ON DEVELOPING NOVEL ENERGY-RELATED NANOSTRUCTURED MATERIALS BY ATOMIC LAYER DEPOSITION
Expected completion date	Aug 2011
Estimated size(pages)	300
Total	0.00 CAD

CURRICULUM VITAE

Name: Xiangbo Meng

Place of Birth: Xingtai, Hebei Province, P. R. China

Post-secondary Education: Department of Mechanical & Materials Engineering
The University of Western Ontario, London, ON, Canada
2009-2011, PhD

Department of Chemical & Biochemical Engineering
The University of Western Ontario, London, ON, Canada
2005-2008, Ph.D.

Department of Mechanical and Electrical Engineering
China University of Petroleum, Beijing, P. R. China
1996-1999, Master

Department of Chemical Engineering
Northwest University, Xi'an, Shaanxi, P. R. China
1990-1994, B.E.Sc.

Work Experience: Teaching & Research Assistant (2005-2011)
The University of Western Ontario, ON, Canada

Research Associate (2003-2004)
China University of Petroleum, Beijing, P. R. China

Research Engineer (1999-2002)
National Engineering Research Center for Catalyst and Petroleum
Processing Technology (NERC-CPPT)
Research Institute of Petroleum Processing (RIPP), SINOPEC,
P. R. China

Research Assistant (1996-1999)

China University of Petroleum, Beijing, P. R. China

Engineer (1994-1996)

Cangzhou Refinery, SINOPEC, P. R. China

Relevant Publications:

(A) *Peer-reviewed Journal Papers Based on This Thesis (First Author)*

1. **Xiangbo Meng**, Yong Zhang, Shuhui Sun, Ruying Li, and Xueliang Sun, Three Growth Modes and Mechanisms for Highly Structure-tunable SnO₂ Nanotube Arrays of Template-directed Atomic Layer Deposition, *Journal of Materials Chemistry*, 2011, **21**, 12321-12330.
2. **Xiangbo Meng**, Dongsheng Geng, Jian Liu, Ruying Li, and Xueliang Sun, Controllable Synthesis of Graphene-based Titanium Dioxide Nanocomposites by Atomic Layer Deposition, *Nanotechnology*, 2011, **22**, 165602. (**Featured article and front cover page**)
3. **Xiangbo Meng**, Yu Zhong, Yifan Sun, Mohammad Norouzi Banis, Ruying Li, and Xueliang Sun, Nitrogen-doped carbon nanotubes coated by atomic layer deposited SnO₂ with controlled morphology and phase, *Carbon*, 2011, **49**, 1133-1144.
4. **Xiangbo Meng**, Mihnea Ionescu, Mohammad Norouzi Banis, Yu Zhong, Hao Liu, Yong Zhang, Shuhui Sun, Ruying Li, and Xueliang Sun, Heterostructural Coaxial Nanotubes of CNT@Fe₂O₃ via Atomic Layer Deposition: Effects of Surface Functionalization and Nitrogen-doping, *Journal of Nanoparticle Research*, 2011, **13**, 1207-1218.

5. **Xiangbo Meng**, Dongsheng Geng, Jian Liu, Mohammad Norouzi Banis , Yong Zhang, Ruying Li, and Xueliang Sun, Non-Aqueous Approach to Synthesize Amorphous/Crystalline Metal Oxide-Graphene Nanosheet Hybrid Composites, *Journal of Physical Chemistry C*, 2010, **114**, 18330-18337.
6. **Xiangbo Meng** and Xueliang Sun, Emerging Applications of Atomic Layer Deposition for Lithium-ion Batteries, to be submitted.
7. **Xiangbo Meng**, Mohammad Norouzi Banis, Dongsheng Geng, Yong Zhang, Ruying Li, and Xueliang Sun, Controllable Atomic Layer Deposition of One-dimensional nanostructured TiO₂, to be submitted.
8. **Xiangbo Meng**, Jian Liu, Mohammad Norouzi Banis, Jinli Yang, Ruying Li, and Xueliang Sun, Tunable Atomic Layer Deposition of CNT-based Lithium Titanium Oxide Nanocomposites, to be submitted.

(B) Peer-reviewed Journal Papers Related with This Thesis (Coauthor)

9. Yougui Chen, Jiajun Wang, **Xiangbo Meng**, Yu Zhong, Ruying Li, Xueliang Sun, Siyu Ye, and Shanna Knights, Atomic layer deposition assisted Pt-SnO₂ hybrid catalysts on nitrogen-doped CNTs with enhanced electrocatalytic activities for low temperature fuel cells, *Int. J Hydrogen Energy*, 2011, **36**, 11085-11092.
10. Xifei Li, Dongsheng Geng, Yong Zhang, **Xiangbo Meng**, Ruying Li, and Xueliang Sun, Superior cycle stability of nitrogen-doped graphene nanosheets as anode for lithium ion batteries, *Electrochem. Commun.*, 2011, **13**, 822-825.
11. Yougui Chen, Jiajun Wang, **Xiangbo Meng**, Yu Zhong, Ruying Li, Xueliang Sun, Siyu Ye, and Shanna Knights,

Controllable deposition of SnO₂ and its structural effect on the electrochemical durability and electrocatalytic activity of Pt electrocatalysts for PEMFC, submitted.

12. Xifei Li, Abirami Dhanabalan, **Xiangbo Meng**, Lin Gu, Xueliang Sun, and Chunlei Wang, Novel fractal nano-porous SiO₂ films on nickel foam fabricated by sol-gel assisted electrostatic spray deposition, 2011, submitted.
13. Xifei Li, **Xiangbo Meng**, Dongsheng Geng, Jinli Yang, Jian Liu, Ruying Li, and Xueliang Sun, Three dimensional sandwich-structured crystalline and amorphous SnO₂-graphene nanosheet composites with superior Li⁺ storage for high performance lithium ion battery anode materials, 2011, submitted.

(C) Previous Publications

14. **Xiangbo Meng**, Hui Zhang, and Jingxu Zhu, Characterization of particle size evolution of the deposited layer during electrostatic powder coating processes, *Powder Technol.*, 2009, **195**, 264-270.
15. **Xiangbo Meng**, Jingxu Zhu, and Hui Zhang, Influence of different powders on characteristics of particle charging and deposition during corona charging processes, *J. Electrostat.*, 2009, **67**, 663-671.
16. **Xiangbo Meng**, Jingxu Zhu, and Hui Zhang, The characteristics of particle charging and deposition during powder coating processes with ultrafine powder, *J. Phys. D. Appl. Phys.*, 2009, **42**, 065201.
17. **Xiangbo Meng**, Hui Zhang, and Jingxu Zhu, The characteristics of particle charging and deposition during powder coating processes with coarse powder, *J. Phys. D. Appl. Phys.*, 2008, **41**, 195207.

18. **Xiangbo Meng**, Jingxu Zhu, and Hui Zhang, The characteristics of current density distribution during corona charging processes of different particulates, *J. Phys. D. Appl. Phys.*, 2008, **41**, 172007.
19. **Xiangbo Meng**, Hui Zhang, and Jingxu Zhu, A general empirical formula of current- voltage characteristics for point-to-plane geometry corona discharges, *J. Phys. D. Appl. Phys.*, 2008, **41**, 065209.
20. Zhongli Ji, **Xiangbo Meng**, and Mingxian Shi, Characteristics of Instantaneous Flow outside Filter Tube of Ceramic Filter During Pulse Backfluch, *China Filtration and Separation*, 2001, **22**, 1-4.
21. Zhongli Ji, **Xiangbo Meng**, and Mingxian Shi, Experimental Measures of the Injecting Performance of the Back Pulse Jetting System of a Ceramic Filter (II)—the Measuring and Analysis of the Instantaneous Entrainment Ratio, *Chemical Engineering & Machinery*, 2000, **27**, 251-253.
22. Zhongli Ji, **Xiangbo Meng**, and Mingxian Shi, Experimental Measures of the Injecting Performance of the Back Pulse Jetting System of a Ceramic Filter (I) - the Measuring and Analysis of the Jetted Gas Flow, *Chemical Engineering & Machinery*, 2000, **27**, 187-189.
23. Zhongli Ji, **Xiangbo Meng** & Mingxian Shi, The Pulse-backing Cleaning Processes of Ceramic Filter, *Petroleum Science*, 2000, **3**, 20-24.
24. Zhongli Ji, and **Xiangbo Meng**, Measurement and Analysis of Flow Field inside Filtering Candle of Ceramic Filter During Pulse Cleaning Process, *Journal of the University of Petroleum*, 2000, **24**, 73-75.
25. Zhongli Ji, **Xiangbo Meng**, Fuxin Ding & Mingxian Shi, Instantaneous Velocity outside Filtration Element in Ceramic

Filter, *Journal of Chemical Industry and Engineering*, 2000, **51**, 165-168.

- 26. Xiangbo Meng**, and Zhongli Ji, Measurement and Analysis of Flow Parameters During Pulse Back Cleaning Process of Ceramic Filters, *Journal of the University of Petroleum*, 1999, **23**, 57-59.

(D) Conference Presentations and Abstracts

- 1. Xiangbo Meng** and Xueliang Sun, Highly tunable fabrication of nanostructured materials by atomic layer deposition, 11th International Conference on Atomic Layer Deposition, Cambridge, Massachusetts, USA, Jun. 2011.
- 2. Xiangbo Meng** and Xueliang Sun, Atomic layer deposition: a fine-tuning technique for synthesizing nanostructured materials, CAMBR (Center for Advanced Materials and Biomaterials Research) Distinguished Lecturer and Research Day, London, ON, Jun. 2011.
- 3. Xiangbo Meng**, Ruying Li, and Xueliang Sun, Atomic layer Deposition: a new technique to synthesize novel nanocomposites for renewable clean energy conversion and storage, **International Conference on Frontier Topics in Nanostructures and Condensed Matter Theory**, London, ON, Canada (Mar. 9-11,2011).
- 4. Xiangbo Meng**, Xifei Li, Yougui Chen, Dongsheng Geng, Yu Zhong, Ruying Li, Xueliang Sun, Atomic layer deposition (ALD): a new technique to synthesize nanostructured composites for energy conversion and storage, **The Electrochemical Society Inc. (Canadian Section)**, London, ON, Canada (Sept. 18, 2010).
- 5. Xifei, Li, Xiangbo Meng**, Dongsheng Geng, Jian Liu, Jiajun Wang, Yong Zhang, Yu Zhong, Dongniu Wang, Yongliang Li,

- Jinli Yang, Ruying Li, and Xueliang Sun, Nitrogen doped CNTs and SnO₂/graphene as anode materials for high performance lithium ion batteries, **The 15th International Meeting on Lithium Batteries (IMLB 2010)**, Montreal, QC, Canada (Jun. 27-Jul. 2, 2010,).
6. Xifei Li, Dongsheng Geng, **Xiangbo Meng**, Jiajun Wang, Jian Liu, Yongliang Li, Dongniu Wang, Jinli Yang, Ruying Li, and Xueliang Sun, Graphene and SnO₂/graphene as anodes of lithium-ion batteries, **The 15th International Meeting on Lithium Batteries (IMLB 2010)**, Montreal, QC, Canada (Jun. 27-Jul. 2, 2010,).
 7. Songlan Yang, Jian Wang, **Xiangbo Meng**, Ruying Li, Xueliang Sun, and Tsun Kong Sham, Characterization of Individual Fe₂O₃ Coated Carbon Nanotube by Scanning Transmission X-ray Microscopy, **VUVX2010: The 37th International Conference on Vacuum Ultraviolet and X-ray Physics**, Vancouver, BC, Canada (Jul. 11-16, 2010).
 8. Xifei Li, Jinli Yang, Jian Liu, Dongniu Wang, Yongliang Li, Jiajun Wang, Yong Zhang, Dongsheng Geng, **Xiangbo Meng**, Ruying Li, and Xueliang Sun, Nanostructured cathodes and anodes of high performance lithium ion batteries for EVs and HEVs applications, **NanoOntario 2010**, London, ON, Canada (May 16-18, 2010).
 9. **Xiangbo Meng**, Ruying Li & Xueliang Sun, Atomic layer deposition: a new technique for the elegant synthesis of nanostructured materials, **NanoOntario 2010**, London, ON, Canada (May 16-18, 2010).
 10. **Xiangbo Meng**, Hui Zhang, and Jesse Zhu, Small better than large: the mystery in powder coating processes, **1st PTRC (Particle Technology Research Centre) Research Symposium**, The University of Western Ontario, London,

Ontario, Canada (July 11, 2008).

11. Matthew Krantz, Qing Huang, and **Xiangbo Meng**, Ultrafine powder coating, **The 3rd OCE (Ontario Centers of Excellence) Annual Discovery Conference Student (Video) Competition**, Toronto, Ontario, Canada (May 12-13, 2008).

Awards and Honors:

1. **NSERC Postdoctoral Fellowship** (Natural Sciences and Engineering Research Council of Canada) (CND\$40,000/year) , 2011.
2. **Student Award** (US\$500) at 11th International Conference on Atomic Layer Deposition, Cambridge, Massachusetts, USA, 2011.
3. **Invited speaker** at 11th International Conference on Atomic Layer Deposition, Cambridge, Massachusetts, USA, 2011.
4. Nomination to **The 2009 National CAGS/UMI (Canadian Association for Graduate Studies/University Microfilms International) Distinguished Dissertation Award** for the Category of Engineering, Medical Sciences, and Natural Sciences by the Dean of Graduate Studies at The University of Western Ontario.
5. **The Best PhD Thesis** selected by The School of Graduate and Postdoctoral Studies Awards Selection Committee at The University of Western Ontario in 2009.
6. **2nd Prize** for OCE Student Competition (CND \$1,500), Ultrafine powder coating, *The 3rd OCE (Ontario Centers of Excellence) Annual Discovery Conference Student (Video) Competition*, Toronto, Ontario, Canada, May 12-13, 2008.
7. **Western Engineering Scholarship** from 2005-2011, The University of Western Ontario.